University of South Carolina
Scholar Commons

Theses and Dissertations

1-1-2013

Measurement and Three-Dimensional Modeling of Hydrodynamic Processes In the Inner Shelf and Surf Zone

Nirnimesh Kumar
University of South Carolina

Follow this and additional works at: https://scholarcommons.sc.edu/etd

Part of the Life Sciences Commons

Recommended Citation

Kumar, N.(2013). *Measurement and Three-Dimensional Modeling of Hydrodynamic Processes In the Inner Shelf and Surf Zone.* (Doctoral dissertation). Retrieved from https://scholarcommons.sc.edu/etd/2343

This Open Access Dissertation is brought to you by Scholar Commons. It has been accepted for inclusion in Theses and Dissertations by an authorized administrator of Scholar Commons. For more information, please contact digres@mailbox.sc.edu.

Measurement and Three-dimensional Modeling of Hydrodynamic Processes in the Inner Shelf and Surf Zone

by

Nirnimesh Kumar

Bachelor of Technology (Hons.)
Indian Institute of Technology, Kharagpur 2007

Master of Science
University of South Carolina 2010

Submitted in Partial Fulfillment of the Requirements

for the Degree of Doctor of Philosphy in

Marine Science

College of Arts and Sciences

University of South Carolina

2013

Accepted by:

George Voulgaris, Major Professor

Alexander Yankovsky, Committee Member

James L. Pinckney, Committee Member

John C. Warner, External Examiner

Lacy Ford, Vice Provost and Dean of Graduate Studies

© Copyright by Nirnimesh Kumar, 2013
All Rights Reserved.

Acknowledgments

This dissertation is representative of the work I conducted in last six years, most of which could not have been possible without the help and support of many individuals. The PhD journey would be way less interesting without George Voulgaris as my dissertation advisor. When I started working in the Coastal Processes and Sediment Dynamics (CPSD) Lab in 2007, I had almost no experience in data analysis or for working in field experiments. Nevertheless, George's office door was always open for me, and he was always patient in answering my questions. Also, George was fairly straightforward with his opinion, which certainly helped in getting an idea about my work quality, and at the same time allowed me to improve at each step. In last two years, my interactions with George had been more like a friend, and he has yielded to me the confidence to work independently.

A significant chunk of Chapter 3 and 5 of this work was conducted while working with John Warner at US Geological Survey, Woods Hole. John and his family were kind to host me at multiple occasions during my stay in Falmouth. John also agreed to be my dissertation committee member, and always had time for discussions or at times hour long phone conversations on coding esoteric mathematical equations. His constant support and encouragement, and not to mention vast knowledge of the numerical models, was helpful in finishing this work. In addition, I am also indebted to Jeff List for helping me with data analysis in the last two chapters of this dissertation. He also helped me in substantially improving my writing skill.

At USC I had wonderful time interacting with my committee members Sasha Yankovsky and Jay Pinckney. Sasha always welcomed discussions about physical

oceanographic concepts, and helped me in improving my understanding of geophysical fluid dynamics. It is also worth mentioning that Sasha is the best physical oceanography teacher I ever had. Jay was one of the major contributors for my knowledge in Biological oceanography, and he always made sure I present my work with implications in real life. His comments and suggestions have certainly made me relate my work to other research areas.

While working on this dissertation, I had the opportunity to interact with Rocky Geyer and Steve Lentz. Their knowledge contributed to my understanding of the vortex force formalism methodology used in this study. In addition, Steve provided me dataset for comparisons in Chapter 3. Falk Feddersen graciously provided comments and suggestions for last two chapters of this manuscript.

I thank Marinna Martini, Jonathan Borden and Brandy Armstrong for careful planning and execution of the 2010 Cape Hatteras field study, followed by a significant effort into data post-processing. Marinna helped me a lot in improving my data processing skills. The bathymetric dataset used in Chapter 6 was created by Brandy. She also let me stay at her place on multiple occasions. During my visits to US Geological Survey, Woods Hole, I also interacted with many scientists, which was fruitful in guiding my research. Many thanks to Maitane Olabarrieta, Soupy Dalyander, Rich Signell, Neil Ganju and Ilgar Safak.

This journey would not have been fun without my peers at USC. Si Chen was always a step ahead of me in this game, which forced me to finish the dissertation defense few weeks after hers. She has always been a terrific friend in discussing science questions, class homework, USC gossip and a great advisor in making life decisions. Timothy Nelson was a great lab mate not only in scientific discussions, but also in walking through dense bushes in laying cables during installation of radar systems. Rosario Sanay taught me the basics of using the ROMS modeling system. Jeff Morin taught the basics of data processing and also in planning of field deployments. In

addition, I thank Kerry McCarney Castle, Jessica Chassereau, Legna Torres, Joe Bell and Bridget Cotti Rausch for being terrific friends.

Even before I started working at the Univ. of South Carolina, my interests in Coastal Oceanography were encouraged and supported by Ashwini Otta during his brief stay at IIT Kharagpur. It has been more than six years since I finished my undergraduate education, nonetheless Ashwini is always happy to see me and discuss my progress. My friends from IIT Kharagpur, Goparaju Sreechakra, Shashi Bhushan Singh, Anshuman Mishra and Jayadev Acharya have been my support group for all these years. Many thanks for always being a phone call away. Smitalee Prusty, I wish I was as smart as you are. I have looked up to you as a source of inspiration from our 6th grade till the end of this degree.

My mother, father and sister were supportive for my decision to pursue a Ph.D. degree instead of pursuing a "real" job. Their trust and faith on me has always made me stick to my roots. Monica Jethwani has seen me struggle, fail and eventually succeed in the doctoral program. Not to mention innumerable flights and driving trips, home cooked meal, and constant love and support.

Computing support for this work was provided by Research Computing Center and Center for Computational Research and Cyber Infrastructure through Phil Moore and Jerry Ebalunode.

Funding for this study was provided by National Science Foundation (Award: OCE-1132130; 0451989 and 0535893) and Carolinas Coastal Processes Project, a cooperative study supported by the US Geological Survey.

Abstract

Wind stress and surface gravity waves play an important role in creating and modifying flows on the shelf. The importance of surface waves increases in shallow waters especially within the inner shelf and the surf zone. Understanding the generation and maintenance mechanisms of these flow patterns is a requirement for a number of environmental and ecological processes including the transport and fate of sediment, pollutants, buoyant river discharge and anthropogenic material introduced to the coastal zone. This dissertation examines inner shelf and surf zone circulation patterns through: (a) the development and validation of appropriate techniques to incorporate the effect of surface gravity waves on mean flows using the modeling framework of Regional Ocean Modeling System (ROMS) and the wave propagation model Simulating Waves Nearshore; and (b) a combination of field observations from acoustic instruments, High Frequency (HF) radars and coupled wave-current interaction based modeling system.

In the first chapter of this dissertation, the circulation module is extended for surf zone applications through modification and implementation of depth dependent radiation stress formulations which are used to simulate three-dimensional flows due to depth-limited breaking of incoming waves and their interaction with non-uniform bathymetry. It is identified that the radiation stress approach can perform satisfactorily inside the surf zone, but creates incorrect flow patterns outside the surf zone for shoaling and non-breaking waves.

In the second chapter, the aforementioned short-comings of the radiation stress formulation are addressed by implementation of the Vortex Force (hereinafter VF)

Formalism within the framework of the coupled ROMS-SWAN modeling system. This modification is shown to allow for the correct incorporation of surface wave effects and enabling the updated modeling system to work seamlessly from the inner shelf all the way to the surf zone. The VF formalism is evaluated against field data for wave breaking driven currents and also for non-breaking wave driven flows outside the surf zone and is shown to perform exceptionally well.

In the third chapter, a practical application of the modified modeling system is presented where the model can be used as a rip current forecasting system. Although this application is presented using the Radiation Stress formulation, the same methodology can be used with the Vortex Force formalism. As a part of this work a methodology for incorporating bathymetry uncertainties in such prediction system is also presented.

In the fourth chapter in-situ point measurements of waves and currents obtained at various locations throughout the nearshore region of Cape Hatteras, North Carolina (USA) are presented. The data are used to reveal the alongshore momentum balance around a cuspate foreland system. The analysis indicates that on the windward side of the cape, a balance between wind and bottom stress is present in deeper waters, while on the leeward side, no balance exists between wind and bottom stress. Closure of the balance requires development of a pressure gradient in response to wind forcing. In shallower waters, wave breaking, VF, and nonlinear advective acceleration terms are found to be important as well.

A similar momentum balance analysis is carried out using the results of the Coupled Ocean-Atmosphere-Wave-Sediment transport modeling system which is set up in a nested framework capable of resolving wave variability and flows throughout the inner shelf to coastline, including the surf zone. Analysis of the simulated results reveals a contribution of pressure gradient term on both sides of Cape Hatteras. On the windward side, pressure gradient and wind stress balance the bottom stress, while

on the leeward side the wind stress is balanced by the pressure gradient. The shallow shoal complex extending seaward from Cape Hatteras point acts like a coastline in regulating wave propagation and flow pattern for different synoptic wind and wave conditions.

Table of Contents

Acknowledgments iii

Abstract vi

List of Tables xii

List of Figures xv

Chapter 1 Introduction 1

1.1 Scope of this Dissertation 4

Chapter 2 Implementation and modification of a three dimensional radiation stress formulation for surf zone and rip-current applications 11

2.1 Introduction 13

2.2 Implementation of Updated Forcings 16

2.3 Nearshore Circulation Cell Cases 30

2.4 Discussion 44

2.5 Limitations of Mellor, 2011 Approach 50

2.6 Conclusions 53

Chapter 3 Implementation of the vortex force formalism in the Coupled Ocean-Atmosphere-Wave-Sediment Transport (COAWST) modeling system for inner shelf and surf zone applications 78

3.1 Introduction 81

3.2 Model Formulation 85

3.3 Numerical Implementation 89

3.4 Model Simulations 101

3.5 Discussion 132

3.6 Summary and Conclusions 137

Chapter 4 A Methodology for the Prediction of Rip Currents using a three-dimensional Numerical, Coupled, Wave-Current Model 165

4.1 Introduction 167

4.2 Background on Rip Current Development 169

4.3 Objectives 172

4.4 Methodology 173

4.5 Study Case: Duck, NC 179

4.6 Discussion 182

4.7 Conclusions 184

Chapter 5 Alongshore momentum balance analysis on a cuspate foreland 193

5.1 Introduction 195

5.2 Data Collection 196

5.3 Results 199

5.4 Momentum Balance Analysis 203

5.5 Discussion 210

5.6 Summary and Conclusions 217

Chapter 6 Modeling the inner-shelf and surf zone flow dynamics around a cuspate foreland using coupled wave-current interaction model 234

6.1 Introduction 236

6.2 Site Description 238

6.3 Model Description and Set-Up 239

6.4 Model Validation 246

6.5 Results 254

6.6 Discussion 261

6.7 Conclusions 269

Chapter 7 Conclusions 303

7.1 Future Directions 309

Bibliography 312

Appendix A- Copyright Permissions 342

List of Tables

Table 2.1 RMS error (normalized by the maximum value) for the simulated current velocities using M03, M08-11_{top} and M08-11_{vrt} formulations for Case2 (DUCK94 experiment). 75

Table 2.2 The RMS error (normalized by the maximum value) for the simulated current velocities using M03 and M08-11_{vrt} formulations for Case5 (nearshore barred morphology with rip channels). 75

Table 3.1 COAWST options available for the computation of non-conservative wave forces (for details see Sec. 3.2). 160

Table 3.2 List of the components which constitute the total pressure gradient force (Eqn. 50). 161

Table 3.3 Model configuration for different DUCK' 94 simulations. RS_{2D} refers to simulations conducted using depth-averaged, radiation stress based model, while simulations done using the VF formalism are referred to as VF. α_r is the coefficient which determines the percentage of wave breaking induced dissipation contributing to creation of wave rollers (Eqn. 3.34), while c_{ew} is the percentage of total dissipation going as turbulent kinetic energy (Eqns. 3.43 and 3.48). 162

Table 3.4 Normalized root mean square error $\epsilon_{rms}(j,k) = \left\{ \dfrac{\sum_{i=1}^{n}(d_{ij} - m_{ijk})^2}{\sum_{i=1}^{n}(d_{ij})^2} \right\}^{0.5}$ for the cross-shore and longshore velocity estimates for DUCK' 94 for various locations across the profile and the different model simulations (Runs 2-10, see Table 3.3). d_{ij} and m_{ijk} represent measured (from Garcez-Faria et al., 1998, 2000) and model estimated velocity values at the 7 cross-shore locations (j) and various elevations (i) above the sea bed (for measurement locations see Fig. 3.10). Station 1 is closest to the shoreline. Numbers in bold typeface indicate minimum values. 163

Table 3.5 The RMS error (normalized by the maximum observed value) for the simulated cross-shore velocities for nearshore barred beach with rip channels (sec 3.4.3). 164

Table 3.6 The RMS error (normalized by the maximum value) for the simulated cross-shore and longshore velocities for wave-induced flows in the inner shelf (sec 3.4.4). 164

Table 5.1 List of instruments deployed around Cape Hatteras point during February, 2010. Key: AQD: Nortek aquadopp, ADCP: Teledyne RD Instruments acoustic Doppler current profiler. 220

Table 5.2 Correlation coefficient (r) between wind stress and local alongshelf (v) and cross-shore (u) velocity components. r values in italics are not significant at the 95% confidence level. 230

Table 5.3 Standard deviation of local alongshore depth-averaged momentum balance terms. No values are shown for terms/site combinations which could not be calculated. All units in 10^{-6} ms^{-2}. . . . 231

Table 5.4 Correlation coefficient (r) between bottom stress (BS) and forcing terms of depth-averaged momentum balance.r values in italics are not significant at the 95% confidence level. Key: SS = surface stress; BA = breaking acceleration. 231

Table 5.5 Correlation coefficient (r) between forcing and response terms of depth-averaged momentum balance.r values in italics are not significant at the 95% confidence level. Bold typeface values represent the maximum correlation coefficient value for given combination of forcing and response terms. Key: BA= Breaking acceleration; NA= Nonlinear advective acceleration; VF= Vortex Force; SS= Surface Stress; BS= Bottom Stress; LA=Local Acceleration; and SC= Stokes-Coriolis term. 232

Table 5.6 Slope (m) and intercept (c) for the relation [R=mF+c]. F is the forcing term determined from Table 5.4 to have maximum correlation to the response term (R). 95% confidence interval for m and c are shown. On using the algorithm of Krystek and Anton (2007) instead of using a standard linear regression technique, and assuming 50% uncertainty in both forcing and response terms, only slightly modifies the regression coefficients and slopes shown here. 233

Table 6.1 Correlation coefficient (r) and model skill (S) for simulating wave parameters at offshore buoys 300

Table 6.2 Correlation coefficient (r) and model skill (S) for simulating wave parameters around the shoal complex. 301

Table 6.3 Correlation coefficient (r) and model skill (S) for simulating vertical profile (u_z, v_z) and depth-averaged (u_d, v_d) eastward and northward flows. 301

Table 6.4 Correlation coefficient (r) and model skill (S) for simulating along and cross-shore surface Lagrangian velocities against measurements from VHF Radar. 301

Table 6.5 Description of wind direction, significant wave height, and wave direction for six events considered during the simulation period. . . 302

List of Figures

Figure 1.1 Schematic showing vertical distribution of offshore directed Eulerian mean flow (blue arrows) and Stokes drift (red arrows) within the surf zone and inner shelf. The solid horizontal green line represents the adjusted mean sea level in presence of surface gravity waves, while the dashed horizontal line is the resting mean sea-level. This figure has been modified from Lentz et al., 2008. 9

Figure 1.2 Time series of low-pass filtered (a) along and cross-shore wind velocity (ms^{-1}) from NOAA meteorological station in Folly Island, SC; (b) depth-averaged, Eulerian mean cross-shore velocity (solid red, ms^{-1}) calculated by averaging the vertical profile of cross-shore velocity, and the depth-averaged Stokes drift (solid black, ms^{-1}) estimated using a formulation based on significant wave height, wave direction and peak wave period. The sign of Stokes drift has been reversed for comparison to Eulerian mean flows; (c) Significant wave height (m); (d) Vertical profile of subtidal cross-shore velocity (ms^{-1}); and (e) Vertical profile of subtidal alongshore velocity (ms^{-1}) obtained from an Acoustic Doppler Current Profiler deployed in Folly Island, SC at a water depth of 6 m (see Voulgaris et al., 2008). 10

Figure 2.1 Case 1: Obliquely incident waves on a planar beach using the original radiation stress forcing M03, the updated forcing applied at the top layer M08-11_{top}, and with a vertical distribution as defined by Eqn. 10 of M08-11_{vrt}. Cross-shore distribution of: (a) significant wave height, water depth and sea surface elevation; The water depth and wave height have been scaled as h/20 and Hsig/10, respectively; (b) depth averaged Eulerian mean cross-shore velocity $\overline{u^e}$; and (c) depth averaged Eulerian mean alongshore velocity $\overline{v^e}$. 56

Figure 2.2 Comparison of vertical profile of cross-shore Eulerian mean velocity, u_e (x, z) between simulations using M03 (solid grey line), M08-11_{top} (dashed black line), M08-11_{vrt} (solid black line). The sea surface elevation (ζ, dotted grey line) is also shown. Vertical black lines indicate locations of model sampling and zero value for each profile. 57

Figure 2.3 Case 2: Obliquely incident waves on a barred beach (DUCK94 experiment) using the original radiation stress forcing M03, the updated forcing applied at the top layer M08-11_{top}, and with a vertical distribution as defined by Eqn. 10 of M08-11_{vrt}. Cross-shore distribution of: (a) significant wave height (H_{sig}) and water depth (h). The water depth and wave height values shown are scaled as $h/10$ and $H_{sig}/2$, respectively, for plotting purposes; (b) sea surface elevation (ζ); (c) depth averaged Eulerian mean cross-shore velocity ($\overline{u^e}$); and (d) depth averaged Eulerian mean alongshore velocity ($\overline{v^e}$). 58

Figure 2.4 Comparison of vertical profiles of (a) cross-shore (u_e(x, z)); and (b) longshore (v_e(x, z))Eulerian mean velocities; from model simulations using M03 (solid grey lines); M08-11top (dashed black lines), M08-11vrt (solid black lines) and field measurements (grey squares). Vertical grey lines indicate locations of model sampling and zero velocity value for each profile. The horizontal velocity profile data are from Garcez-Faria et al. (1998, 2000). 59

Figure 2.5 Color shading of significant wave height distribution over the computational domain after 2 hours of model simulation for two-way coupling between ROMS and SWAN. Note the significant wave height at offshore boundary is 1.5 m at the ends and decreases to a minimum value of 1 m at the center of the domain. The alongshore and cross-shore domain has been scaled by a value of (λ=2π/1000). Black dashed lines indicate the location of transects shown in Figure 2.8, while grey dashed line shows the location of the surf zone. The horizontal, black, dotted lines indicate the location of alongshore transect shown in Figure 2.17. 60

Figure 2.6 Rip current simulation results for the bottom half of the computational domain (Case 3, two-way coupling) after 2 hours of simulation. (a) Depth averaged Lagrangian mean velocity distribution ($\overline{u^l}$); (b) Transport stream function (ψ) showing formation of circulation cell in the surf zone; (c) Transport stream function (ÏĹ) calculated using the analytical solution provided by Bowen, 1969 for the present model setup. Note: λx=π/2 (shown by grey dashed line) is the location where waves start breaking. 61

Figure 2.7 Transport stream function, ψ over the computational domain for Reynolds number (Re) values of (a) 500, (b) 125, (c) 62.5, and (d) 42. Note the solution gets skewed about the individual centers of the circulation cells with increased Re values causing a narrower outflow from shallower to deeper waters and broader inflow from deeper to shallower waters. Also note that the individual circulation cells are not exactly symmetric about the line y= π. The grey circulation cell in (a), (b), and (c) is same as (d); it is shown for comparison purposes. The vertical, grey dashed line shows the location where waves start breaking. 62

Figure 2.8 Contour plots showing the vertical structure of the Eulerian, cross-shore (a, b, c) and alongshore velocity (d, e, f) along three transects located at λy=$\pi/5$ (a, d), λy=$\pi/2$ (b, e), and λy=$4\pi/5$ (c, f) from the southern lateral boundary (see dashed lines in Figure 2.5). Solid black line corresponds to zero velocity. . 63

Figure 2.9 (a) Depth averaged Eulerian mean, velocity (black arrows) after 1 hour of simulation. Light grey lines in background depict the bathymetry contours; (b) Contour of significant wave height distribution over the computational domain. The incident wave height at the offshore boundary of the domain is 0.92 m. Contour plots showing the vertical structure of cross-shore Eulerian mean velocity, u_e(x, z)) along two transects located at (c) y=0 m, (d) y=40 m from the southern lateral boundary (see grey lines in Figure 2.9b). The grey dotted alongshore transect in Fig. 2.9b is the location at which alongshore momentum balance term is shown in Fig. 2.17(c). 64

Figure 2.10 Transport stream function (ψ) over the computational domain computed from the model results after (a) depth averaging the horizontal Lagrangian mean velocity field; (b) and from Noda (1974) paper. 65

Figure 2.11 Bathymetry for Case 5, showing the longshore bar and the rip channels. The solid black lines show the location of vertical transects at which the cross-shore velocity distribution is discussed in Fig. 2.14. The 4 horizontal white lines represent the alongshore transects at which cross-shore momentum balance terms are shown in Fig. 2.15 and alongshore momentum balance term is shown in Fig. 2.17(d). 66

Figure 2.12 Contours of significant wave height after 30 minutes of model simulation using (a) the original version of the model as in HW09 and; (b) the modified M08-11 formulations for the vertical distribution of the radiation stress (M08-11_{vrt}). Bathymetric contours and depth integrated Eulerian, mean currents over the computational domain using (c) the original version of the model as in HW09 and; (d) the modified M08-11 formulations for the vertical distribution of the radiation stress (M08-11_{vrt}). The black line (2.12c) depicts a velocity of 0.5 ms^{-1}. 67

Figure 2.13 Cross-shore variation of mean sea surface elevation at two locations corresponding to alongshore positions centered at the middle of the rip channel (black) and alongshore bar (grey). 68

Figure 2.14 Vertical structure of cross-shore Eulerian mean velocity u_e *(x, z)* at the center of rip channel (a and b) and bar (c and d) derived from original version of the model as in HW09 (a and c) and the M08-11_{vrt} formulations (b and d); (e) Comparison of normalized model derived cross-shore velocity with normalized data from Haas and Svendsen, 2002 (key: symbols ● and ■ denote data at the center and 4 m off the channel, grey line (center of the channel M03), black dash dot (center of the channel M08-11_{vrt}), blue dashed line (M08-11_{vrt}, 4 m off the channel). 69

Figure 2.15 Alongshore variation of the depth averaged cross-shore momentum balance equation terms. Horizontal advection (ADV_H , $\partial/\partial x(U^2h) + \partial/\partial y(UVh)$, black line), bottom stress (BT, τ_x^b/ρ, grey line) and radiation stress forcing ($\partial S_{xy}/\rho\partial y$, black dashed) terms are shown in (a) to (d). Cross-shore pressure gradient (PG, gh($\partial\eta/\partial x$), black line), radiation stress forcing (RAD_H, $\partial S_{xx}/\rho\partial x$, grey line) and horizontal viscosity ($VISC_H$, $\partial(A_H/\rho\partial u/\partial x)\partial x$, black dashed) are shown in (e) to (h). The distances at which the terms are estimated are 40 m (a) and (e), 30 m (b) and (f), 26 m (c) and (g), and 20 m (d) and (h) from the shoreline (see Fig. 2.11). 70

Figure 2.16 Contour of sediment transport proxy (P_{st}) over computational domain for the run of Case 3 of alongshore variable wave forcing. 71

Figure 2.17 (a) Depth averaged, alongshore, Eulerian velocity, $\overline{v^e}$ at alongshore transects shown by dotted line in Fig. 2.5 for Case 3, dotted line in Fig. 2.9b for Case 4 and alongshore transect onshore of the rip channel (Fig. 2.11) for Case 5; Alongshore variation of the depth averaged alongshore momentum balance terms for (b) Case 3 and (c) Case 4 for alongshore transect as 2.17(a), (d) Case 5 for alongshore transect as 2.17(a). The alongshore normalizing length scale (L_y) used in (b), (c) and (d) are 1000 m, 80 m and 90 m, respectively, and represent the corresponding perturbation length in forcing or bathymetry (key: alongshore pressure gradient (PG, gh($\partial\eta/\partial y$), black line), radiation stress forcing (RAD_H, ($\partial S_{yy}/\rho\partial y+ \partial S_{xy}/\rho\partial x$), black dashed), horizontal advection (ADV_H , $\partial/\partial x(UVh) + \partial/\partial y(V^2h)$, grey line), bottom stress (BT, τ_y/ρ, grey dashed-dot line)) 72

Figure 2.18 Circulation (depth averaged, Eulerian mean current vector, top row), significant wave height distribution (middle row) and vorticity field (bottom row) results for different wave incident angles (columns one to four correspond to angles 0, 5, 10 and 20 degrees, respectively). The thin grey lines in top row, column one shows the alongshore transects at which relevant terms are plotted in Figure. 2.19. Note: The bathymetry used in this case is same as Figure 2.11, but only the relevant part of the domain has been shown here. 73

Figure 2.19 Eulerian mean cross-shore velocities (top panel) and absolute value of alongshore gradient of Eulerian alongshore velocities (bottom panel) at 3 alongshore transects located (a) 16 m, (b) 22 m, (c) 28 m from the shoreline as shown by grey lines n Fig. 2.18 (top panel, column (a)) for waves incident at angles 0°, 5°, 10°, 20°. 74

Figure 2.20 Model forcing (wave height) and non dimensional depth (a and c) and bottom bathymetry (b and d) used to test the Mellor (2008) formulation. (a) and (b) are identical as in Ardhuin et al. (2008). Forcing in (c) is the same as (a) but the bathymetry (d) has a reduced bottom slope (note differences in horizontal scale between b and d). 76

Figure 2.21 Vertical distribution of Lagrangian mean velocity, u^l (x, z) (Eulerian mean velocity + Stokes drift) calculated using (a) M08-11_{top} with a domain geometry as in Ardhuin et al. (2008); (b) M08-11_{vrt} on the same domain as (a); and (c) M08-11_{vrt} with a similar geometry but reduced bottom slope (note differences in horizontal scale), uniform vertical mixing and bottom friction. Contour line spacing is 0.01 ms^{-1} in (a), (b) and 0.002 ms^{-1} in (c). Note different scales in colorbar used in (c). 77

Figure 3.1 Obliquely incident waves on a planar beach simulated using the VF, the RS_{2D} model and analytical solution (see Eqn. 3.49). Cross-shore distribution of (a) root-mean-square wave height (H) and water depth (h); (b) sea surface elevation, ζ^c and depth-induced wave dissipation (ϵ_b). 140

Figure 3.2 Cross-shore sections of Eulerian (a, b and c) and Stokes (d, e and f) velocities from the VF model. (a) cross-shore (u); (b) longshore (v); and (c) vertical (w) Eulerian velocities. (d) cross-shore (u^{st}); (e) alongshore (v^{st}); (f) vertical (w^{st}) Stokes velocities; Cross-shore distribution of (g) depth-averaged, cross-shore Eulerian velocity ($\overline{u}$) and Stokes velocity ($\overline{u^{St}}$); and (h) depth-averaged, alongshore ($\overline{v}$) Eulerian velocity for obliquely incident waves on a planar beach simulated using the VF, the RS_{2D} model and analytical solution (see Eqn. 3.49). 141

Figure 3.3 Vertical and horizontal cross-shore distribution of the various cross-shore (x) and longshore (y) momentum balance terms. Cross-shore terms: (a) x- breaking acceleration (x-BA) ; (b) x-horizontal advection (x-HA); (c) x-horizontal vortex force (x-HVF); (d) x- pressure gradient (x-PG); (e) x- vertical mixing (x-VM); and (f) x-vertical advection (x-VA); Longshore terms: (g) y- breaking acceleration (y-BA) ; (h) y-horizontal advection (y-HA); (i) y-horizontal vortex force (y-HVF); (j) y- pressure gradient (y-PG); (k) y- vertical mixing (y-VM); and (l) y-vertical advection (y-VA)term. 142

Figure 3.4 Cross-shore variation of depth-averaged (a) cross-shore; (b) longshore momentum balance terms; and (c) decomposed PGF terms in cross-shore as described in Eqn. 3.50. 143

Figure 3.5 Obliquely incident waves on a barred beach simulated using the VF model (no roller model, i.e., Run 2) and the RS_{2D} (Run 1) model (see Table 3.3). Cross-shore distribution of: (a) root mean square wave height (H) from SWAN (solid black line), observed wave height (from Elgar et al., 1997; grey circles) and water depth (h). (b) Sea surface elevation (ζ^c) and depth-induced wave dissipation (ϵ_b). (c) Depth-averaged, cross-shore Eulerian velocity, ($\overline{u}$). (d) Depth-averaged, longshore Eulerian velocity ($\overline{v}$) along with observed velocity (from Feddersen et al., 1998; grey circles). 144

Figure 3.6 Cross-shore variability of (a) total dissipation (breaking + roller dissipation) and depth-averages of three-dimensional (b) cross-shore, $\overline{u}$ and (c) longshore velocity, $\overline{v}$ estimates, for different values of α_r (Runs 2-6, Table 3.3). 145

Figure 3.7 Comparison of model results (Runs 2, 4 and 6; i.e., VF model with α_r=0, 0.5 and 1, respectively) with observed vertical profiles (grey squares) of cross-shore (a) and longshore (b) velocities. Vertical grey lines indicate profile measurement locations and zero value for each profile (Data from Garcez-Faria et al. 1998; 2000). Vertical structure of eddy viscosity (c), K_v and turbulent kinetic energy (d), TKE from model simulations at the same cross-shore locations as the velocities. 146

Figure 3.8 Comparison of model results (Runs 6, 9 and 10; VF model with rollers, α_r=1 and wave-induced mixing with $c_{\epsilon w}$=0, 0.01 and 0.05, respectively) with observed vertical profiles (grey squares) of cross-shore (a) and longshore (b) velocities. Vertical grey lines indicate profile measurement locations and zero value for each profile (Data from Garcez-Faria et al. 1998; 2000). Vertical structure of eddy viscosity (c), K_v and turbulent kinetic energy (d), TKE model simulations at the same cross-shore locations as the velocities. 147

Figure 3.9 Cross-shore sections showing horizontal and vertical variability of Eulerian and Stokes velocity components for Run 6 (VF model with wave rollers, α_r=1 and no wave mixing). (a) cross-shore (u); (b) longshore (v); and (c) vertical (w) Eulerian velocities; (d) Cross-shore (u^{St}); (e) longshore (v^{St}); and (f) vertical (w^{St}) Stokes velocity. 148

Figure 3.10 Cross-shore and vertical distribution of the terms contributing to the cross-shore (x) and longshore (y) momentum balance for Run 6 (VF model with wave rollers, α_r=1 and no wave mixing). Cross-shore terms: (a) x-breaking acceleration (x-BA) ; (b) Eulerian, x-horizontal advection (x-HA); (c) x- horizontal vortex force (x-HVF); (d) x- pressure gradient (x-PG); (e) x-vertical mixing (VM); (f) x-vertical advection (VA); and alongshore terms: (g) y-breaking acceleration (y-BA); (h) Eulerian, y-horizontal advection (y-HA); (i) y-horizontal vortex force (y-HVF); (j) y-pressure gradient (y-PG); (k) y-vertical mixing (y-VM); and (l) y-vertical advection (y-VA). 149

Figure 3.11 Cross-shore variation of depth-averaged (a) cross-shore and (b) longshore momentum balance terms. (c) Decomposed PGF terms in cross-shore as described in Eqn. 49 for Run 6 (VF model with wave rollers, α_r=1 and no wave mixing). 150

Figure 3.12 Rip channel case. (a) Bathymetric domain; (b) significant wave height (contours) and direction (arrows); and (c) vorticity vector after 1 hour of model simulation. Black arrows in (c) show the depth averaged, Eulerian velocity vector. The white line in (c) shows velocity strength of 0.5 ms^{-1}. The solid white lines in (a) show the transects along which cross-shore and longshore momentum balances are described in Figures 3.15 to 16. 151

Figure 3.13 Vertical structure of cross-shore Eulerian velocity at (a) the center of rip channel and (b) over the bar. Results derived from VF based model simulations. (c) Comparison of normalized model derived cross-shore velocity with normalized data from Haas and Svendsen, 2002 (key: symbols ■ and ■ and grey and black lines denote data and model results at the center and 8 m off the channel, respectively). 152

Figure 3.14 Example of unstable rip current conditions simulated using with a linear bottom friction (μ=0.002 m) and a horizontal mixing of 0.05 m^2s^{-1}. Snapshots of vorticity and depth-averaged, Eulerian velocity vector for six different time steps with a time interval of 20 min. Only the computational domain in the vicinity of the rip channel is shown here. 153

Figure 3.15 Cross-shore distribution of vertical profiles of contributing terms in cross-shore (x)- and longshore (y) momentum balance at y=180m (see Fig. 3.12 for transect location). Cross-shore terms: (a) x-breaking acceleration (x-BA); (b) Eulerian, x-horizontal advection (x-HA); (c) x-horizontal vortex force (x-HVF); (d) x-pressure gradient (x-PG); (e) x-vertical mixing (x-VM); (f) x-horizontal mixing (x-HM); Longshore terms: (g) y-breaking acceleration (y-BA); (h) Eulerian, y-horizontal advection (HA); (i) y-horizontal vortex force (y-HVF); (j) y-pressure gradient (y-PG); (k) y-vertical mixing (y-VM); and (l) y-horizontal mixing (y-HM). 154

Figure 3.16 Longshore distribution of vertical profile of contributing terms in cross-shore (x) and longshore (y) momentum balance at x=70m (see Fig. 3.12 for transect location). Cross-shore terms: (a) x-breaking acceleration (x-BA); (b) Eulerian, x-horizontal advection (x-HA); (c) x-horizontal vortex force (x-HVF); (d) x-pressure gradient (x-PG); (e) x-vertical mixing (x-VM); (f) x-vertical mixing (x-VM); Longshore terms: (g) y-breaking acceleration (y-BA); (h) Eulerian, y-horizontal advection (y-HA); (i) y-horizontal vortex force (y-HVF); (j) y-pressure gradient (y-PG); (k) y-vertical mixing (y-VM); and (l) y-horizontal mixing (y-HM). 155

Figure 3.17 Cross-shore (a) and longshore (b) velocity profiles from model simulations with constant vertical viscosity (K_M) values ranging from 10^{-6} to 10^{0} m^2s^{-1}. The model simulations were carried out assuming a normally incident wave with significant wave height of 2 m and wave period of 7 s. 156

Figure 3.18 Observed (from Lentz et al, 2008) and simulated cross-shore (a) and longshore (b) velocity profiles for different ranges of significant wave height (Hsig). Individual model profiles estimates for wave height values from 0 to 3.5 m with an interval of 0.25 m are shown as thin grey lines while the thicker solid lines show velocity profiles averaged over specific wave height ranges as shown in insert. Simulations were carried out with a constant viscosity of 10^{-5} m^2s^{-1}. 157

Figure 3.19 Cross-shore distribution of cross-shore (a, b) and longshore (c, d) momentum balance terms from the VF model (a, c) and RS_{2d} (b, d) model simulations for obliquely incident waves on a planar beach (Sec 3.4.1). 158

Figure 3.20 Cross-shore distribution of cross-shore (a, b) and longshore (c, d) momentum balance terms from the VF (a, c) and RS_{2D} (b, d) models for obliquely incident spectral waves on a barred beach (Sec. 3.4.2). The VF and RS_{2D} simulation corresponds to Run 6 (VF model with wave rollers, α_r=1 and no wave mixing) and Run 2 (radiation stress model) as described in Table 3.3. 159

Figure 4.1 Schematic diagram showing the length scales required to construct a bar trough morphology domain to model rip current channel. (a) Plan view; (b) and (c) beach profiles at rip channel and over bar respectively. The bar length (L) will be 3.3 times the length of the surf zone width (X_c) which will be estimated from empirical orthogonal functional (EOF) analysis on time series of beach profile, while the channel width (L_t) will be taken L/5. 185

Figure 4.2 EOF analysis of 20 year long, monthly beach profile record at Duck, NC and the creation of a synthetic profile. (a) Individual profiles (grey lines) and mean profile (black line) as obtained by EOF; (b) Cross-shore profile of bar functions obtained from EOF analysis on individual profiles. The solid and dashed lines show two most commonly occurring bar distribution; (c) Solid black and grey lines correspond to the barred beach profiles obtained by adding the mean profile in (a) to bar distribution in (b). The dashed black and grey lines show the rip channel profile obtained by joining a straight line from bar trough to end or beginning of the bar crest for Case A and B, respectively. 186

Figure 4.3 Joint probability distribution of bar characteristics (bar width, height, distance from shoreline) for Duck NC. Bar characteristics identified from the EOF analysis (see Fig. 4.2). Note two distinct bars occurring that correspond to typically observed summer and winter profiles. 187

Figure 4.4 Synthetic bar-trough morphology for cases A and B (left and right panels, respectively) and corresponding depth-averaged current vectors for an incoming wave with 2m height, period of 8s, approximately perpendicular to the coastline. The solid white lines show the bathymetry contour, while the black arrows show the direction and magnitude of the flow field. The dashed grey lines indicate location of transects at which the vertical profile of cross-shore velocity are considered in Fig. 4.5, 4.6 and 4.7. 188

Figure 4.5 Vertical distribution of cross-shore velocity at the center of the rip channel (a and c) and bar (b and d) for bathymetric domain corresponding to case A (a and b) and B (c and d), respectively. Thick black lines show the cross-shore profile of significant wave height. The location of transects is shown in Fig. 4.4. 189

Figure 4.6 Cross-shore velocity (color contours) and significant wave height (black line) distribution along a transect through the rip channel location (case A) for three tidal stages: (a) high; (b) mean and (c) low water levels. Thin black lines represent wave height distribution across the domain as estimated by SWAN. Note how the speed of the rip current increases with decreasing water level, while the offshore location of the maximum rip speed remains the same. The arrow direction indicates direction of flow; while the color contours indicate strength of the current. . . 190

Figure 4.7 Cross-shore velocity (color contours) and significant wave height (black line) distribution along a transect through the rip channel location (case B) for three tidal stages: (a) high; (b) mean and (c) low water levels. Thin black lines represent wave height distribution across the domain as estimated by SWAN. Note how the speed of the rip current increases with decreasing water level, while the offshore location of the maximum rip speed remains the same. The arrow direction indicates direction of flow, while the color contours indicate strength of the current (units in color bar are m/s). The relative location of the bar is shown as a grey line. 191

Figure 4.8 Circulation (depth averaged current vector, top row) and significant wave height distribution (bottom row) for the bathymetric domain corresponding to case B but with a varying channel width, (a) L_t=20m; (b) L_t=40m; (c) L_t=60m; (d) L_t=80m; (e) L_t=100m. Note: Only relevant part of the model domain has been shown here. 192

Figure 5.1 Map showing the study area (Cape Hatteras, NC), the nearshore bathymetry and data collection sites. Bathymetry contours shown are in m. The prefix "N" and "O" in the station names suggest nearshore (mean water depth less than 8 m) and offshore sites, respectively. The stations used in the analyses are shown with a larger font. Solid black lines are the transects along which the beach profiles are provided in (c). The location of the NOAA Diamond Shoals buoy is shown in (b). 219

Figure 5.2 Meteorological and wave data from the Diamond Shoals buoy (NOAA/NDBC Station ID: 41025) for February, 2010. Time series of (a) wind velocity vector in oceanographic convention; (b) significant wave height; (c) surface wave spectrum (m^2/Hz). The 0.1 Hz cut-off used to separate sea and swell frequencies is also shown; (d) peak (black dots) and mean (solid black line) wave period); (e) Atmospheric pressure (solid black line); and (f) air (black) and water (gray) temperature. Dark gray shaded areas correspond to passage of synoptic meteorological fronts, and light gray shaded regions are the swell events. 221

Figure 5.3 Time series of (a) water depth, (b) root mean square wave height, (c) Peak (dots) and mean (solid) wave period, and (d) mean wave direction (°N) for the east (left panel, subscript 1) and south sides (right panel, subscript 2), respectively. The shaded areas indicate periods of frontal passage (dark gray shade) and swell events (light gray shade) as in Figure 5.2. 222

Figure 5.4 Synoptic description of wind forcing and depth-averaged subtidal currents described by their mean (black arrows) and vector variance ellipses for the full period of data collection for each site (see Table 5.1). The local coordinate (x, y) systems used at each side are also shown. 223

Figure 5.5 Time series of local (a) subtidal alongshore (solid black) and cross-shore (solid gray) wind stress; (b) alongshore ; and (c) cross-shore currents on the east (left panel, subscript 1) and the south side (right panel, subscript 2). The vertical scale in (b) and (c) is shifted vertically for each station for clarity. Dark and light gray shaded regions correspond to the periods of frontal passage and swell events, respectively. The coordinate systems for the east and south sides are shown in Figure 5.4. . . . 224

Figure 5.6 Time series of low-pass filtered (a) surface stress, (b) breaking acceleration for the east (left panel, subscript 1) and south (right panel, subscript 2) sides No depth-limited wave breaking was observed a site O2, O1 and N9 during the deployment period. 225

Figure 5.7 Time series of low-pass filtered response terms in depth-averaged alongshore momentum balance (equation [2]) for the east (left panel, subscript 1) and south (right panel, subscript 2) sides and for different sites (see key). (a) Local Acceleration; (b) Coriolis acceleration; (c) Stokes-Coriolis force; (d) Nonlinear Advective Acceleration; (e) Vortex Force and (f) Bottom stress. Please note that the vertical scales in d, e and f, are 10 times the vertical scale in a, b and c. 226

Figure 5.8 Time series of response (gray) and forcing (black) terms at north (left panel, subscript 1) and west (right panel, subscript 2). The relevant forcing and response terms at each site are listed in Tables 4 and 5. Note the different vertical scales used. 227

Figure 5.9 Time series of (a) average (between Site O1 and N9) observed (black) and predicted (gray) alongshore velocity (ms-1); (b) predicted (black) pressure gradient terms and local alongshore wind speed from NOAA-NDBC Diamond shoals buoy (for definition of local coordinate system see Figure 5.4). 227

Figure 5.10 (a) Map of the South and Mid Atlantic Bight showing the cuspate shapes of coastlines from Long Bay, (SC) to Cape Hatteras point (NC). The locations of NOAA tide gauges used to estimate pressure gradients are shown as squares. The three different coordinate systems used for determining local alongshore and cross-shore components of wind velocity for different regions of the coastline are shown in red. (b) Time series of low-pass filtered pressure gradient term, $-g\partial\eta/\partial y$ (black) between Wrightsville Beach (location A) and Beaufort, NC (location B), and low-pass filtered alongshore (gray) wind velocity from Frying Pan Shoals, (c) Same as in (b) but the pressure gradient is estimated between Duck, NC (location C) and Chesapeake Bay, VA (location D) , and the along coastline wind velocity is estimated using the local coastline orientation between the tide gauges. 228

Figure 5.11 Cross-shore distribution of (a) Linear bottom drag coefficient (black) and water depth (gray); Color shading of (b) absolute value of wind stress (m^2s^{-2}); (c) significant wave height (m); (d) absolute value of breaking acceleration (m^2s^{-2}); (e) alongshore current (ms^{-1}); and (f) vortex force (m^2s^{-2}) showing spatial (along y-axis) and temporal (along x-axis) variation. Log scale is used for (b), (d) and (f). 229

Figure 6.1 Map showing the study area (Cape Hatteras, NC, USA), the nearshore bathymetry and data collection sites (red squares). The prefixes "N" and "O" in the station names suggest nearshore (mean water depth less than 8 m) and offshore sites, respectively. Solid black lines in (c) show transects along which almost alongshelf (transect I) and cross-shelf (transect II) surface currents from the model and the VHF radar are compared (see Figure 6.12). The locations of NOAA Diamond Shoals buoy, Frying Pan Shoals, Cape Lookout Buoy and Oregon Inlet are shown in (b). 272

Figure 6.2 Wind rose diagram showing wind speed and direction (in oceanographic convention) using (a) 5 years (2006-2010) of meteorological data from Diamond Shoals NOAA-NDBC Buoy (Station ID-41025, Fig. 6.1b); (b) meteorological data from February 1 to March 20, 2010; (c) Joint probability distribution of peak period and significant wave height from 2005-2010. The color shading represents the number of observations; (d) same as in (c) but for Feb. 2010. 273

Figure 6.3 Numerical grid domains and bathymetry for the parent (a) and subsequent child grids (b and c) used for the circulation and the wave propagation models. Gray squares in (a) show the locations of NOAA-NDBC buoys. Solid black lines represent bathymetric contours in m. Transects along which flows and momentum balances are discussed in Figures 6.18 and 19 are shown as dotted black lines in (c). Along and cross-shoal transects for which vertical variability of flow is discussed in Figures 6.14-17 are shown as gray lines. Gray box in (c) shows the region for which along and cross-shoal momentum balances are discussed in Figures 6.20-26. Orthogonal coordinate systems for transects 1, 2 and 3 are shown using red arrows. 274

Figure 6.4 Color shading showing time stack of (a) observed frequency spectrum at Site O2; (b) simulated frequency spectrum using Spectral wave input at the open boundary; (c) simulated frequency spectrum using bulk wave input at the open boundary. Also the time series of (d) observed (solid blue) and simulated (red and gray) significant wave height (H_{sig}) and (e) observed (solid blue) and simulated (red and gray) mean wave direction are shown. 275

Figure 6.5 Meteorological and wave data from the Diamond Shoals buoy (NOAA/NDBC Station ID: 41025) for February and March, 2010. Time series of (a) wind velocity vector in oceanographic convention; (b) significant wave height; (c) peak (black squares) and mean (solid black line) wave period; (d) Atmospheric pressure (solid black line); and (e) air (black) and water (gray) temperature. Dark gray shaded areas correspond to passage of synoptic meteorological fronts. 276

Figure 6.6 Comparison between simulated and measured frequency wave spectra (log10 (S_f), a, b, c and d), significant wave heights (H_{sig} in m, e, f, g and h), mean periods (T_m in s, i, j, k and l) and directions (θ_m in degrees from North, m, n, o and p) for the location (see Figure 6.3) of the NOAA-NDBC buoys at Frying Pan Shoals, Diamond Shoals, Delaware Bay and Virginia Beach. No wave direction is available for Diamond Shoals and Delaware Bay buoys during the model simulation period. 277

Figure 6.7 Time series of model simulated (solid gray) and measured (solid gray) (a) Significant wave height (H_{sig}, m); (b) Mean wave period (T_m, s); (c) Mean wave direction (θ_m, degrees from north) at sites O1, O2 and O3. Color shading representing time stack of observed and modeled frequency wave spectrum log10 (Sf) are shown in (d) and (e), respectively. 278

Figure 6.8 Time series of model simulated (solid gray) and measured (solid gray) (a) Significant wave height (H_{sig}, m); (b) Mean wave period (T_m, s); (c) Mean wave direction (θ_m, degrees from north) at sites N5, N6, N9 and N8. Color shading representing time stack of observed and modeled frequency wave spectrum log10 (Sf) are shown in (d) and (e), respectively. 279

Figure 6.9 Time series of vertical variability and depth averaged subtidal flow components for sites O1, O2 and O3. Vertical variability of (a) observed and (b) simulated east flow component, (c) observed and (d) simulated north flow component. Time series of measured (solid black) and modeled (solid gray) depth-averaged, subtidal eastward and northward flows are shown in (e) and (f), respectively. All flows are in ms^{-1}. 280

Figure 6.10 Time series of vertical variability and depth averaged subtidal flow components for sites N5, N6m N8 and N9. Vertical variability of (a) observed and (b) simulated east flow component, (c) observed and (d) simulated north flow component. Time series of measured (solid black) and modeled (solid gray) depth-averaged, subtidal eastward and northward flows are shown in (e) and (f), respectively. All flows are in ms^{-1}. 281

Figure 6.11 Comparison between measured and simulated depth-averaged subtidal flows described by their mean (black and red arrows, respectively) and vector variance ellipses (gray and blue, respectively) for the full period of data collection for each site. . . . 282

Figure 6.12 Color shading showing time stack of measured (a, c) and model simulated (b, d) subtidal, Lagrangian, radial surface currents at a cross-shore (a, b) and alongshore (c, d) transect. The location of these transects are shown in Figure 6.1c. 283

Figure 6.13 Color shading showing time stack of measured (a, c) and model simulated (b, d) gradient of cross-shore ($\partial u/\partial x$, a, b) and alongshore ($\partial v/\partial y$, c, d) subtidal, Lagrangian, radial surface current. The transect locations are same as in Figure 12. 284

Figure 6.14 Model skill in simulating cross-shore gradient of cross-shore (red squares in a and b, $\partial u/\partial x$) and alongshore gradient of alongshore (blue squares in a and b, $\partial u/\partial x$) subtidal, radial velocities as a function of along/cross-shore distance (a) and time (b) 285

Figure 6.15 Spatial distribution of depth-averaged, subtidal flows (ms^{-1}, black arrows) over the smallest child grid (see Figure 4c) is shown on (a) Feb. 4; (b) Feb. 6; (c) Feb. 7; (d) Feb. 11; (e) Feb. 27 and (f) March 13, 2010. The color shading represents the bathymetry. Magnitude and direction of the flow vector are represented through the length and direction of the arrow, respectively. White arrows represent the magnitude and the direction of wind velocity vector. 286

Figure 6.16 Color shading of significant wave height and mean wave direction (black arrows) over the smallest child grid (see Figure 6.3c) is shown on (a) Feb. 4; (b) Feb. 6; (c) Feb. 7; (d) Feb. 11; (e) Feb. 27 and (f) March 13, 2010. The arrows designate a direction, and their length do not have a physical meaning. 287

Figure 6.17 Color shading showing along-shoal variation of vertical profile of cross-shoal (ms^{-1}, a1-f1), along-shoal (a2-f2) and vertical (a3-f3) Eulerian mean flows on (a1-a3) Feb. 4; (b1-b3) Feb. 6; (c1-c2) Feb. 7; (d1-d3) Feb. 11; (e1-e3) Feb. 27 and (f1-f3) March 13, 2010. The location of the along-shoal transect is shown in Fig. 6.4c (see Transect 3). Positive cross-shoal flows are directed towards the northeast, while positive along-shoal flows are northwestward. Solid black line is the zero contour line. 288

Figure 6.18 Color shading showing cross-shoal variation of vertical profile of cross-shoal (ms^{-1}, a1-f1), along-shoal (a2-f2) and vertical (a3-f3) Eulerian mean flows on (a1-a3) Feb. 4; (b1-b3) Feb. 6; (c1-c2) Feb. 7; (d1-d3) Feb. 11; (e1-e3) Feb. 27 and (f1-f3) March 13, 2010. The location of the cross-shoal transect is shown in Fig. 6.4c (see Transect 4). Positive cross-shoal flows are directed towards the northeast, while positive along-shoal flows are northwestward. Solid black line is the zero contour line. 289

Figure 6.19 Color shading showing along-shoal variation of vertical profile of cross-shoal (ms^{-1}, a1-f1), along-shoal (a2-f2) and vertical (a3-f3) Stokes drift on (a1-a3) Feb. 4; (b1-b3) Feb. 6; (c1-c2) Feb. 7; (d1-d3) Feb. 11; (e1-e3) Feb. 27 and (f1-f3) March 13, 2010. The location of the along-shoal transect is shown in Fig. 6.4c (see Transect 3). Positive cross-shoal flows are directed towards the northeast, while positive along-shoal flows are northwestward. Solid black line is the zero contour line. . . . 290

Figure 6.20 Color shading showing cross-shoal variation of vertical profile of cross-shoal (ms^{-1}, a1-f1), along-shoal (a2-f2) and vertical (a3-f3) Stokes drift on (a1-a3) Feb. 4; (b1-b3) Feb. 6; (c1-c2) Feb. 7; (d1-d3) Feb. 11; (e1-e3) Feb. 27 and (f1-f3) March 13, 2010. The location of the cross-shoal transect is shown in Fig. 6.4c (see Transect 4). Positive cross-shoal flows are directed towards the northeast, while positive along-shoal flows are northwestward. Solid black line is the zero contour line. 291

Figure 6.21 Color shading showing time stack of model simulated, subtidal, depth-averaged local alongshore velocities (in ms^{-1}, a, c) and wind stresses (in ms^{-2}, b, d) for two local cross-shore oriented transects on the east (Transect 1) and the south side (Transect 2) of Cape Hatteras point. The location and extent of these transects are shown in Figure 6.3c. 292

Figure 6.22 Color shading showing spatial distribution of along (a-f) and cross-shoal (g-l) momentum balance terms at locations within and adjacent to the shoal complex (see Figure 6.3c for the spatial extent of region shown area) for February 4, 2010. Key: PG (a, g)-Pressure gradient; NA (b, h)- Nonlinear advective acceleration; BS (c, i)- Bottom stress; BA (d, j)- Breaking acceleration; VF (e, k)- Vortex Force; and SS (f, l)- Surface stress. Prefix A and C represent along and cross. All units are in 10^{-4} ms^{-2}. 293

Figure 6.23 Same as in Figure 6.22 but for February 6, 2010. 294

Figure 6.24 Same as in Figure 6.22 but for February 7, 2010. 295

Figure 6.25 Same as in Figure 6.22 but for February 11, 2010. 296

Figure 6.26 Same as in Figure 6.22 but for February 27, 2010. 297

Figure 6.27 Same as in Figure 6.22 but for March 13, 2010. 298

Figure 6.28 Cross-shore distribution of terms in local alongshore momentum balance for Transects 1 and 3, representing shorefaces with varying shoreline orientation (see Figure 6.3c for transect location). (a1, a2) Bottom stress; (b1, b2) Nonlinear advective acceleration; (c1, c2) Coriolis acceleration; (d1, d2) Vortex Force; (e1, e2) Local Acceleration; (f1, f2) Wind stress; (g1, g2) Pressure gradient and (h1, h2) wave breaking induced acceleration. All quantities have a unit of 10^{-5} ms^{-2}. 299

Figure 6.29 Spatial distribution showing magnitude and direction of (a) depth-averaged tidal residual current and (b) temporal mean of depth-averaged, subtidal currents for the entire simulation period. The arrow length and direction denote the flow magnitude and direction, respectively. Solid gray arrow is the mean wind velocity vector during the simulation period. 300

Figure 7.1 Vertical profile of Stokes drift along the direction of wave propagation (ms^{-1}) estimated using spectral formulation (solid black) in Eqn. 7.3 and bulk formulation (solid red) in Eqn. 3.2 311

Chapter 1

Introduction

The nearshore region of the coastal zone serves an important role for both commercial and recreational purposes. Surface gravity waves and winds constitute the primary forcing in this region which are responsible for the generation of flow patterns that subsequently drive sediment transport affecting the morphological evolution of the coastline (i.e., accretion and/or erosion), and the dispersal of nutrients and pollutants available through terrestrial runoff and anthropogenic waste disposal (Boehm et al., 2000; Grant et al., 2005; Spydell et al., 2007). Due to its proximity to the coastline, generation and modification of nearshore circulation patterns also dependents on local morphology and shoreline orientation. For example, interaction of surface gravity waves with local and offshore morphology can lead to generation of rip currents in the surf zone (Shepard and Inman, 1954; Dalrymple, 1975; Long and Özkan-Haller, 2008); a process responsible for more than 50% of drowning related rescues (Source: United States Lifesaving Association). Furthermore, complicated offshore bathymetry can lead to gradients in wave forcing in the nearshore with the development of alongshore gradient in wave forcing that can affect local circulation patterns. Accurate prediction of the effect of wind and wave forcing in developing the aforementioned circulation patterns require the development of numerical modeling techniques that capture the physical processes operating at the various scales present in the nearshore.

Two distinct zones can be identified in the nearshore: (a) the surf zone that extends from the shoreline to the breaking zone which is characterized by large wave dissipation due bathymetrically controlled wave breaking (e.g., Galvin, 1972) and (b) the wave shoaling zone (Longuet-Higgins and Stewart, 1964). The latter area constitutes the shoreward part of the inner shelf, while the inner shelf is the interface between the wave-breaking zone and the mid-shelf (Lentz, 1994), a region usually dominated by wind-driven flow and density stratification. The latter process provides buoyancy forcing that inhibits vertical mixing, while the former process tends to increase vertical mixing and generate flows along the wind direction and eventually may lead to formation of an Ekman Layer (Ekman, 1905).

The extent of the surf zone is decided by depth-limited breaking of surface gravity waves. During the wave breaking process, excessive flux of momentum (due to convergence of wave-induced stress, Longuet-Higgins, 1962) is responsible for the development of accelerations due to wave breaking, leading to flow generation. A common example of this phenomenon is creation of alongshore drift due to depth-limited breaking of obliquely incident waves (Longuet-Higgins, 1970ab). Surface gravity waves are also associated with a mean mass flux towards the direction of wave propagation known as the Stokes drift (Stokes, 1847); its development is due to the fact that wave orbital velocity has both a spatial and a temporal variability leading to a net movement in the direction of wave propagation. The interaction of this inshore directed wave-induced mass flux with the impervious coastline boundary leads to the creation of an offshore directed Eulerian mean flow which for simple bathymetric profiles is seen as near bed intensified return flows usually referred to as the undertow (Svendsen, 1984). Figure 1.1 shows a schematic of inshore directed Stokes drift and offshore directed Eulerian mean flow. In a depth-averaged sense, the Stokes drift is balanced by the Eulerian mean flow, however it is noteworthy that within the surf zone, the vertical structure of Stokes drift is surface intensified and is different than the parabolic

profile of undertow (Garcez-Faria et al., 1998, 2000). Outside the surf zone, both Stokes drift and the undertow may have similar vertical distribution (e.g., Lentz et al., 2008, Kirincich et al., 2009) leading to zero net cross-shore Lagrangian (sum of Eulerian mean and Stokes drift) transport. This balance between the Eulerian mean flow and Stokes drift is sensitive to changes in local bathymetry and vertical mixing due to turbulence (Lentz et al., 2008). Also, in reality these wave-induced Eulerian mean flows are superimposed onto wind- and tidally driven currents and together with buoyancy forcing can lead to a complicated vertical distribution of flow.

As an example ~40 days of low-pass filtered (subtidal) flow data and wave height measured at ~6m of water depth in the transition zone adjacent to Folly Beach, SC (Voulgaris et al., 2008) is shown in Figure 1.2. A positive cross-shore flow is directed offshore; while a positive alongshore flow is directed towards the northeast direction. During strong wave conditions (Fig. 1.2c), the depth-averaged, subtidal, cross-shore Eulerian mean flow almost balances the Stokes drift (Fig. 1.2b). The vertical distribution of subtidal, cross-shore velocity (Fig. 1.2d) during these periods of strong wave conditions is similar to the schematic shown in Fig. 1.1, with a surface intensified flow structure. On the contrary during weak wave conditions, a two layered flow is observed suggesting development of an Ekman layer dynamics within the water column. The vertical profile of subtidal alongshore current (Fig. 1.2e) also depicts a vertical structure with strong flows at the surface and weaker flows near the sea bed. This example suggests that flow at a particular depth can exhibit different flow structure depending on the forcing conditions, and the nearshore circulation can have a distinct three-dimensional (x, y, and z) variability, with strong implications for associated geological and biological processes.

In order to correctly simulate the flow pattern in the inner shelf and the surf zone using a numerical model, it is necessary to include the effect of waves on currents (i.e., Wave Effect on Currents, WEC) and change in wave properties due to current

structure (i.e., Current Effect on Waves, CEW). Since surface gravity waves have a shorter temporal scale in comparison to mean flow, most numerical models inculcate the effect of waves through averaging of fast oscillations over longer time scales. The terms corresponding to WEC in the mean flow equations can be represented as a gradient of radiation stress tensor or through a vortex force formalism method. The radiation stress tensor is defined as excess flux of momentum due to presence of waves (Longuet-Higgins and Stewart, 1964), while the vortex force formalism representation splits the wave-averaged effects into gradients of Bernoulli head and a vortex force. The Bernoulli head is an adjustment of pressure in accommodating incompressibility (Lane et al., 2007), while vortex force is physically represented as the interaction between Stokes drift and the mean flow vorticity.

The ability of a model to accurately simulate coastal flows can only be verified using in situ or remote measurements. Traditionally such measurements can only resolve the temporal variability of the three-dimensional flow structure at a single point using acoustic current profilers. However, strong bathymetric gradients as well as spatial variability of atmospheric forcing can extensively modify the flow response. The development of HF radars (Teague et al., 1997) provide an alternative method for understanding spatial and temporal change surface flows and potentially wave forcing (Voulgaris et al., 2011; Padaun and Washburn, 2012). HF Radars allow for a wide coverage area with measurements of Lagrangian mean flows (Ardhuin et al., 2008) and frequency-directional wave spectrum (Hisaki, 1996) although these measurements are limited to the ocean surface.

1.1 Scope of this Dissertation

This dissertation focuses on investigating the role surface gravity waves and winds play in modifying the circulation patter in the nearshore and inner-shelf through the use of advanced 3-D numerical techniques and verifications using in-situ measure-

ments. Chapters 2 and 3 deal with improving the physics of a three-dimensional modeling system called the Coupled Ocean Atmosphere Wave and Sediment Transport (COAWST) modeling system (Warner et al., 2010) so that the wave-current interaction effect is accurately represented in the development of nearshore currents. The remaining three chapters (Chapters 4, 5 and 6) are dedicated to application of the developed modeling systems to specific nearshore cases. In particular Chapter 4 presents an application of the model for the prediction of rip currents while Chapters 5 and 6 deal with the study of the circulation pattern found around cuspate foreland systems utilizing both field measurements (Chapter 5) and model application (Chapter 6). A brief description of the contents of each chapter is presented below.

Chapter 2:

This chapter focuses on implementation of a three-dimensional radiation stress based approach of Mellor (2008; 2011) to Regional Ocean Modeling System (ROMS). This implementation allows for coupling of wave propagation and ocean circulation model to study wave breaking driven three-dimensional flows. The coupled modeling system is validated against analytical solutions, laboratory experiments and field observations. The questions addressed in this chapter are:

(a) Does the original three-dimensional radiation stress formulations described in Mellor (2008; 2011) create realistic flow patterns in the inner-shelf and surf zone?

(b) Can the discrepancies in flow structure observed by using Mellor (2008; 2011) approach be reduced by providing alternate distribution of vertically varying radiation stress terms?

Chapter 3:

In this Chapter, I expand on the findings of Chapter 2 where it was shown that the three-dimensional radiation stress approach, a widely used approach, fails to seam-

lessly work from the inner-shelf to the surf zone. This limitation hinders simultaneous modeling of processes varying from open ocean to coastal spatial scales. These limitations are addressed in this Chapter by implementing a vortex force formalism based approach in the Coupled Ocean Atmosphere Wave and Sediment Transport (COAWST) modeling system. The questions addressed in this chapter are:

(a) What new wave-averaged terms need to be incorporated within a three-dimensional modeling system when using a vortex force formalism approach?

(b) What should be the vertical distribution of non-conservative forcing terms like depth-limited wave breaking, surface and bottom streaming?

(c) How does the momentum balance in cross-shore and longshore direction change when using this new vortex force based approach, in comparison to a more traditional radiation stress based method?

The performance of updated modeling system with the vortex force formalism is examined through presentation of cases both within the surf zone, and in the inner-shelf region.

Chapter 4:

The modeling system developed in Chapter 2 is implemented to study prediction of rip currents. The relevant questions raised in this part of the work are:

(a) What are the limitations of existing rip current forecasting system used by National Ocean and Atmospheric Administration (NOAA) as a surf zone forecast?

(b) How do we use a combination of existing numerical modeling system along with historical bathymetric data for developing a better prediction system?

It is suggested that lack of information about bathymetric variation is a major missing component in accurate prediction of rip currents. As an effort to overcome this limitation, Empirical Orthogonal Functional analysis is used on time series of historical beach profile data to determine parameters which constrain the spatial and temporal

variability of beach profiles. These parameters are then used to construct barred beach morphology with rip channels, for modeling of realistic scenarios of rip-current circulation for a particular region. A case study based on this technique is presented and discussed for DUCK, NC, the site of the US Army Corps of Engineering, Field Research Facility (FRF).

Chapter 5:

In this chapter, in-situ measurement of waves and currents obtained at various locations in the nearshore region of Cape Hatteras, North Carolina, US, are presented and analyzed to investigate the subtidal dynamics through a simplified alongshore momentum balance for inner shelf and surf zone. The questions considered in this chapter are:

(a) What is the role of abrupt change in coastline orientation to wave propagation, wave breaking and wind-driven flows?

(b) What are the major forcing and response terms in the alongshore momentum balance for inner shelf and surf zone regime of the east and the south side of Cape Hatteras, NC?

The momentum balance analysis conducted in this chapter is the first one to incorporate the effect of vortex force terms in field observation based momentum balance analyses.

Chapter 6:

The work presented in Chapter 5 is combined with numerical simulations of the modeling system presented in Chapter 3 in order to study wave propagation and circulation pattern around Cape Hatteras, North Carolina (US). Usage of this three-dimensional modeling system allows for further verification of the contrast in flow pattern and alongshelf momentum balance revealed by the measurements presented

in Chapter 5. Major questions addressed in this chapter are:

(a) What is the large scale role of cuspate embayments and associated forelands in modifying the wind and wave breaking driven circulation?

(b) How does the momentum balance pattern change on the windward and leeward sides of a sub-aqueous, shallow, shoal complex?

(c) What is the physical role of the shoal complex in regulating flow perpendicular to the shoal axis?

(d) What are the dominant pathways for enhanced offshore transport from a cuspate foreland?

A nesting process is utilized in this study, which allows for grid refinement process for both the circulation module, and the wave propagation model. This is the first study which addresses the role of wave propagation along with subtidal flows around a shoal complex.

Chapter 7:

Finally this dissertation concludes with a summary of the main findings presented throughout this work and presents some recommendations for future work.

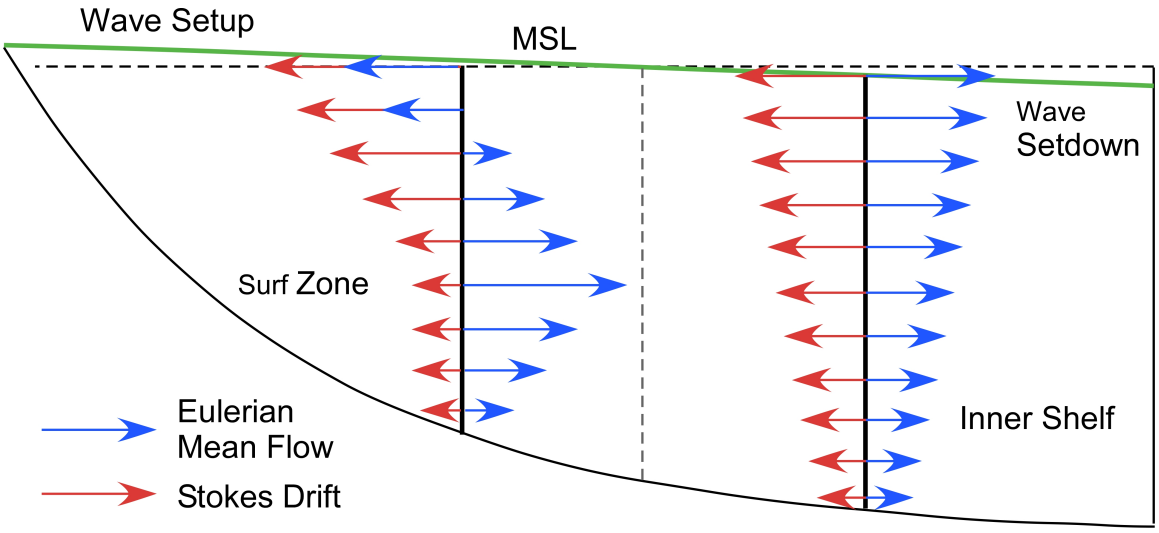

Figure 1.1: Schematic showing vertical distribution of offshore directed Eulerian mean flow (blue arrows) and Stokes drift (red arrows) within the surf zone and inner shelf. The solid horizontal green line represents the adjusted mean sea level in presence of surface gravity waves, while the dashed horizontal line is the resting mean sea-level. This figure has been modified from Lentz et al., 2008.

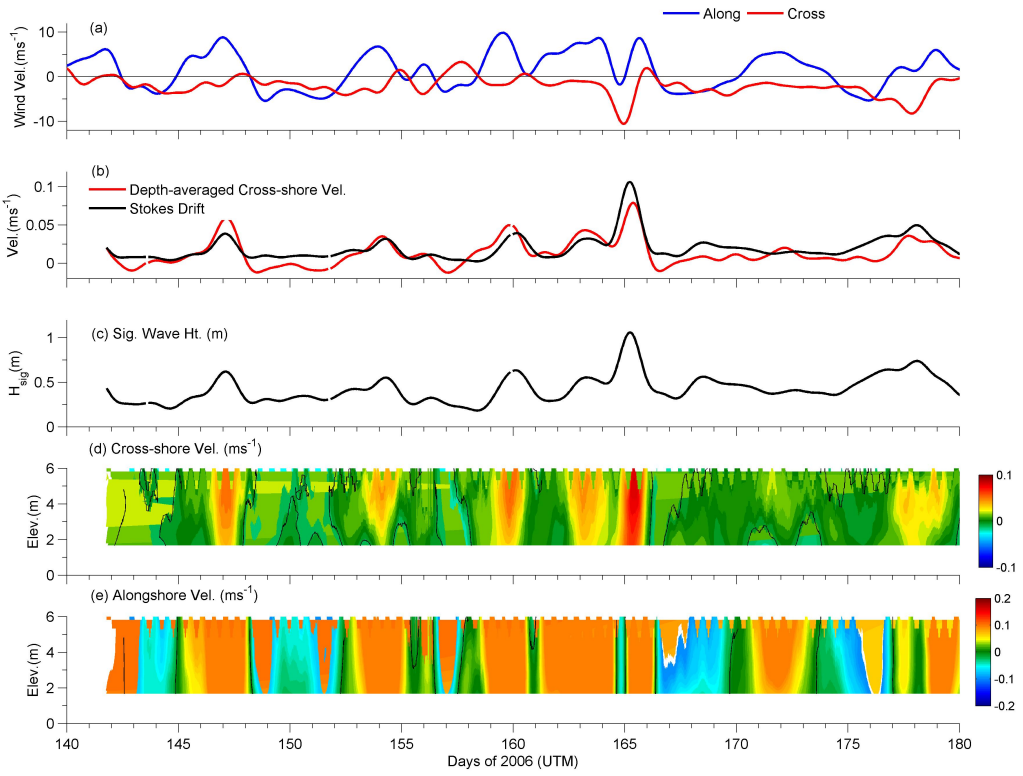

Figure 1.2: Time series of low-pass filtered (a) along and cross-shore wind velocity (ms^{-1}) from NOAA meteorological station in Folly Island, SC; (b) depth-averaged, Eulerian mean cross-shore velocity (solid red, ms^{-1}) calculated by averaging the vertical profile of cross-shore velocity, and the depth-averaged Stokes drift (solid black, ms^{-1}) estimated using a formulation based on significant wave height, wave direction and peak wave period. The sign of Stokes drift has been reversed for comparison to Eulerian mean flows; (c) Significant wave height (m); (d) Vertical profile of subtidal cross-shore velocity (ms^{-1}); and (e) Vertical profile of subtidal alongshore velocity (ms^{-1}) obtained from an Acoustic Doppler Current Profiler deployed in Folly Island, SC at a water depth of 6 m (see Voulgaris et al., 2008).

Chapter 2

Implementation and modification of a three dimensional radiation stress formulation for surf zone and rip-current applications[1]

[1]This chapter has been published as "Kumar, N., Voulgaris, G., and Warner, J.C., 2011. Implementation and modification of a three-dimensional radiation stress formulation for surf zone and rip-current applications, Coastal Engineering, Volume 58, Issue 12, December 2011, Pages 1097-1117, ISSN 0378-3839, 10.1016/j.coastaleng.2011.06.009.". In addition, part of this manuscript is also is also published in author's Master's thesis titled "3-D Modelling of nearshore circulation using ROMS-SWAN: Model upgrades and evaluation" and has been repeated here for completeness and linking of the overall work conducted by the author. See Appendix A for more details.

Abstract

Regional Ocean Modeling System (ROMS v 3.0), a three-dimensional numerical ocean model, was previously enhanced for shallow water applications by including wave-induced radiation stress forcing provided through coupling to wave propagation models (SWAN, REF/DIF). This enhancement made it suitable for surf zone applications as demonstrated using examples of obliquely incident waves on a planar beach and rip current formation in longshore bar trough morphology (Haas and Warner, 2009). In this chapter, I present an update to the coupled model which implements a wave roller model and also a modified method of the radiation stress term based on Mellor (2008, 2011a, b and c) that includes a vertical distribution which better simulates non-conservative (i.e., wave breaking) processes and appears to be more appropriate for sigma coordinates in very shallow waters where wave breaking conditions dominate. The improvements of the modified model are shown through simulations of several cases that include: (a) obliquely incident spectral waves on a planar beach; (b) obliquely incident spectral waves on a natural barred beach (DUCK' 94 experiment); (c) alongshore variable offshore wave forcing on a planar beach; (d) alongshore varying bathymetry with constant offshore wave forcing; and (e) nearshore barred morphology with rip-channels. Quantitative and qualitative comparisons to previous analytical, numerical, laboratory studies and field measurements show that the modified model replicates surf zone recirculation patterns (onshore drift at the surface and undertow at the bottom) more accurately than previous formulations based on radiation stress (Haas and Warner, 2009). The results of the model and test cases are further explored for identifying the forces operating in rip current development and the potential implication for sediment transport and rip channel development. Also, model analysis showed that rip current strength is higher when waves approach at angles of 5° to 10° in comparison to normally incident waves.

2.1 Introduction

Wave-induced circulation in the nearshore has been the subject of a number of experimental studies over the last 50 years. Theoretical and analytical studies were initiated in the 60s and 70s with the works of Longuet-Higgins and Stewart (1964), Longuet-Higgins (1970a, b) and Bowen (1969). These theories were later incorporated in numerical models that have been developed in the last 20 years. Such models are predominantly phase-averaged operating in 1-D (across the surf) or 2-D (assuming uniform along-coast bathymetry and depth-integrated). They solve the depth averaged Navier Stokes equation focusing on either simulating the development of longshore currents (Church and Thornton, 1993; Stive and DeVriend, 1994; Feddersen et al., 1998; Ruessink et al., 2001), or rip current circulation (e.g., Yu and Slinn, 2003; Reniers et al., 2004a). Phase resolving 2-D Boussinesq models (e.g., Chen et al., 1999), although considered to be more comprehensive in modeling wave evolution in the nearshore, are computationally expensive, and their use is limited at present. Lately, point-vortex models (Terrile et al., 2007; Kennedy et al., 2006) have been also used to study generation, maintenance and advection of breaking wave induced vortices which are associated with the formation of rip currents.

Overall one dimensional and two dimensional models provide useful information about circulation patterns but are intrinsically not able to resolve three-dimensional dynamics. It is imperative to resolve the three dimensional circulation to fully investigate such processes as circulation dynamics for nearshore water quality applications, transport into and out of the surf zone, sediment transport dynamics, coastal erosion and morphodynamics. In order to fill this need, initially quasi three-dimensional models like SHORECIRC (Svendsen et al., 2002) were developed. These models have been previously applied to study rip currents (Haas et al., 2003) and surf beat phenomena (van Dongeren et al., 1995) in nearshore environments. Lately, full three-dimensional

wave-current coupled models have been developed and implemented in the coastal ocean extending their application to the wave breaking dominated environment of the surf zone. DELFT 3D flow model uses an approximate Generalized Lagrangian Mean (GLM) approach (Groeneweg and Klopman, 1998) to associate wave effects on mean currents. Wave forcing in form of dissipation of wave energy is applied as shear stress on the water surface, consistent with simplified formulations presented by Dingemans et al. (1987), as implemented by Walstra et al. (2000) and Lesser et al. (2004). Newberger and Allen (2007a, b) added wave forcing in the form of surface stress and body forces in the Princeton Ocean Model (POM), which has evolved as "Nearshore POM". Using the vortex force formalism method described in McWilliams et al. (2004), Uchiyama et al. (2010) (hereafter referred to as U10) compares model simulations (using UCLA-ROMS, see Table 1 in Shchepetkin and McWilliams, 2009) to field observations from a barred beach environment.

Mellor (2003, 2005) (hereafter referred to as M03 and M05, respectively) described depth dependent formulation for radiation stress terms, which has been implemented in publicly available version of ROMS (Rutgers-ROMS, see Table 1 in Shchepetkin and McWilliams, 2009) by Warner et al. (2008, hereafter referred to as W08). This has been used to study oblique incidence of waves on a planar beach and rip currents formed on alongshore bar trough morphology (Haas and Warner, 2009; hereafter referred to as HW09). Following Ardhuin's et al. (2008a) remarks, Mellor (2008) modified his original formulation and provided a new approach for depth dependent radiation stresses to alleviate the creation of erroneous gradients of mean currents for unforced wave conditions. Bennis and Ardhuin (2011) argued that the depth-dependent equations for radiations stress presented in Mellor (2008) when vertically integrated does not yield the expected depth averaged radiation stress formulations presented by Longuet-Higgins and Stewart (1964) and Phillips (1977). Subsequently, Mellor (2011a, b) argued that this discrepancy occurs due to difficulty in correct rep-

resentation of vertical boundary conditions in Cartesian coordinates and he suggested implementation of his method using sigma coordinate equations. The equations are now provided in a sigma coordinate system along with exclusion of some incorrect vertical gradient terms in Eqn. 51, M03 (for details see Mellor, 2011b).

In this chapter, the Mellor (2008) method including the updates presented in Mellor (2011a, b and c) have been implemented in ROMS (hereafter referred to as M08-11) and evaluated for an idealized situation of non-breaking and shoaling waves on a steep sloping topography (see Section 2.5). These results do identify the generation of "unexpected" flow structure as in Bennis and Ardhuin (2011) although Mellor (2011c) suggests this flow *"...must be a surface contribution to the phase averaged momentum equation due to wave's intrinsic surface pressure field"*. Despite the ongoing scientific debate, the Mellor (2008) formulation without the updates presented in Mellor (2011a, b and c) is still being widely used to study wave induced flow through various models (e.g., FVCOM, Wang and Shen, 2010; CH3D, Sheng and Liu, 2011). Furthermore, the current version of ROMS publicly available at https://www.myroms.org/ still utilizes Mellor (2005). This work presents a modified M08-11 formulation which reduces the discrepancy in the flow structure, and I contend makes the formulation useful for engineering applications in a surf zone setting. To support this both qualitative and quantitative comparisons for three and two dimensional flow fields corresponding to conditions favorable for the development of longshore currents and rip current cell circulation are provided (see below).

The objectives of this chapter are to provide to the community with an independent and comprehensive assessment of the performance of the Mellor (2008, 2011a, b and c) approach under realistic conditions and to present the implementation of a modified M08-11 formulation that includes changes in the vertical distribution of radiation stress to account for shallow water, into the ROMS model. The performance of the new implementation is evaluated using 5 study cases. These consist

of: (a) obliquely incident waves on a planar beach; (b) obliquely incident waves on a natural barred beach (DUCK94 experiment); (c) uniform nearshore bathymetry with alongshore varying wave forcing; (d) alongshore varying bathymetry with constant offshore forcing; and (e) nearshore barred morphology with rip-channels.

The outline of this chapter is as follows. Modifications to the model are presented in Section 2.2, together with the results for the case of obliquely incident waves on a planar beach (Case 1) and barred beach (Case 2), respectively. Section 2.3 presents the results of the numerical experiments for the alongshore variable forcing, alongshore varying bathymetry and nearshore barred morphology with rip-channels (Cases 3, 4, and 5, respectively). The model results are compared to existing analytical solutions (Bowen, 1969), numerical solutions (Noda, 1974) and laboratory studies (Haller et al., 2002; Haas and Svendsen, 2002). Section 2.4 discusses the results with main emphasis on the effect of wave angle of approach to the development of rip-currents as it is revealed through the numerical experiments and some implications for model applications related to morphodynamic development. Finally, the conclusions are presented in Section 2.5.

2.2 Implementation of Updated Forcings

ROMS is a three dimensional, free surface, topography following numerical model, which solves finite difference approximations of Reynolds Averaged Navier Stokes (RANS) equations using hydrostatic and Boussinesq approximations with a split-explicit time stepping algorithm (Shchepetkin and McWilliams, 2005; Haidvogel et al., 2008; Shchepetkin and McWilliams, 2009). ROMS includes several options for certain model components, such as various advection schemes (second, third and fourth order), turbulence closure models (e.g., Generic Length Scale mixing, Mellor-Yamada, Brunt-Väisälä frequency mixing, user provided analytical expressions, K-profile parameterization), boundary conditions, etc. As Shchepetkin and McWilliams (2009)

state, currently there are four variations of ROMS-family codes. In this contribution Rutgers University ROMS is used which was first introduced by Haidvogel et al. (2000) and subsequently any reference to ROMS denotes this particular version.

Warner et al. (2008a) improved ROMS for nearshore applications through the incorporation of the M03 and M05 radiation stress forcing methods. The model equations were presented in W08 in Cartesian coordinates (x, y, s) based on the equations originally given by Haidvogel and Beckmann (1999) and Haidvogel et al. (2008). Recently these formulations have been commented on by Shchepetkin and McWilliams (2009) who presented clarifications to the model formulations. For completeness and to avoid confusion, the equations are presented in horizontal, orthogonal curvilinear and vertical terrain following coordinates (ξ, η, s) following the definitions and notations of Shchepetkin and McWilliams (2009).

2.2.1 ROMS equation of motion

The horizontal momentum equations are given as:

$$\begin{aligned}
&\frac{\partial}{\partial t}\left(\frac{H_z u^l}{mn}\right)+\frac{\partial}{\partial \xi}\left(\frac{u^l H_z u^l}{n}\right)+\frac{\partial}{\partial \eta}\left(\frac{v^l H_z u^l}{m}\right)+\frac{\partial}{\partial s}\left(\frac{w^s u^l}{mn}\right)\\
&-\left[\left(\frac{f}{mn}\right)+v^l\frac{\partial}{\partial \xi}\left(\frac{1}{n}\right)-u^l\frac{\partial}{\partial \eta}\left(\frac{1}{m}\right)\right]H_z v^l=-\frac{H_z}{n}\left(\frac{1}{\rho_o}\left.\frac{\partial P}{\partial \xi}\right|_z\right)-\frac{\partial}{\partial s}\left(\overline{u'w'}-\frac{\nu}{H_z}\frac{\partial u^e}{\partial s}\right)\\
&-\frac{\partial}{\partial \xi}\left(\frac{H_z S_{\xi\xi}}{mn}\right)-\frac{\partial}{\partial \eta}\left(\frac{H^z S_{\eta\xi}}{mn}\right)+\frac{H_z}{mn}\left(F_u+D_u\right)
\end{aligned} \tag{2.1}$$

$$\begin{aligned}
&\frac{\partial}{\partial t}\left(\frac{H_z v^l}{mn}\right)+\frac{\partial}{\partial \xi}\left(\frac{u^l H_z v^l}{n}\right)+\frac{\partial}{\partial \eta}\left(\frac{v^l H_z v^l}{m}\right)+\frac{\partial}{\partial s}\left(\frac{w^s v^l}{mn}\right)\\
&+\left[\left(\frac{f}{mn}\right)+v^l\frac{\partial}{\partial \xi}\left(\frac{1}{n}\right)-u^l\frac{\partial}{\partial \eta}\left(\frac{1}{m}\right)\right]H_z u^l=-\frac{H_z}{n}\left(\frac{1}{\rho_o}\left.\frac{\partial P}{\partial \eta}\right|_z\right)-\frac{\partial}{\partial s}\left(\overline{v'w'}-\frac{\nu}{H_z}\frac{\partial v^e}{\partial s}\right)\\
&-\frac{\partial}{\partial \xi}\left(\frac{H_z S_{\xi\eta}}{mn}\right)-\frac{\partial}{\partial \eta}\left(\frac{H_z S_{\eta\eta}}{mn}\right)+\frac{H_z}{mn}\left(F_v+D_v\right)
\end{aligned} \tag{2.2}$$

$$
\begin{aligned}
-\left.\frac{\partial P}{\partial \xi}\right|_z &= -g\rho|_{s=0}\frac{\partial \zeta}{\partial \xi} - g\int_s^0 \frac{\partial p}{\partial \xi}H^z ds \\
-\left.\frac{\partial P}{\partial \eta}\right|_z &= -g\rho|_{s=0}\frac{\partial \zeta}{\partial \eta} - g\int_s^0 \frac{\partial p}{\partial \eta}H^z ds
\end{aligned}
\tag{2.3}
$$

where m^{-1} and n^{-1} are Lamé metric coefficients; u and v are the mean components of velocity in the horizontal (ξ and η) directions, respectively; subscripts l and e define Lagrangian and Eulerian mean velocity; w_s is the mean component of the vertical velocity in the vertical (s) direction. Note that no vertical Stokes velocity is defined in the M08-11 method. At this juncture it is important to point out that the contribution of radiation stress in Eqns. 2.1 and 2.2 is implemented on the basis of Mellor (2011b) and does not contain the incorrect terms corresponding to vertical gradient of radiation stress (see M03, M08 and Mellor, 2011b).

2.2.2 Continuity Equation and Scalar Transport

The continuity equation is written as:

$$
\frac{\partial}{\partial t}\left(\frac{H_z}{mn}\right) + \frac{\partial}{\partial \xi}\left(\frac{H_z u^l}{n}\right) + \frac{\partial}{\partial \eta}\left(\frac{H_z v^l}{m}\right) + \frac{\partial}{\partial s}\left(\frac{w^s}{mn}\right) = 0 \tag{2.4}
$$

while the scalar transport is given by:

$$
\begin{aligned}
&\frac{\partial}{\partial t}\left(\frac{H_z C}{mn}\right) + \frac{\partial}{\partial \xi}\left(\frac{u^l H_z C}{n}\right) + \frac{\partial}{\partial \eta}\left(\frac{v^l H_z C}{m}\right) + \frac{\partial}{\partial s}\left(\frac{w^s C}{mn}\right) = \\
&-\frac{\partial}{\partial s}\left(\overline{c'w'} - \frac{\nu_\theta}{H_z}\frac{\partial C}{\partial s}\right) + C_{src}
\end{aligned}
\tag{2.5}
$$

finally, it should be noted that the Lagrangian mean velocity is related to Eulerian mean velocity (u^e) and Stokes drift (u^s) as:

$$
u^l = u^e + u^s \tag{2.6}
$$

The Stokes velocities are computed based on wave properties provided by the wave model. To solve the system of equations (2.1-2.5), the Lagrangian mean velocities (u^l) are replaced with their equivalent Eulerian mean and Stokes summation

(u^e+u^s). The advective and local acceleration terms corresponding to Stokes drift are moved to the right hand side of momentum balance equation and computed in a manner similar to a purely Eulerian advection. The ROMS model therefore solves for the Eulerian velocity as the prognostic variable. The vertical sigma coordinates vary from -1 at the bottom to 0 at the free surface; z is the vertical coordinate positive upwards with z=0 at mean sea level; ζ is the wave-averaged sea surface elevation; D (= h+ζ) is the total water depth while h is the depth below mean sea level of the sea floor; H_z is the grid cell thickness; and f is the Coriolis parameter. Overbar indicates time average, while prime ($'$) indicates a fluctuating turbulent quantity. Pressure is P; ρ and ρ_o are total and reference densities of sea water; g is the acceleration due to gravity; and ν and ν_θ are molecular viscosity and diffusivity; F_u and F_v are forcing terms (e.g., wind stress and thermal forcing, etc); C represents a tracer quantity; C_{src} are tracer source/sink terms; finally, D_u and D_v are diffusive terms (viscosity and diffusion) explained in details in the ROMS user guide (wikiROMS, www.myroms.org). For Cartesian coordinates (x, y and s), Lamé metric coefficients are unity and the curvilinear terms ($v^l\partial/\partial\xi$(1/n)- $u^l\partial/\partial\eta$ (1/m)) reduce to zero.

These equations are closed by parameterization of the Reynolds stresses and turbulent tracer fluxes as:

$$\left(\overline{u'w'}\right) = -K_m\frac{\partial u^e}{\partial z}; \left(\overline{v'w'}\right) = -K_m\frac{\partial v^e}{\partial z}; \left(\overline{c'w'}\right) = -K_H\frac{\partial c}{\partial z} \tag{2.7}$$

2.2.3 Radiation Stress Formulations

In this section the radiation stress formulation presented by Mellor (2008, 2011a, b) is discussed. Ardhuin et al. (2008a) pointed out that the implementation of depth dependent radiation stress equations described by M03 and M05 is not accurate and it requires inclusion of higher order wave kinematics. Mellor (2008) attempted to address these issues and developed a modification to his original formulation for the

radiation stress tensor which is given as:

$$S_{\alpha\beta} = kE\left(\frac{k_\alpha k_\beta}{k^2}F_{cs}F_{cc} - \delta_{\alpha\beta}F_{sc}F_{ss}\right) + \delta_{\alpha\beta}E_D \tag{2.8}$$

where, k is the wave number and E is the wave energy, while the parameter F denotes the vertical distribution defined as:

$$\begin{aligned}
F_{ss} &= \frac{sinhkD\,(s+1)}{sinhkD}; F_{cs} = \frac{coshkD\,(s+1)}{sinhkD} \\
F_{sc} &= \frac{sinhkD\,(s+1)}{coshkD}; F_{cc} = \frac{coshkD\,(s+1)}{coshkD} \\
\delta_{\alpha\beta} &= \begin{pmatrix} 1 \text{ if } \alpha = \beta \\ 0 \text{ if } \alpha \neq \beta \end{pmatrix} \\
E_D &= 0 \text{ if } z \neq \zeta; \int_{-h}^{\zeta} E_D dz = E/2
\end{aligned} \tag{2.9}$$

As described in M08:

"in a finite difference rendering of E_D, the top vertical layer of incremental size δz and only the top layer would be occupied by $\partial E_D/\partial\xi = (\delta z)^{-1}\partial(E/2)/\partial\xi$ " (hereafter this formulation is referred to as M08-11_{top}). In the present work it is observed that on application of E_D as a surface stress or as a contribution at the first vertical cell, strong offshore advection occurs at the transition zone from inner shelf to surf zone, where wave shoaling occurs. This offshore advection in the wave shoaling zone occurs due to a positive gradient of cross-shore radiation stress ($\partial S_{xx}/\partial x$) at the surface layer, which is significantly reduced on implementing E_D as surface intensified body force (sec 2.2.5, Case 1). Furthermore and equally if not more importantly, the term E_D is a function of wave energy, and contains both conservative and non-conservative wave effects, which should have different vertical dependencies. Based on this understanding, U10 presented two different penetration scales for the conservative (Vortex Force and Bernoulli Head) and non-conservative (wave breaking) wave effects. In order to avoid aforementioned deficiencies in E_D formulation for application in shallow waters, the forcing is vertically distributed using a function (F_{ED}) with a length that scales with

the root mean square wave height (H_{rms}). The chosen distribution is similar to type-III of U10:

$$F_{ED} = \frac{FB}{\int_{-h}^{\zeta} FB dz}; FB = cosh\left(\frac{2\pi}{H_{rms}} D(s+1)\right) \tag{2.10}$$

so that Eqn. 8 is implemented as:

$$S_{\alpha\beta} = kE\left(\frac{k_\alpha k_\beta}{k^2} F_{cs} F_{cc} - \delta_{\alpha\beta} F_{sc} F_{ss}\right) + \delta_{\alpha\beta}\frac{E}{2} F_{ED} \tag{2.11}$$

and hereafter referred to as M08-11_{vrt}. In this chapter the work is focused on wave current interaction in the surf zone where the non-conservative wave effects are dominant, which justifies the modification presented in Eqn. 2.10.

The wave fields required to compute the radiation stress terms are provided by SWAN (Booij et al., 1999), a third generation, phase averaged, wave propagation model, which conserves wave action density (energy density divided by relative frequency). The details of coupling ROMS to SWAN have been provided in W08 and are not discussed further in here.

2.2.4 Wave Roller Model

In addition to the radiation stress term, spatial distribution of wave energy is affected by wave breaking processes. This is usually incorporated through the inclusion of wave rollers (e.g., Ruessink et al., 2001) that modifies the radiation stress and associated longshore and cross-shore velocities. In our application of ROMS, the roller energy (E_r) is distributed using a vertical distribution function R_z that is added to radiation stress distribution so that Eqn. 2. 11 becomes:

$$S_{\alpha\beta} = kE\left(\frac{k_\alpha k_\beta}{k^2} F_{cs} F_{cc} - \delta_{\alpha\beta} F_{sc} F_{ss}\right) + \delta_{\alpha\beta}\frac{E}{2} F_{ED} + \frac{k_\alpha k_\beta}{k} E_r R_z \tag{2.12}$$

W08 calculated E_r using an empirical formulation based on Svendsen (1984) which depends on the fraction of breaking waves (Q_b), significant wave height (H_{sig}), roller area (A_r), wave propagation speed (c) and wavelength (L).

Nairn et al. (1990) suggested that wave dissipation due to depth induced breaking contributes to creation of wave rollers. This sink term when related to local wave parameters, can be used to determine E_r. The wave rollers in this mechanism act as a storage of dissipated energy causing a lag effect in momentum transfer. This kind of surface roller model, evolving in time is termed as Roller Evolution Model (Reniers et al., 2002b; 2004) and is based on the equation for roller action density A^r which is given by:

$$\frac{\partial A^r}{\partial t} + \nabla \cdot \left(A^r \vec{\mathbf{c}}\right) = \frac{\alpha_r \epsilon_b - \epsilon_r}{\sigma} \tag{2.13}$$

where A^r is related to E_r as:

$$E_r = A^r \sigma \tag{2.14}$$

and

$$\vec{c} = u + \sigma k^2 \vec{\mathbf{k}} \tag{2.15}$$

where c is the phase speed of the primary wave; u is the mean velocity; k $(=2\pi/L)$ is the wave number for a wavevector $\vec{\mathbf{k}}$; and ϵ_b is the wave dissipation due to wave breaking. The latter can be obtained directly from the wave model (SWAN) or can be empirically calculated externally as (Church and Thornton, 1993):

$$\epsilon_b = \frac{3\sqrt{\pi}}{16}\rho_o g \frac{B_b^3 f_p}{D} H_{rms}^3 \left[1 + tanh\left\{8\left(\frac{H_{rms}}{\gamma_b D}\right)\right\}\right]\left[1 - \left\{1 + \left(\frac{H_{rms}}{\gamma_b D}\right)^2\right\}^{\frac{-5}{2}}\right] \tag{2.16}$$

where f_p is the peak wave frequency, H_{rms} is the root mean square wave height, D is the total water depth, B_b and γ_b are empirical coefficients dependent on the type of wave breaking.

The parameter α_r, in Eqn. 2.13, can vary between 0 and 1. A value of 1 corresponds to full wave dissipation due to breaking being used as a feeder for roller energy calculation, while 0 means no wave dissipation is used as source for roller energy. The choice of an empirical value for α_r depends on the beach type and wave conditions (see U10). The roller dissipation energy is parameterized as:

$$\epsilon^r = \frac{g sin\beta E_r}{c} \tag{2.17}$$

where β is an empirical constant (=0.1, Reniers et al., 2004).

Eqn. 2.13 is solved within the ROMS module for radiation stress calculation using a first order upwind scheme (Patankar, 1980), with a barotropic (fast) time stepping. E_r calculated using Eqn. 2.14 is substituted in Eqn. 2.12 and distributed vertically using a surface intensified distribution, R_z such that:

$$R_z = F_{ED} \tag{2.18}$$

where F_{ED} is a forcing function that scales with the wave height (see, Eqn. 2.11).

Along with creation of wave rollers, depth induced wave breaking also creates enhanced turbulence and mixing of momentum within the wave breaking zone (Feddersen and Trowbridge, 2005). These processes have been added to the local turbulence closure model by using a spatially variable empirical parameterization of wave induced eddy diffusivity based on U10 (their Eqn. 59) , which has a length scale of local wave height and has the same vertical distribution as the roller energy (Eqn. 2.18).

2.2.5 Case 1: Obliquely incident waves on a planar beach

The effects of updated forcing methods are examined through simulations for obliquely incident waves on a planar beach. This case has been previously discussed by HW09 using the M03 formulation (thus the results corresponding to M03 are same as HW09). The model domain has a cross-shore width (x) of 1,180 m and an alongshore length (y) of 140 m. The grid resolution is 20 m for both directions. The water depth varies from 12 m at the offshore boundary to 0 m at the shoreline. The vertical domain consists of 30 equally spaced vertical layers. The boundary conditions are periodic in the alongshore (i.e., north and south boundaries), closed at the shoreline, and Chapman like radiation condition (Chapman, 1985) at the offshore end of the domain. Effect of earth rotation has not been included. The bottom stress has been formulated using

a quadratic bottom drag with a C_d value of 0.0015. The turbulence closure scheme is Generic Length Scale (GLS, k-ϵ) as described in Warner et al. (2005). For this simulation, wave forcing is provided by SWAN, which propagates an offshore JONSWAP wave spectrum with a significant wave height of 2 m, a peak period of 10 seconds and a 10° angle of incidence. The effect of wave rollers and enhanced wave breaking induced mixing has not been considered for this study, consistent with HW09.

U10 conducted similar tests on the same setup using the vortex force formalism (McWilliams et al., 2004) to compute the wave forcings. Results were compared to those in HW09, which were based on the original vertical distribution of M03. Here the vertical structure of cross-shore velocity between M03 and the present model using both M08-11$_{\text{top}}$ and M08-11$_{\text{vrt}}$ is compared in order to reveal the differences between the older and newer formulations, but also to examine the performance of the radiation stress vertical distribution shown in Eqn. 2.10.

The cross-shore distribution of wave height, water depth and sea surface elevation after 6 hours of model simulation time are shown in Figure 1a. The free surface is very close to zero at the offshore boundary and gradually decreases landward with a maximum setdown at x=560 m. The waves start breaking at $x > 560$ m as determined by wave setdown and reduction in wave height. A comparison of the depth averaged, cross-shore and longshore Eulerian velocities for the different simulations (i.e., M03, M08-11$_{\text{top}}$ and M08-11$_{\text{vrt}}$ formulations) are shown in Figures 2.1b and c. The cross-shore profile of the depth averaged cross-shore velocity (Fig. 2.1b) is identical for all three simulations with the maximum current occurring at 700 m. The depth averaged, Eulerian mean flow has similar structure and opposite sign to the wave induced Stokes drift (not shown), which when added together makes the net Lagrangian mean flow nil. The strength of the maximum depth averaged longshore velocity (Fig. 2.1c) for M08-11$_{\text{top}}$ and M08-11$_{\text{vrt}}$ is slightly weaker in comparison to M03. This reduction in

longshore velocity in M08-11_{top} and M08-11_{vrt} is compensated for by an increase in longshore velocity further offshore.

The vertical structure of the cross-shore Eulerian velocity at five different locations across the shoreface and for each simulation is shown in Figure 2.2. At the furthest offshore location (x=100 m), the M03 cross-shore velocity profile shows offshore directed velocity increasing in strength from 0 ms^{-1} at z=-4 m to 0.15 ms^{-1} at z=-10.5 m. For z > -4 m, the velocity is directed onshore with maximum strength at the surface layer. At the same location, the M08-11_{vrt} results show no velocity at the surface, increasing towards the bed with an offshore directed velocity of 0.15 ms^{-1}. The M08-11_{top} simulations are similar to those of M08-11_{vrt} except near the surface, where an offshore velocity of 0.10 ms^{-1} is observed at the surface layer. The velocity profile at x=300 m follows a similar trend as that for M03 and M08-11_{vrt}, while for M08-11_{top}, offshore advection at the surface layer is observed with a velocity on the order ~ 0.2 ms^{-1}.

At the location just offshore of the wave breaking zone (i.e., x=500 m), M03 runs have maximum offshore directed velocity (~ 0.2 ms^{-1}) at the bottom layer, which decreases to 0 at the surface. For the M08-11_{top} run, strongest offshore flow is at the bottom layer which decreases to a magnitude ~ 0.1 ms^{-1} at z=0 m. The velocity profile from M08-11_{vrt} run has maximum offshore velocity at z=-6 m with a strength of ~ 0.2 ms^{-1}, reducing to ~ 0.05 ms^{-1} at the surface.

Within the surf zone (x > 500 m), the original model (M03) run predicts a strong offshore directed velocity near the bed. At the surface, the velocity is still directed offshore but with a significantly reduced strength. The M08-11_{top} and M08-11_{vrt} results are very similar within the surf zone. Close to the bottom boundary, velocity is directed offshore with a higher value than that observed for the M03 run. Near the surface, velocity is directed onshore as expected in the surf zone while an offshore directed undertow is developed near the bottom (also see Fig. 1, in Longuet-Higgins,

1953). This vertical segregation of flow leads to the development of a cross-shore circulation cell with a vertical velocity (not shown here) directed upwards at x~500 m and downwards close to the shoreline at x~900 m. This is generally consistent with field observations of cross-shore velocity profiles within the surf zone that show similar vertical flow segregation for both barred (Garcez-Faria et al., 2000) and non-barred planar beaches (Ting and Kirby, 1994).

Overall, the M03 formulation predicts onshore velocity for areas outside the surf zone and fails to reproduce the recirculation pattern within the surf zone. The M08-11 based simulation with stress applied to the top layer (M08-11_{top}) works well within the surf zone but creates offshore advection of cross-shore velocity near the surface. However this offshore advection is eliminated when implementing Eqn. 2.10 (M08-11_{vrt}). Furthermore, at the breaking zone; the M08-11_{vrt} model results are qualitatively in agreement with the field observations of Garcez-Faria et al. (2000) that show slight onshore flow near the surface and offshore flows below, increasing with proximity to the bed (see Fig. 1c in Garcez-Faria et al., 2000).

2.2.6 Case2: Obliquely incident waves on a barred beach, DUCK94 Experiment

In this case study, the M03, M08-11_{top} and M08-11_{vrt} formulations are further evaluated by comparing model simulated surf zone velocities to measurements obtained during the DUCK94 experiment (Garcez-Faria et al., 1998, 2000). On 12th October, 1994, strong longshore and cross-shore currents occurred in response to passage of a low pressure storm system. These velocities were measured at 7 different surf zone locations for approximately an hour at each site, using a vertical stack of 7, two component electromagnetic current meters (ECM) which were at an elevation of 0.42, 0.68, 1.01, 1.47, 1.79, 2.24 and 2.57 m above the sea bed (Garcez-Faria et al., 1998; Garcez-Faria et al., 2000). The tidal variability during this period of data col-

lection was minimal and the bathymetric contours were assumed alongshore uniform (Garcez-Faria et al., 2000). During this period, directional wave spectrum was measured along the shoreline at 8 m water depth using 10 pressure sensors (Long et al., 1996). Additionally, 11 fixed ECMs and 13 pressure sensors were used to measure the cross-shore variability of velocity and wave height in the surf zone (Elgar et al. 1998). Other details regarding data acquisition and processing can be found in Gallagher et al. (1996, 1998) and Elgar et al. (1998).

The bathymetry as well as the hydrodynamic conditions is shown in Fig. 2.3a. The nearshore bar is located 130 m from the shoreline. The model domain is alongshore uniform, has a cross-shore width (x) of 780 m and an alongshore length (y) of 800 m, with a grid resolution of 2 m and 80 m in x and y directions, respectively. The water depth varies from 7.26 m at the offshore boundary to 0 m at the shoreline. A tidal elevation of 0.7 m is added to the water level. The vertical domain has been distributed in 32 equally spaced vertical layers. The boundary conditions are periodic in the alongshore (i.e., north and south boundaries), closed at the shoreline, and Chapman like radiation condition (Chapman, 1985) at the offshore end of the domain. Effect of earth rotation has not been included. The bottom stress has been formulated using a logarithmic bottom drag with a bottom roughness length (z_0) of 0.003 (Feddersen et al., 1998). The turbulence closure scheme is Generic Length Scale (GLS, k-ϵ) as described in Warner et al. (2005). Wave forcing is provided by SWAN, which propagates an offshore JONSWAP wave spectrum with a significant wave height of 2.3 m, a peak period of 6 s and a 13° angle of incidence. The effect of wave rollers and enhanced wave breaking induced mixing has been considered in all the simulations. Wave dissipation (ϵ_b) obtained from SWAN is used to feed the roller evolution model (Eqn. 14) with α_r=1.

Figure 2.3 shows the significant wave height, sea surface elevation and barotropic cross-shore and longshore flows (depth averaged from three dimensional flows). The

significant wave height after 3 hours of model simulation shows that wave breaking occurs over the bar crest and close to the shoreline (Fig. 2.3a). Simulation from all the three formulations show a wave setup (Fig. 2.3b) at cross-shore locations with wave breaking. The sea surface elevation from M08-11_{top} and M08-11_{vrt} are similar, while M03 predicts slightly smaller values. The depth averaged, Eulerian, cross-shore velocity (Fig. 2.3c) shows same cross-shore distribution from all the three simulations. It is directed offshore and is strongest over the bar crest (0.14 ms^{-1}) and further shoreward (0.19 ms^{-1}). It is important to point out that the depth averaged, cross-shore velocity for this case is equal to the sum of mass flux due to Stokes drift and wave roller induced mass flux, which confirms the mean continuity balance between barotropic Eulerian mean flows and net onshore directed mass flux. The strongest longshore velocity was measured over the bar trough during the experiment (Feddersen et al. 1998). M03 derived depth averaged longshore velocity (Fig. 2.3d) are weaker than the observed flows, while results from simulations using M08-11_{top} and M08-11_{vrt} formulation show better agreement to the observed dataset (Figure 2.3d).

Measured (Garcez-Faria et al., 1998, 2000) and modeled vertical distributions of cross-shore and longshore Eulerian mean velocities are shown in Fig. 2.4. M08-11_{top} and M08-11_{vrt} runs exhibit a strong vertical shear in the cross-shore velocity, with onshore directed velocity at the surface and offshore directed undertow near the bottom. This surf zone recirculation pattern is most intense over the bar crest and decreases shoreward and further offshore. Shoreward of the bar-crest, M08-11_{top} and M08-11_{vrt} show similar vertical profiles, while seaward of the bar crest M08-11_{top} has a higher vertical shear than M08-11_{vrt}. Overall, these model simulations successfully replicate the vertical structure shown by the observed data. M03 runs show relatively milder undertow at the bar crest with hardly any vertical shear. Furthermore, no onshore directed flow is simulated at the surface from M03 formulations. M08-11_{top} and M08-

11_{vrt} runs show maximum longshore velocity shoreward of the bar crest (Fig. 2.4b) along with close agreement to measured flows. The inclusion of roller evolution model with α_r=1 and enhanced mixing due to wave breaking contributes to shifting the location of peak longshore velocity from over the bar crest to further shoreward. At locations offshore of the bar crest longshore velocities from the M08-11_{vrt} formulation are slightly weaker and show relatively better agreement in comparison to M08-11_{top}. Irrespective of the inclusion of wave roller and wave-induced mixing, the M03 run (Fig. 2.4b) creates strongest longshore flow at the bar-crest. It underestimates the longshore flow in the bar trough, while further offshore it shows better agreement to observed flows.

The normalized root mean square error (defined as in Newberger and Allen, 2007b) in modeled cross-shore and longshore velocities (ε_u, ε_v) for simulation using M03, M08-11_{top} and M08-11_{vrt} formulations are (0.83, 0.30), (0.58, 0.31) and (0.55, 0.20), respectively. The errors for M08-11_{top} and M08-11_{vrt} are similar to the model skill shown by Newberger and Allen, 2007b (0.45-0.70 and 0.12-0.50) and U10 (0.43 and 0.09). Similarly, normalized (by the maximum value) root mean square errors (defined as in Sheng and Liu, 2011) were estimated for all seven stations (see Fig. 4) and they are listed in Table 1. The M03 simulated longshore velocities have an overall error of 30% with larger errors, in excess of 40%, occurring at stations located near the bar region, while smaller errors (<10 %) are found at stations away from the bar. The M03 simulated cross-shore flows have a total error of 44 % with the largest error (>100 %) occurring at the furthest offshore station (Table 1). On the other hand, the errors from the M08-11_{top} and M08-11_{vrt} simulations are similar in magnitude for both longshore and cross-shore velocities, with the smallest error produced by the M08-11_{vrt} simulations of longshore velocities at the two offshore station locations. The total errors in simulated flows for DUCK94 experiment are 15.4% and 24.7%, in longshore and cross-shore velocities, respectively for M08-11_{vrt}.

Overall, it is evident that M03 fails to create a surf zone recirculation pattern and errors in cross-shore flows from M03 run are significantly higher than for M08-11_{top} and M08-11_{vrt}. It is interesting to point out that for the DUCK94 experiment wave shoaling is not observed within the computational domain. In presence of a wave shoaling region, the performance of M08-11_{top} would deteriorate as it creates strong offshore flows at the surface layer unlike the M08-11_{vrt} formulation (see section 2.2.5).

2.3 Nearshore Circulation Cell Cases

Rip currents have been the subject of modeling (Bowen et al., 1969b; Tam, 1973; Noda, 1974; Dalrymple, 1975; Haas et al., 2000; Haller et al., 2001; Haas et al., 2003) but also experimental studies in both the field (MacMahan et al., 2005; Aagaard et al., 1997; Brander and Short, 2001; Sonu, 1972) and the laboratory (Haller et al., 2002; Drønen et al., 2002). They provide a good example for testing nearshore numerical models as they invoke a number of nearshore processes and wave and current interaction patterns. In this section the M08-11_{vrt} formulation is applied to examine its performance on rip current development by comparing to previously published work.

Initially, two ideal cases are presented where rip current cells develop in response to alongshore variability of wave forcing (Case 3) and alongshore variable bottom bathymetry (Case 4). The former condition can be the result of temporal variability in wave group forcing (e.g., Long and Özkan-Haller, 2009) or due to the incidence of intersecting wave trains of similar frequency (e.g., Dalrymple, 1975). On the other hand, the latter condition is not uncommon in barred beach profiles. In each case, alongshore differences in wave setup, caused by alongshore variation of the wave breaking position, create an alongshore pressure gradient which in turn drives a longshore current. In both cases the creation of an alongshore gradient in wave setup leads

to the development of a circulation cell like pattern in the surf zone as described in Bowen (1969) and Noda (1974).

In addition, the laboratory studies of rip currents by Haller et al. (2002) are well documented and provide an excellent set of data for comparison to numerical model results. HW09 provided a qualitative comparison of rip current formation to results from Haller et al. (2002). Expanding on this previous work, the modified model is used to simulate the formation of rip currents on an alongshore bar trough morphology (Case 5), which is a scaled-up experiment of the laboratory study conducted by Haller et al. (2002) and Haas and Svendsen (2002).

2.3.1 Case3: Alongshore variable wave forcing

The setup of this case study includes incidence of alongshore variable wave height distribution on a planar beach as described by Bowen (1969). The present case study differs from Bowen's setup as spectral instead of monochromatic waves is used and the domain size has been increased to resemble realistic field conditions. The alongshore uniform, planar bathymetry is analytically described by:

$$d = tan\beta \cdot x \cdot (1 + \epsilon \cdot cos(\lambda \cdot y)) \tag{2.19}$$

For $\epsilon \ll 1$, this can be approximated as $d \approx \tan \beta x$. The beach slope tan βx is 0.02 and the water depth (d) varies from 12 m offshore to 0 m close to the shoreline. The domain is 650 m in the cross-shore and 1,000 m in the alongshore direction, with a resolution of 5 and 10 m, respectively. In the following discussion, results only from the area 600 m (x from 0 m to 600 m) by 1000 m (y from 0 to 1000 m) are shown, so that boundary effects are excluded. Vertically, the domain is distributed in 10 equally distributed sigma layers. Closed boundary conditions are used at the two lateral sides and the shoreline, while Neumann boundary conditions have been used at the offshore boundary. A logarithmic bottom friction is used with a roughness

length of 0.005 m, a value close to those reported from field studies (e.g., Feddersen et al., 1998).

The wave model (SWAN) is run for the same grid as ROMS. The wave forcing applied at the offshore boundary is directed perpendicular to the domain, has a period of 5 s and an alongshore varying wave height described (see eqns. 30 and 31 in Bowen, 1969) by:

$$H = \gamma \frac{(1-K)tan\beta}{f} x\,(1 + 0.2cos\,(\lambda y)) \tag{2.20}$$

where λ is the alongshore wave number of the wave height variability ($2\pi/L_y$, with L_y=1,000 m), f is a scaling constant, tanβ is the beach slope, K (a parameter which relates wave setup to slope) is calculated as $(1+8/3\gamma^2)^{-1}$ and γ (=0.6) is the depth-induced wave breaking constant (Battjes and Janssen, 1978; Eldeberky and Battjes, 1996). The alongshore and cross-shore domain is scaled by a value of (λ=$2\pi/1000$) for this case. The wave forcing is described by a directional spectrum consisting of 20 frequency bands in the range 0.04 Hz to 1 Hz, and 36 directional bins of 10° each from 0° to 360° with a directional spreading of 6°. The bottom friction used in SWAN is based on the eddy viscosity model of Madsen et al. (1988) with a bottom roughness length scale of 0.05 m. The modeling system for this case is configured in one way coupling where there is no feedback of the currents or water levels to the wave model, and in a two way coupling mode where exchange of wave and current information takes place between ROMS and SWAN at a synchronization interval of 20 s. Both model configurations were run for a simulation time of two hours over which the computational domain achieves stability. Unlike Yu and Slinn (2003) very small differences were observed between the final results of one and two way coupling based simulations. This difference from Yu and Slinn (2003) can be attributed to a number of reasons including differences in wave forcing, bottom friction values and on the width of the rip current jet in the two cases. As Yu and Slinn (2003) mention the current effect on waves is stronger for narrow offshore rip currents as in their

case, while in the present study the rip system is approximately 250 m wide. In the following sections the two way coupled results are discussed, unless stated otherwise.

The wave height distribution over the domain is shown in Figure 2.5. The wave incident at the offshore boundary is alongshore variable with a maximum value of 1.5 m at the lateral boundaries and a minimum value of 1 m at the center of the domain. At the center of the domain (i.e., $\lambda \cdot y = \pi$), the incident wave height initially decreases and then increases before it starts breaking in shallower water depths. The initial decrease is due to bottom friction and depth induced dissipation and the increase after that is due to interaction of the incoming wave field with the outgoing currents. This outgoing current locally increases the wave height by a small value (0.05-0.10 m).

The depth averaged Lagrangian (Eulerian mean + Stokes) mean velocity and the associated streamlines are compared to analytically derived streamlines - following Bowen (1969) - assuming a breaking position of $\lambda \cdot x = \pi/2$ (Fig. 2.6). The flow patterns are symmetrical about $\lambda \cdot y = \pi$; therefore only the bottom half is shown and discussed here. The flow pattern within the surf zone ($\lambda \cdot x < \pi/2$) is onshore, offshore and alongshore directed at $\lambda \cdot y = 0$, π, and $\pi/2$, respectively. The longshore current within the surf zone increases from 0 to 0.2 ms^{-1} and then reduces to 0 ms^{-1} at $\lambda \cdot y = \pi$. For locations outside the breaking zone ($\lambda \cdot x > \pi/2$), the longshore current is relatively weaker and is directed from $\lambda \cdot y = \pi$ to $\lambda \cdot y = 0$. Within the surf zone, the streamline patterns observed are similar for both the analytical solution (Fig. 2.6c) and the model simulation (Fig. 2.6b). It is important to note that longshore symmetry of streamlines about the center of circulation is observed, which suggests that the strength of offshore and onshore directed flow at $\lambda \cdot y = 0$ and $\lambda \cdot y = \pi$ are of the same magnitude. Outside the surf zone (i.e., for $\lambda \cdot x > \pi/2$), the two streamline patterns differ. The model based streamlines show uniform distribution pointing at equal strength of longshore and cross-shore velocity from $\pi/2 < \lambda\, x < 6\pi/5$. The analytical

solution (Fig. 2.6c) suggests reduction in velocity when moving further offshore (seen by increase in distances between the corresponding streamlines). These differences occur because the analytical solution includes only bottom friction as a parameter for dissipation, whereas the model simulations include additional dissipative and mixing processes, which make the velocity distribution uniform outside the surf zone. Overall, even though different bottom friction, turbulence closure schemes etc. are used, qualitatively the results are comparable to Bowen 1969 (their Fig. 6) and to the results of LeBlond and Tang (1974) who included wave-current interaction in their analytical solution.

In order to examine the effect of lateral mixing on circulation pattern, a sensitivity analysis is implemented based on a Reynolds number defined as VL_y/A_H, where V is the maximum longshore velocity magnitude, L_y is the alongshore wavelength of the forcing perturbation and A_H is the horizontal coefficient of viscosity (Fig. 2.7). Small changes in bottom friction affect the maximum velocity value but not the circulation pattern (not shown here). On the other hand, changes in horizontal mixing, affect both velocity strength and circulation pattern. As the Reynolds number increases, the solutions become more skewed, i.e., outflowing current at the location of lower waves tends to become narrow and the onshore flow broadens. This effect is shown in Fig. 2.7 where the stream function for different values of Reynolds number is presented. As A_H decreases from 6 to 0.5, the Reynolds number increases from 42 to 500, making the solution more skewed about the individual circulation cell centers. Qualitatively this solution compares well to both the theory of Arthur (1962) and the results derived by Bowen (1969) by numerically solving the non linear problem for streamline distribution.

The vertical structure of the cross-shore and longshore Eulerian mean velocities along three profiles at $\lambda \cdot \mathrm{y} = \pi/5$, $\pi/2$ and $4\pi/5$ (for locations see Fig. 2.5), corresponding to locations where the depth averaged cell flow is directed onshore, along-

shore and offshore, respectively, are shown in Fig. 2.8, respectively. These results correspond to simulation runs with A_H=0.5 m^2s^{-1}. The first location (Fig. 2.8a) corresponds to bigger waves, which start breaking further offshore ($\lambda \cdot x \sim 0.5\pi$). The region onshore of location $\lambda \cdot x = 0.5\pi$ shows a vertical segregation of the flow. The onshore flow observed at the surface layer at $\lambda \cdot y = \pi/5$ (Fig. 2.8a) is stronger than the surface onshore flow at $\lambda \cdot y = \pi/2$ (Fig. 2.8b). Presence of a circulation pattern in the domain reinforces current directed towards the shoreline at $\lambda \cdot y = \pi/5$. The offshore flow in this case is weak and is limited to the bottom boundary. The vertically integrated flow is directed onshore as shown in Fig. 2.6a. Outside the surf zone (i.e., $\lambda \cdot x > 0.5\pi$), the flow is predominantly weak, onshore directed ($\sim$ 0.05 ms^{-1}) at the upper half of the sigma layers and gradually decreases to no flow at the bottom layer (Fig. 2.8a).

At the third vertical profile (Fig. 2.8c), the incoming waves are small and break close to the shoreline ($\lambda \cdot x \sim 0.4\pi$). The flow field close to the surface is weakly (<0.05 ms^{-1}) onshore directed as this velocity at the surface is reduced by the rip current jet directed offshore. Also the onshore flow is limited to the top layer. The offshore directed undertow is stronger in this case and occupies the largest part of the water column. The vertically averaged flow is strongly offshore directed. Outside the wave breaking zone (i.e., $\lambda \cdot x > 0.4\pi$) the velocity strength steadily decreases from 0.2 ms^{-1} to 0.05 ms^{-1}.

Panels d, e, and f, in Fig. 2.8, shows the vertical structure of longshore velocity at the same locations as in Figs. 2.8a, b, and c, respectively. At $\lambda \cdot y = \pi/5$ (Fig. 8d), longshore velocity within the surf zone ($\lambda \cdot x < 0.45\pi$) has a strength of 0.1 ms^{-1} while at $\lambda \cdot y = \pi/2$ (Fig. 8e), velocity is positive and strongest (0.2 ms^{-1}) at the surface, gradually decreasing to 0.15 ms^{-1} near the bed. This is reflected in the strong depth averaged longshore velocity observed within the surf zone in Fig. 2.6a. At $\lambda \cdot y = 4\pi/5$ (Fig. 2.8f), velocity within the surf zone is stronger than that at $\lambda \cdot$

y =$\pi/5$. This occurs because the streamlines in this case are not symmetrical about the center of the circulation (Fig. 2.7a) and the offshore flow occurs over a smaller area in comparison to broadened onshore flow. Offshore of $\lambda \cdot$ x = 0.45π (outside the surf zone), the alongshore flow is small and gradually increases to -0.10 ms^{-1} for the rest of the vertical domain for $\lambda \cdot$ y =$\pi/5$, $\pi/2$ and $4\pi/5$.

2.3.2 Case4: Alongshore Varying Bathymetry

In this case study the alongshore bathymetry of the beach is varied to produce a sinusoidal pattern according to (Noda, 1974):

$$d(x,y) = tan\beta \cdot x\left(1 + \alpha \cdot exp\left(-\left(\frac{x}{\alpha/3}\right)\right)^{1/3} \cdot sin^{10}\left(\frac{\pi y}{L_y}\right)\right) \tag{2.21}$$

where the beach slope (tanβ) is 0.025, the wavelength(L_y) of the alongshore variation is 80 m and α is a constant (20). This analytical expression generates a periodic beach bathymetry with channels concentrated at alongshore distances which are multiple of L_y, while it produces a straight coastline at x=0 m.

The numerical model domain is 110 m and 560 m in the cross-shore and alongshore directions, respectively, with a resolution of 2 m in both directions. Application of Eqn. 21 over the domain generates 7 channel-like features. In the following discussion, results only from the central feature, over an area 100 m (x from 0 to 100 m) by 80 m (y from 240 to 320 m) is shown, so that boundary effects are excluded. Ten equally spaced sigma layers were used in the vertical direction. Closed boundary conditions are implemented in the lateral and coastline and Neumann conditions at the offshore boundary. Logarithmic bottom friction has been implemented with a roughness length of 0.005 m.

The same grid is used by the SWAN wave model and the wave forcing is a directional spectrum as that used in Case 3 but with a directional spreading of 2°. Wave conditions are similar to those used by Noda (1974) with a significant wave height of

0.92 m, peak wave period of 4 s and normally incident at the offshore boundary. The other variable parameters are the same as in Case 3 (i.e., depth induced breaking constant, γ=0.6 and bottom friction with roughness length of 0.05 m). The ROMS-SWAN system in this case is operated in a two way coupling mode, exchanging wave current information at a 20 s interval. The results presented here are after 1 hour of simulation after the model has achieved stability.

The depth averaged Eulerian mean velocity and wave height distribution are shown in Figs. 2.9a and b, while the vertical distribution of the cross-shore current for two transects corresponding to y=240 and 280 m are shown in Figs. 2.9c and d. The results indicate the development of rip currents and the interaction of the waves with the bathymetry which is exhibited as alongshore differences in wave breaking position (not shown in here). In addition, it is characteristic that the wave height slightly increases over the area of the rip current development (see cross-shore locations 60 to 80 m) due to the interaction of strong outgoing current with the incoming waves.

The vertical profile of cross-shore Eulerian mean velocity at a transect located at y=240 m is shown in Fig. 2.9c. Wave breaking starts at x=70 m as determined by a vertical shear observed in the cross-shore velocity profile. Further offshore (x > 70 m), the entire water column shows an onshore directed velocity due to the background circulation pattern observed in the domain (Fig. 2.9a). In a normal surf zone circulation pattern (see Case 1, Fig. 2.2), onshore flow is observed near the surface. This onshore surface flow is further enhanced in this case, due to the presence of the onshore component of the circulation cell. The offshore flow is limited to elevations close to the bottom boundary other than in very shallow waters (z<-0.5 m) where the entire water column is directed offshore. The vertical profile of cross-shore velocity at y=280 m is depicted in Fig. 2.9d. Wave breaking takes place at 1.5 m depth; some 60 m from the shoreline (see Fig. 2.9b).

The rip current strength is approximately 0.5 ms^{-1} at the bottom layer and weakens close to the surface. In shallow waters (1 m), rip current strength decreases and close to the shoreline, a vertical shear in velocity is observed. The vertical structure of the cross-shore flow at y=0 and 40 m is similar to that at locations $\lambda \cdot y = \pi/5$ and $4\pi/5$ respectively for Case 2 and are shown in Figs. 2.8a and c.

The normalized stream function calculated using the depth averaged Lagrangian mean velocities from the model output is shown in Fig. 2.10, together with the stream function generated by Noda (1974). In both cases the streamlines converge at y=40 m, creating a flow pattern from shallower to deeper waters, simulating a rip current like situation. The maximum value of stream function occurs close to x=60 m for Noda (1974) and x=70 m for our simulations. Both results are almost symmetrical around an imaginary line located at y=40 m. It is worth noticing that our system of stream function is shifted slightly to the right in comparison to Noda (1974).

The depth averaged cross-shore velocity in the rip channel is approximately 0.5 ms^{-1} (Fig. 2.9a), a value more reasonable than that of Noda (1974), where for the same setting he predicted a rip current velocity in excess of 4 ms^{-1}. The differences in distribution of stream function and magnitude of rip current velocity occurs because, as acknowledged by Noda (1974, see pp. 4105), his depth averaged model was rather simplified as it only accounts for pressure gradient, radiation stress and bottom friction and does not account for current-induced wave refraction and modifications of the wave field due to Doppler shift, as in the present model. Furthermore, the unrealistic rip current velocity predicted by Noda (1974) implies that the stream function might not be accurate enough for direct comparison with our model, which seems to give more realistic results.

2.3.3 Case 5: Comparison to Scaled Laboratory Studies

This case study investigates the dynamics for a barred beach bathymetry that develops rip currents. The application is based on a laboratory scale experiment and is similar to a case demonstrated in HW09. However there are two major differences: (a) in HW09 the wave driver was a monochromatic wave model (REF/DIF), while here a spectral wave model (SWAN) is used; and (b) the domain used in HW09 was identical to the laboratory experiments while in our simulations the domain has been scaled by a factor of 10 (kinematic similarity, Hughes, 1993) to create more realistic field conditions.

The bathymetry domain (Fig. 11) is an idealized version of that used by Haller et al. (2002) and Haas and Svendsen (2002). The scaling of the domain by a length scale, $N_L = 10$, leads to a maximum depth of 5 m, a nearshore bar of 0.60 m located 40 m off the coastline, cross-shore domain width of 146 m and alongshore length of 262 m. To avoid interaction of rip channel flow with the lateral boundaries, the domain was extended laterally by 40 m in either direction. Rip channels are spaced 92 m apart and the channel width is 18.2 m which makes the ratio of channel width to rip current spacing 0.2, a value consistent with those found in the field (e.g., Huntley and Short, 1992; Aagaard et al., 1997, Brander and Short, 2001). The model grid has a horizontal resolution of 2 m in both directions and consists of 8 equally spaced sigma layers. The boundary conditions at shoreline, offshore boundary and lateral ends are no flow conditions (i.e., closed boundary conditions at the coast, lateral boundaries and offshore) and are the same as the laboratory experiments of Haller et al., (2002). Bottom friction (bottom roughness of 0.015 m) similar to that of HW09 is used in this work. Simulations were carried out with both the modified vertical distribution (Eqn. 10) of the radiation stress (M08-11_{vrt}, see section 2) and the original version (M03) used in HW09.

At the offshore boundary, SWAN was forced with 0.5 m waves with peak period of 3.16 s, and directional spreading of 3° propagating perpendicular to the shoreline. From these values, SWAN computes a wave spectrum based on a JONSWAP distribution. The spectral resolution is 20 frequency bands in the frequency range between 0.04 Hz and 1 Hz, and 36 directional bins of 10° each from 0° to 360°. The other variable parameters are the same as in Case 3 and 4 (i.e., depth induced breaking constant, γ=0.6 and bottom friction with roughness length of 0.05m). The time steps used for ROMS and SWAN are 2 and 10 s respectively, and the coupling between the models takes place at 20 s intervals. Initial comparisons are done only for 30 minutes of simulation time. The model remains stable because a higher bottom friction coefficient and horizontal mixing than typically observed in the field is used.

The wave height distribution over the domain using the original and newer versions of ROMS (i.e., M03 and M08-11$_{\text{vrt}}$ formulations, respectively) is shown in Fig. 2.12a and b. At the location of the rip channel, the increase in wave height due to offshore directed rip current is lower in the M08-11$_{\text{vrt}}$ than the M03 simulations. The waves propagating over the bar break and generate a higher wave setup than the setup generated by waves propagating over the channel. This creates feeder currents moving from the bar towards the channel. Waves approaching the shoreline over the channel become steeper, decrease in wavelength and increase in height due to interaction with the rip current. These bigger waves break close to the shoreline creating longshore currents which move away from the channel at shallow depths. This phenomenon can be further confirmed by comparing the mean sea surface elevation over the bar and channel for M08-11$_{\text{vrt}}$ based simulations (Fig. 2.13). The elevation is lower at the location of the channel than over the bar. On the other hand, closer to the shoreline the sea surface at the channel location is higher than over the bar driving the observed flow patterns.

M03 simulated depth averaged, Eulerian mean, cross-shore velocity (see Figs. 2.12c and d) at the channel is 25% stronger than that predicted by M08-11_{vrt}. The stronger offshore directed velocity locally increases the wave height at the location of the rip channel in M03. Further offshore of the rip channel, the magnitude of cross-shore velocity is similar in both M03 and M08-11_{vrt} and hence the wave height pattern is also similar. The primary circulation pattern with feeder currents exiting through the rip channel and return flow over the bar is evident irrespective of the formulation used. These circulation cells are symmetric both with respect to the rip channel and the axis of the alongshore bar.

Noticeable differences in secondary circulation patterns for M03 and M08-11_{vrt} based simulations can be seen in Figs. 2.12c and d. Waves with greater wave height in the vicinity of the rip channel, for M03 formulations, drive a larger setup and stronger alongshore pressure gradient close to the shoreline in comparison to M08-11_{vrt} formulations. As a consequence the secondary circulation pattern close to the shoreline is stronger for the M03 than the M08-11_{vrt} based simulations.

The vertical variability of cross-shore Eulerian mean velocity at the center of the channel is shown in Figs. 2.14a and b for M03 and M08-11_{vrt}, respectively. Inshore of the bar location, wave breaking induces onshore directed velocity at the surface extending all the way to the bed for M03 (Fig. 2.14a), while for the M08-11_{vrt} simulation a return flow develops near the bed (Fig. 2.14b). Over the bar and shoreward the cross-shore flow structure differs between the two simulations (Figs. 2.14c and d). The M03 simulation (Fig. 2.14c) shows the development of offshore flow throughout the water column, while the improved model simulation results in an onshore flow near the sea surface with a stronger return flow near the bed. Further offshore, both simulations give similar results. These findings show that the vertical distribution of the radiation stress in M03 fails to create a surf zone vertical recirculation system, while the M08-11_{vrt} run provides more realistic results

that show qualitative agreement to field observations of cross-shore velocity profile for barred beaches (see Fig. 1c; Garcez-Faria et al., 2000).

The scaled numerical experiment conditions correspond to Test B of Haller et al. (2002) and Test R of Haas and Svendsen (2002). Thus, the results of those lab experiments is used to provide a semi-quantitative comparison between the measured and modeled vertical structure of the cross-shore velocity field. For this comparison all of the bin averaged velocities from Test R (Fig. 11, Haas and Svendsen, 2002) and for all reported locations (Fig. 2.14e) is used. The measured and simulated velocities are normalized by the corresponding maximum cross-shore velocities at the bar crest (i.e., x= 27 m, Fig. 2.14e), respectively. The simulated normalized cross-shore current vertical structure from the upgraded model agrees well with the experimental data. Inside the channel, rip current speed is greatest at the level of the bar crest and decreases toward the water surface and bed. However no experimental data are available near the water surface. Just off the bar, the normalized data show the best agreement with our simulation using M08-11_{vrt}. Such a relative agreement between data and model persists in areas further offshore of the bar location.

A normalized root mean square error analysis is presented (Table 2) by comparing the normalized, simulated flows from M03 and M08-11_{vrt} and the measured flows in the rip channel. M03 based simulations show high error (>30%) at stations within the rip channel and at locations further offshore. On the contrary, M08-11_{vrt} shows relatively smaller errors against the measurements at all the stations. The total error in M08-11_{vrt} results is 11.7% versus 20.1% for M03.

For steady flow, the depth and time averaged cross-shore (x) momentum equation can be written as:

$$\frac{\partial}{\partial x}\left(U^2 h\right) + \frac{\partial}{\partial y}\left(UVh\right) = -gh\frac{\partial \eta}{\partial x} - \frac{1}{\rho}\left(\frac{\partial S_{xx}}{\partial x} + \frac{\partial S_{xy}}{\partial y}\right) - \frac{\partial}{\partial x}\left(A_H \frac{\partial U}{\partial x}\right) - \frac{\tau_x^b}{\rho} \qquad (2.22)$$

where U and V are the depth averaged cross and along shore Lagrangian mean velocities, respectively, h is the total depth, ρ is the fluid density, S_{ij} represents the

components of the radiation stress tensor, τ_x^b is the component of the bottom stress acting in the x-direction and A_H is the horizontal viscosity coefficient.

The depth averaged distribution of these terms from modified model simulations are, shown in Fig. 2.15. Alongshore variation of the depth averaged horizontal advection, bottom friction and gradient of alongshore radiation stress ($\partial S_{xy}/\partial y$) in the cross-shore direction, are shown in Figs. 2.15a-d for four locations (40, 30, 26 and 20 m respectively from the shoreline, see Fig. 2.9). Since horizontal advection and bottom stress depend on velocity magnitude and gradients, these terms become important within and in the vicinity of the rip channel as seen in Figs. 2.15b and c. Close to the shoreline and further offshore, bottom friction and horizontal advection become less significant. For normally incident waves, S_{xy} and $\partial S_{xy}/\partial y$ should be 0 at all the locations, as is observed in Figs. 2.15a, b, c and d for all alongshore positions other than the rip channel. Local wave refraction effects due to interaction of rip currents with incoming waves lead to the development of $\partial S_{xy}/\partial y$ within the rip channel. These terms are partially in balance with the horizontal advection terms, at locations within and outside the rip channel area (Figs. 2.15a, b and c). $\partial S_{xy}/\partial y$ becomes relatively insignificant very close to the shoreline (Fig. 2.15d).

The alongshore variation of depth averaged horizontal viscosity, pressure gradient and radiation stress at the same transect locations as for the other terms (see above) are shown in Figs. 2.15e-h. At distances 40 m from the shoreline, where no wave breaking occurs, the gradient of cross-shore radiation stress ($\partial S_{xx}/\partial x$) and pressure gradient terms are insignificant. Within the surf zone, $\partial S_{xx}/\partial x$ is balanced by the pressure gradient for all alongshore locations (Figs. 2.15 f, g and h). As wave breaking initiates at the bar crest, $\partial S_{xx}/\partial x$ is weaker within the rip channel (Figs. 2.15 f, g) than over the bar. When waves propagate over the channel and break close to the shoreline, pressure gradient and $\partial S_{xx}/\partial x$ obtain greater values than at other alongshore positions (Fig. 2.15h). The horizontal viscosity is always small except

at locations with increased rip velocities, thus increasing the mixing within the rip channels. All these numerical simulation results are found to be qualitatively similar and in agreement with the experimentally-derived results of Haller et al. (2002).

2.4 Discussion

Overall results presented here indicate that the modification of the M08-11 formulation with the introduction of a vertical distribution function as shown in Eqn. 2.10 (M08-11_{vrt}) mitigates some of the shortcomings of the original method and provides results consistent with previous solutions both in the depth averaged and the vertical distribution of the circulation patterns. In this section, our findings are explored for a more comprehensive discussion of the forces operating in rip current development. In particular the implication for sediment transport and rip channel development, along with the variability of rip current strength as a function of the wave incident angle is discussed.

2.4.1 Cell circulation and potential morphological impacts

Our Case 3 has re-affirmed how small differences in offshore wave height distribution can lead to the development of rip-current circulation patterns. However, one of the fundamental questions is the association of rip currents with bathymetry (i.e., bar-channel morphology). One suggestion from this work is that although a rip current circulation may develop due to offshore variable wave conditions, a positive feedback with the sea bed through sediment transport might lead to the bar-channel configuration that is usually associated with rip currents. In a simplified approach, results from Case 3 is used to assess the sediment transport patterns that such rip cells may create. Assuming that the combined action of wave oscillatory motion and mean current is the main mechanism for sediment resuspension and that the mean current is the advective transport mechanism (i.e., ignoring the effects of wave asymmetry),

a simplified proxy for sediment erosion or accumulation can be established:

$$P_{ST} = \frac{(U_t^2)\,\overline{u}}{\partial x} + \frac{(V_t^2)\,\overline{v}}{\partial y} \tag{2.23}$$

where U_t is the total instantaneous maximum velocity, comprising the vector sum of the wave orbital velocity and mean current vector, and u and v are the cross-shore and longshore Eulerian mean velocities, while the overbar denotes mean values. Although this simple proxy does not account for settling of sediment and other processes important in morphological evolution (see Warner et al., 2008), it gives some indication of the trend for bed evolution under these conditions. As shown in Fig 2.16, the erosion potential is greatest at alongshore location λy $=\pi$, which corresponds to the area influenced by the outgoing rip current. The erosion potential reduces on moving towards the side boundaries λy $=0$ and λy $=2\pi$. Such tendency suggests that alongshore changes in wave forcing creating a rip current cell eventually might contribute to the development of the typical bar-channel configuration.

2.4.2 Driving forces for Rip cell circulation

As described earlier, rip cells can be developed either due to alongshore variability in the offshore forcing of wave height (Case 3) or due to variability in the nearshore bathymetry (Case 4). In this section the difference in the forces that drive the cell circulation are examined through an analysis of the depth and time averaged alongshore momentum balance (steady state, U and V are depth averaged Lagrangian mean velocities):

$$\frac{\partial}{\partial x}(UVh) + \frac{\partial}{\partial y}\left(V^2 h\right) = -gh\frac{\partial \eta}{\partial y} - \frac{1}{\rho}\left(\frac{\partial S_{yy}}{\partial y} + \frac{\partial S_{xy}}{\partial x}\right) - \frac{\partial}{\partial y}\left(A_H \frac{\partial V}{\partial y}\right) - \frac{\tau_y^b}{\rho} \tag{2.24}$$

These terms are plotted in Fig. 2.17 as a function of alongshore distance (normalized by the length scale of the offshore forcing (Case 3) or bathymetric perturbation as in Cases 4 and 5). The transects were taken well within the surf zone ensuring uniform alongshore water depth for Case 5 (Fig. 2.11, alongshore transect inshore

of rip channel), and are located at the middle of the surf zone for Cases 3 and 4 (see dotted line in Figs. 2.5 and 2.9b, respectively). The transect location for each case corresponds qualitatively to where the alongshore flows of the circulation cell (Fig 2.17a) converge to feed the main rip current. Case 3 produces an alongshore variability of the longshore current that resembles the alongshore variability of the wave forcing, but is 90° out of phase. A similar alongshore variability is observed for Cases 4 and 5, although in these cases the peak longshore feeder current is stronger than in Case 3 and located close to the center of the rip cell.

The pressure gradient term (PG) shown in Figs. 2.17b, c and d co-oscillates with the feeder current for each case. This indicates that pressure gradient is the dominant driver for both cases. However, within each case, the other terms exhibit similar relative behavior with the exception of the radiation stress ($\mathrm{RAD_H}$) term that changes sign for each case. In Case 3 (Fig 2.17b), $\mathrm{RAD_H}$ is positive to the left of the rip channel and negative to the right, while the opposite is true for Cases 4 and 5 (see Fig. 2.17c and d). Also it is noticeable that the absolute values of the terms for Case 3 and Cases 4 and 5 are almost an order of magnitude different, while the resulting absolute current velocities are of the same order. This increase in magnitude between the terms is attributed to the fact that in Cases 4 and 5, the undulated bathymetry creates local wave refraction effects that lead to increased values of the S_{xy} term. This term qualitatively should be directed away from the center of the channel (location of minimum value) attaining a maximum value near the bathymetric highs. In terms of gradient, this corresponds to zero values at the center and either side of the channel as appears to be the case in Fig. 2.17c and d (zero values at 0.3, 0.5 and 0.7, respectively). In Case 3, the radiation stress gradient term is solely due to S_{yy} and it has a small value. This increased importance of radiation stress gradient in Cases 4 and 5 is compensated by an increase in the absolute value of the pressure gradient. The latter is driven partially by increased wave setup over the

shoals due to bathymetry, but also due to increased wave height caused by focusing of the waves over the shoal due to refraction (i.e., the same process that increases the importance of the radiation stress gradient term). Thus overall, independent of the conditions (i.e., variable forcing or bathymetry), alongshore pressure gradient appears to be the main mechanism for the generation of feeder currents. Any increase in the alongshore radiation stress term is compensated by a similar increase in pressure gradient so that the net forcing remains of the same order. In all the cases discussed above, the horizontal advection contribution is dominant only within the rip channel area. Of the terms $\partial(VVh)/\partial y$ and $\partial(UVh)/\partial x$ responsible for horizontal advection, the latter has a greater magnitude in the vicinity of the rip channel because of stronger cross-shore velocity within the channel area.

2.4.3 Obliquely Incident Waves on LBT

In order to assess the effect of wave incidence angle on the development of rip current circulation, a longshore bar-trough morphology domain as in Case 5 was subjected to offshore waves with a height of 0.5 m and a period of 3.16 s incident at angles of 0°, 5°, 10° and 20° with respect to the shore normal. The model uses two-way coupling, allowing for interaction of waves and currents, and the results are shown in Fig. 2.18.

The top panel (Fig. 2.18) shows the depth averaged Eulerian mean velocity field in the rip channel for obliquely incident waves. As the incidence angle increases from 0° to 20°, the angle of exit of the rip current increases with respect to the shore normal. The trend is linear and for angles greater than 20°, the current becomes almost parallel to the shoreline. Svendsen et al. (2000) simulated rip currents on barred beaches incised by channels using SHORECIRC and observed similar behavior of strong inertia of alongshore flow and weak rip currents for high wave angle of incidence. As expected, the strength of longshore velocity increases as the wave angle of incidence increases.

The wave height distribution over the domain, for different wave incidence angles, is shown in the middle panel of Fig. 2.18. When waves are normally incident, the rip current flow makes the waves steeper at the location of the channel, locally increasing the wave height (Fig. 2.18 column (a)). For a wave incidence of 5°, wave steepening at the rip channel is also observed, but the increase in wave height is smaller than that observed for 0°. At higher angle of incidence (10°), wave current interaction reduces as only the component of the rip current along the direction of wave propagation interacts directly with the incoming waves. For waves coming at an angle of 20° to shore normal, the difference in wave breaking location over the bar and the channel is negligible, further hinting at the lack of substantial rip currents.

Circulation pattern at the channel location is depicted through the vorticity vector (Fig. 2.18, bottom panel). For normal incidence, primary and secondary circulation cell formation occurs outside the rip channel and close to the shoreline, respectively. These cells are symmetric about the rip channel center with opposite sign of vorticity indicating reverse sense of circulation. Such vortices are similar to the macrovortices formed due to wave breaking examined both analytically and computationally in Brocchini et al. (2004) and Kennedy et al. (2006). When waves are incident at 5°, the secondary circulation pattern weakens but the primary circulation pattern is reinforced as seen by increase in the magnitude of vorticity vector. Stretching and alongshore advection of vortices is also observed in this case. At a wave incidence of 10°, the secondary circulation cell close to the shoreline disappears and the vortices close to the channel become weak. The vorticity at the channel for 20° incidence shows only one circulation cell which is constrained at the original location where primary circulation was observed.

Fig. 2.19 (top panel) shows the Eulerian mean cross-shore velocity for varying angles of incidence (0°, 5°, 10°, 20°) in three columns (a), (b) and (c) corresponding to alongshore transects onshore and within the rip channel (see Fig. 2.18a top panel,

alongshore transects). Rip current velocity at these locations is stronger when wave incidence is at 5° and 10°. Onshore of the channel, maximum offshore directed flow within the channel area occurs for 5° whereas at transects within the channel, rip current velocity is slightly higher for 10° in comparison to 5° incidence (Fig. 2.19, top panel, column c). Higher angle of incidence (> 20°) inhibits rip currents due to inertia of alongshore motion. Aagaard et al. (1997) observed a similar increase in the rip current velocity due to oblique incidence and attributed this phenomenon to *"wind enhanced longshore current"*. Haller et al. (2002) observed an abrupt increase in cross-shore velocity for wave incidence angle of 10° in their test F. The reason for this behavior is suggested to be due to increase in alongshore radiation stress forcing in alongshore direction created by breaking of obliquely incident waves at the bar crest.

The contribution of longshore velocity on rip current circulation pattern is determined by correlating the gradient of Eulerian mean longshore velocity in alongshore direction (GAV) to the rip current magnitude. A steep gradient of longshore velocity from one end of channel to other signifies a sharp change in longshore velocity. The reduction of longshore velocity feeds the alongshore momentum in cross-shore direction which intensifies the cross-shore velocity. Fig. 2.19 (bottom panel) shows GAV in alongshore direction for 0°, 5°, 10° and 20° angle of incidence for all three transects. The GAV values for 0° and 5° incidence show similar distributions pointing at presence of a circulation pattern whereas GAV distribution for 10° and 20° incidence are different implicating a loss of the circulation cells.

GAV is maximum for 5° at all locations except at the alongshore transect at the center of the rip channel, where this quantity is equally steep for 10° (Fig. 2.19, bottom panel, column c). Thus most of alongshore momentum for 5° incidence advects through the rip channel due to the inherent rip current circulation in the domain. At a higher angle of incidence, the circulation pattern is destroyed and momentum transfer

in cross-shore direction reduces. This information of maximum rip current velocity for oblique incidence is useful for prediction of rip currents when waves coming at a small angle may be more hazardous.

2.5 Limitations of Mellor, 2011 Approach

Mellor (2003) introduced depth dependent formalism for radiation stresses to accommodate wave averaged effects on mean currents. These formulations when vertically integrated are consistent with the depth integrated solution of Longuet-Higgins and Stewart (1964). Ardhuin et al. (2008) showed that use of the M03 formulation in non-breaking wave propagation over an uneven topography produces a spurious circulation pattern at the location where $\partial h/\partial x \neq 0$. Subsequently, a new set of depth dependent equations for wave current interaction was presented (Mellor, 2008, 2011a, b and c), which is further modified and implemented in this chapter for applications in the surf zone. Mellor (2008, see Section 2) suggested that for variable topography, the new set of equations would cause some errors but overall there is a good chance that these equations can be applied to shallow water environment (i.e., $kD \approx 1$, where k is the wave number and D is the total water depth), when effects of viscosity and turbulence are included. In this section the above argument is tested by carrying out two numerical simulations corresponding to the setup originally proposed by Ardhuin et al. (2008, 2011) and to a setup that uses a milder slope as that found in Duck, NC and including friction and mixing processes. Both setups are forced with a shoaling, non-breaking monochromatic wave with a significant wave height of 1.02 m and wave period of 5.24 s, propagating from east to west. These runs are described in some detail below.

In the setup resembling Ardhuin's et al. (2008, 2011) conditions, the bottom profile has a channel in which the water depth smoothly transitions from 6 m to 4 m ($\partial h/\partial x_{max} = 0.0266$), and is symmetric about the vertical axis at the center (i.e.,

x= 300 m, Fig. 2.20a). The non dimensional water depth kD, varies from 0.85 < kD < 1 (Fig. 2.20b). The model domain is alongshore uniform with a cross-shore width (x) of 600 m and an alongshore length (y) of 800 m. Grid resolution is 4 m and 100 m in x and y direction, respectively. The vertical domain has been distributed in 32 equally spaced vertical layers. The boundary conditions are constant flux at east and west boundary (Neumann conditions) and closed in the north and south. Effect of earth's rotation, bottom stress and viscosity has not been included in this case. Simulations have been carried out using both M08-11_{top} and M08-11_{top} formulations.

In the absence of wave breaking, mixing and bottom friction the only dynamic effects occur due to changes in wave height. Shoaling of waves in shallower waters create divergence of the Stokes drift, which is compensated by the Eulerian mean current. The correct representation of Lagrangian mean velocity field (Eulerian mean + Stokes) for this wave field and domain setup is a flow along the direction of wave propagation (U_l = 0.025 ms^{-1}) at the surface, which decreases gradually to no flow at z= -2 m and then changes to a return flow of U_l = -0.01 ms^{-1} close to the bottom layer. The flow field at the surface and bottom follows the bathymetric contours (see Fig. 2, in Bennis and Ardhuin, 2011).

The vertical profile of Lagrangian cross-shore velocity based on M08-11_{top} is shown in Fig. 2.21a. At the location where $\partial h/\partial x \neq 0$ and where the waves are propagating upslope, spurious flow pattern is observed in the upper half of the water column showing a current along the direction of wave propagation ($U_l$max=0.15 ms^{-1}) and a compensating flow, of same strength but opposite sign, in the lower half of the water column. A reversed flow structure is established on the down-slope wave propagation region (Fig. 2.21a). On using M08-11_{vrt} based formulations (Fig. 2.21b), a significant part of the water column shows a weak flow, $U_l \approx$ 0.01-0.10 ms^{-1} towards wave propagation direction, while the surface layer shows a relatively stronger flow of 0.20-0.25 ms^{-1} in the opposite direction. The flow field is reversed when waves propagate

down the slope. Irrespective of updating the formulation for radiation stresses, in an idealistic situation, M08-11_{top} and M08-11_{vrt} based simulations still create incorrect flow patterns for unforced waves traversing on a sloping bottom. This is consistent with Bennis and Ardhuin (2011) and Ardhuin et al. (2008).

The second setup uses a milder, more realistic slope dh/dx_{max}= 0.0066, that is an average value for continental shelf environments (e.g., Hayes, 1967), bottom friction (quadratic drag, Cd=0.003) and mixing (constant eddy viscosity, 0.0028 m^2s^{-1}). The domain is also symmetric about the vertical axis at the center (i.e., x= 1200 m, Fig. 2.20c). The non dimensional water depth kD, is the same as before. The model domain is alongshore uniform with a cross-shore width (x) of 2,400 m and an alongshore length (y) of 800 m. Grid resolution and vertical domain remain the same as previously. In this run the Lagrangian mean velocity (Fig. 2.21c) is along the direction of wave propagation at the surface layer except at the upslope wave propagation location where small perturbations in the velocity flow field are observed. Compensating return flow in the lower half of water column is also observed. However, the strength of Lagrangian mean velocity is reduced by a factor of ~ 5 when compared to the ideal conditions (Figs. 2.21a and b). Also it is noticeable that velocity contours "attempt" to follow the bathymetric contours, as in Bennis and Ardhuin (2011).

The maximum velocity at the surface in Fig. 2.21c is twice the velocity calculated by Bennis and Ardhuin (2011) hence the flow field may be still slightly "erroneous" although Mellor (2011c) argues that this might be expected. Bennis and Ardhuin (2011) also state that the problem is not just a question of vertical distribution of radiation stress, but one of a relatively large and spurious source of momentum. Nevertheless, our results using our modified distribution of radiation stress, realistic mixing and bottom slope reduce the "erroneous" flows (Fig. 2.21a) by a factor of 4. In addition, all the simulations presented in this contribution (Cases 1-5) are for surf zone conditions, where the wave breaking induced flow is an order of magnitude higher

than the topography-induced flow shown in Fig. 2.21c (i.e., realistic shelf slope and mixing). This suggests that the errors identified by Bennis and Ardhuin (2011) might be inconsequential for practical applications in the surf zone using our modifications. These errors will be more insignificant when injection of wave turbulence and wave roller processes are included.

2.6 Conclusions

A full three-dimensional, finite difference, circulation model Regional Ocean Modeling System (ROMS) coupled with spectral, phase averaged, wave propagation model SWAN has been updated to the formulations presented by Mellor (2008; 2011a,b and c) and used to study nearshore circulation processes after a modification of the three dimensional radiation stress formulation. Although the scientific debate on the applicability of Mellor's (2008) original approach is ongoing (see Ardhuin et al., 2008; 2011 and Mellor 2011a, b and c), this paper provides an independent assessment of the method for practical applications in the surf zone. The focus here was complex flow regimes, including alongshore variability in wave height and water depth, i.e., phenomenon responsible for rip current like structure formation in the surf zone.

The results indicate that the implementation of the updated radiation stress forcing (M08-11_{top}) may create spurious flow fields in the wave shoaling region. Modified vertical distribution (M08-11_{vrt}) that incorporates wave height as a scale, significantly reduces these spurious flows. Furthermore, unlike the M03 formulation as implemented in HW09, M08-11_{vrt} formulations successfully create a surf zone recirculation pattern (onshore flows at surface and offshore directed undertow near the bottom) for obliquely incident waves on a planar beach. Comparison of model simulated littoral velocity profiles to the energetic flow fields observed during DUCK94 experiment further suggests the applicability of M08-11_{vrt} formulation to study nearshore circulation. The relative rms error in velocity profiles simulated using M08-11_{vrt} are 24

% and 15.4 % in cross-shore and longshore flow, respectively when compared against field observations from Garcez-Faria et al. (1998, 2000). These errors are smaller than errors obtained by recent studies conducted by Sheng and Liu (2011) for laboratory measured cross-shore flows.

Comparisons of the depth integrated circulation of the three-dimensional runs were found to be in agreement with the general dynamics for formation of nearshore circulation cell on normal incidence of alongshore varying wave height over a planar bathymetry (Bowen, 1969) and under alongshore variable bathymetry forced with alongshore uniform wave height (Noda, 1974). Furthermore, it has been shown that increasing the Reynolds number by decreasing the viscosity, the circulation cells become skewed with the offshore directed flow becoming narrower and faster while onshore flow broadens and becomes slower. The development of the model provided us with insights on the vertical distribution of the cross-shore velocities in these circulation patterns allowing us to provide an insight into wave breaking induced flow at the surface and bottom boundary layer.

The new formulation of radiation stress forcing demonstrated a strong agreement with the scaled-up laboratory experiments of Haller et al. (2002) and Haas and Svendsen (2002). The normalized velocities within the rip channel show a relative rms error of 11% when compared to normalized, measured flows by Haas and Svendsen (2002). This further suggests that the model is capable of successfully representing complex flows due to changes in bathymetry.

By using a proxy for sediment transport, it is determined that rip current circulation cells formed due to differences in alongshore wave forcing may lead to formation of alongshore barred beaches interrupted by rip channels.

Finally, the effect of obliquely incident waves on rip channels is studied and it is found that rip current strength observed within the channel is stronger when waves

come at angles of 5° and 10° in comparison to normally incident waves. This information may be helpful in the prediction of rip currents (Voulgaris et al., 2011).

Overall the implementation of Mellor (2008) based distribution of vertical radiation stress along with a vertical scaling as a function of wave height (M08-11$_{\mathrm{vrt}}$) improves the ability of coupled ROMS-SWAN model in resolving wave and current effects in the surf zone. This modeling tool can be used to understand the physical mechanisms driving phenomena observed in surf zone along with prediction of nearshore circulation. However, the introduction of term E_D in Mellor (2008) creates significantly "unexpected" flows for shoaling and non breaking waves on a sloping topography, which can be reduced and controlled by dissipative momentum mixing through wave breaking induced turbulence. Caution must be applied for application of Mellor (2008) formulations for studies conducted outside the surf zone, where aforementioned dissipative mechanisms are absent.

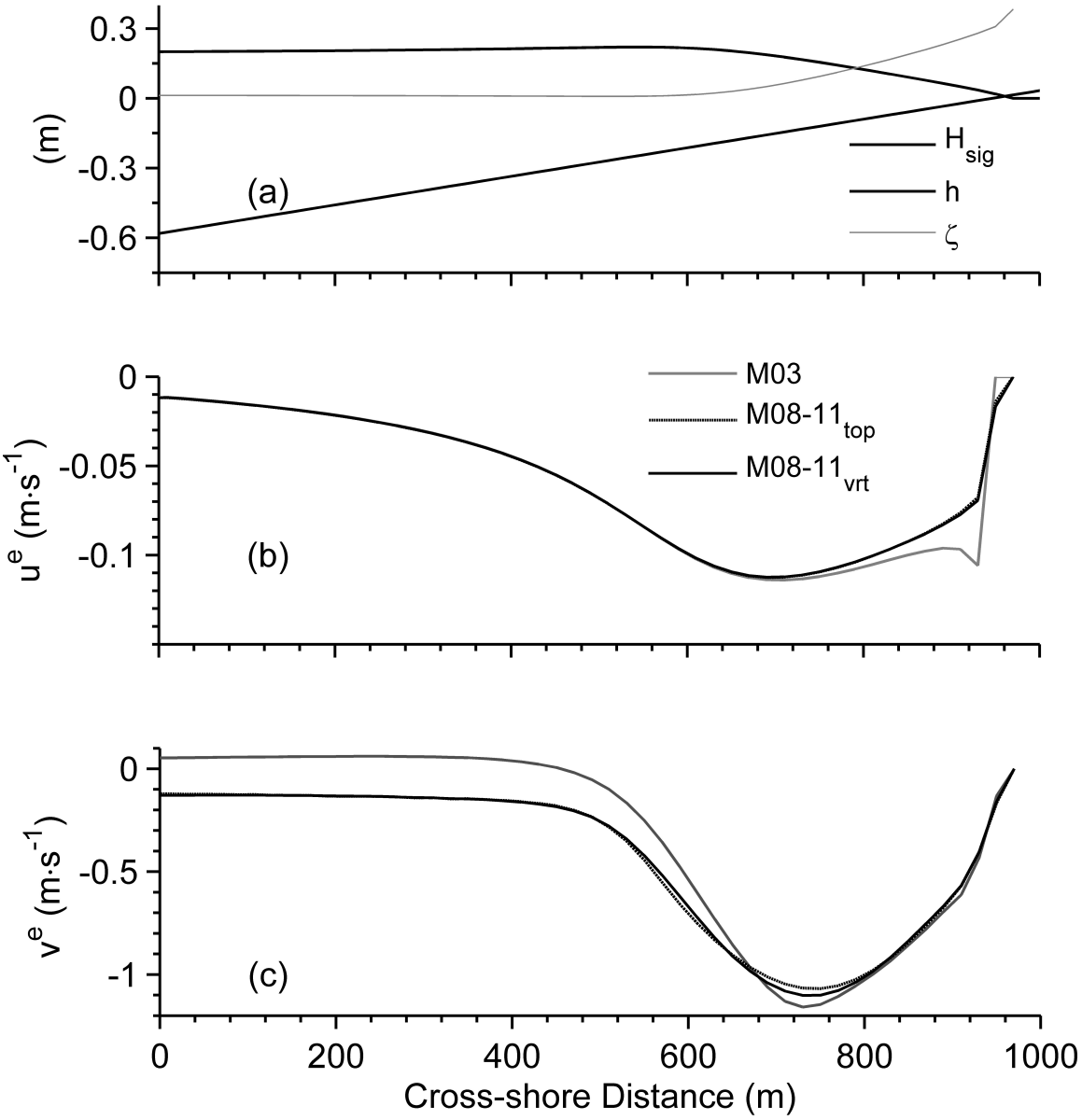

Figure 2.1: Case 1: Obliquely incident waves on a planar beach using the original radiation stress forcing M03, the updated forcing applied at the top layer M08-11_{top}, and with a vertical distribution as defined by Eqn. 10 of M08-11_{vrt}. Cross-shore distribution of: (a) significant wave height, water depth and sea surface elevation; The water depth and wave height have been scaled as h/20 and Hsig/10, respectively; (b) depth averaged Eulerian mean cross-shore velocity $\overline{u^e}$; and (c) depth averaged Eulerian mean alongshore velocity $\overline{v^e}$.

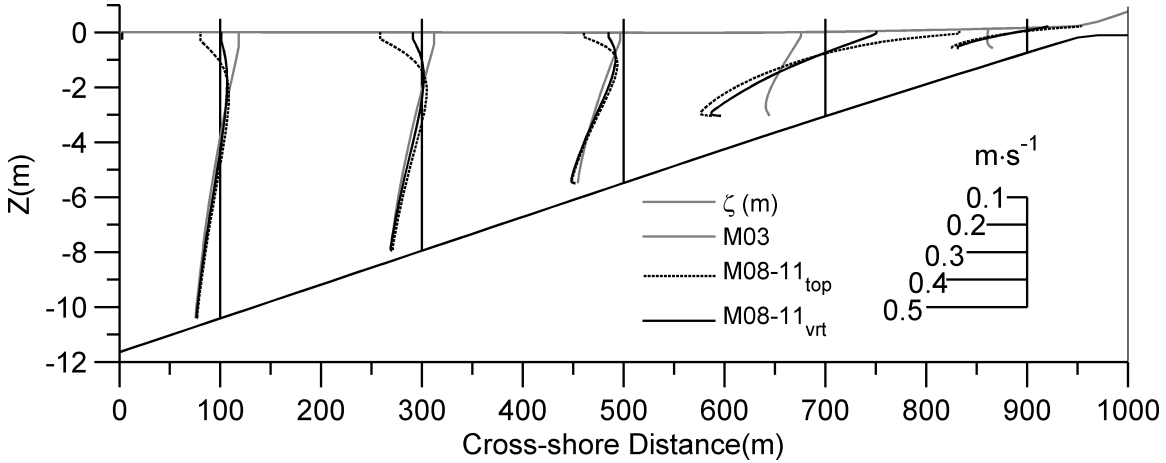

Figure 2.2: Comparison of vertical profile of cross-shore Eulerian mean velocity, u_e (x, z) between simulations using M03 (solid grey line), M08-11$_{\text{top}}$ (dashed black line), M08-11$_{\text{vrt}}$ (solid black line). The sea surface elevation (ζ, dotted grey line) is also shown. Vertical black lines indicate locations of model sampling and zero value for each profile.

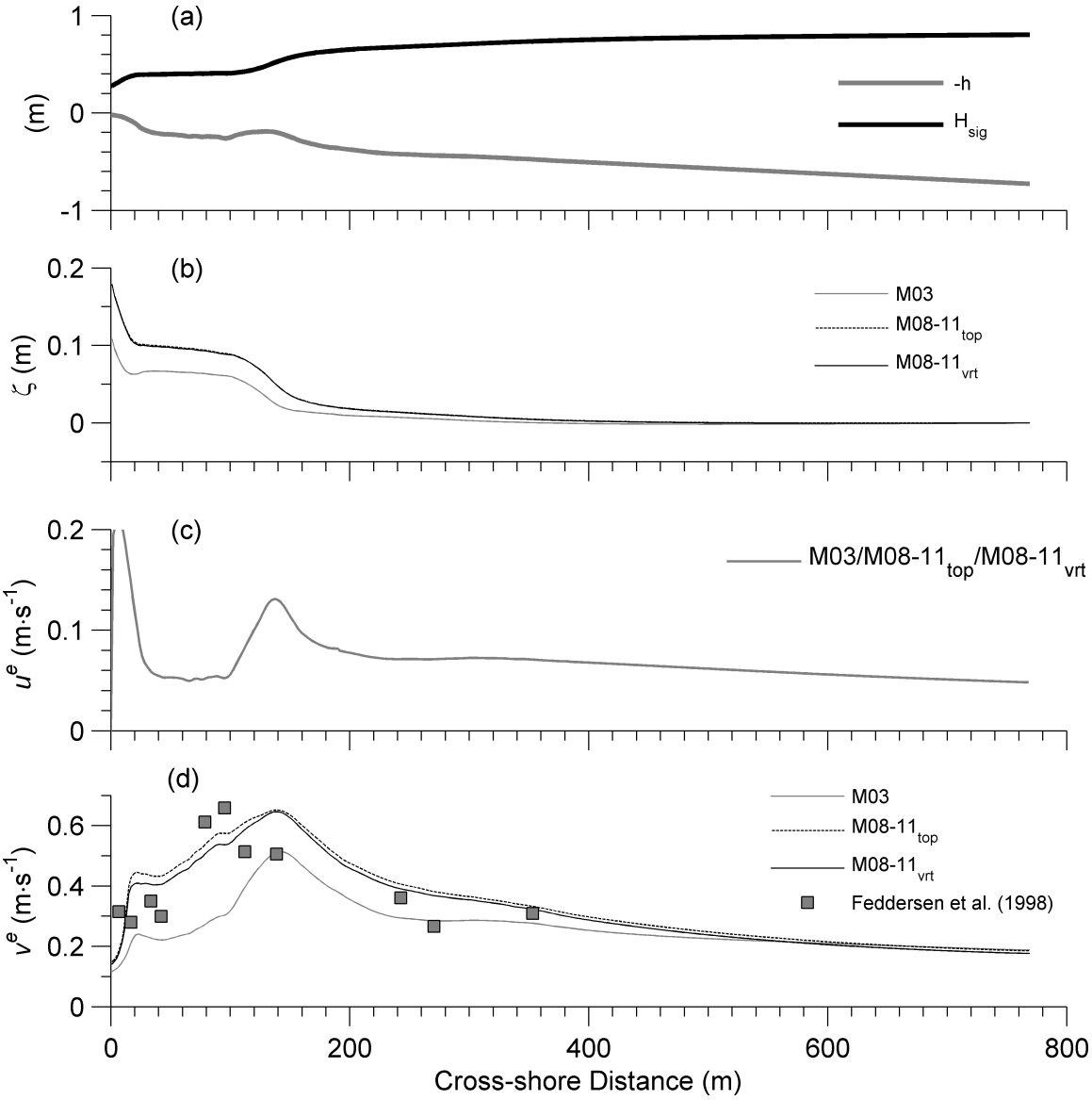

Figure 2.3: Case 2: Obliquely incident waves on a barred beach (DUCK94 experiment) using the original radiation stress forcing M03, the updated forcing applied at the top layer M08-11_{top}, and with a vertical distribution as defined by Eqn. 10 of M08-11_{vrt}. Cross-shore distribution of: (a) significant wave height (H_{sig}) and water depth (h). The water depth and wave height values shown are scaled as $h/10$ and $H_{sig}/2$, respectively, for plotting purposes; (b) sea surface elevation (ζ); (c) depth averaged Eulerian mean cross-shore velocity ($\overline{u^e}$); and (d) depth averaged Eulerian mean alongshore velocity ($\overline{v^e}$).

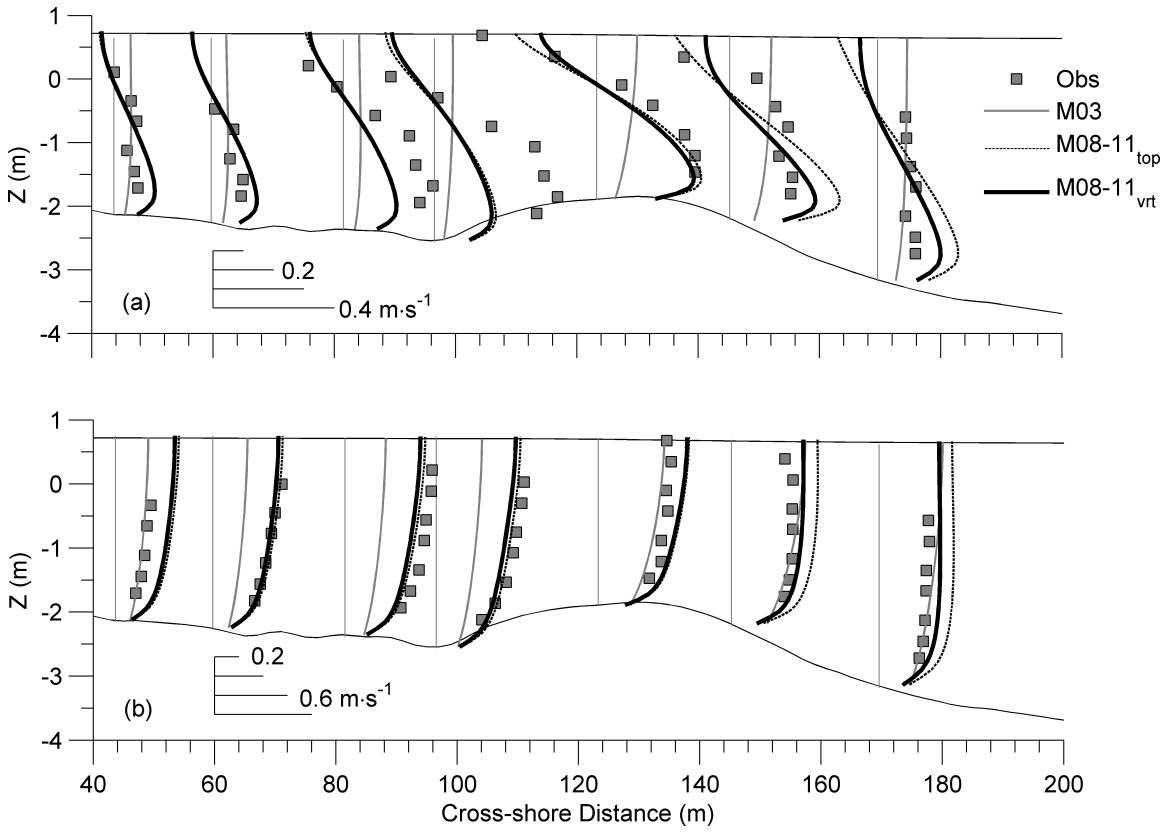

Figure 2.4: Comparison of vertical profiles of (a) cross-shore (u_e(x, z)); and (b) longshore (v_e(x, z))Eulerian mean velocities; from model simulations using M03 (solid grey lines); M08-11top (dashed black lines), M08-11vrt (solid black lines) and field measurements (grey squares). Vertical grey lines indicate locations of model sampling and zero velocity value for each profile. The horizontal velocity profile data are from Garcez-Faria et al. (1998, 2000).

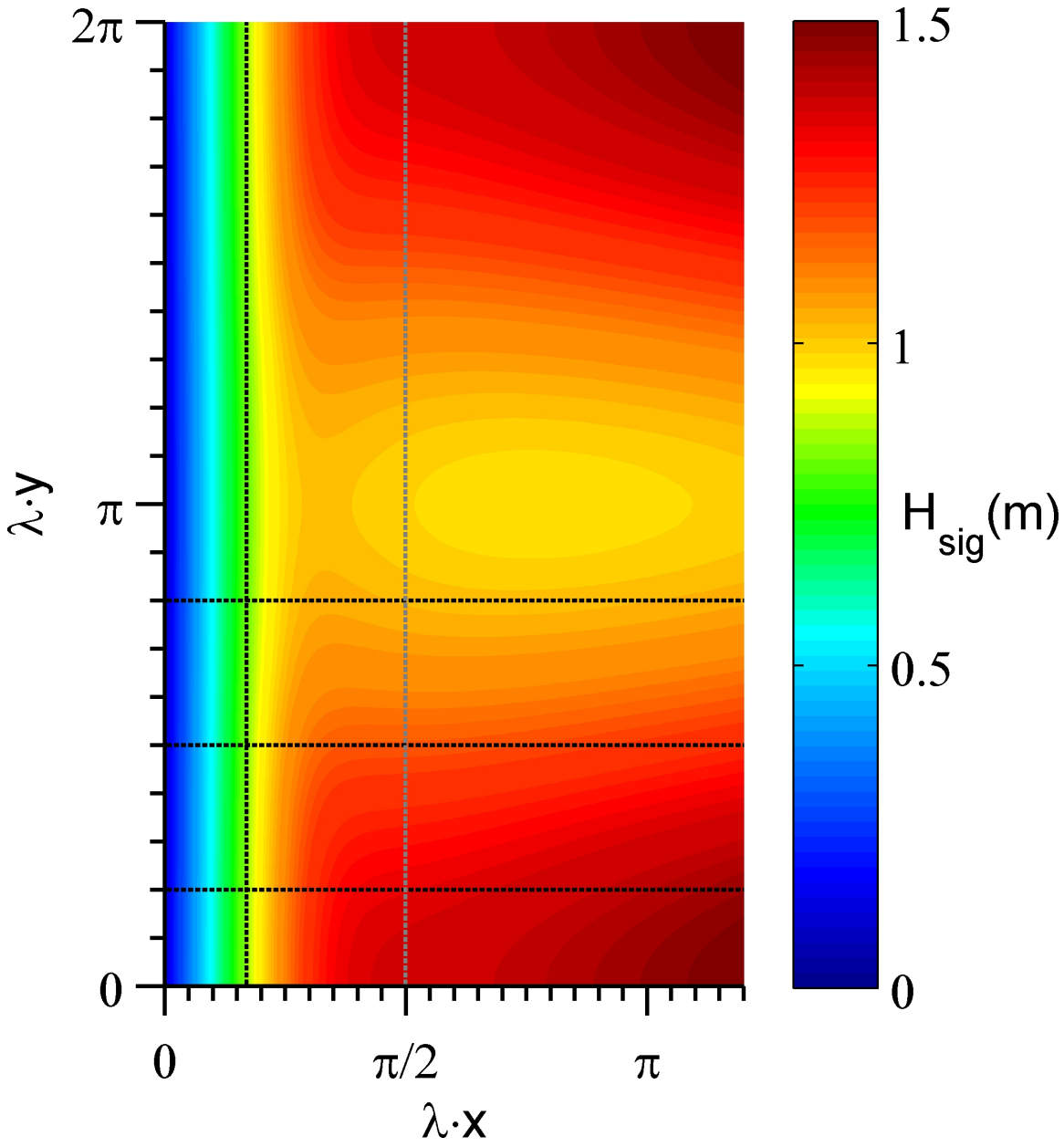

Figure 2.5: Color shading of significant wave height distribution over the computational domain after 2 hours of model simulation for two-way coupling between ROMS and SWAN. Note the significant wave height at offshore boundary is 1.5 m at the ends and decreases to a minimum value of 1 m at the center of the domain. The alongshore and cross-shore domain has been scaled by a value of (λ=2π/1000). Black dashed lines indicate the location of transects shown in Figure 2.8, while grey dashed line shows the location of the surf zone. The horizontal, black, dotted lines indicate the location of alongshore transect shown in Figure 2.17.

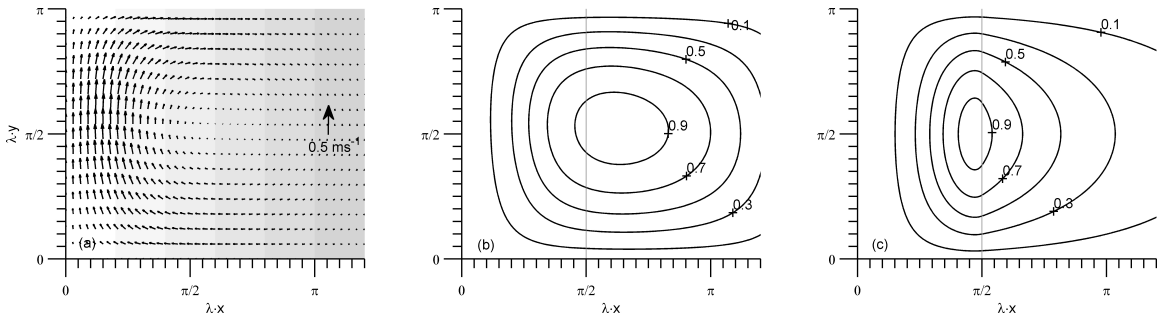

Figure 2.6: Rip current simulation results for the bottom half of the computational domain (Case 3, two-way coupling) after 2 hours of simulation. (a) Depth averaged Lagrangian mean velocity distribution ($\overline{u^l}$); (b) Transport stream function (ψ) showing formation of circulation cell in the surf zone; (c) Transport stream function (ÏĹ) calculated using the analytical solution provided by Bowen, 1969 for the present model setup. Note: λx=$\pi/2$ (shown by grey dashed line) is the location where waves start breaking.

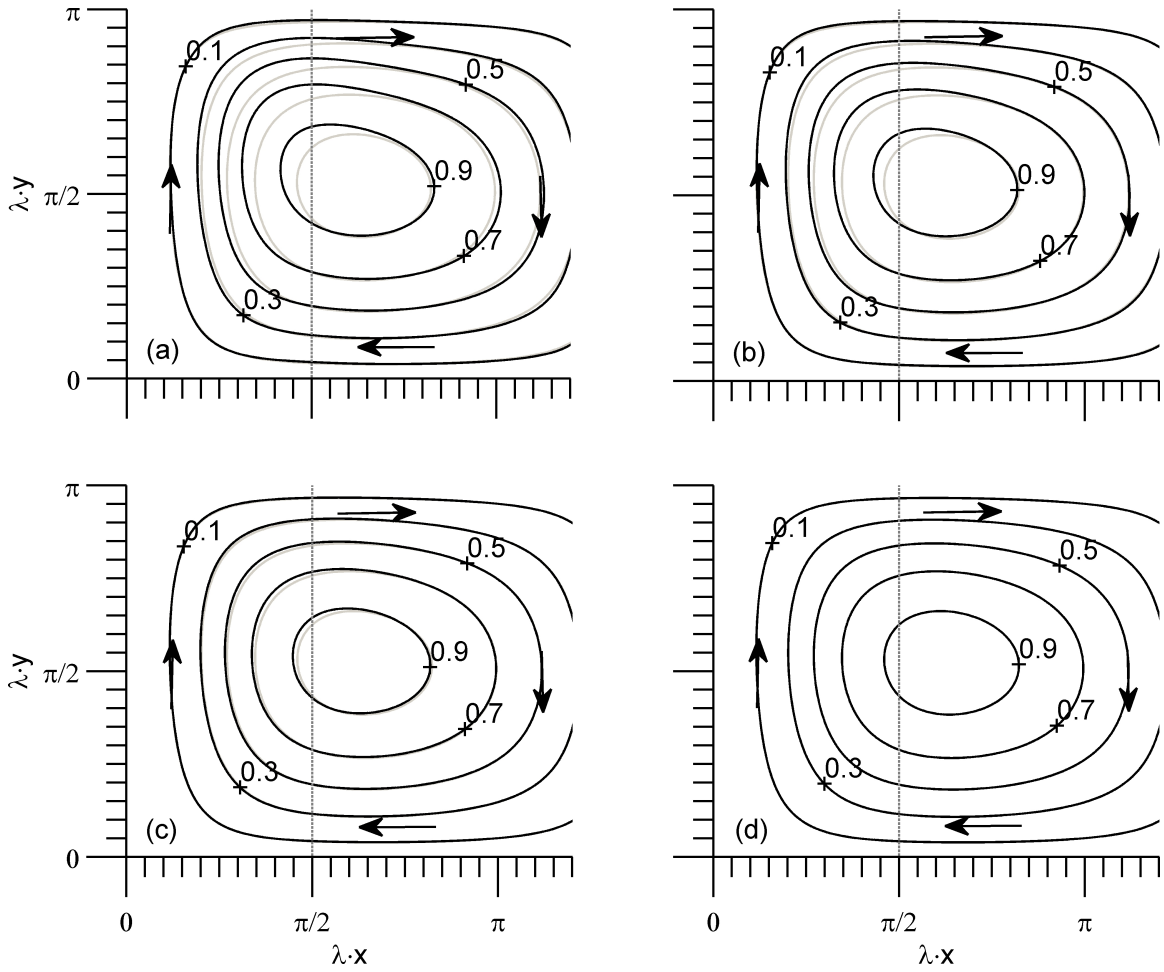

Figure 2.7: Transport stream function, ψ over the computational domain for Reynolds number (Re) values of (a) 500, (b) 125, (c) 62.5, and (d) 42. Note the solution gets skewed about the individual centers of the circulation cells with increased Re values causing a narrower outflow from shallower to deeper waters and broader inflow from deeper to shallower waters. Also note that the individual circulation cells are not exactly symmetric about the line y= π. The grey circulation cell in (a), (b), and (c) is same as (d); it is shown for comparison purposes. The vertical, grey dashed line shows the location where waves start breaking.

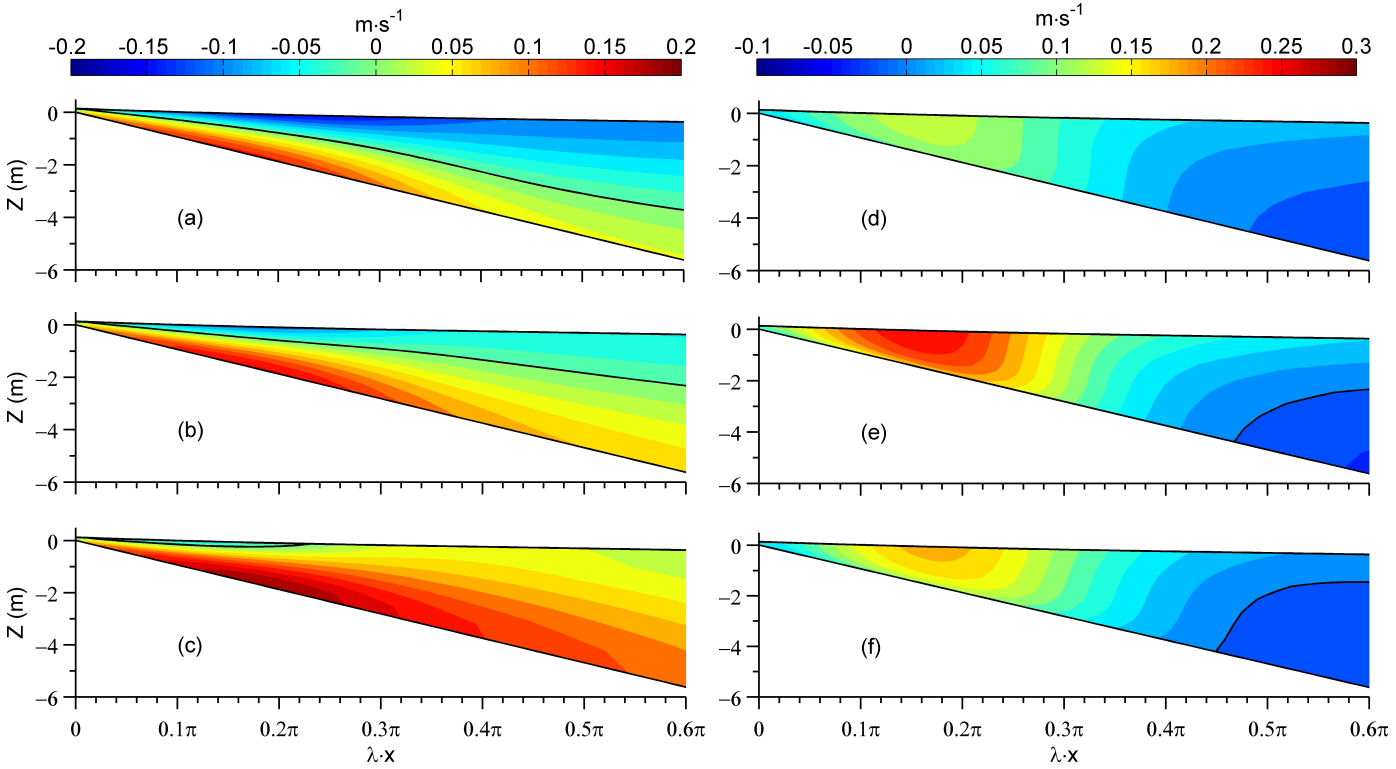

Figure 2.8: Contour plots showing the vertical structure of the Eulerian, cross-shore (a, b, c) and alongshore velocity (d, e, f) along three transects located at $\lambda y=\pi/5$ (a, d), $\lambda y=\pi/2$ (b, e), and $\lambda y=4\pi/5$ (c, f) from the southern lateral boundary (see dashed lines in Figure 2.5). Solid black line corresponds to zero velocity.

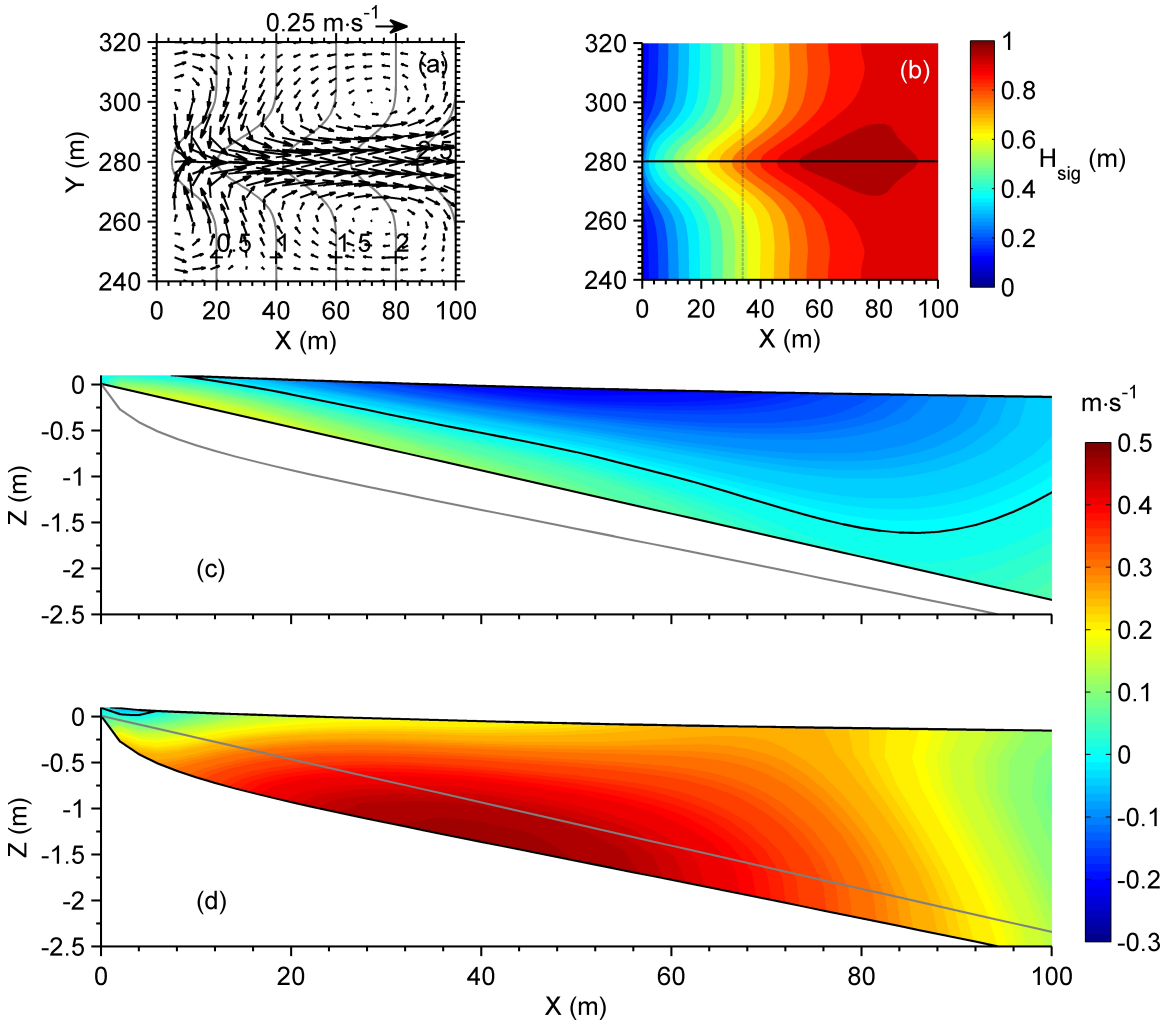

Figure 2.9: (a) Depth averaged Eulerian mean, velocity (black arrows) after 1 hour of simulation. Light grey lines in background depict the bathymetry contours; (b) Contour of significant wave height distribution over the computational domain. The incident wave height at the offshore boundary of the domain is 0.92 m. Contour plots showing the vertical structure of cross-shore Eulerian mean velocity, u_e(x, z)) along two transects located at (c) y=0 m, (d) y=40 m from the southern lateral boundary (see grey lines in Figure 2.9b). The grey dotted alongshore transect in Fig. 2.9b is the location at which alongshore momentum balance term is shown in Fig. 2.17(c).

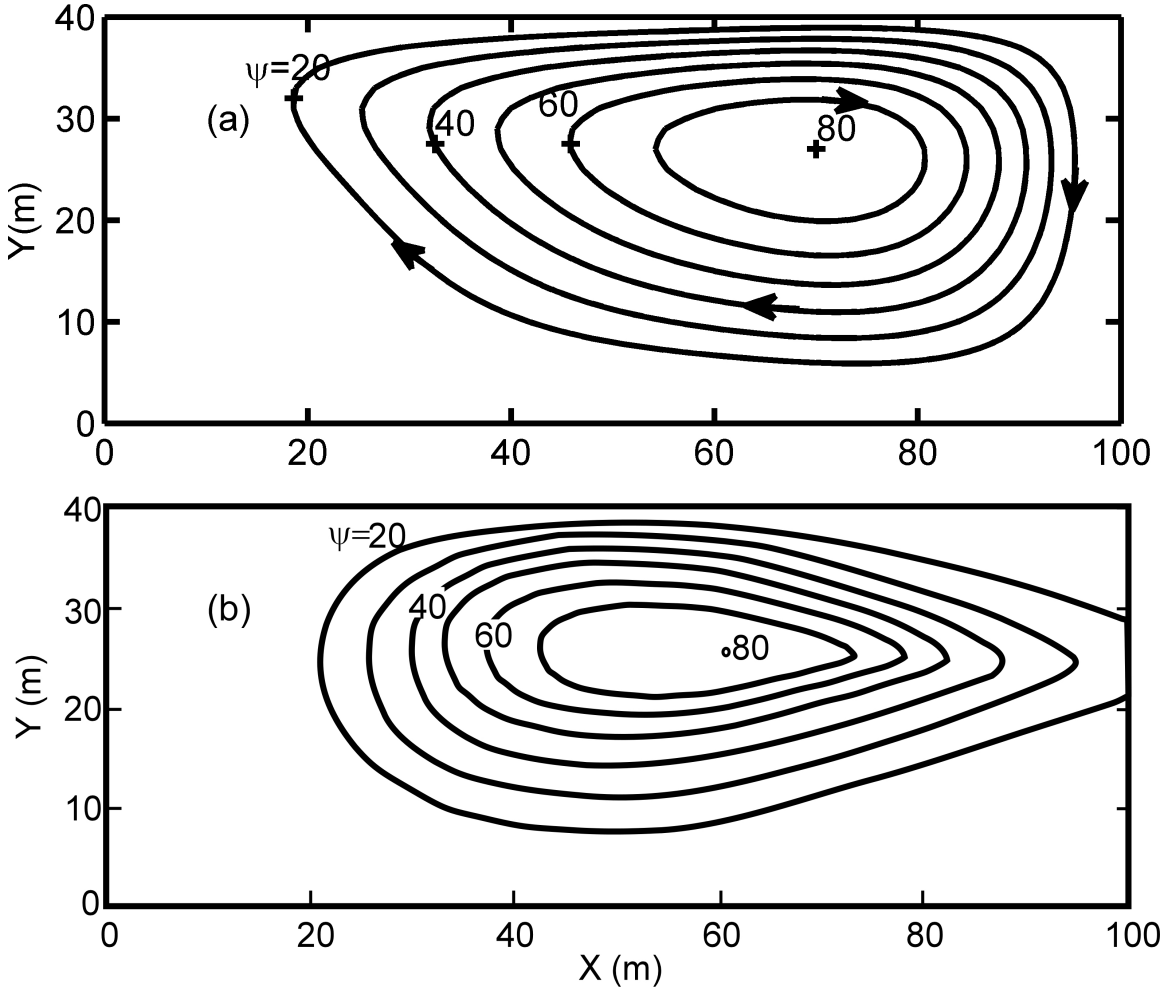

Figure 2.10: Transport stream function (ψ) over the computational domain computed from the model results after (a) depth averaging the horizontal Lagrangian mean velocity field; (b) and from Noda (1974) paper.

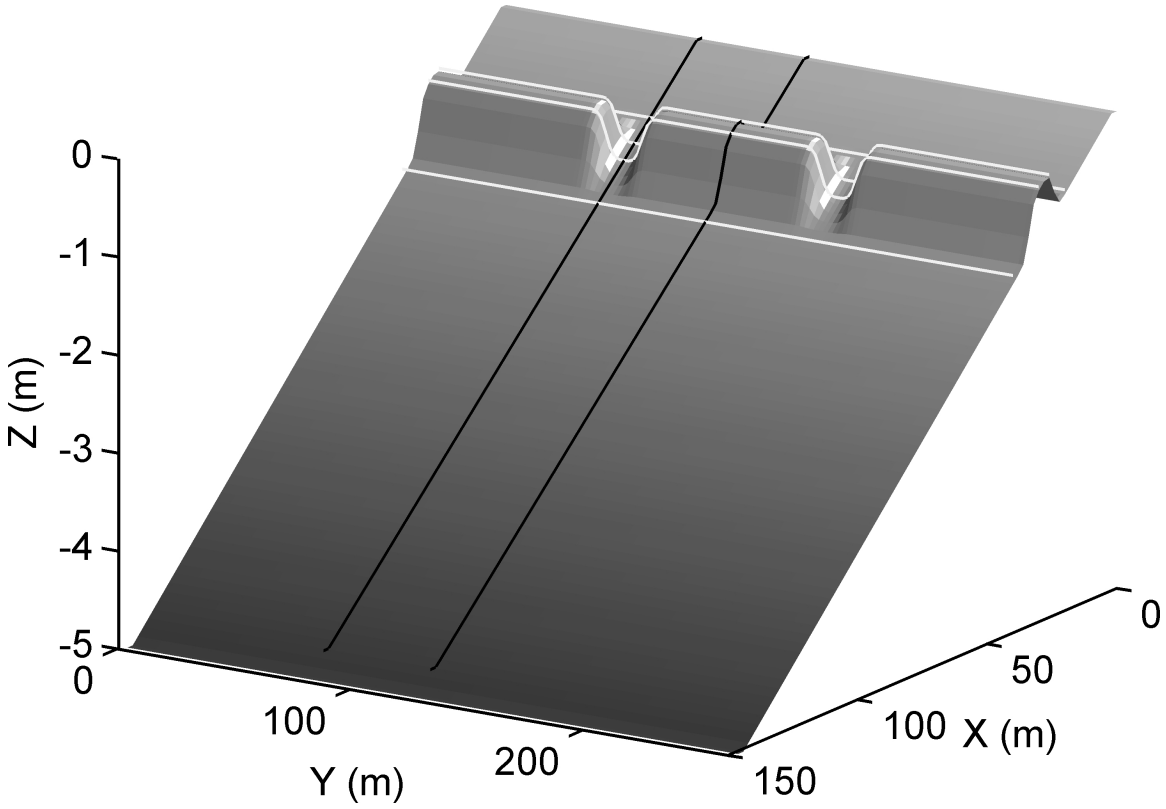

Figure 2.11: Bathymetry for Case 5, showing the longshore bar and the rip channels. The solid black lines show the location of vertical transects at which the cross-shore velocity distribution is discussed in Fig. 2.14. The 4 horizontal white lines represent the alongshore transects at which cross-shore momentum balance terms are shown in Fig. 2.15 and alongshore momentum balance term is shown in Fig. 2.17(d).

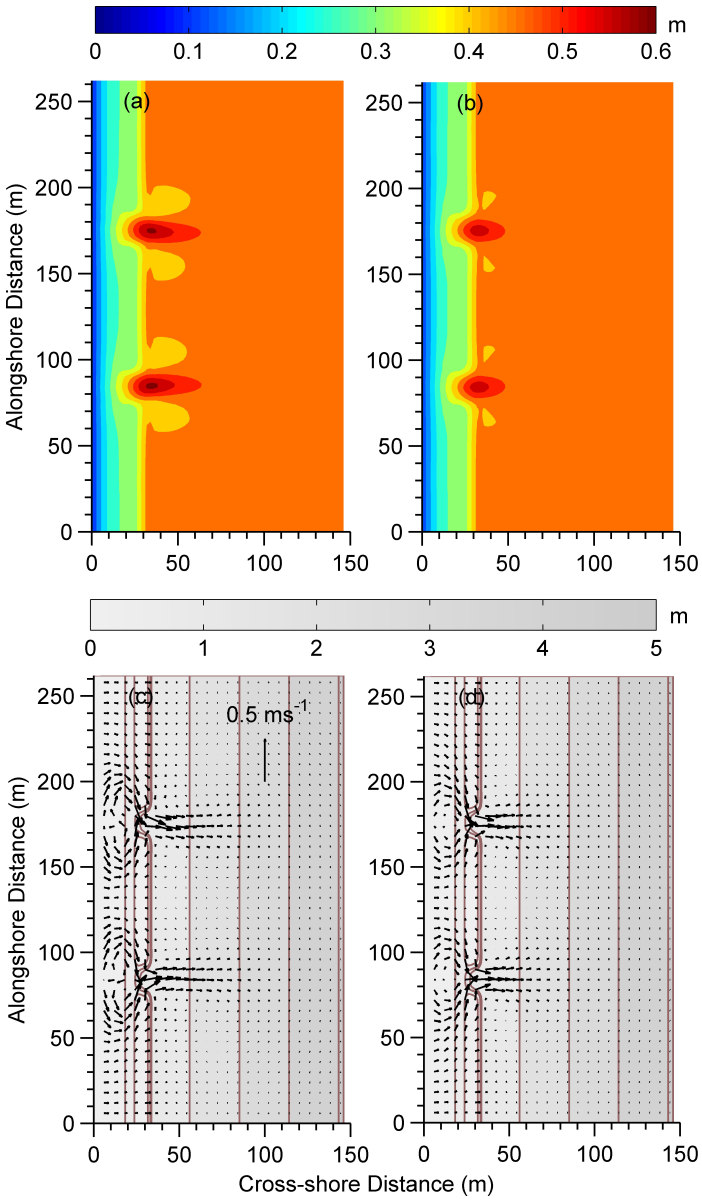

Figure 2.12: Contours of significant wave height after 30 minutes of model simulation using (a) the original version of the model as in HW09 and; (b) the modified M08-11 formulations for the vertical distribution of the radiation stress (M08-11$_{\mathrm{vrt}}$). Bathymetric contours and depth integrated Eulerian, mean currents over the computational domain using (c) the original version of the model as in HW09 and; (d) the modified M08-11 formulations for the vertical distribution of the radiation stress (M08-11$_{\mathrm{vrt}}$). The black line (2.12c) depicts a velocity of 0.5 ms^{-1}.

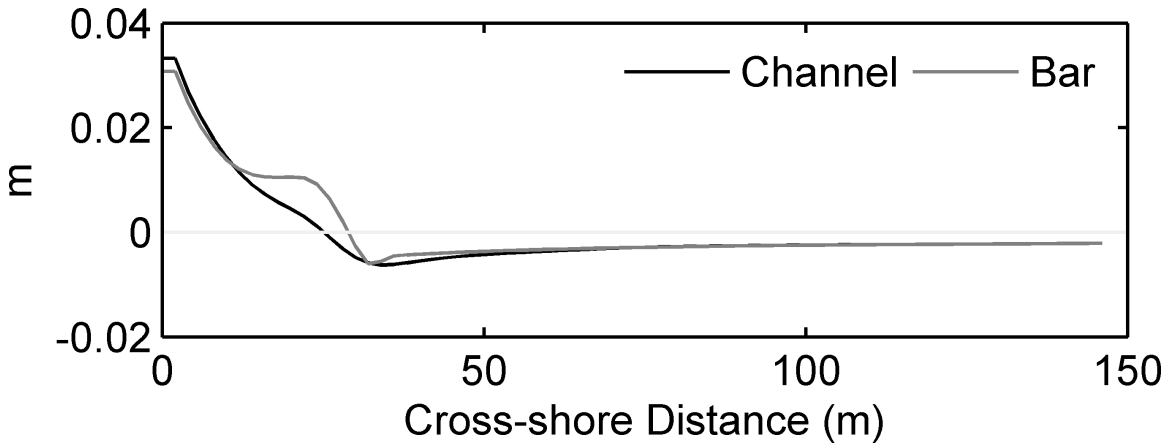

Figure 2.13: Cross-shore variation of mean sea surface elevation at two locations corresponding to alongshore positions centered at the middle of the rip channel (black) and alongshore bar (grey).

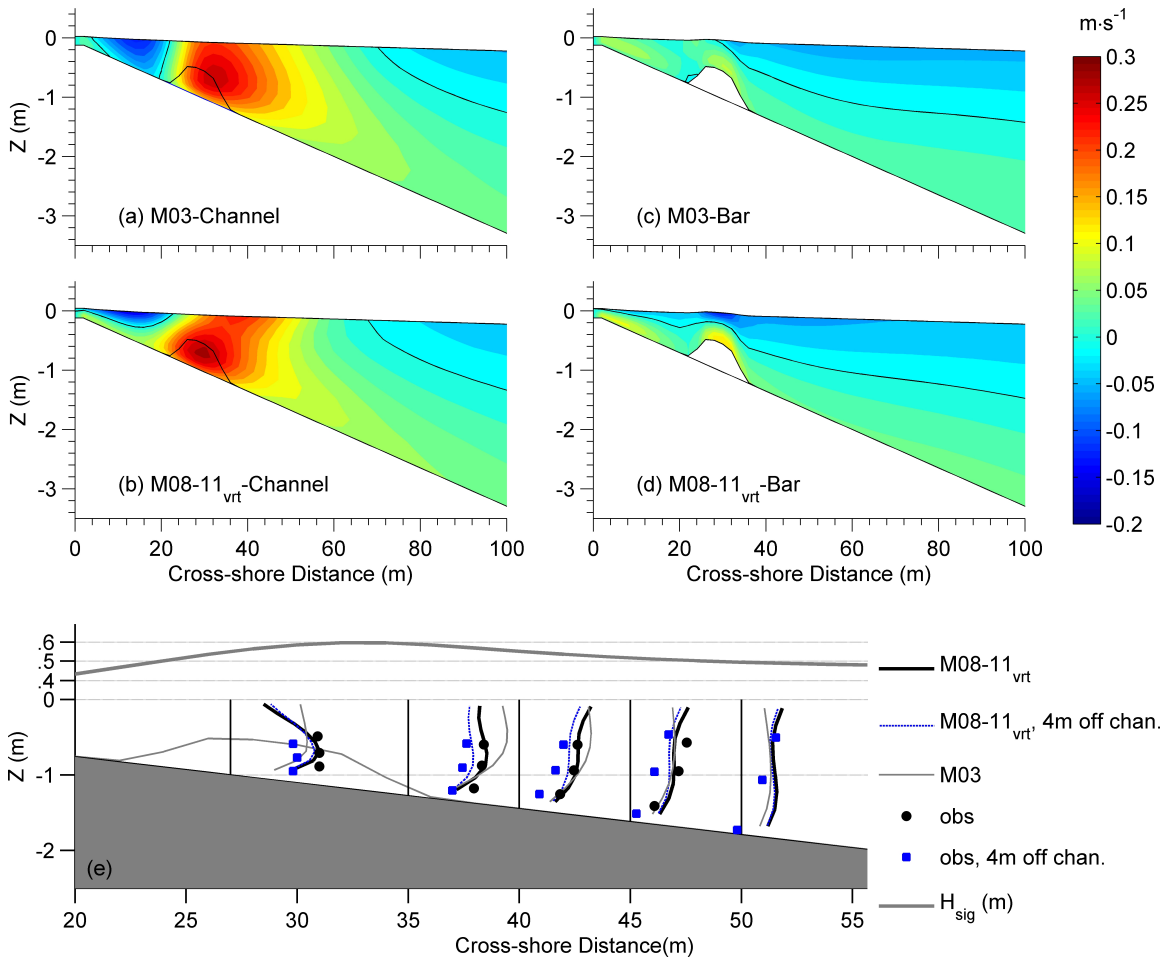

Figure 2.14: Vertical structure of cross-shore Eulerian mean velocity u_e (x, z) at the center of rip channel (a and b) and bar (c and d) derived from original version of the model as in HW09 (a and c) and the M08-11$_{\mathrm{vrt}}$ formulations (b and d); (e) Comparison of normalized model derived cross-shore velocity with normalized data from Haas and Svendsen, 2002 (key: symbols ● and ■ denote data at the center and 4 m off the channel, grey line (center of the channel M03), black dash dot (center of the channel M08-11$_{\mathrm{vrt}}$), blue dashed line (M08-11$_{\mathrm{vrt}}$, 4 m off the channel).

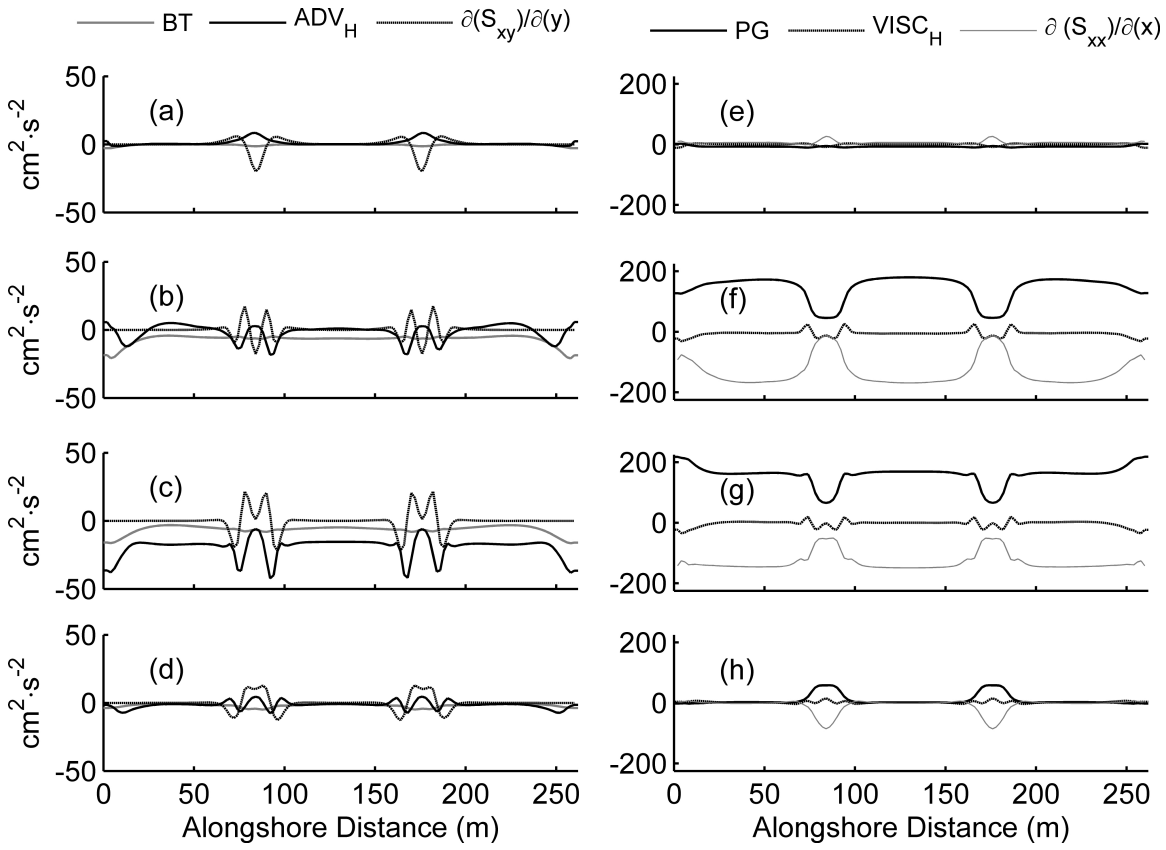

Figure 2.15: Alongshore variation of the depth averaged cross-shore momentum balance equation terms. Horizontal advection (ADV_H , $\partial/\partial x(U^2h) + \partial/\partial y(UVh)$, black line), bottom stress (BT, τ_x^b/ρ, grey line) and radiation stress forcing ($\partial S_{xy}/\rho\partial y$, black dashed) terms are shown in (a) to (d). Cross-shore pressure gradient (PG, gh($\partial\eta/\partial x$), black line), radiation stress forcing (RAD_H, $\partial S_{xx}/\rho\partial x$, grey line) and horizontal viscosity ($VISC_H$, $\partial(A_H/\rho\partial u/\partial x)\partial x$, black dashed) are shown in (e) to (h). The distances at which the terms are estimated are 40 m (a) and (e), 30 m (b) and (f), 26 m (c) and (g), and 20 m (d) and (h) from the shoreline (see Fig. 2.11).

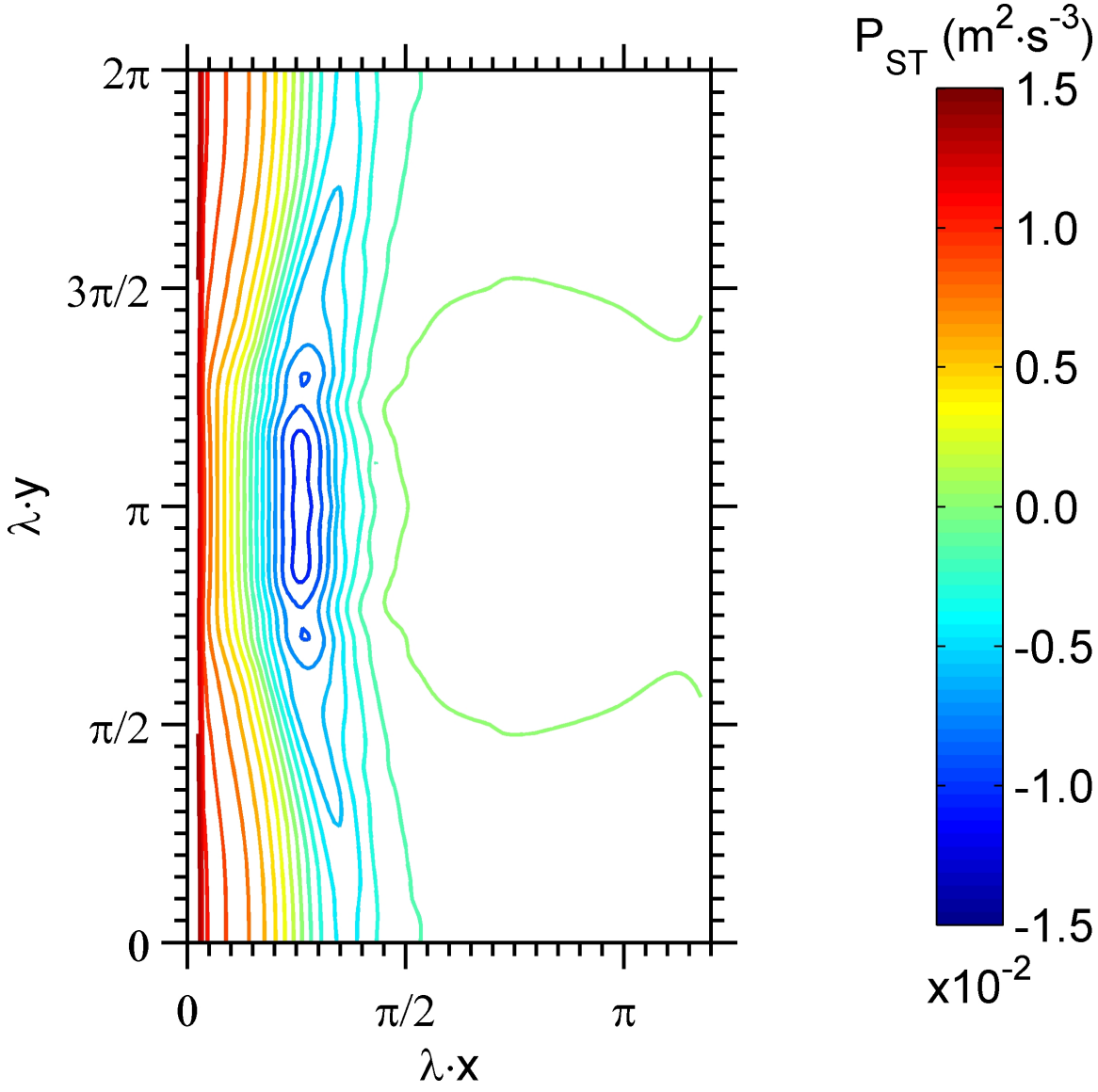

Figure 2.16: Contour of sediment transport proxy (P_{st}) over computational domain for the run of Case 3 of alongshore variable wave forcing.

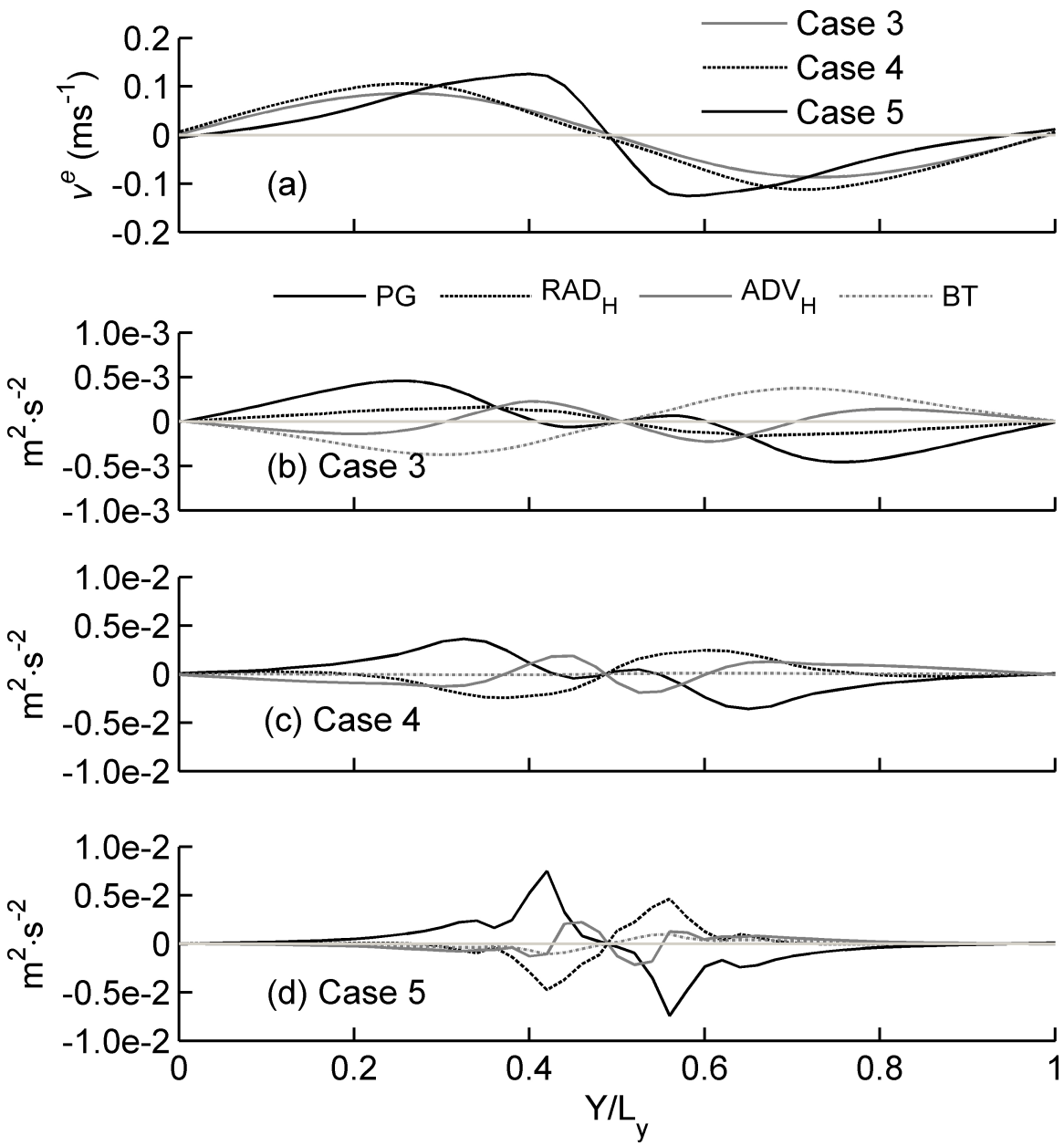

Figure 2.17: (a) Depth averaged, alongshore, Eulerian velocity, $\overline{v^e}$ at alongshore transects shown by dotted line in Fig. 2.5 for Case 3, dotted line in Fig. 2.9b for Case 4 and alongshore transect onshore of the rip channel (Fig. 2.11) for Case 5; Alongshore variation of the depth averaged alongshore momentum balance terms for (b) Case 3 and (c) Case 4 for alongshore transect as 2.17(a), (d) Case 5 for alongshore transect as 2.17(a). The alongshore normalizing length scale (L_y) used in (b), (c) and (d) are 1000 m, 80 m and 90 m, respectively, and represent the corresponding perturbation length in forcing or bathymetry (key: alongshore pressure gradient (PG, gh($\partial\eta/\partial y$), black line), radiation stress forcing (RAD_H, ($\partial S_{yy}/\rho\partial y + \partial S_{xy}/\rho\partial x$), black dashed), horizontal advection (ADV_H , $\partial/\partial x(UVh) + \partial/\partial y(V^2h)$, grey line), bottom stress (BT, τ_y/ρ, grey dashed-dot line))

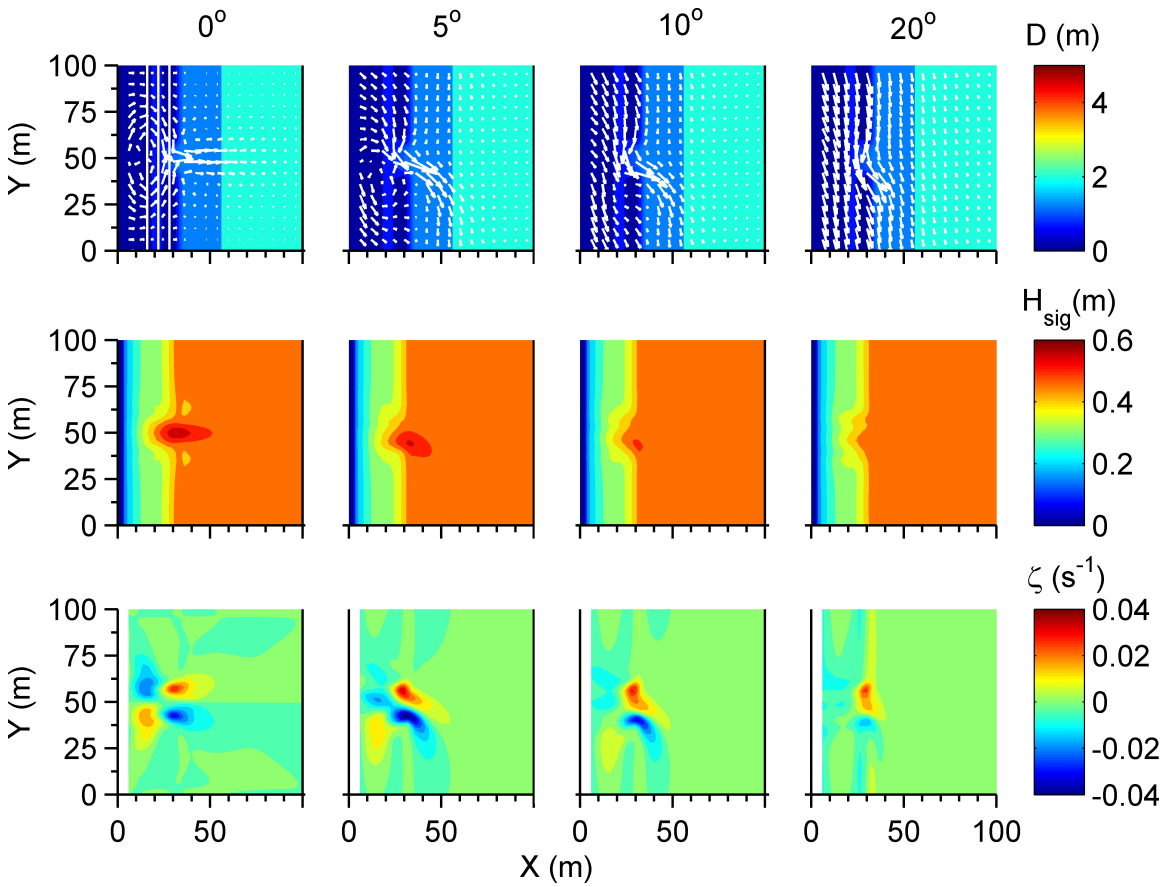

Figure 2.18: Circulation (depth averaged, Eulerian mean current vector, top row), significant wave height distribution (middle row) and vorticity field (bottom row) results for different wave incident angles (columns one to four correspond to angles 0, 5, 10 and 20 degrees, respectively). The thin grey lines in top row, column one shows the alongshore transects at which relevant terms are plotted in Figure. 2.19. Note: The bathymetry used in this case is same as Figure 2.11, but only the relevant part of the domain has been shown here.

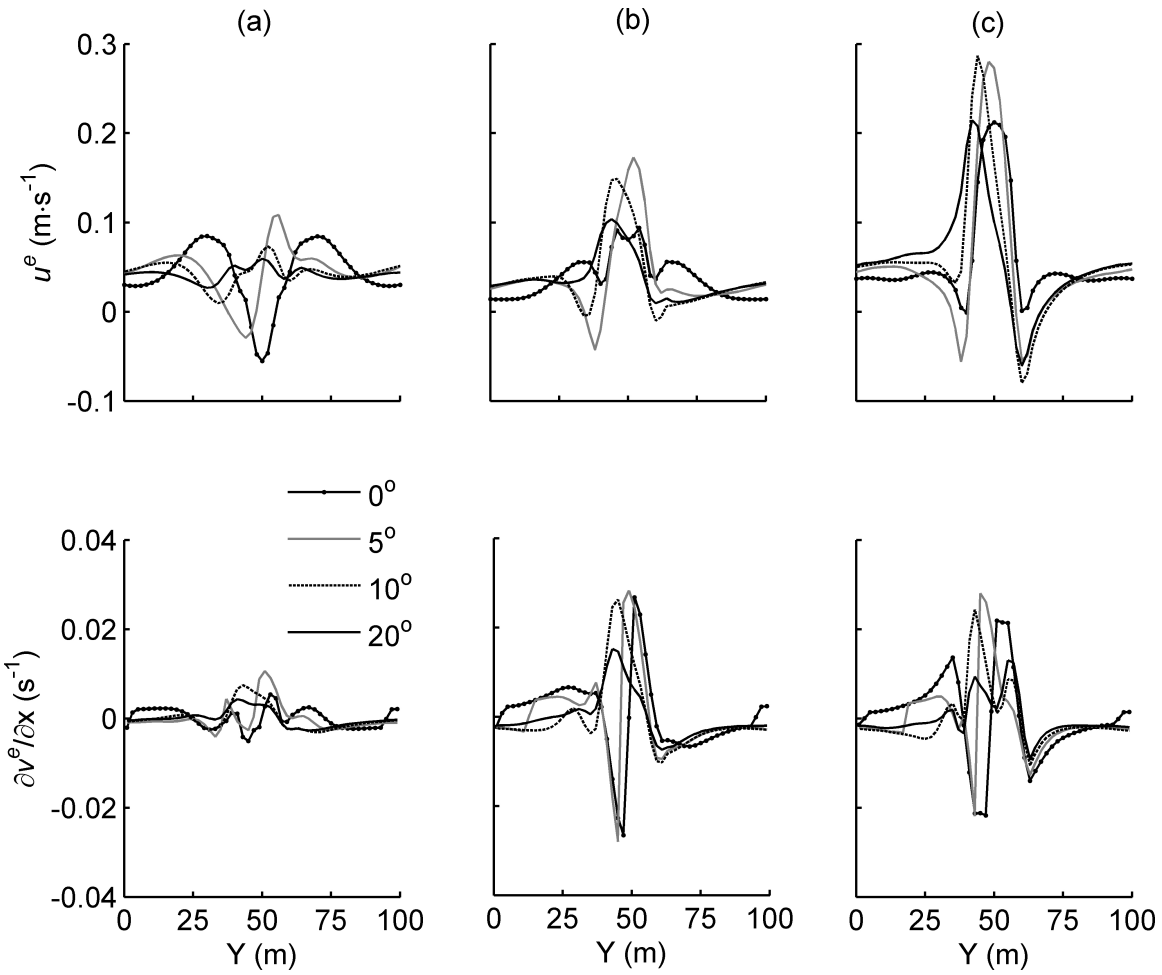

Figure 2.19: Eulerian mean cross-shore velocities (top panel) and absolute value of alongshore gradient of Eulerian alongshore velocities (bottom panel) at 3 alongshore transects located (a) 16 m, (b) 22 m, (c) 28 m from the shoreline as shown by grey lines n Fig. 2.18 (top panel, column (a)) for waves incident at angles 0°, 5°, 10°, 20°.

Table 2.1: RMS error (normalized by the maximum value) for the simulated current velocities using M03, M08-11$_{\text{top}}$ and M08-11$_{\text{vrt}}$ formulations for Case2 (DUCK94 experiment).

	RMS Error (%)					
	M03		M08-11$_{\text{top}}$		M08-11$_{\text{top}}$	
Station No.	u^e	v^e	u^e	v^e	u^e	u^e
1	49.6	10.5	36.6	62.5	37.1	60.5
2	56.7	41.4	30.2	04.3	30.7	03.7
3	62.5	48.7	38.8	09.7	40.8	10.4
4	69.7	41.0	16.4	06.5	23.7	07.0
5	60.4	12.3	51.6	21.4	42.6	24.5
6	24.1	15.1	75.4	38.2	52.2	16.7
7	100.9	12.0	58.8	49.0	60.5	23.5
Overall	44.6	29.7	**23.9**	18.0	24.7	**15.4**

Table 2.2: The RMS error (normalized by the maximum value) for the simulated current velocities using M03 and M08-11$_{\text{vrt}}$ formulations for Case5 (nearshore barred morphology with rip channels).

	RMS Error (%)	
	M03	M08-11$_{\text{vrt}}$
Station No	u^e	u^e
1	30.2	19.2
2	19.0	19.2
3	18.9	12.4
4	37.6	16.7
5	62.1	26.6
Overall	20.1	**11.7**

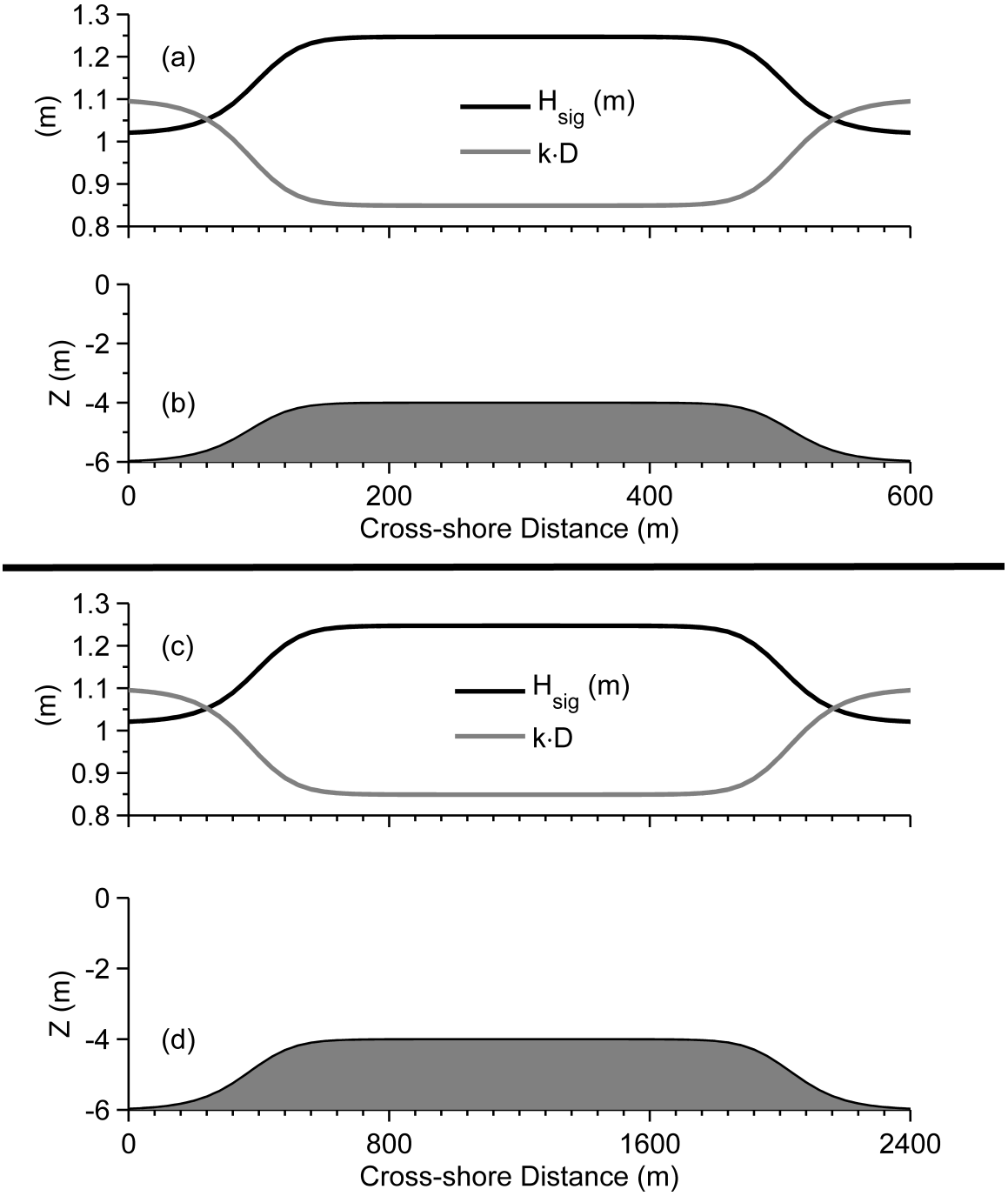

Figure 2.20: Model forcing (wave height) and non dimensional depth (a and c) and bottom bathymetry (b and d) used to test the Mellor (2008) formulation. (a) and (b) are identical as in Ardhuin et al. (2008). Forcing in (c) is the same as (a) but the bathymetry (d) has a reduced bottom slope (note differences in horizontal scale between b and d).

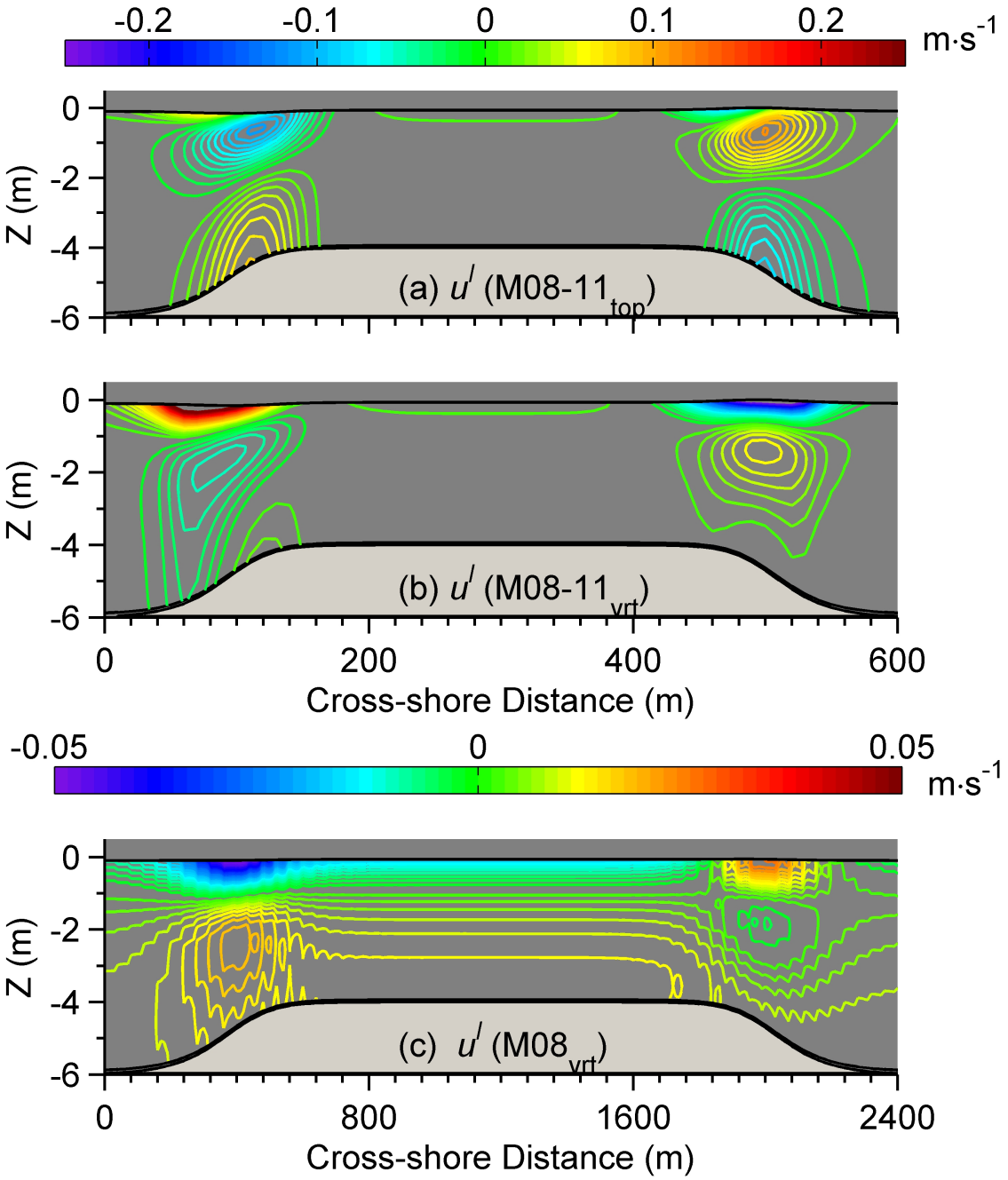

Figure 2.21: Vertical distribution of Lagrangian mean velocity, u^l (x, z) (Eulerian mean velocity + Stokes drift) calculated using (a) M08-11_{top} with a domain geometry as in Ardhuin et al. (2008); (b) M08-11_{vrt} on the same domain as (a); and (c) M08-11_{vrt} with a similar geometry but reduced bottom slope (note differences in horizontal scale), uniform vertical mixing and bottom friction. Contour line spacing is 0.01 ms^{-1} in (a), (b) and 0.002 ms^{-1} in (c). Note different scales in colorbar used in (c).

Chapter 3

Implementation of the vortex force formalism in the Coupled Ocean-Atmosphere-Wave-Sediment Transport (COAWST) modeling system for inner shelf and surf zone applications[1]

[1]This chapter has been published as Kumar, N., Voulgaris, G., Warner, J.C., and Olabarrieta, M., (2012).Implementation of the vortex force formalism in the coupled ocean-atmosphere-wave-sediment transport (COAWST) modeling system for inner shelf and surf zone applications, Ocean Modelling, Volume 47, 2012, Pages 65-95, ISSN 1463-5003, 10.1016/j.ocemod.2012.01.003. See Appendix A for more details.".

Abstract

The coupled ocean-atmosphere-wave-sediment transport modeling system (COAWST) enables simulations that integrate oceanic, atmospheric, wave and morphological processes in the coastal ocean. Within the modeling system, the three-dimensional ocean circulation module (ROMS) is coupled with the wave generation and propagation model (SWAN) to allow full integration of the effect of waves on circulation and vice versa. The existing wave-current coupling component utilizes a depth dependent radiation stress approach. In here we present a new approach that uses the vortex force formalism. The formulation adopted and the various parameterizations used in the model as well as their numerical implementation are presented in detail. The performance of the new system is examined through the presentation of four test cases. These include obliquely incident waves on a synthetic planar beach and a natural barred beach (DUCK' 94); normal incident waves on a nearshore barred morphology with rip channels; and wave-induced mean flows outside the surf zone at the Martha's Vineyard Coastal Observatory (MVCO).

Model results from the planar beach case show good agreement with depth-averaged analytical solutions and with theoretical flow structures. Simulation results for the DUCK' 94 experiment agree closely with measured profiles of cross-shore and longshore velocity data from Garcez-Faria et al. (1998, 2000). Diagnostic simulations showed that the nonlinear processes of wave roller generation and wave-induced mixing are important for the accurate simulation of surf zone flows. It is further recommended that a more realistic approach for determining the contribution of wave rollers and breaking induced turbulent mixing can be formulated using non-dimensional parameters which are functions of local wave parameters and the beach slope. Dominant terms in the cross-shore momentum balance are found to be the quasi-static pressure gradient and breaking acceleration. In the alongshore direction, bottom stress, breaking acceleration, horizontal advection and horizontal

vortex forces dominate the momentum balance. The simulation results for the bar / rip channel morphology case clearly show the ability of the modeling system to reproduce horizontal and vertical circulation patterns similar to those found in laboratory studies and to numerical simulations using the radiation stress representation. The vortex force term is found to be more important at locations where strong flow vorticity interacts with the wave-induced Stokes flow field. Outside the surf zone, the three-dimensional model simulations of wave-induced flows for non- breaking waves closely agree with flow observations from MVCO, with the vertical structure of the simulated flow varying as a function of the vertical viscosity as demonstrated by Lentz et al. (2008).

3.1 Introduction

Coupling of rapidly oscillating surface gravity waves to slowly varying currents creates unique flow patterns in both inner shelf and surf zone environments. The effect of mean currents on surface gravity waves is exhibited as a Doppler shift in wave frequency, accompanied with a change in phase speed. Conversely, the effect of rapidly oscillating surface gravity waves on mean flow is manifested through the provision of additional momentum and mass flux to the mean flow. This coupling is usually accommodated by averaging the fast oscillations over longer time scales and provides a mechanism for the inclusion of the so called Wave Effect on Currents (WEC).

Wave-current interaction can be expressed in an Eulerian reference frame by assuming an analytic continuation of the wave-induced velocities above the air-sea interface (e.g., Garrett, 1976; McWilliams et al., 2004; Smith, 2006; Newberger and Allen, 2007a). A Generalized Lagrangian Mean (GLM) Framework (Andrews and McIntyre, 1978ab; Ardhuin et al., 2008) provides a formulation which is generally equivalent to the Eulerian mean, with a physical interpretation of the velocity above the wave trough level as a quasi-Eulerian velocity. Finally, the alternate Generalized Lagrangian Mean framework (Andrews and McIntyre, 1978a; Groeneweg and Klopman, 1998; Ardhuin et al., 2008b) is a distinct approach which works with the Lagrangian mean velocity. This may also be obtained using a vertically moving average (Mellor, 2003; 2005; 2008; 2011). The prognostic variables in Eulerian and Lagrangian mean flow equations are the quasi-Eulerian mean and Lagrangian mean velocity, respectively. The quasi-Eulerian mean velocity is the difference between Lagrangian mean velocity and the wave pseudo-momentum (e.g., Jenkins, 1989; Bennis et al., 2011). A detailed description of available Eulerian, GLM and "alternative" GLM averaging techniques along with their advantages and disadvantages in identifying the role of fast oscillations on mean circulation can be found in Ardhuin et al.

(2008) and Bennis et al. (2011). In the present work we concentrate on the three-dimensional momentum equations and their representation in an Eulerian reference frame.

The terms corresponding to WEC in the mean flow equations can be represented as the gradient of radiation stress tensor or as Vortex Force (VF, Craik and Leibovich, 1976). The radiation stress tensor is defined as the flux of momentum due to surface gravity waves (Longuet-Higgins and Stewart, 1964), while the VF representation splits the wave-averaged effects into gradients of a Bernoulli head and a vortex force. The Bernoulli head is an adjustment of pressure in accommodating incompressibility (Lane et al., 2007), while, after wave averaging, the vortex force is a function of wave-induced Stokes drift and flow vorticity.

Recently, a number of three-dimensional, hydrostatic[2] ocean models have been developed and used to study wave-current interaction. Newberger and Allen (2007a) using an Eulerian framework, added wave forcing in form of surface and body forces, and depth- averaged VF terms in the Princeton Ocean Model (POM), which has evolved into "Nearshore POM". McWilliams et al. (2004, hereinafter MRL04) developed a multi-scale asymptotic theory for the evolution and interaction of currents and surface gravity waves of finite depth. This method separates currents, long waves and surface gravity waves on the basis of differences in their spatial and temporal variation, as a function of the wave slope. The work of MRL04 was implemented in UCLA ROMS and extended for applications within the surf zone by Uchiyama et al. (2010, hereinafter U10).

[2]Non-hydrostatic ocean models have also been developed and used to study wave-current interaction. The models resolving non-hydrostatic pressure have been used to study propagation of shortwaves on a deep basin, internal waves and tides (Kanarska et al., 2007), internal solitary wave shoaling and breaking, lock-exchange problem (Lai et al., 2010), and wave propagation, shoaling and breaking in the surf zone (Zijlema et al., 2011). Nevertheless, most of the model simulations conducted using non-hydrostatic models are validated against laboratory test cases, while hydrostatic ocean models are utilized for majority of realistic nearshore field experiments.

The VF formalism based model presented by U10 separates the effects of wave forcing into conservative (Bernoulli head and vortex force) and non-conservative (wave dissipation induced acceleration) contributions. A separation between conservative and non-conservative forces is pertinent as the former has a known vertical distribution, while the latter can presently only be expressed with an empirical vertical profile. U10 presented the non-conservative wave forcings with a depth-limited wave dissipation calculated using the formulations of Thornton and Guza (1983) and Church and Thornton (1993), bottom streaming and a wave roller model based on Reniers et al. (2004a). The turbulence closure model is K-profile parameterization (KPP) with additional mixing due to wave breaking following Apotsos et al. (2007). The circulation model is coupled to a spectrum-peak WKB (Wentzel Kramer Brillouin) wave refraction model.

The methodology presented by MRL04 and U10 can be extrapolated for modeling with nesting components that requires seamless simulation of processes simulated at a variety of scales for water depths from the deep ocean to the surf zone. Such applications include the development of rip current prediction system (e.g., Voulgaris et al., 2011), sediment transport studies (e.g., Kumar et al., 2011b), and nearshore water quality prediction systems (Grant et al., 2005) amongst others. Thus it is imperative that these types of models are made available to the scientific community through the upgrade of existing public domain modeling systems. As a primary step in this direction we implement the VF approach to the three-dimensional ocean model ROMS, coupled with the wave model Simulating Waves Nearshore (SWAN), within the framework of the COAWST modeling system (Warner et al., 2010). This modeling system allows for simulating wave driven flows and sediment transport in the intertidal region (see Kumar et al., 2011b) through wetting and drying algorithms, a capability not available in the U10 model implementation. Furthermore, the U10 model uses a KPP parameterized mixing scheme that fails to accurately represent

the mixing in bottom boundary layer and in nearshore regions where the surface and bottom boundary layer interact (Durski et al., 2004).

The implementation of VF formalism into the COAWST modeling system is conducted with significant modifications to the method of U10 which includes: (a) Enhanced mixing implementation using the Generic Length Scale (GLS) scheme with the addition of wave-induced mixing in the form of surface boundary condition (Feddersen and Trowbridge, 2005). (b) Improved vertical structure of depth-limited wave dissipation induced acceleration that scales with the wave height. This cosh-based distribution is limited to the surface layer in deeper water, while in shallow waters (where the water depth is similar to wave height) the dissipation effect is delivered to the depth of water column influenced by wave propagation (c) Improved implementation of wave dissipation input which is provided by the wave driver model directly rather than being estimated locally using empirical formulations (Thornton and Guza, 1983; Church and Thornton, 1993); (d) Incorporation of bottom streaming using multiple formulations and wave-induced tangential flux at the surface as an option. The objectives of this manuscript are: (a) to describe the implementation of the VF formalism; (b) validate the model using analytical, laboratory and field observations applicable to both surf zone and inner shelf environments; and (c) provide a set of standard test cases for model comparisons.

The versatility and general applicability of the model presented here are demonstrated over a number of cases that not only include commonly used case (see U10, Newberger and Allen, 2007b) of obliquely incident waves on a planar and barred beach, but extend beyond to include applications of the model for the study of complex flow regimes developed in a nearshore barred beach with rip channels as well as for the study of wave-induced flow fields outside the surf zone in the inner shelf. Depth-averaged flow fields from VF representation are compared to those obtained using a two-dimensional numerical model based on radiation stress representation,

and identify the role of different forcing terms. A comparison to three-dimensional flows from a radiation stress representation has been avoided in absence of any self-consistent theory (see Ardhuin et al., 2008b; Bennis et al., 2011; Kumar et al., 2011a) for the same.

The outline of the chapter is as follows. The model formulation is presented in section 3.2, while its numerical implementation is described in section 3.3. The new model capabilities are demonstrated in section 3.4 through presentation of four test cases that cover both surf zone and inner shelf processes: (a) obliquely incident waves on a synthetic planar beach; (b) obliquely incident waves on a natural, sandy, barred beach (DUCK' 94 experiment); (c) nearshore barred morphology with rip channels; and (d) structure of undertow observed on the inner shelf. Discussion on differences and similarities of flow structure derived by expressing WEC using VF and radiation stress representations are shown in section 3.5 followed by a summary and conclusion section.

3.2 Model Formulation

The ocean component of COAWST is the Regional Ocean Modeling System (ROMS), a three-dimensional, free surface, topography following numerical model, which solves finite difference approximation of Reynolds Averaged Navier Stokes (RANS) equations using hydrostatic and Boussinesq approximation with a split explicit time stepping algorithm (Shchepetkin and McWilliams, 2005; Haidvogel et al., 2008; Shchepetkin and McWilliams, 2009). ROMS includes several options for several model capabilities, such as various advection schemes (second, third and fourth order) and turbulence closure models (e.g., Generic Length Scale mixing, Mellor-Yamada, Brunt-Väisälä frequency mixing, user provided analytical expression and K-profile parameterization). As Shchepetkin and McWilliams (2009) state, currently there are four variations of ROMS-family codes. In this contribution we use a version based on the Rutgers Uni-

versity ROMS which was first introduced by Haidvogel et al. (2000) and subsequently any reference to ROMS denotes this particular version.

3.2.1 VF Equations

The VF approach was implemented following the conventions described in MRL04 and based on the formulation as presented in U10, with several key modifications that are applicable for this particular modeling system. Terms corresponding to wave effect on current are assembled and shown on the right hand side of the equations presented below. Boldface typesets are used for horizontal vectors only, while the vertical component is represented by a normal typeset so that a three-dimensional current vector is designated as (**u**, w). Following the above conventions the model equations can be written as:

$$
\begin{aligned}
&\frac{\partial \mathbf{u}}{\partial t} + \left(\mathbf{u}\nabla_{\perp}\right)\mathbf{u} + w\frac{\partial \mathbf{u}}{\partial z} + f\hat{z}\times\mathbf{u} + \nabla_{\perp}\phi - \mathbf{F} - \mathbf{D} + \frac{\partial}{\partial z}\left(\overline{\mathbf{u}'w'} - \nu\frac{\partial \mathbf{u}}{\partial z}\right) = -\nabla_{\perp}\mathcal{K} + \mathbf{J} + \mathbf{F}^{w} \\
&\frac{\partial \phi}{\partial z} + \frac{g\rho}{\rho_0} = -\frac{\partial \mathcal{K}}{\partial z} + K \\
&\nabla_{\perp}\mathbf{u} + \frac{\partial w}{\partial z} = 0 \\
&\frac{\partial c}{\partial t} + \left(\mathbf{u}\nabla_{\perp}\right)c + w\frac{\partial c}{\partial z} - C_{source} + \frac{\partial}{\partial z}\left(\overline{c'w'} - \nu_{\theta}\frac{\partial c}{\partial z}\right) = -\left(\mathbf{u}^{St}\nabla_{\perp}\right)c - w^{St}\frac{\partial c}{\partial z} \\
&+ \frac{1}{2}\frac{\partial}{\partial z}\left[\mathcal{E}\frac{\partial c}{\partial z}\right]
\end{aligned}
\tag{3.1}
$$

where (**u**, w) and ($\mathbf{u}^{\mathrm{St}}$, w^{St}) are Eulerian mean and Stokes velocities, respectively. At this stage it is pertinent to point out that the velocities presented in this paper are the quasi-Eulerian mean velocities. This velocity is defined as the Lagrangian mean velocity minus the Stokes drift (Jenkins, 1989). Below the wave troughs it is very nearly equal to the one that is measurable by a fixed current meter. Above the wave troughs, it provides a smooth extension of the velocity profile all the way to the mean sea level, as assumed in the MRL04 theory. For consistency purposes with the

notation of MRL04 and U10, in the remaining of the paper these quasi-Eulerian mean velocities are referred to as Eulerian mean velocities. f is the Coriolis parameter, ϕ is the dynamic pressure (normalized by the density ρ_o); $\mathbf{F}$ is the non-wave, non-conservative force; $\mathbf{D}$ represents the diffusive terms (viscosity and diffusion); ($\mathbf{J}$, K) is the VF and $\mathcal{K}$ is the lower order Bernoulli head as described in MRL04 (see Sec. 9.6 in MRL04); F^w is the sum of momentum flux due to all non-conservative wave forces; c is any material tracer concentration; C_{source} are tracer source/sink terms and $\mathcal{E}$ is the wave-induced tracer diffusivity. An overbar indicates time average, and a prime indicates turbulent fluctuating quantity. ρ and ρ_o are total and reference densities of sea water; g is the acceleration due to gravity; and ν and ν_θ are the molecular viscosity and diffusivity, respectively. The vertical coordinate (z) range varies from $h(x) \le z \le \zeta + \hat{\zeta}$, where ζ and $\hat{\zeta}$, are the mean and quasi-static sea (wave-averaged) level components, respectively. All wave quantities are referenced to a local wave-averaged sea level, $z = \zeta + \hat{\zeta}$.

The three-dimensional Stokes velocity ($\mathbf{u}^{\mathrm{St}}$, w^{St}) is defined for a spectral wave-field as:

$$\begin{aligned} \mathbf{u}^{St}(z) &= \frac{2E}{c}\frac{\cosh[2\mathcal{Z}]}{\sinh[2\mathcal{H}]}\mathbf{k} \\ w^{St}(z) &= -\nabla_\perp \int_{-h}^{z} \mathbf{u}^{St} dz' \end{aligned} \tag{3.2}$$

where *h(x)* is the resting depth; E is the wave energy; c is the phase speed of the waves; $\boldsymbol{k}$ is the wave number vector and k is its magnitude, and $\mathcal{H}$ and $\mathcal{Z}$ are the normalized vertical lengths defined as:

$$\begin{aligned} \mathcal{H} &= k\left(h + \zeta + \hat{\zeta}\right) \\ \mathcal{Z} &= k\left(z + h\right) \end{aligned} \tag{3.3}$$

where $D = \left(h + \zeta + \hat{\zeta}\right)$ is the wave-averaged thickness of the water column. Finally, the wave energy (E), phase speed (c), and intrinsic frequency (σ) are given by:

$$\begin{aligned} E &= \frac{1}{8} g H^2 \\ c &= \frac{\sigma}{k} \\ \sigma &= \sqrt{gk \tanh\left[\mathcal{H}\right]} \end{aligned} \tag{3.4}$$

where H is the root mean square wave height.

The VF ($\mathbf{J}$, K) and the Bernoulli head ($\mathcal{K}$) terms shown in Eqn. 3.1 are expressed as:

$$\begin{aligned} \mathbf{J} &= -\hat{z} \times \mathbf{u}^{St} \left(\left(\hat{z} \nabla_{\perp} \times \mathbf{u} \right) + f \right) - w^{St} \frac{\partial \mathbf{u}}{\partial z} \\ K &= \mathbf{u}^{St} \frac{\partial u}{\partial z} \\ \mathcal{K} &= \frac{\sigma H^2}{16 k \sinh^2\left[\mathcal{H}\right]} \int_{-h}^{z} \frac{\partial^2 \mathcal{V}}{\partial z'^2} \sinh\left[2k(z - z')\right] dz' \end{aligned} \tag{3.5}$$

The wave-induced tracer diffusivity in Eqn. 3.1 is defined as:

$$\mathcal{E} = \frac{1}{8} \frac{\partial}{\partial t} \left(\frac{H \sinh[\mathcal{Z}]}{\sinh[\mathcal{H}]} \right) \tag{3.6}$$

while the quasi-static sea level component is given by:

$$\hat{\zeta} = \frac{-P_{atm}}{g \rho_o} - \frac{H^2 k}{8 \sinh[2\mathcal{H}]} \tag{3.7}$$

The term $\hat{\zeta}$ contains inverse barometric response due to changes in atmospheric pressure ($Patm$) and a wave-averaged set-up/set-down (with respect to the still water).

It is important to note that in the above formulations the total contribution of Bernoulli head has been separated in two parts of different order each. The higher order contribution is a quasi-static balance between mean pressure, mean surface elevation and the wave stresses, which is absorbed here as a part of the quasi-static sea level component ($\hat{\zeta}$) in Eqn. 3.7. The lower order quasi-static balance has been expressed as $\mathcal{K}$ in Eqn. 3.5.

When using a spectral wave model such as SWAN, wave height ($H = H_{sig}/\sqrt{(}2)$) and bottom orbital velocity (u_{orb}) values are provided after integrating the energy over

all frequencies and directions, while wavenumber (k), wave direction and, frequency (f) are those corresponding to the peak frequency. Wave dissipation due to depth-limited breaking, whitecapping and bottom friction is also provided by SWAN.

3.2.2 Boundary Conditions

The kinematic and pressure boundary conditions are given as:

$$\begin{aligned} & w|_{-h} + \mathbf{u}\|_{-h}\nabla_\perp h = 0 \\ & w|_{\zeta+\hat{\zeta}} - \frac{\partial\zeta}{\partial t} - \left(\mathbf{u}|_{\zeta+\hat{\zeta}}\nabla_\perp\right)\zeta = \nabla_\perp\overline{\mathbf{U}}^{St} + \frac{\partial\hat{\zeta}}{\partial t} + \left(\mathbf{u}|_{\zeta+\hat{\zeta}}\nabla_\perp\right)\hat{\zeta} \\ & g\zeta - \phi|_{\zeta+\hat{\zeta}} = g\mathcal{P} \end{aligned} \tag{3.8}$$

where $\overline{\mathbf{U}}^{St}$is the depth-averaged Stokes velocity and $\mathcal{P}$ is the wave-averaged forcing surface boundary condition (see section 9.3 in MRL04) defined as:

$$\mathcal{P} = \frac{H^2}{8\sigma} \left\{\frac{\tanh[\mathcal{H}]}{\sinh[2\mathcal{H}]}\left(-\frac{\partial\mathcal{V}}{\partial z}\bigg|_{\zeta+\hat{\zeta}} + \cosh[2\mathcal{H}]\,\frac{\partial\mathcal{V}}{\partial z}\bigg|_{-h} + \int_{-h}^{\zeta+\hat{\zeta}}\frac{\partial^2\mathcal{V}}{\partial z'^2}\cosh[2kz']dz'\right) - 2k\tanh[\mathcal{H}]\mathcal{V}_{\zeta+\hat{\zeta}}\right\} \tag{3.9}$$

The equations corresponding to barotropic mode have not been presented here for brevity, although details can be found in U10.

3.3 Numerical Implementation

For implementation into the modeling system, the equations presented in section 3.2 are expressed in a mass flux form. The wave-induced terms are no longer retained to the right hand side and the lower order Bernoulli head becomes part of the dynamic pressure.

First we define the following quantities:

$$\begin{aligned} \left(\mathbf{u}^l, \omega^l\right) &= (\mathbf{u}, \omega_s) + \left(\mathbf{u}^{St}, \omega_s^{St}\right) \\ \zeta^c &= \zeta + \hat{\zeta} \\ \phi_c &= \phi + \mathcal{K} \end{aligned} \tag{3.10}$$

where ζ^c is the composite sea level, ϕ^c is the sum of Bernoulli head and the dynamic pressure, while to lowest order the Lagrangian mean velocity (u^l, ω^l) is represented as the sum of Stokes ((u^{St}, ω_s^{St})) and Eulerian mean velocities (u, ω_s). ω_s is the vertical Eulerian mean velocity in a sigma coordinate system.

The continuity and momentum balance equations in horizontal (ξ,η) orthogonal curvilinear and vertical (s) terrain following coordinate system are:

$$\frac{\partial}{\partial t}\left(\frac{H_z}{mn}\right)+\frac{\partial}{\partial \xi}\left(\frac{H_z u^l}{n}\right)+\frac{\partial}{\partial \eta}\left(\frac{H_z v^l}{m}\right)+\frac{\partial}{\partial s}\left(\frac{\omega_s^l}{mn}\right)=0 \tag{3.11}$$

$$\begin{aligned}
&\underbrace{\frac{\partial}{\partial t}\left(\frac{H_z u}{mn}\right)}_{\text{ACC}}+\underbrace{\frac{\partial}{\partial \xi}\left(\frac{H_z u}{n}u\right)+\frac{\partial}{\partial \eta}\left(\frac{H_z v}{m}u\right)+u\frac{\partial}{\partial \xi}\left(\frac{H_z u^{St}}{n}\right)+u\frac{\partial}{\partial \eta}\left(\frac{H_z v^{St}}{m}\right)}_{\text{HA}}\\
&+\underbrace{\frac{\partial}{\partial s}\left(\frac{\omega_s}{mn}u\right)+u\frac{\partial}{\partial s}\left(\frac{\omega_s^{St}}{mn}\right)}_{\text{VA}}-\underbrace{H_z\left(\frac{fv}{mn}\right)}_{\text{COR}}-\underbrace{H_z\left(\frac{fv^{St}}{mn}\right)}_{\text{StCOR}}=-\underbrace{\frac{H_z}{n}\left(\left.\frac{\partial \phi^c}{\partial \xi}\right|_z\right)}_{\text{PG}}\\
&\underbrace{+H_z v^{St}\left(\frac{1}{n}\frac{\partial v}{\partial \xi}-\frac{1}{m}\frac{\partial u}{\partial \eta}\right)-\omega^{St}\frac{\partial}{\partial s}\left(\frac{u}{mn}\right)}_{\text{HVF}}+\underbrace{H_z\frac{\mathcal{F}^{\xi}}{mn}}_{\text{BF}}+\underbrace{H_z\frac{\mathcal{F}^{w\xi}}{mn}}_{\text{BA+RA+BtSt+SuSt}}+\underbrace{H_z\frac{\mathcal{D}^{\xi}}{mn}}_{\text{HM}}\\
&\underbrace{-\frac{\partial}{\partial s}\left(\overline{u'w'}-\frac{\nu}{H_z}\frac{\partial u}{\partial s}\right)}_{\text{VM}}+\underbrace{\hat{\mathcal{F}}^u}_{\text{FCurv}}
\end{aligned} \tag{3.12}$$

$$\begin{aligned}
&\underbrace{\frac{\partial}{\partial t}\left(\frac{H_z v}{mn}\right)}_{\text{ACC}}+\underbrace{\frac{\partial}{\partial \xi}\left(\frac{H_z u}{n}v\right)+\frac{\partial}{\partial \eta}\left(\frac{H_z v}{m}v\right)+v\frac{\partial}{\partial \xi}\left(\frac{H_z u^{St}}{n}\right)+v\frac{\partial}{\partial \eta}\left(\frac{H_z v^{St}}{m}\right)}_{\text{HA}}\\
&+\underbrace{\frac{\partial}{\partial s}\left(\frac{\omega_s}{mn}v\right)+v\frac{\partial}{\partial s}\left(\frac{\omega_s^{St}}{mn}\right)}_{\text{VA}}+\underbrace{H_z\left(\frac{fu}{mn}\right)}_{\text{COR}}+\underbrace{H_z\left(\frac{fu^{St}}{mn}\right)}_{\text{StCOR}}=-\underbrace{\frac{H_z}{m}\left(\left.\frac{\partial \phi^c}{\partial \eta}\right|_z\right)}_{\text{PG}}\\
&\underbrace{-H_z u^{St}\left(\frac{1}{n}\frac{\partial v}{\partial \xi}-\frac{1}{m}\frac{\partial u}{\partial \eta}\right)-\omega^{St}\frac{\partial}{\partial s}\left(\frac{v}{mn}\right)}_{\text{HVF}}+\underbrace{H_z\frac{\mathcal{F}^{\eta}}{mn}}_{\text{BF}}+\underbrace{H_z\frac{\mathcal{F}^{w\eta}}{mn}}_{\text{BA+RA+BtSt+SuSt}}+\underbrace{H_z\frac{\mathcal{D}^{\eta}}{mn}}_{\text{HM}}\\
&\underbrace{-\frac{\partial}{\partial s}\left(\overline{v'w'}-\frac{\nu}{H_z}\frac{\partial v}{\partial s}\right)}_{\text{VM}}+\underbrace{\hat{\mathcal{F}}^v}_{\text{FCurv}}
\end{aligned} \tag{3.13}$$

for the 'x' and 'y' (ξ and η) directions, respectively; where m^{-1} and n^{-1} are the Lamé metric coefficients, and H_z is the grid-cell thickness. The vertical sigma coordinates s varies from -1 at the bottom to 0 at the free surface. $\mathbf{F} = (\mathcal{F}^{\xi}, \mathcal{F}^{\eta})$ is the non-wave body force; $(\mathcal{D}^{\xi}, \mathcal{D}^{\eta})$ represents the parameterized momentum mixing terms; and $\mathbf{F}_w = (\mathcal{F}^{w\xi}, \mathcal{F}^{w\eta})$ is the momentum flux from non-conservative wave terms described in 3.3.1 below. In a Cartesian coordinate system m and n are unity and the curvilinear terms $\left(\hat{\mathcal{F}}^{u}, \hat{\mathcal{F}}^{v}\right)$ become zero.

In the momentum balance equations (Eqns. 3.12 and 3.13), the first term on the left hand side is the local acceleration (ACC), second to fifth terms constitute the horizontal advection (HA), sixth and seventh terms are vertical advection (VA), eighth and the ninth term represent Coriolis (COR) and Stokes-Coriolis (StCOR) forces, respectively. On the right hand side of the momentum balance equations, the first term is the pressure gradient (PG), and the combination of the second and the third term is the horizontal vortex force (HVF). The non-wave body force (BF) is the fourth term, while the contribution of breaking and roller acceleration, and bottom and surface streaming is represented collectively by the fifth term (BA+RA+BtSt+SuSt). Horizontal (HM) and vertical mixing (VM) are sixth and the seventh terms, respectively. The last term on the right hand side is the curvilinear metric term given by Eqns. 3.15 and 3.16.

The geopotential function derived after depth integrating the vertical momentum balance equation (see Eqn. 3.1) is:

$$\phi^{c} = g\left(\zeta^{c} - \hat{\zeta}\right) - \left(g\mathcal{P} - \mathcal{K}\right)|_{\zeta^{c}} + \int_{s}^{0}\left[\frac{g\rho}{\rho_0} - K\right]H_z ds \tag{3.14}$$

The curvilinear terms $\hat{\mathcal{F}}^{u}$ and $\hat{\mathcal{F}}^{v}$ in Eqns. (3.12) and (3.13), respectively are:

$$\begin{aligned}\hat{\mathcal{F}}^{u} = {} & H_z\left[-u\frac{\partial}{\partial\eta}\left(\frac{1}{m}\right) + v\frac{\partial}{\partial\xi}\left(\frac{1}{n}\right)\right]v^{St} + H_z\left[-u\frac{\partial}{\partial\eta}\left(\frac{1}{m}\right) + v\frac{\partial}{\partial\xi}\left(\frac{1}{n}\right)\right]v \\ & + H_z\left[-u^{St}\frac{\partial}{\partial\eta}\left(\frac{1}{m}\right) + v^{St}\frac{\partial}{\partial\xi}\left(\frac{1}{n}\right)\right]v\end{aligned} \tag{3.15}$$

$$\begin{aligned}\hat{\mathcal{F}}^v = & H_z\left[-u\frac{\partial}{\partial\eta}\left(\frac{1}{m}\right)+v\frac{\partial}{\partial\xi}\left(\frac{1}{n}\right)\right]u^{St}-H_z\left[-u\frac{\partial}{\partial\eta}\left(\frac{1}{m}\right)+v\frac{\partial}{\partial\xi}\left(\frac{1}{n}\right)\right]u \\ & +H_z\left[-u^{St}\frac{\partial}{\partial\eta}\left(\frac{1}{m}\right)+v^{St}\frac{\partial}{\partial\xi}\left(\frac{1}{n}\right)\right]u\end{aligned} \tag{3.16}$$

The vertical motion past sigma surfaces is given by:

$$\omega_s^l = \left[w^l-\left(\frac{\partial}{\partial t}+\mathbf{u}^l\nabla_\perp z\right)\right]\Bigg|_s \tag{3.17}$$

The vertical mass flux through the sigma surfaces is calculated as:

$$W^l = \int_{-1}^{s}\left(\frac{\partial U^l}{\partial\xi}+\frac{\partial V^l}{\partial\eta}\right)ds' - \frac{1}{mn}\left(\frac{z+h}{\zeta+h}\right)\frac{\partial\zeta^c}{\partial t} \tag{3.18}$$

where $U^l = H_z u^l/n$, $V^l = H_z v^l/n$, and $W^l = \omega_s^l/(mn)$ are grid-cell volume fluxes.

The three-dimensional tracer equation is:

$$\begin{aligned}&\frac{\partial}{\partial t}\left(\frac{H_z c}{mn}\right)+\frac{\partial}{\partial\xi}\left(\frac{H_z u}{n}c\right)+\frac{\partial}{\partial\eta}\left(\frac{H_z v}{m}c\right)+\frac{\partial}{\partial s}\left(\frac{\omega_s}{mn}c\right)=C_{source}-\frac{\partial}{\partial\xi}\left(\frac{H_z u^{St}}{n}c\right) \\ &-\frac{\partial}{\partial\eta}\left(\frac{H_z v^{St}}{m}c\right)-\frac{\partial}{\partial s}\left(\frac{\omega_s^{St}}{mn}c\right)-\frac{\partial}{\partial s}\left(\overline{c'w'}-\frac{\nu_\theta}{H_z}\frac{\partial c}{\partial s}\right)+\frac{\partial}{\partial s}\left(\frac{\mathcal{E}}{H_z}\left(\frac{\partial c}{\partial s}\right)\right)\end{aligned} \tag{3.19}$$

where $\mathcal{E}$ is the wave-induced tracer diffusivity as defined as in Eqn. 8.

Eqns. (3.12), (3.13) and (3.19) are closed by parameterization of the Reynolds stresses and turbulent tracer fluxes as:

$$\overline{u'w'} = \frac{K_M}{H_z}\frac{\partial u}{\partial s}; \overline{v'w'} = \frac{K_M}{H_z}\frac{\partial v}{\partial s}; \overline{c'w'} = \frac{K_H}{H_z}\frac{\partial c}{\partial s} \tag{3.20}$$

where K_M is the momentum eddy viscosity and K_H is the eddy diffusivity. Along with the kinematic and pressure boundary conditions (Eqn. 3.8), the surface wind and bottom stresses are prescribed as vertical boundary condition for the Reynolds stresses given as:

$$\begin{aligned}\frac{K_m}{H_z}\frac{\partial u}{\partial s}\Big|_{s=0} &= \tau_s^\xi(\xi,\eta,t) \\ \frac{K_m}{H_z}\frac{\partial v}{\partial s}\Big|_{s=0} &= \tau_s^\eta(\xi,\eta,t) \\ \frac{K_m}{H_z}\frac{\partial u}{\partial s}\Big|_{s=-1} &= \tau_b^\xi(\xi,\eta,t) \\ \frac{K_m}{H_z}\frac{\partial u}{\partial s}\Big|_{s=-1} &= \tau_b^\eta(\xi,\eta,t)\end{aligned} \tag{3.21}$$

where, $\tau_s = \left(\tau_s^{\xi}, \tau_s^{\eta}\right)$ and $\tau_b = \left(\tau_b^{\xi}, \tau_b^{\eta}\right)$ are surface wind stress and bottom stress, respectively.

Although many different methods are available to incorporate bottom stress in ROMS (see Warner et al., 2008a), in the present application we use the simple quadratic drag method or the wave-current interaction method of Madsen (1994).

The horizontal momentum, continuity and tracer equations as well as the geopotential function along with the boundary conditions (Eqns. 3.11-3.21) are solved to obtain the Eulerian mean velocity ($\mathbf{u}$, ω) and composite sea level (ζ^c) as the prognostic variables.

The wave parameters required for calculating the Stokes velocities, WEC terms, and momentum flux from non-conservative wave forcing terms, $\mathbf{F^w}$ (see next section for details) are provided through coupling to the wave model (SWAN). SWAN receives information about sea surface elevation, bathymetric change, and a circulation field from ROMS to determine the effect of currents and total water depth on wave propagation. In turn, ROMS receives information on surface and bottom wave parameters (height, orbital velocity, period, wavelength and direction), wave dissipation due to bottom friction, wave breaking, and whitecapping for non-conservative WEC processes. This exchange of information between the circulation and wave models occurs at user defined intervals in a two-way coupling scenario. One-way coupling of data feeding from wave to circulation model can be used if the impact of currents on wave field is negligible, or simply from the wave model to the ocean for processes such as enhanced bottom stress computations. A detailed discussion about model coupling can be found in Warner et al. (2008ab).

3.3.1 Parameterization of non-conservative wave forcing, $\mathbf{F^w}$

Waves propagating towards the shoreline lose energy through three different dissipation mechanisms: (a) bottom friction (ϵ^{bf}); (b) whitecapping (ϵ^{wcap}); and (c)

depth-induced wave breaking (ϵ^b). The energy lost by these processes is included in the momentum balance (Eqns. 3.12 and 3.13) through the non-conservative wave forcing/acceleration term $\mathbf{F^w}$:

$$\mathbf{F^w}\left(\mathcal{F}^{w\xi}, \mathcal{F}^{w\eta}\right) = \mathbf{B^{bf}} + \mathbf{B^{sf}} + \mathbf{B^{wb}} = \mathbf{B^{bf}} + \mathbf{B^{sf}} + \mathbf{B^{wcap}} + \mathbf{B^b} + \mathbf{B^r} \tag{3.22}$$

where $\mathbf{B^{bf}}$ and $\mathbf{B^{sf}}$ are accelerations due to bottom and surface streaming, respectively, while$\mathbf{B^{wb}}$ denotes accelerations due to wave breaking. The latter is further decomposed to accelerations due to whitecapping ($\mathbf{B^{wcap}}$), depth-limited wave breaking ($\mathbf{B^b}$) and wave roller ($\mathbf{B^r}$). It is important to point out that the contribution of bottom friction (ϵ^{bf}) is manifested in the form of bottom streaming, while the wave breaking induced acceleration (ϵ^b) is further divided into depth-limited breaking and roller contribution (see next few paragraphs). The model options used to activate these formulations within the COAWST modeling system are listed in Table 3.1.

Bottom Streaming ($\mathbf{B^{bf}}$) term

Interaction of waves with the sea bed leads to wave dissipation due to friction within the wave boundary layer. Three different bottom friction formulations are available in SWAN that are based on: (a) empirical formulations (JONSWAP) by Hasselmann et al. (1973); (b) the drag law model of Collins (1972); and (c) eddy viscosity model of Madsen et al. (1988). These formulations can be used to calculate ϵ^{bf} for a spectral wave field. In addition, the option for dissipation due to bottom drag using the parameterization presented by Reniers et al. (2004b) as in U10 has also been implemented (see Table 3.1). This option estimates ϵ^{bf} using:

$$\epsilon^{bf} = \frac{1}{2\sqrt{\pi}}\rho_0 f_w \left|u^3_{orb}\right|; |u^w_{orb}| = \frac{\sigma H}{2\sinh kD}; f_w = 1.39\left(\frac{\sigma z_0}{|u^w_{orb}|}\right)^{0.52} \tag{3.23}$$

where, u^w_{orb} is the bottom orbital velocity and f_w is the wave friction factor (Soulsby, 1995).

Dissipation of wave energy in the wave boundary layer causes the instantaneous, oscillatory wave bottom orbital velocities (u' and w') to be slightly in phase from quadrature causing a wave stress (bottom streaming) in the wave bottom boundary layer, along the direction of wave propagation (Longuet-Higgins, 1953; Phillips, 1977; Xu and Bowen, 1994; Lentz et al., 2008). This stress can be provided as a bottom stress or a body force. We have implemented two approaches to allow the effects of bottom streaming on the mean flows. First, following U10, the effect of bottom streaming in momentum balance is accounted for by using the wave dissipation due to bottom friction with an upward decaying vertical distribution.

$$\mathbf{B}^{bf} = \frac{\epsilon^{bf}}{\rho_o \sigma}(k) f^{bf}(z) \tag{3.24}$$

where $f^{bf}(z)$ is a vertical distribution function given by:

$$f^{bf}(z) = \frac{\cosh\left(k_{wd}\left(\zeta^c - z\right)\right)}{\int_{-h}^{\zeta^c} \cosh\left(k_{wd}\left(\zeta^c - z\right)\right) dz} \tag{3.25}$$

with k_{wd} being a decay length which is a function of wave bottom boundary layer thickness (δ_w) and given by:

$$k_{wd} = a_{wd}\delta_w \tag{3.26}$$

where a_{wd} is an empirical constant (=1 in here) and δ_w is a function of semi-orbital excursion (A^w_{orb}), Nikuradse roughness (k_n) and bottom roughness length (z_0).

$$A^w_{orb} = \frac{\left|u^w_{orb}\right|}{\sigma}; k_n = 30 z_o \tag{3.27}$$

As a second approach of bottom streaming, the method of Xu and Bowen (1994) is implemented (see Table 3.1) where:

$$\mathbf{B}^{bf} = \frac{1}{\rho_o}\left\langle u'w'\right\rangle = \frac{H^2\sigma^2 k}{8\sinh^2 kh}\left[\left(-\beta z \sin\beta z + \beta z\cos\beta z - \cos\beta z\right)e^{-\beta z} + e^{-2\beta z}\right] \tag{3.28}$$

with $\beta = \sqrt{\sigma/2K_m}$, where K_m is the eddy viscosity.

The first method is more suitable when the vertical resolution of the model is not high enough to resolve the wave bottom boundary layer while the second method is preferred for simulations that use high vertical resolution.

Surface Streaming ($\mathbf{B^{sf}}$) term

Similar to the concept of bottom streaming, at the surface of the water column the wave-induced stress develops a thin viscous boundary layer known as surface streaming (Longuet-Higgins, 1953; Xu and Bowen, 1994 and Lentz et al., 2008). This contribution to non-conservative wave forcing is parameterized as (Xu and Bowen, 1994):

$$\mathbf{B}^{sf} = \frac{K_m H^2 \sigma}{2} \boldsymbol{k} \cdot k \coth kh \tag{3.29}$$

and it is implemented as a surface boundary condition (see section 4). The effect of surface streaming can be interpreted in a similar manner as that of wind stress acting on the ocean surface (Weber et al., 2006). This effect may not be significant in a dynamic environment like the surf zone, but could be significant outside the surf zone as shown by Lentz et al. (2008).

Wave Breaking ($\mathbf{B^{wb}}$) Terms

Non-conservative wave forcing due to wave breaking is traditionally defined only in a depth-averaged form (Longuet-Higgins, 1964; Smith, 2006). Newberger and Allen (2007a) implement the force due to depth induced breaking ($\mathbf{B^b}$) as a surface stress, while Walstra et al.(2000), U10 and Kumar et al.(2011a) implement it as a surface intensified body force through the development of ad-hoc vertical distribution functions. In the present work, we use a surface intensified distribution of $\mathbf{B^{wcap}}$, $\mathbf{B^b}$ and $\mathbf{B^r}$ as in Kumar et al. (2011a).

Whitecapping induced acceleration (B^{wcap})

Whitecapping can occur in any water depth (van der Westhuysen et al., 2007; Jones and Monismith, 2008) as a response to wave steepening. Presently SWAN provides many different expressions for calculation of wave dissipation due to whitecapping

(e.g., Rogers et al., 2003; van der Westhuysen et al., 2007). The associated acceleration is given as:

$$\mathbf{B}^{wcap} = \frac{\epsilon^{wcap}}{\rho_o \sigma}\mathbf{k} f^b(z) \tag{3.30}$$

where ϵ^{wcap} is the dissipation from SWAN, and $f^b(z)$ is the vertical distribution function such that:

$$f^b(z) = \frac{FB}{\int_{-h}^{\zeta^c} FB dz}; FB = \cosh\left(\frac{2\pi}{H}(z+h)\right) \tag{3.31}$$

Bathymetry induced breaking and acceleration (B^b)

Depth limited wave breaking dissipation (ϵ^b) is computed in SWAN using a spectral version of the bore model based on Battjes and Janssen (1978), which depends on the ratio of wave height to water depth (see, Eldeberky and Battjes, 1996). Alternative empirical relationships for depth-induced breaking have been provided by Thornton and Guza (1983) and Church and Thornton (1993) and have been added as options (see Table 3.1). These formulations are:

$$\epsilon_b = \frac{3\sqrt{\pi}}{16}\rho_o g \frac{B_b^3 f_p}{D^5} H^7 \tag{3.32}$$

$$\epsilon_b = \frac{3\sqrt{\pi}}{16}\rho_o g \frac{B_b^3 f_p}{D} H^3 \left[1 + tanh\left\{8\left(\frac{H_{rms}}{\gamma_b D}\right)\right\}\right]\left[1 - \left\{1 + \left(\frac{H_{rms}}{\gamma_b D}\right)^2\right\}^{\frac{-5}{2}}\right] \tag{3.33}$$

where, H is the root mean square wave height; f_p is the wave frequency; g is the acceleration due to gravity; B_b and γ_b (the ratio of wave height to water depth) are empirical parameters.

The acceleration due to the depth-limited breaking dissipation is:

$$\mathbf{B}^b = \frac{(1-\alpha^r)\epsilon^b}{\rho_o \sigma}\mathbf{k} f^b(z) \tag{3.34}$$

where, α^r is the percentage of wave dissipation involved in creation of wave rollers (described in details below), and $f^b(z)$ is a vertical distribution function, where we have decided to use the same function as defined in Eqn. 3.30.

Wave Rollers and Roller Acceleration (B^r)

Within the surf zone the spatial distribution of wave dissipation is dominated by wave breaking that depends on bathymetry, but it is further modified due to the action of wave rollers. Wave rollers act as storage of dissipated wave energy, which is gradually transferred to the mean flow causing a lag in the transfer of momentum (Svendsen, 1984; Nairn et al., 1990). Warner et al. (2008a) and Haas and Warner (2009, hereinafter HW09) demonstrated the implementation and application into the ROMS model of a roller formulation based on Svendsen (1984). However, U10 presented a wave roller model which is similar to that of Reniers et al. (2004a) and Stive and DeVriend (1994). To provide additional capabilities, we also implemented this time dependent advective roller model into the COAWST system. The equations for evolution of wave rollers are similar to spectral wave evolution equation and can be represented as:

$$\frac{\partial \mathcal{A}^r}{\partial t} + \nabla \cdot (\mathcal{A}^r \vec{c}) = \frac{\alpha_r \epsilon_b - \epsilon_r}{\sigma} \tag{3.35}$$

where, $\mathcal{A}^{\mathrm{r}}$ is the roller energy density; c is the phase speed of the primary wave, ϵ^b is the wave dissipation; ϵ^r is the roller dissipation rate; σ is the wave frequency and α^r is an empirical parameter denoting the contribution of wave dissipation in creation of wave roller (see below). The roller energy density is related to roller energy by:

$$\mathcal{A}^r = \frac{E^r}{\sigma} \tag{3.36}$$

The phase speed of the primary wave is given by:

$$\vec{c} = \overline{\mathbf{u}} + \sigma k^2 \vec{k} \tag{3.37}$$

where, $\overline{\mathbf{u}}$ is the mean velocity, and k is the wave number. The roller dissipation rate is:

$$\epsilon^r = \frac{g \sin \beta E^r}{c} \tag{3.38}$$

where, c is the phase velocity (Eqn. 3.4) and $\sin\beta = 0.1$ is an empirical constant (Reniers et al., 2004a). As suggested by Tajima and Madsen (2006) and U10, the quantity α_r in Eqn. 3.34 can vary between 0 and 1, providing a control on the amount of wave energy expended for the creation of wave rollers. This choice of α_r would be contingent upon wave breaking type (i.e., spilling, plunging, surging) which in turn depends on beach slope and type (Short, 1985).

The contribution of wave rollers in form of acceleration is given by:

$$\mathbf{B}^r = \frac{\epsilon^r}{\rho_o \sigma}\mathbf{k} f^b(z) \tag{3.39}$$

Combining Eqns. 3.30, 3.34 and 3.39 and after some re-organization the total acceleration contribution of the wave breaking term is written as:

$$\mathbf{B}^{wb} = \frac{(1-\alpha^r)\epsilon^b + \epsilon^r + \epsilon^{wcap}}{\rho_o \sigma}\mathbf{k} f^b(z) \tag{3.40}$$

3.3.2 Mass flux due to wave rollers

The continuity equation (Eqn. 3.11) accommodates the mass flux due to Eulerian and Stokes transport. Wave rollers also contribute to associated mass flux increasing the total Stokes transport (Svendsen, 1984; Reniers et al., 2004a). The roller Stokes transport is given by:

$$\mathbf{U}^r = \frac{E^r}{\rho_o \sigma}\mathbf{k} == \frac{\mathcal{A}^r}{\rho_o}\mathbf{k} \tag{3.41}$$

and the total Stokes and roller transport becomes:

$$\mathbf{U}^{St} = \frac{(E + E^r)}{\rho_o \sigma}\mathbf{k} = \frac{(\mathcal{A} + \mathcal{A}^r)}{\rho_o}\mathbf{k} \tag{3.42}$$

The vertical profile of $\mathbf{U^r}$ has a distribution similar to that of the Stokes velocity. Since the effect of wave rollers is usually limited to the surface, a surface intensified distribution (e.g., HW09) may be more suitable. Simulations conducted using Stokes vs. surface intensified distribution provide similar results, so in the present implementation we use a Stokes velocity type distribution.

3.3.3 Enhanced mixing due to wave breaking

Wave breaking induced dissipation leads to mixing of momentum in the water column (Agrawal et al., 1992). In surf zone this enhanced mixing can also be responsible for sediment resuspension in the water column (Voulgaris and Collins, 2000). The vertical scale of this mixing can be empirically related to the wave height (Rapp and Melville, 1990), which for shallow waters is usually of the same order as the water depth. This leads to a region in the water column of overlapped mixing due to wave breaking and turbulence from the bottom layer (Feddersen and Trowbridge, 2005).

Following Umlauf and Burchard (2003) as implemented in Warner et al. (2005), a generalized expression for transport of turbulent kinetic energy (k) and generic length scale (ψ) can be written as:

$$\begin{aligned} \frac{\partial k}{\partial t} + \mathbf{u}\nabla k &= \frac{\partial}{\partial z}\left(\frac{K_M}{\sigma_k}\frac{\partial k}{\partial z}\right) + P + B - \epsilon \\ \frac{\partial \psi}{\partial t} + \mathbf{u}\nabla \psi &= \frac{\partial}{\partial z}\left(\frac{K_M}{\sigma_\psi}\frac{\partial k}{\partial z}\right) + \frac{\psi}{k}\left(c_1 P + c_3 B - c_2 \epsilon F_{wall}\right) \end{aligned} \tag{3.43}$$

where P and B are the shear and buoyancy production, respectively, σ_k and σ_ψ are turbulence Schmidt numbers for k and ψ, respectively, and F_{wall} is a wall function *.c1*, *c2* and *c3* are coefficients defined in detail in Warner et al. (2005). The generic length scale (ψ) is defined as:

$$\psi = \left(c_\mu^o\right)^p k^m l^n \tag{3.44}$$

where, c_μ^o is a numerical constant; m, n and p are specified to relate ψ to a turbulent quantity.

The turbulence due to injection of surface flux of TKE is given as surface boundary conditions (Craig and Banner, 1994; Feddersen and Trowbridge, 2005):

$$\left.\frac{K_M}{\sigma_k}\frac{\partial k}{\partial z}\right|_{\zeta^c} = \overline{\epsilon_w} \tag{3.45}$$

where $\overline{\epsilon_w}$ is the downward TKE flux due to breaking waves. The surface boundary condition for ψ due to wave breaking is (Carniel et al., 2009):

$$\frac{K_M}{\sigma_\psi}\frac{\partial k}{\partial z}\bigg|_{\zeta^c} = -\frac{\sigma_k}{\sigma_\psi}\left(c_\mu^o\right)^p m k^{m-1}\left(\kappa\left(z_o - z\right)\right)^n \mathcal{Y} - \frac{\nu_t}{\sigma_\psi}\left(c_\mu^o\right)^p n k^m \kappa^n \left(z_o - z\right)^{n-1} \tag{3.46}$$

In deep waters, $\mathcal{Y} = c_w\left(u_s^*\right)^3$, where u_s^* is the friction velocity; and c_w is a parameter that depends on the sea state, with a typical value of c_w=100 (Carniel et al., 2009). In the surf zone, $\mathcal{Y} = \overline{\epsilon_w} z_o$ is the surface roughness or the surface mixing length. For breaking wave conditions, the surface roughness is provided using the closure model of Stacey (1999):

$$z_o = \alpha_w H \tag{3.47}$$

where α_w = 0.5. In the surf zone, part of the wave dissipation contributes to the flux of momentum (i.e., $(1-\alpha^r)\epsilon^b + \epsilon^{wcap}$), while the remaining amount (i.e., $\alpha^r\epsilon^b$) is expended for the creation of wave rollers. Furthermore, part of the wave and roller dissipation (ϵ^r) also contributes to turbulence mixing within the surf zone. Feddersen and Trowbridge (2005) assume that 25% of wave energy dissipation goes into the water column as TKE, while Jones and Monismith (2008) use a value of 6%.

In the present work, the contribution of wave dissipation as surface flux of TKE is expressed through an empirical coefficient $c_{\epsilon w}$ which can be manually adjusted (see section 3.2.3) based on data availability. The surface flux of TKE is therefore:

$$\overline{\epsilon_w} = c_{\epsilon w}\left[(1-\alpha^r)\epsilon^b + \epsilon^r + \epsilon^{wcap}\right] \tag{3.48}$$

In order to conserve the total contribution to momentum balance due to wave dissipation, the amount of wave dissipation introduced as surface flux of TKE is subtracted from Eqn. 39.

3.4 Model Simulations

The modeling system with the VF formalism described above is applied to idealized and realistic surf zone and inner shelf environments to study the spatial variation and

vertical structure of cross-shore and longshore flows. Four simulations are presented in detail, provided as standard test cases. The first two cases consist of creation of alongshore currents and undertow due to oblique incidence of spectral waves on a planar and a natural, barred beach assuming alongshore uniformity. The third case introduces three-dimensionality in the domain and flow development as it simulates a nearshore barred morphology interrupted by rip channels. The fourth case is designed to demonstrate the applicability of the model for inner shelf applications and simulates wave-induced cross-shore flows in the inner shelf. For all cases, an orthogonal coordinate system is defined so that x and y represent the cross-shore and longshore directions, respectively with positive x towards the open ocean. Correspondingly, positive cross-shore velocity values indicate offshore directed flow.

3.4.1 Test Case 1: Obliquely incident waves on a planar beach

The effect of VF formalism is examined through simulations for obliquely incident waves on a planar beach. This case has been previously discussed by HW09 and Kumar et al. (2011a) using depth dependent radiation stress formulations based on Mellor (2003) and Mellor (2008), respectively, and by U10 using a VF based model. In the simulations presented here, we use our implementation of the VF formulations which utilizes a different vertical distribution of wave dissipation and turbulence closure scheme than U10 (Eqns. 3.31 and 3.43).

The model domain has a cross-shore (x) width of 1,180 m and an alongshore (y) length of 140 m, with a 20 m grid resolution. The resting water depth varies from 12 m at the offshore boundary to 0 m at the shoreline. The vertical domain consists of 30 equally distributed vertical layers. The boundary conditions are periodic in the alongshore (i.e., north and south boundaries) and closed at the shoreline. At the offshore side we use Flather radiation condition (Flather, 1976) for free surface and Neumann boundary conditions for barotropic and baroclinic velocities (includ-

ing boundary condition for Stokes velocities). The effect of earth rotation is not included. The bottom stress has been formulated using a quadratic bottom drag with a cd value of 0.0015. The turbulence closure scheme is Generic Length Scale (GLS, k-ϵ) as described in Warner et al. (2005). Wave forcing is provided by SWAN, which propagates an offshore JONSWAP wave spectrum with a root mean square wave height (H) of 1.4 m, a peak period of 10 s and a 10° angle of incidence. The barotropic and baroclinic time steps used are 0.16 and 5 s, respectively. Effects of wave rollers, wave breaking induced mixing and bottom streaming are not included for this simulation, which is consistent with Kumar et al. (2011a), HW09 and U10.

Uchiyama et al. (2009) showed that in the presence of wave and current fluctuations, the mean continuity balance at steady state can be integrated in the cross-shore direction to yield a balance between barotropic Eulerian mean and Stokes velocities (i.e., $\overline{u} = -\overline{u^{St}}$). This information along with the wave parameters and dissipation due to wave breaking (ϵ^b) can be used to solve for sea-surface elevation and barotropic longshore velocity using the following approximate equations:

$$\begin{aligned} \frac{\partial \zeta^c}{\partial x} &= -\rho g h \left[\frac{\partial S_{xx}}{\partial x}\right] - \rho c_d \left|\mathbf{V}\right| \overline{u} \\ \rho c_d \left|\mathbf{V}\right| \overline{v} &= \frac{\partial S_{xy}}{\partial x} = \frac{\epsilon_b k_y}{\sigma} \end{aligned} \tag{3.49}$$

where $|\mathbf{V}|$ is magnitude of the barotropic velocity vector, while S_{xx} and S_{xy} are onshore and longshore components of onshore radiation stress.

The results from the VF model simulation are compared to the analytical solutions of ζ^c and $\overline{v}$ obtained using Eqn. 3.49, with a c_d value identical to that used in the numerical simulation, as well as to results from the depth-averaged, Lagrangian, radiation stress based model presented in Warner et al. (2008a, hereafter referred to as $\mathrm{RS_{2D}}$). In the latter model the wave forcing was provided as depth-averaged radiation stress (i.e., similar to Longuet-Higgins, 1970a and b).

Wave Parameters and Sea-surface elevation

Figures 3.1a and b show the wave height, depth-induced dissipation and sea surface elevation. Wave shoaling occurs in the region 500 to 1,000 m; inshore of this region the waves start breaking in the depth-limited environment (Fig. 3.1a). Depth-induced dissipation (ϵ_b, Fig. 3.1b) remains zero during wave shoaling. Inshore of x= 500 m, ϵ_b increases monotonically to a maximum value of 0.07 m^3s^{-3} at x= 300 m, and then decreases gradually to zero at the shoreline. This depth-induced wave dissipation is the wave forcing which contributes to the momentum flux (Eqns. 3.34 and 3.13), leading to creation of longshore currents. Estimates of ζ^c from VF, RS_{2D} and the analytical solution (Eqn. 3.49) are in close agreement as shown in Figure 3.1b, with a slight difference at the coastline most likely due to lateral mixing or friction. Outside the surf zone, in the wave shoaling region, the mean sea level decreases (wave set-down), while within the surf zone, the mean sea level increases (wave set-up) as shown in Figure 3.1b.

Nearshore Flows

Vertical variability of Eulerian mean and Stokes velocities from the VF simulation are shown in Figure 3.2. Inside the surf zone (x<500; Fig. 3.2a) the Eulerian mean cross-shore flow is inshore near the surface and offshore directed close to the sea bed. This vertical segregation of the cross-shore flow creates a circulation cell within the surf zone with downward and upward directed vertical velocities (see Fig. 3.2c), consistent with field observations of cross-shore velocity profiles for barred (Garcez-Faria et al., 2000), planar (Ting and Kirby, 1994) and laboratory (Roelvink and Reniers, 1994) beaches. Outside the surf zone the velocity is weakly offshore throughout the entire water column. These results are also consistent with U10, regardless of the differences in turbulence closure schemes and vertical distribution of wave dissipation. Depth-averaging the cross-shore Eulerian mean velocities shown in Figure 3.2a, we obtain

velocities (Fig. 3.2g) that are equal in magnitude and opposite in sign to the depth-averaged Stokes velocity. This balance is indicative of a steady state solution achieved by the model and mass flux conservation.

The longshore velocity (Fig. 3.2b) attains its maximum value of approximately -1 ms^{-1} at x= 250 m and decreases to zero at the coastline and towards offshore. Vertically, the velocity shows maximum value at the surface and slightly lower values near the sea bed. Depth averaging these velocities, we find that the maximum alongshore velocity from the VF simulation is further inshore in comparison to the analytical solution, which shows a maximum value at x= 300 m, at the same location as the maximum ϵ_b (Fig. 3.1b). This difference is mainly due to the inclusion of vertical viscous mixing, horizontal advection and VF leading to spreading and distribution of the momentum flux in the surf zone, something not included in the simplified analytical solution of Eqn. 48. Comparison to results obtained by RS_{2D} simulations are discussed separately in Section 5.

The cross-shore Stokes velocity (Fig. 3.2d) is one and two orders higher than the longshore (Fig. 3.2e) and vertical Stokes velocity (Fig. 3.2f), respectively. Close to the sea surface, cross-shore velocity varies from zero at the offshore boundary to a maximum value of ~ -0.15 ms^{-1} at the location of maximum wave breaking (i.e., x= 300 m), decreasing with increasing water depth. Further inshore of this position, the cross-shore velocity reduces to zero. Longshore velocity is weaker in strength, but shows a distribution similar to that of the cross-shore Stokes velocity. Since the vertical Stokes velocity is calculated as divergence of horizontal mass flux (Eqn. 3.2), at the location of maximum breaking, the vertical Stokes velocity is zero. Inshore of this point, the velocity is positive with a maximum value at the surface, decreasing with increasing water depth. Offshore of the break point, the velocity is negative and downwards directed, with a vertical structure similar to other Stokes velocity

components. The vertical Stokes velocity has similar magnitude (± 0.005 ms^{-1}) but opposite sign to the vertical Eulerian mean flows (Fig. 3.2c).

Three-dimensional momentum balance

The relative contribution of the cross-shore (x) and longshore (y) momentum balance terms are described here, using the nomenclature as shown in Eqns. 3.12 and 3.13 corresponding to acceleration (ACC), horizontal and vertical advection (HA and VA), Coriolis force (COR), Stokes-Coriolis force (StCOR), pressure gradient (PG), horizontal VF (HVF), horizontal and vertical mixing (HM and VM), and breaking and roller acceleration (BA and RA). Though the contribution of vertical vortex force (**K**, Eqn. 3.1) can be analyzed separately as a part of the geopotential function (Eqn. 3.14), in this work we have added it to the HVF term, as its importance is negligible in all the cases discussed here.

In the cross-shore direction (Fig. 3.3), since earth rotation and roller efect were not considered, the RA, COR and StCOR terms are zero. The horizontal advection (HA, Fig. 3.3b), horizontal vortex force (HVF, Fig. 3.3c) and vertical advection (VA, Fig. 3.3f) terms are negligible. The balance is mainly between three terms: BA, VM and PG. Within the surf zone (x<350m), the wave breaking acceleration (BA, Fig. 3.3a) term is the largest with a high value at the sea surface, sharply decreasing to a negligible value below 1 m under the surface. A significant portion of the BA contribution is balanced by a relatively strong vertical mixing (VM, Fig. 3.3e) which is enhanced close to surface layer. At water depths where BA becomes negligible, the VM changes sign and becomes negative. At the location where waves start breaking (i.e., 350 m <x < 500 m), the contribution of pressure gradient (PG, Fig. 3.3d) is negligible, but increases toward the shoreline, with a vertically uniform distribution. Close to the sea surface, both PG and VM terms add to balance the BA contribution while further below the balance is mainly between PG and VM, with the

latter term also becoming vertically uniform. It is important to note that comparing the present momentum balance to that obtained from simulations using models based on depth varying radiation stress (e.g., Kumar et al., 2011a) and quasi-3D models such as SHORECIRC (e.g., HW09) we find that in the VF formulation, the VM term is responsible for vertically redistributing the BA and balancing PG. In the former two models the primary balance occurs between vertically uniform PG and almost vertically uniform radiation stress contribution.

The major terms in alongshore momentum balance are BA, HA, HVF, VM and VA, while PG is negligible. BA (Fig. 3.3g) is dominant only in the surface layer within the wave breaking zone where significant part of it is balanced by the VM term (Fig. 3.3k). Further below the sea surface (> 1 m), VM changes sign from positive to negative, and when added to VA and HVF the sum balances HA (Figs. 3.3h, i, k and l). HA and VA terms (Figs. 3h and l) show opposite signs over the entire water column, which can be attributed to vertical segregation of cross-shore velocity (Fig. 3.2a) and change in the gradient, inshore and offshore of the location of maximum undertow. The HVF term (Fig. 3.3i) is zero at the location of maximum longshore velocity (as $\partial v/\partial \xi$ is zero, see Eqn. 3.13), and has opposite signs on either side of this point. Overall, at locations inshore of the longshore flow maximum (x < 260 m) the sum of BA, HA and HVF is balanced by the sum of VA and VM near the sea surface; close to the bed, the sum of HVF, VM and VA is balanced by HA. Similar balances also occur at locations further offshore (x > 260 m).

Balance of vertically-integrated three-dimensional momentum balance

The vertically averaged cross-shore momentum balance terms (Fig. 3.4a) show a balance between PG and BA similar to that presented analytically by Bowen et al. (1968) for a planar beach. The contribution of the remaining terms (including HVF) is negligible. Vertical integration of the longshore momentum terms (Fig.

3.4b) shows a primary balance between the BStr (vertical integral of VM term, Eqn. 3.21) and the BA terms. A secondary balance occurs between the HVF and the HA terms. The horizontal vortex force (HVF) term is positive seaward of the location of maximum longshore current and becomes negative inshore that location, and the horizontal advection (HA) is of similar magnitude as the HVF but of opposite sign. This secondary balance suggests a balance between Stokes and anti-Stokes (Eulerian mean) flows; however, these terms do not cancel out completely due to differences in vertical structure of Stokes and Eulerian mean flows (see Sec 5).

In the present modeling framework, the terms contributing to the total pressure gradient force ($\nabla\phi$ from Eqn. 3.14 = $\boldsymbol{P^{tot}}$, i.e., gradient of dynamically relevant kinematic pressure), excluding the vertical vortex force ($\mathbf{K}$), can be decomposed into two terms that describe individual contributions from the Eulerian non-WEC ($\boldsymbol{P^{c}}$) and WEC ($\boldsymbol{P^{wec}}$) contributions. The latter can be further divided into a quasi-static response ($\boldsymbol{P^{qs}}$), a Bernoulli head ($\boldsymbol{P^{bh}}$, see Eqn. 5) and a surface pressure boundary correction ($\boldsymbol{P^{pc}}$) (see Table 2):

$$\begin{aligned}\mathbf{P}^{tot} &= \mathbf{P}^{c} + \mathbf{P}^{wec} = (\mathbf{P}^{c}) + \mathbf{P}^{qs} + \mathbf{P}^{bh} + \mathbf{P}^{pc} \\ &= -\nabla_{\perp}\left(g\zeta^{c} + \int_{-h}^{\zeta^{c}} \frac{g\rho}{\rho_{o}} dz\right) + g\nabla_{\perp}\zeta^{c} + g\nabla_{\perp}\,\mathcal{K}|_{\zeta_{c}} + g\nabla_{\perp}\,\mathcal{P}|_{\zeta_{c}}\end{aligned} \tag{3.50}$$

Analysis of the individual components of pressure gradient force (PG, Fig. 3.4c) show that major contribution to P^{totx} is from the non-WEC response of the system to wave breaking, (i.e., P^{cx}). Outside the surf zone, quasi-static response (P^{qs}) and P^{cx} balance each other which cause the wave set-down at this location. The terms corresponding to Bernoulli head and dynamic surface boundary correction are negligible for this planar beach case.

3.4.2 Test Case 2: Obliquely incident waves on a natural, barred beach (DUCK'94 Experiment)

In this test case we simulated wave-induced currents for a natural, barred beach corresponding to the DUCK'94 experiment (Gallagher et al., 1998; Elgar et al., 1997; Feddersen et al., 1998). Simulations are compared to data collected on Oct 12th, 1994, when strong velocities were observed in the surf zone due to waves generated by winds associated with the passage of a low-pressure storm system (Garcez-Faria et al., 2000). During this period, both waves and winds were directed towards the southwest generating a longshore flow down-coast (i.e., towards southeast, see Garcez-Faria et al., 1998).

The measured bathymetry, shown in Figure 3.5a, originates with the shoreline at x=0 and the nearshore bar located near x=130 m. The model domain is assumed alongshore uniform with a cross-shore (x) width of 780 m and a horizontal resolution of 2 m. The water depth varies from 0 m at the shoreline to 7.26 m at the offshore boundary. A tidal elevation of 0.70 m was added to the water level and assumed constant over the simulation period (simulations with tidal variability did not show substantial changes in the model results). The vertical dimension is discretized with 32 equally distributed layers. The boundary conditions are periodic in the alongshore (i.e., north and south boundaries) and closed at the shoreline. At the offshore end we use Flather radiation condition (Flather, 1976) for free surface and Neumann boundary conditions for barotropic and baroclinic velocities (including boundary condition for Stokes velocities). Effect of earth rotation is not included. Bottom stress due to the combined action of waves and currents is estimated using a benthic boundary layer formulation (Madsen, 1994) as described in Warner et al. (2008). Weak horizontal momentum diffusion of the order 0.05 m^2s^{-1} is also applied to obtain smooth solutions. The turbulence closure scheme used is Generic Length Scale (GLS, k-ϵ). Wind stress forcing of 0.25 and 0.16 Nm^{-2} is imposed in the cross-shore and longshore

directions, respectively. Wave forcing is provided by SWAN, which propagates an offshore JONSWAP wave spectrum with a significant wave height of 2.3 m, a peak period of 6 s and a 13° angle of incidence. The model simulation is carried out for a period of 3 hours with a baroclinic and barotropic time stepping of 3.0 and 0.1 s, respectively.

Ten different simulations were carried out in order to identify the behavior of wave rollers and wave-induced mixing. The simulations are designated as Run # (where # is the simulation number) and the differences between individual Runs are listed in Table 3.3. Run 1 is conducted using the two-dimensional (x-y), depth-averaged, Lagrangian, radiation stress based model (RS_{2D}, i.e., no vertical distribution of wave forcing or flows, and the wave forcing is depth-averaged radiation stress contribution as in Longuet-Higgins, 1970a), while for Runs 2 to 10 we use the vortex force formulation as described in this paper (VF). Run 2 does not include the effect of wave rollers and wave-induced mixing. Runs 3 to 6 do include the effect of wave rollers but each run assumes a different fraction (Eqn. 3.34) of depth-induced dissipation (ϵ_b) being used for roller generation. Finally, Runs 7 to10 are used to distinguish the contribution of wave-induced mixing.

Wave parameters and sea-surface elevation

In this section we first examine two runs: (a) Run 1 (radiation stress based, depth-averaged model with no rollers) and (b) Run 2 (baseline experiment using VF model without wave rollers and mixing), to compare the flow pattern simulated by a two and three-dimensional model.

Measured (Elgar et al., 1997) and simulated H are in a close agreement throughout the profile (Fig. 3.5a), despite the fact that the wave solution does not account for the effect of currents (one-way coupling). Depth-limited wave breaking, as exhibited through the wave dissipation (ϵ_b) parameter, takes place predominantly over the bar-

crest and then a second time close to the shoreline (Fig. 3.5b). Over the bar-trough (60 m < x < 100 m), the wave dissipation is negligible, as shown by the relatively stable wave height along this region (Fig. 3.5a).The overall trend of sea-surface elevation (ζ^c) for both Runs 1 and 2 is a wave set-down outside and wave setup inside the surf zone (Fig. 3.5b). At the bar-crest and further shoreward, ζ^c from Run 1 shows a continuous increase, unlike Run 2, which suggests slight decrease at these locations due to dominant contribution of Bernoulli head (see section 3.5).

Nearshore Flows

The cross-shore profiles of depth-averaged, cross-shore and longshore velocities from Runs 1 (RS_{2D}, no vertical flow distribution) and 2 (VF, no rollers/mixing, vertically averaged velocities) are shown in Figures 3.5c and d. Although the depth-averaged cross-shore velocities from Runs 1 and 2 are identical (Fig. 3.5c), the longshore velocities show significant difference both in terms of cross-shore variability and magnitude (Fig. 3.5d). Strongest longshore velocity from Run 1 occurs at the bar-crest and at locations close to the shoreline, which does not agree with the observations. On the other hand, maximum longshore current from Run 2 is at a location inshore of the bar-crest, and is in better agreement with measured velocities. This inshore shift of the maximum longshore current is due to vortex force and mixing due to shear, details of which are provided in section 3.2.7 and 3.5.

Effect of wave roller

Wave roller generation is controlled through the parameter α_r, which defines the fraction of wave dissipation allowed to act as the source term in the roller evolution equation (Eqns. 3.35, 36 and 38). When α_r=0, no wave rollers are included, while when α_r=1 the total of the depth-induced dissipation (ϵ_b) is used as a source for the

creation of wave rollers. The roller dissipation is calculated empirically (Eqn. 3.38) which contributes to roller acceleration in the momentum balance along with breaking acceleration (Eqn. 3.39). Five simulations with no wave-induced mixing and α_r values of 0.25, 0.5, 0.75 and 1 (Runs 2 to 6, respectively, see Table 3) were carried out and the total dissipation ($=(1-\alpha_r)\epsilon_b + \epsilon_r$) for each run is shown in Figure 3.6a. When α_r=0, maximum depth-induced dissipation is observed at the bar-crest and close to the shoreline. As the value of α_r increases, the contribution of breaking dissipation decreases and the contribution of roller dissipation increases. The advection of wave rollers with a speed equal to the phase speed of the surface gravity waves leads to an onshore movement of the total dissipation peak (Fig. 3.6a). For α_r=1, the total dissipation decreases at the bar-crest and close to the shoreline, and increases in the bar-trough region, providing a wider distribution of the energy lost by breaking waves. Physically this mechanism modifies the setup in the transition zone (Nairn et al., 1990), creates a delay in the transfer of energy from wave breaking to the mean flow (Reniers and Battjes, 1997; Ruessink et al., 2001) and accounts for the associated mass flux in the direction of wave propagation (Svendsen, 1984). In the next three sub-sections we describe the physical impact of wave rollers in modifying the cross-shore profile of barotropic flows, cross-shore profile and vertical structure of cross-shore and longshore current, vertical profile of eddy viscosity and turbulent kinetic energy. The simulated flows are also compared to field measurements of cross-shore and longshore velocities.

In absence of any other forcing mechanism and under steady state conditions, the vertically averaged Stokes flow is balanced by an opposing Eulerian mean flow (Uchiyama et al., 2009). In absence of wave rollers (Fig. 3.6b) this flow is strongest at the location of wave breaking (i.e., bar-crest and at the shoreline). As the contribution of wave rollers increase, the rollers contribute an onshore directed mass flux, leading to a stronger return flow in the offshore direction (Fig. 3.6b). Changes in wave roller

contribution also affect the cross-shore variation of the depth averaged longshore currents (see Fig 6c). When α_r=0 (Run 2), the maximum longshore velocity is predicted just inshore of the bar-crest. Increasing the wave roller delays the transfer of energy from waves to mean flow, leading to a more uniform distribution of flow within the areas inshore and offshore of the bar-trough (80-100 m). When α_r=1, relatively stronger longshore velocity is modeled inshore of the bar-trough.

Simulated profiles of cross-shore and longshore velocity from Runs 2, 4 and 6 (i.e., VF based model with α_r=0, 0.5 and 1, respectively, see Table 3.3) are compared to observations (Garcez-Faria et al., 1998, 2000) at seven different cross-shore locations spanning the region between the bar-trough and crest (Figs. 3.7a and b). The normalized root mean square (rms) errors (defined same way as in Newberger and Allen, 2007b) for each simulation and cross-shore location are listed in Table 3.3.

The observed cross-shore velocities (Fig. 3.7a) show a strong vertical shear at the bar-trough and bar-crest regions, creating a circulation pattern with inshore directed flows at the surface and offshore directed undertow close to the bed. Simulated velocity profiles from Runs 2, 4 and 6 (VF based model with α_r=0, 0.5 and 1, respectively) show similar general pattern. When α_r=0 (Run 2), the velocity shear is strongest over the bar-crest, while when α_r=1 (Run 6) velocity shear increases at the bar-trough region (Fig. 3.7a). It is also shown that the undertow strength increases with an increased roller contribution due to additional return flows generated to compensate for the increased mass flux due to rollers. Overall, Run 6, a case where the entire wave dissipation is converted to wave rollers (i.e, α_r=1), shows the best agreement with the measured cross-shore velocities as revealed by their least rms error values.

The measured longshore velocity is highest in the bar-trough region and gradually decreases on either side (Fig. 3.7b). When the roller effect is not considered (i.e., α_r=0, Run 2), the longshore velocity maximum occurs in the region between the bar-trough and crest (x ~ 110 m). As the roller contribution increases to 50% (i.e.,

α_r=0.5, Run 4), this local maximum is shifted further inshore at x= 100 m (Fig. 3.7b). When the total dissipation is used to generate wave rollers (α_r=1, Run 6), the longshore velocity peak moves inshore to x~ 80 m, with a smoother distribution of velocity in the bar-trough region. Velocity strength over the bar-crest decreases from 0.7 ms^{-1} for α_r=0, to 0.5 ms^{-1} for α_r=1. The offshore velocity (x > 200 m) values do not change significantly by changing the roller contribution as roller/breaking dissipation offshore of the bar-crest is negligible (Fig. 3.6a).

Interestingly, using the mean normalized rms error from all seven stations, the results from Run 2 (VF model with no effect of rollers/wave-induced mixing) show the best overall agreement with the observations. Considering the variability observed in model performance at different cross-shore locations, it is clear that inclusion of wave rollers provides better agreement of longshore and cross-shore flows at the bar-crest and bar-trough region, but at locations further offshore, simulations with no rollers/mixing effects show a better agreement to observed profiles. These findings suggest that inclusion of processes like wave rollers requires careful definition of the amount of wave-dissipation responsible for driving the wave roller model (i.e., value of α_r). Furthermore, it appears more sensible for this value to be a function of the cross-shore position within the surf zone (see Cambazoglu and Haas, 2011).

The effect of wave rollers on the vertical distribution of vertical mixing (K_v) and turbulent kinetic energy (TKE) is also examined using the same runs as those described in the previous paragraphs. At α_r=0 (Run 2), the strongest velocity shear is observed offshore of the bar-crest (Fig. 3.7a), which corresponds to an increased region of TKE production and increased K_v levels (Figs. 3.7c and d). As the roller contribution increases, the velocity shear at the bar-crest reduces, while an increase in velocity shear further inshore is observed. This is reflected by a decrease in TKE and K_v (Figs. 3.7c and d) at the bar-crest and spreading of the TKE in the region between bar-crest and trough. Subsequently the vertical mixing within the bar-trough region

also starts increasing. Overall, the roller contribution modifies the shear production and associated TKE and K_v, by moving the entire pattern further inshore and dispersing the breaking induced energy transformation more uniformly within the surf zone. It is interesting to point out that the K_v values obtained in the present case are almost twice the magnitude of those used by U10 in their simulations. This occurs because the GLS mixing utilizes the ambient flow field to create the shear production and associated eddy viscosity profiles, while in U10 the K_v values were derived using a K-profile parameterization. These differences in K_v values also explain the small differences between results obtained by U10 and the present work.

Effect of wave-induced mixing

Wave-induced mixing is provided as a surface flux of TKE in the GLS turbulence closure scheme (see Eqns. 3.43-48, also Feddersen and Trowbridge, 2005), controlled by the empirical parameter$c_{\epsilon w}$ that modifies the contribution from the breaking and roller dissipation. Feddersen and Trowbridge (2005) suggested a value of 0.25, while Jones and Monismith (2008) used a value of 0.06 for their simulations. We carried out a limited in scope sensitivity analysis by using $c_{\epsilon w} = 0$, 0.01 and 0.05 for Runs 6, 9, and 10, respectively, all of which correspond to VF model based simulation with roller contribution of α_r=1.0 (see Table 3.3). Simulated profiles of cross-shore and longshore velocity from these runs are compared to field measurements (Figs. 3.8a and b), and the normalized rms errors are shown in Table 3.4. Simulations conducted using a $c_{\epsilon w} = 0.25$ (not shown here) significantly increase the K_v and vertically mix the entire water column, destroying the vertical structure in cross-shore and longshore velocities.

The surface TKE flux increases the total TKE within the water column (Fig. 3.8d), developing a maximum value at the bar-crest and the shoreward boundary

where the total dissipation is greatest. The vertical mixing (K_v) shows a corresponding increase (Fig. 3.8c). When $c_{\epsilon w} = 0$ (i.e., Run 6), K_v values of approximately 0.03 m^2s^{-1} are found over the bar-crest; and for $c_{\epsilon w}$ values of 0.01 and 0.05, these values subsequently increase to 0.05 and 0.06 m^2s^{-1} respectively (Fig. 3.8c). Similar increases in K_v are also seen for locations further offshore of the bar-crest and over the bar-trough.

In general, increasing the surface TKE flux begins to destroy the vertical shear and the associated circulation pattern observed in the cross-shore and longshore velocities (Figs. 3.8a and b). In comparison to Run 6 (VF model with α_r=1.0 and no wave mixing), the simulated cross-shore velocity profiles from Run 9 and 10 (VF model with α_r=1.0, $c_{\epsilon w} = 0.01$ and 0.05, respectively) show higher rms errors at locations within the region between bar-trough and bar-crest, and smaller errors at the station further offshore (see Table 3.4). The comparison of simulated and measured longshore velocity profiles (Fig. 3.8b) suggests that enhanced wave mixing (Runs 9 and 10) reduces the flow magnitude. This reduction deteriorates the agreement of model results to field observations at most of the measurement positions (see Table 3.4). Simulations conducted using α_r=0.5 (not shown here) have shown similar response to that discussed here. We feel this is a typical response in cross-shore and longshore velocity field to increased mixing.

In Figures 3.7a, 3.7b, 3.8a and 3.8b the simulated and measured cross-shore and longshore velocity profiles are compared. Overall, the normalized rms errors obtained in these simulations vary between 0.54 and 0.66 for the cross-shore velocities and 0.20 to 0.3 for the longshore velocities. These values are similar to those of Newberger and Allen (2007b) and at times slightly higher than those shown by U10 (0.42-0.70 and 0.10-0.4 for cross-shore and longshore velocities, respectively). Nevertheless, our simulations show that the model is capable of creating realistic velocity profiles in a surf zone environment. In the remainder of the presentation, we focus on results from

Run 6 (VF model with α_r=1 and no wave mixing) as these simulated profiles show the best agreement to the observed cross-shore and longshore velocity measurements at the majority of the locations.

Cross-shore and Vertical structure of Eulerian mean and Stokes Velocity

The horizontal and vertical distribution of the cross-shore velocity for Run 6 (VF model with α_r=1 and no wave mixing) is shown in Figure 3.9a. As discussed previously, at the location of wave breaking, vertical segregation of flow occurs with an inshore directed flow at the surface and offshore directed flow at the bottom. Maximum strength of this undertow occurs at the bar-crest and close to the shoreline, while relatively weaker values are found in the bar-trough. Outside the surf zone, flow through significant part of the water column is directed offshore with a maximum flow at the bottom layer, decreasing monotonically to a small onshore directed value at the sea surface (Fig. 3.9a). Maximum longshore velocity (Fig. 3.9b) occurs over the bar-trough with a smooth variation in the trough-crest region due to the effect of wave rollers. The strongest flow occurs at the surface, decreasing with an increase in the water depth. Further offshore of the bar-crest, longshore velocity decreases significantly, and most of the modeled longshore flow is wind driven. The vertical velocity (Fig. 3.9c) is directed downwards inshore of the bar-crest and upwards offshore of the bar-crest (x=130m). This pattern along with inshore flows at the surface and offshore directed flow in the center of the water column creates an anticlockwise circulation cell pattern which is similar to that found in the planar beach case presented in section 3.1 (see Fig. 3.2c).

The vertical distribution of wave-induced Stokes drift follows a $\cosh(2kz)$ distribution, with strongest flow near the surface and weakest flow near the sea bed.

Maximum cross-shore and longshore velocities occur over the bar-crest and at very shallow waters further inshore (Figs. 3.9d and e). The cross-shore velocity is stronger than the longshore velocity, while the vertical Stokes velocity (Fig. 3.9f) is of similar strength as its Eulerian mean counterpart. As the flux divergence of longshore and cross-shore Stokes velocities is zero over the bar-crest, the vertical Stokes flow changes sign at this point. The upward and downward flow structure in the present case is opposite in sign to Eulerian mean flows (Fig. 3.9c). Presence of a vertical structure in water depth < 1m, also confirms presence of a vertically varying VF.

Three-dimensional momentum balance

The cross-shore and vertical variation of momentum balances for the VF simulation with wave roller action enabled (α_r=1) and no wave mixing (Run 6) is shown in Figure 3.10. In the cross-shore direction the horizontal momentum balance (see Eqns. 11 and 12) is dominated by the roller acceleration (BA, Fig. 3.10a), pressure gradient (PG, Fig. 3.10d) and vertical mixing (VM, Fig. 3.10e). The horizontal advection (HA, Fig. 3.10b), horizontal vortex force (HVF, Fig. 3.10d) and vertical advection (VA, Fig. 3.10f) terms are insignificant. The BA is surface intensified (Fig. 3.10a) with strongest values occurring at locations where total wave dissipation is maximum. At the surface layer, the BA is balanced by the sum of VM and PG (Figs. 3.10a, c and e), while further below (D > 1 m), BA becomes negligible and PG is balanced by VM (Fig. 3.10e). Similar balance is also observed at the shoreward boundary. This cross-shore momentum balance is similar to that observed for the planar beach example in section 3.1.3.

Analysis of the longshore momentum balance shows that with the exception of PG all remaining terms (i.e., BA, VM, HA, VA and HVF) are significant. The sum of BA and HA terms (Figs. 3.10g and h) is balanced by the sum of VM, VA and HVF (Figs. 3.10k, h and l, respectively). BA (Fig. 3.10g) is strongest in the surface

layer over the bar-crest/trough region and near the shoreline and balanced primarily by the HVF term (Fig. 3.10i). It is noticeable that at these locations of strong BA contribution, VM takes its smallest values. However near the surface and in the region between the bar-crest and shoreline, the VM term becomes more significant. In addition, near the bed the VM term is largest over the bar-crest and together with HVF (Fig. 3.10i) balance HA (Fig. 3.10h). It is noticeable that over the bar-crest BA is balanced mainly by HVF, in the absence of a bar (see planar beach case) BA is balanced by VM.

At this stage it is important to point out that a traditional alongshore momentum balance in a radiation stress approach suggests that gradient of radiation stress ($\partial S_{xy}/\partial x$) is balanced by VM (see HW09). In the present case, a summation of HA (Fig. 3.11h), HVF (Fig. 3.11i) and VA (Fig. 3.11i) is small and dominant balance is between BA and VM at most of the cross-shore locations, i.e., similar to radiation stress approach. However, HA and HVF do not completely cancel each other and have a net-contribution in modifying the flow pattern (see Sec. 3.5).

Balance of vertically-integrated three-dimensional momentum balance

The two-dimensional momentum balance in the cross-shore direction (Fig. 3.11a) demonstrates a balance between pressure gradient (PG) and the breaking /roller acceleration (BA) terms. In the longshore direction the major contributors are vortex forces (VF), horizontal advection (HA), breaking accelerations (BA) and bottom stress (BStr), as was the case for a planar beach (Fig. 4b). It is noticeable that due to non-planar variation in bathymetry in this case, the relative contribution of each term is different than that found for the planar beach case, and the HA and HVF (Fig. 3.11b) are not symmetrical anymore.

Decomposing the pressure gradient force into individual components (Eqn. 3.50) shows that the Eulerian response, P_{cx} is the major contributor (Fig. 3.11c). Unlike the

planar beach, the Bernoulli head (P_{bhx}) plays an important role over the bar-crest and further inshore. This occurs because Bernoulli head is dependent upon the velocity shear, and in this example high velocity shear is present in the region between the trough and crest of the bar. The quasi-static response (P_{qsx}) also becomes dominant at the bar-crest and adds to P_{bh}, while the surface pressure boundary correction (P_{pcx}) is negligible.

3.4.3 Test Case 3: Nearshore barred morphology with rip channels

This case investigates the dynamics of a barred beach bathymetry that develops rip currents for normally incident waves. The application is based on a laboratory scale experiment and is similar to a case demonstrated in HW09, with a few major differences: (a) in HW09 the wave driver was a monochromatic wave model (REF/DIF), while here we use a spectral wave model (SWAN); (b) the HW09 domain was identical to the laboratory experiments while our domain has been scaled by a factor of 20 (kinematic similarity, Hughes, 1993) to create more realistic field conditions (similar scale as Aagaard et al., 1997; Macmahan et al., 2005;); and (c) bottom friction due to combined action of waves and currents (Madsen, 1994, also see section 3.2.1) is used instead of a logarithmic bottom drag.

The bathymetry domain (Fig. 3.12a) is an idealized version of that used by Haller et al. (2002) and Haas and Svendsen (2002). The scaling of the domain by a length scale, NL= 20, leads to a maximum depth of 10 m, a nearshore bar of 1.20 m located 80 m off the coastline, cross-shore domain width of 292 m and alongshore length of 524 m. To avoid interaction of rip channel flow with the lateral boundaries, the domain was extended laterally by 80 m in either direction. Rip channels are spaced 184 m apart and the channel width is 36.4 m which makes the ratio of channel width to rip current spacing 0.2, a value consistent with those found in the field (e.g., Huntley and Short, 1992). The model grid has a horizontal resolution of 2 m in both

directions and consists of 20 equally spaced sigma layers. The boundary conditions at shoreline, offshore boundary and lateral ends are no flow conditions (i.e., closed boundary conditions at the coast, lateral boundaries and offshore) and are the same as the laboratory experiments of Haller et al., (2002). Since the effect of wave rollers is important in a surf zone environment (see section 3.2.2), we use a α_r=0.5 to allow for 50% contribution of roller acceleration to momentum balance. In order to maintain realistic conditions, enhanced mixing due to wave breaking is also considered with a $c_{\epsilon w}$=0.02.

At the offshore boundary, SWAN is forced with 1.0 m waves (H_{sig}) with peak period of 6.3 s, and directional spreading of 8° propagating perpendicular to the shoreline. From these values, SWAN computes a wave spectrum based on a JONSWAP distribution. The spectral resolution is 20 frequency bands in the frequency range between 0.04 Hz and 1 Hz, and 36 directional bins of 10° each from 0° to 360°. A depth induced breaking constant of γ_b=0.6 is chosen to account for depth limited wave breaking (Battjes and Janssen, 1978; Eldeberky and Battjes, 1996), while the eddy viscosity model of Madsen (1988) for bottom friction induced wave attenuation is used with a bottom friction roughness length scale of 0.05 m. Because of the high spatial resolution of the domain a time step of 0.5 s is used for both ROMS and SWAN [3] while the coupling between the two models takes place every 5 s. Comparisons are shown after 1 hour of simulation time. In order to make our results comparable to those presented in HW09 and Kumar et al. (2011a) a relatively higher horizontal mixing coefficient (0.20 m^2s^{-1}) has been used that leads to relatively stable

[3]A time step of 0.5 s leads to a CFL number of ~1. Trial runs with larger time steps in SWAN (1, 2, 3 and 5 s) when compared with the 0.5 s time step run revealed overall RMS differences in wave height of 0.34, 0.83, 0.81 and 0.66% respectively, while the RMS difference in vorticity was 0.009, 0.013, 0.021 and 0.044% respectively. These differences become larger for smaller water depths (1.12, 2.30, 2.23 and 1.96% for wave height and 0.031, 0.045, 0.072, and 0.16 for vorticity for water depths less than 0.5m) This suggests that although the internal limiter in SWAN (Ris, 1999) is effective in making the wave model stable, it does not completely eliminate inaccuracies in the wave results due to large time steps, but the overall differences are found to be relatively small.

flows. The ability of the model to simulate the unstable character of rip currents (e.g., Haas and Svendsen, 2002) is demonstrated through the presentation of a case where a lower, more realistic horizontal mixing coefficient is used (0.05 $^{2}s^{-1}$).

Wave parameters and sea surface elevation

At the rip channel locations, wave - rip current interaction (Fig. 3.12b) causes a local increase of wave steepness. Greater water depths at the channel locations allow for further inshore propagation of these incoming waves, which finally start breaking at x~ 50m. On the other hand, waves propagating over the bar start breaking at x~70 m, become stable (25 m < x < 65 m) and then break again near the shoreward boundary (x < 25 m). The difference in wave breaking pattern over the channel and the bar creates a lateral difference in breaking induced wave set-up at these two locations.

Nearshore Flows

Differences in sea surface elevation due to wave set-up drive mean flow patterns. Higher wave-setup at the bar than the channel creates "feeder" currents directed towards the latter which results in a confluence of flow from both sides leading to the development of the outgoing rip current (Fig. 3.12c). Close to the shoreline, the wave set-up pattern reverses, as the larger waves within the rip channel break further inshore; this creates a higher wave set-up inshore of the channel in comparison to locations inshore of the bar. The waves in the latter location have already dissipated due to wave breaking over the bar. This wave-setup gradient causes alongshore flows inshore the bar, directed away from the channel (see Fig. 3.12c). Overall a primary circulation pattern develops with outgoing feeder currents from the rip channel and return flow over the bar, and a secondary circulation pattern close to the shoreline, with inshore flows directed towards the shoreline and longshore velocity directed away from the rip channel (Fig. 3.12c). Further offshore, the strength of the rip current

gradually decreases until it becomes negligible. These simulated results are consistent with the laboratory studies conducted by Haller et al. (2002), Haas and Svendsen (2002) and the modeling work of Haas et al. (2003), Yu and Slinn (2003) and Kumar et al. (2011a). Flow vorticity vector contours (Fig. 3.12c) show two vortex patterns inshore and offshore of the rip channel, corresponding to the secondary and primary circulation patterns, respectively. Each vortex pattern consists of a pair of vortices of opposite signs, suggesting opposite circulation tendencies.

Vertical profiles of Eulerian mean cross-shore velocities in the rip channel and over the bar are shown in Figures 3.13a and b, respectively. At locations inshore of the rip channel (x < 40 m, Fig. 3.13a) the flow is directed inshore from surface layer to the middle of the water column, while weak offshore directed flow is seen at the bottom layer. Inshore flow is strongest at the surface (~0.3 ms $^{-1}$) and decreases with depth. Within the rip channel and further offshore (40 m < x < 100 m) the flow is directed seaward. Strongest offshore directed flow (of the order of 0.7 ms^{-1}) occurs over the rip channel at x ~ 70 m and close to the middle of the water column with a monotonic decrease in magnitude with increasing or decreasing water depth. Inclusion of horizontal viscous mixing and wave-induced enhancement in mixing reduces the horizontal and vertical shear in velocity by dispersal of momentum, providing smoother solutions. In comparison to flows observed within the rip channel, the flow field is relatively weaker over the bar (Fig. 3.13b). Wave breaking occurs over the bar-crest and at the shoreward boundary. Undertow in the bottom layer with a magnitude of~ 0.3 mstextsuperscript-1 is observed at both breaking locations, while in the surface layer flow is directed towards the shore (Fig. 3.13b). Overall, the velocity profile observed over the bar is similar to that discussed earlier for the DUCK' 94 simulations.

Our scaled numerical experiment conditions correspond to Test B of Haller et al. (2002) and Test R of Haas and Svendsen (2002). We use the results of those lab

experiments to provide a semi-quantitative comparison between the measured and modeled vertical structure of the cross-shore velocity field. For this comparison we use all of the bin averaged velocities from Test R (see Fig. 3.11 in Haas and Svendsen, 2002) and for all reported locations (Fig. 3.13c). The measured and simulated velocities are normalized by the corresponding maximum cross-shore velocity at the center of the rip channel, respectively. The simulated normalized cross-shore current vertical structure from the model simulation agrees well with the experimental data (Fig. 3.13c and Table 3.5). Inside the channel, rip current speed is greatest just below the level of the bar-crest and decreases toward the surface and bed. However no experimental data are available near the surface. Just offshore the bar, the normalized data from the model simulation show a parabolic profile with stronger velocities at the center of the water column, while the experimental data suggest vertically decreasing magnitude of velocity in the water column. The rms error (normalized by maximum observed value, as in Sheng and Liu, 2011) is small within the rip channel (5.8%, Table 3.5) but increases for locations further offshore (Table 3.5). The overall rms error is 12.7%.

Unstable rip current flow

Rip currents are unstable in nature (Haas and Svendsen, 2002), and processes like vortex propagation and vortex shedding have been observed both in numerical simulations and field experiments (see Yu and Slinn, 2003; Haller and Dalrymple, 2001; MacMahan et al., 2005; Reniers et al., 2009). The importance of these vortices lays in the fact that they interact with the incoming wave-induced Stokes drift and create a strong VF in the longshore direction (negligible in cross-shore direction as v^{St} is almost zero), which may play a relevant part in the maintenance and advection of these vortices.

The dynamics of a barred beach with rip channels for normally incident waves are investigated for the same model domain as in Fig. 3.14, and same offshore wave conditions. Unlike the previous simulation (Sec 3.3), in this case we use a linear bottom drag formulation with a drag coefficient of 0.002 ms^{-1} (Yu and Slinn, 2003) and a horizontal mixing coefficient of 0.05 m^2s^{-1}. Snapshots of vorticity vector and mean flow (Fig. 3.14) show the evolution of flow vorticity over the computational domain. The direction of rip current is at an angle to the rip channel, and its strength changes over time. It is also interesting to see that the vorticity pattern has a periodicity of approximately 60 minutes, which agrees with previous model simulations of rip currents (Yu and Slinn, 2003).

Three-dimensional momentum balance

The three-dimensional momentum balance is presented along a cross-shore and a longshore transect. The cross-shore transect is defined by a line that passes through the center of a vortex (i.e., $y = 180$ m, Fig. 3.12), as this is the region where the VF contribution is most significant. This transect is midway on the slope between the bar and the rip channel. The alongshore transect is at location x=70m and it passes through the center of the rip channel (see Fig. 3.12). The horizontal cross-shore momentum balance has a pattern which is similar to that presented for the planar and barred beach cases. PG, BA, HA and VM are the dominant terms, while HM and HVF are negligible (Figs. 3.15a to f). The BA term becomes important at $x <$ 90 m, a location where wave breaking has just initiated within the rip channel while the majority of the waves break further inshore (Fig. 3.15a). As in the other cases, the influence of BA is limited to the sea surface and is balanced by VM. Since the domain is not alongshore uniform, advection becomes important. This is shown in Fig. 3.15b, where the HA contribution is significant on the shoreward side of the bar and when is added to VM, the sum balances the PG term.

The longshore momentum balance analysis shows that PG, HA, HM, HVF and VM are the important terms while BA (Fig. 3.15g) is negligible. The feeder current developed near the rip channel (Fig. 3.15c) is driven by pressure gradients (PG, Fig. 3.15j) due to differences in wave set-up levels over the bar and the channel location, respectively. This PG term is stronger in the vicinity of the bar and it is balanced predominantly by the HVF term (Fig. 3.15i) which is stronger near the sea surface and decreases toward the sea bed. It is near the bed where the positive values of VM (Figs. 3.15k) add to HVF to balance PG. Near the surface the negative values of VM add to PG to balance HVF. Finally, HA (Fig. 3.15h) is half the strength of PG and has similar magnitude and opposite sign as of HM (Fig. 3.15l).

The longshore variation of the cross-shore momentum terms is shown in Figures 3.16a to f, where it is shown that the terms HA, HM and HVF (Figs. 3.16b, f and c, respectively) are insignificant. The intensity of depth-induced wave breaking over the bar-crest is higher than in the rip channel, except at the center of the channel due to wave focusing by the rip currents. This wave breaking pattern is reflected in the contribution of BA which is stronger over the bar, reduces at the channel sides and becomes strong again at the center of the channel (Fig. 3.16a). PG (Fig. 3.16d) is vertically uniform, and in response to BA it takes high values over the bar; at the channel center it takes values approximately 50% lower while at the channel sides it is further reduced to almost 25% of its value over the bar. Near the sea surface, the sum of VM (Fig. 3.16e) and PG balances BA, while in deeper waters within the channel, PG is balanced predominately by VM.

The longshore variability of the longshore momentum terms is primarily due to HA, PG, HVF, and secondary due to VM and HM. The role of BA (Fig. 3.16g) is relatively insignificant and limited to the surface layer. HA (Fig. 3.16h) is zero at the center of the rip channel as no significant longshore velocity is present at this location. In the region 150 to 170 m, the HA term is positive, while from 170 to

190 m it becomes negative. Two more inflexion points with zero HA are observed at longshore locations corresponding to the centers of the two vortices which are found just outside the rip channel (see Fig. 3.12c). As the sense of rotation of vorticity is opposite about the rip channel center, the sign of HA term changes accordingly (i.e., negative for 130 m $< y <$ 150 m and positive for 190 m $< y <$ 210 m). The PG (Fig. 3.16j) term is vertically uniform and has the opposite sign of HA. It is important to note that PG has the same inflexion points as HA which are created by local changes in alongshore pressure gradient signs. These changes are attributed to different wave set-up levels generated by lateral variation of the wave height and associated breaking processes. Waves break over the bar on either side of the channel but also in the center of the channel at the location of maximum rip current. The latter occurs because wave-current interaction at the center of the channel is responsible for an increased wave height which initiates wave breaking at these larger depths. The HVF term (Fig. 3.16i) takes its maximum value at the locations with the strongest vorticity (Fig. 3.12c) and decreases with increasing water depth. It adds to HM (Fig. 3.16l) and PG to balance HA inside the rip channel, while outside the channel it adds to HA to balance PG. HVF decreases toward the channel and it becomes zero at the channel center. Overall, the HA and HVF together preserve the flow vorticity created due to PG.

3.4.4 Test Case 4: Wave-induced cross-shore flows in the inner shelf

One of the justifications for implementing the VF formalism in COAWST was to develop a modeling system capable of a seamless transition from inner shelf and through the surf zone. Cases presented earlier have focused on surf zone processes and the case presented here aims at the region of shoaling waves outside the surf zone. In a recent study conducted by Lentz et al. (2008), observational data of undertow from MarthaâĂŹs Vineyard Coastal Observatory (MVCO) were used to show a strong

correlation between depth-averaged Stokes drift and undertow outside the surf zone in water depths varying from 5-17 m. Furthermore, in calm wind conditions ($\tau_s <$ 0.03 Nm^{-2}) the profile of inner shelf cross-shore Eulerian mean flow was found to not be parabolic (as it has been found to be inside the surf zone, see Figs 8 and 9); instead a maximum offshore flow was observed at the surface, decreasing towards the bottom. In order to explain the observed velocity profiles, Lentz et al. (2008) presented a basic undertow model consisting of the following forces: (a) Hasselmann wave stress (Stokes-Coriolis force); (b) bottom streaming; (c) surface streaming; (d) Coriolis force; and (e) pressure gradient and wave shoaling.

In simulations conducted for similar conditions, we considered non-breaking waves so that $\mathcal{F}$ consists solely of bottom streaming (see Eqn. 3.22), which is provided as a vertically distributed function (see Eqn. 3.28). The geopotential function ϕ^c contains both pressure gradient and the effect of wave shoaling (see Eqn. 13). Finally, surface streaming (Eqn. 3.29) is provided as a surface boundary condition. Unlike Lentz et al. (2008), we do not impose a no-flow boundary condition at the sea bed, but provide a bottom stress as logarithmic bottom drag with a roughness length of 0.001 m.

The model domain is horizontally uniform with a constant water depth of 12 m. The domain is doubly periodic, with cross-shore and longshore widths of 40 m each and a grid resolution of 10 m in both horizontal directions. Vertically the domain is distributed into 150 layers with enhanced resolution of less than 1 cm close to bottom and surface boundaries. High resolution is necessary to correctly depict the bottom streaming induced forcing (Eqn. 27). Horizontally uniform wave forcing in the form of wave height, period, direction and length is provided. Instead of providing a wall at the inshore boundary, a vertically uniform body force is imposed in the direction opposite to that of wave propagation with strength such that the net Lagrangian mean flow is zero, as in Lentz et al. (2008). This body force emulates the effect

of wave shoaling and pressure gradient. Finally, vertical viscosity values (K_M) are vertically uniform and prescribed for a range of values varying from 10^{-6} to 10^{0} m^2s^{-1}.

Effect of vertical viscosity

The first simulation examines the effect of vertical viscosity on the shape of undertow profiles which are shown in Fig. 3.17a. Inshore propagating, normally incident waves with a significant wave height of 2 m and period 7 s are prescribed over the model domain. K_M values are varied from 10^{-6} to 10^{0} m^2s^{-1}. The results show that when K_M takes values between 10^{-6} and 10^{-4} m^2s^{-1}, the undertow profile has a convex shape with weak offshore/inshore flow at the bottom boundary layer and stronger offshore flow at the surface. For larger K_M values (10^{-3}-10^{-2} m^2s^{-1}), the shape of the undertow profile becomes concave consisting of inshore flow at the bottom layer and stronger offshore directed flow at the upper half of the water column. Closer to the sea surface, the velocity magnitude either remains constant or reduces slightly. For even larger K_M values (10^{-1}-10^{0} m^2s^{-1}) the cross-shore velocity profile becomes parabolic in shape with maximum offshore flow at the middle of the water column and slightly reduced flows at the surface and bottom layers. These vertical profiles are similar to those obtained by Lentz et al. (2008).

Longshore velocity profiles for the different vertical viscosity values used are shown in Fig. 3.17b. For K_M values between 10^{-6} and 10^{-5} m^2s^{-1}, the longshore flows are vertically uniform over the majority of the water column with reduced velocities near the sea surface and bed, while stronger vertical shear is observed for K_M values between 10^{-4} and 10^{-3} m^2s^{-1}. These profiles become vertically uniform and negligibly small for K_M values greater than 10^{-3} m^2s^{-1} (see Fig. 3.17b).

The observed changes in cross-shore and longshore vertical profiles as a function of viscosity can be explained on the basis of Eqns. 3.12 and 3.13. For low K_M values

and assuming normally incident waves, Eqns. 3.12 and 3.13 can be simplified to:

$$\underbrace{-H_z\left(\frac{fv}{mn}\right)}_{\text{COR}} \approx \underbrace{-\frac{H_z}{n}\left.\frac{\partial \phi^c}{\partial \xi}\right|_z}_{\text{PG}} + \underbrace{\frac{H_z \mathcal{F}^\xi}{mn}}_{\text{BtSt}} \tag{3.51}$$

$$\underbrace{H_z\left(\frac{fu}{mn}\right)}_{\text{COR}} + \underbrace{H_z\left(\frac{fu^{St}}{mn}\right)}_{\text{StCOR}} \approx 0 \tag{3.52}$$

Eqn. 3.51 suggests that for cross-shore flows, the higher order momentum balance occurs between the Hasselmann stress (fu^{st}, fv^{st}) and Coriolis force, which creates the observed convex profile for cross-shore flows similar to the shape of Stokes drift. The longshore flow is contingent upon pressure gradient (vertically uniform) followed by bottom and surface streaming contribution due to veering (Lentz et al. 2008). This leads to a vertically uniform longshore flow (Fig. 3.17b) with slightly reduced velocities near the surface and bottom layers.

For higher K_M values the contributions of Coriolis force and Hasselmann stress are negligible so that Eqn. 3.12 can be written as:

$$0 \approx \underbrace{-\frac{H_z}{n}\left.\frac{\partial \phi^c}{\partial \xi}\right|_z}_{\text{PG}} + \underbrace{\frac{H_z \mathcal{F}^\xi}{mn}}_{\text{BtSt}} + \underbrace{\frac{\partial}{\partial s}\left(K_m \frac{\partial u}{\partial s}\right)}_{\text{VM}} \tag{3.53}$$

If bottom streaming is provided as a bottom boundary condition and surface streaming as a surface stress (see Lentz et al., 2008), Eqn. 3.53 takes a quadratic form and can be solved analytically for cross-shore flows. In such case, the vertical profile of cross-shore velocity is parabolic in shape with maximum flow at the center (see Fig. 3.3 in Lentz et al., 2008). Numerical solution of Eqns. 3.12 and 3.13 generate a similar in shape profile (Fig. 3.17a) but with smaller curvature since the flows at the surface and bottom are stronger than those obtained by the analytical solution.

Effect of wave height

In a second set of simulations, the effect of wave height on cross-shore and longshore velocity profiles is examined. These simulated velocity profiles are compared to the data presented in Lentz et al (2008) that represent velocity profiles averaged over a variety of wave heights corresponding to times of minimal wind forcing.

The average significant wave height conditions at MVCO are 1.0 m, with a standard deviation of 0.5 m, and peak wave period varying between 4 and 7 s (Lentz et al., 2008). We chose a set of simulations with a constant $K_M = 10^{-5}$ m^2s^{-1} and a normally incident wave height with values from 0 to 3.5 m with an interval of 0.25 m and a peak period of 7 s. Velocity profiles obtained for each wave height value were grouped together into four groups corresponding to wave height intervals of 0-0.75 m, 0.75-1.5 m, 1.5-2.25 m and 2.25-3.5 m and subsequently averaged. These averaged profiles are shown in Fig. 3.18 together with the published data of Lentz et al. (2008). Since a low[4] K_M value was used, the undertow profiles have a convex shape similar to that of the observations. For waves corresponding to the first three groups, model results closely agree with the reported cross-shore velocity profiles of Lentz et al (2008). These profiles have a weak inshore flow at the bottom boundary and offshore directed flow within rest of the water column (Fig. 3.18a). The decrease in the observed velocities near the surface may be due to measurement errors (i.e., contamination of top bin by surface reflections from the sidelobes of the ADCP acoustic pulses during large waves because of reduced water depth in the wave troughs (Lentz et al., 2008). For the group 2.25-3.25 m, the model predicts undertow flows that are higher than the observed ones. The rms error analysis (normalized by maximum observed data,

[4]In the absence of wind forcing and since the flows discussed here are weak, a low K_M value of 10^{-5} m^2s^{-1} provides best agreement to field observations. Use of a GLS mixing scheme will result in a parabolic K_M with maximum value ($\approx 10^{-3}$) at the middle of the water column. The vertical profile of cross-shore velocity will have a parabolic shape similar to the green and black velocity profiles shown in Fig. 3.17a.

Table 3.6) show small errors for first three groups (21-34%), and higher errors for the last group (48%). Longshore velocity is negligible for small waves (0-0.75 m), and of the order 1-2 cms^{-1} for the second and third wave group. The simulated profiles show similar magnitudes for the first three wave groups, though the vertical structure is slightly different. The model simulated longshore flow for waves $\approx$ 2.25 -3.50 m shows similar shape, but weaker flows than the observed ones (Fig. 3.18b). RMS errors in simulated longshore velocities for first three groups are approximately 50%, while for the last group it is 83% (Table 3.6). The overall errors in cross-shore and longshore velocities are 11% and 29%, respectively.

It is important to note that the observations of Lentz et al (2008) are averaged over varying wave heights and periods, while the model simulations were carried out for a particular set of wave heights and a single period. Furthermore, small differences may also occur due seasonal influences on the velocity profiles (see Lentz et al., 2008). Overall, the observed and simulated cross-shore velocity profiles show similar shapes and magnitude suggesting that the model as implemented in this work can successfully simulate inner-shelf flows under the forcing of waves.

3.5 Discussion

VF and RS representations are two different approaches used to incorporate the effects of surface gravity waves on the mean flow. The VF representation treats the conservative (vortex force, Bernoulli head and quasi-static pressure gradient) and non-conservative processes (breaking acceleration etc.) separately. On the other hand, the RS based approach accommodates wave-averaged effects through the gradient of the radiation stress tensor term. The differences between the two approaches are discussed using simulation results from models based on either representation. In particular, velocity and sea-surface elevation simulated results are first compared, followed by an analysis of momentum balance results.

All sea surface height (ζ^c) simulations (i.e., VF, RS_{2D} and Eqn. 3.49), for the planar beach case, show a similar cross-shore structure (see Fig. 3.1b). Also, the Eulerian mean cross-shore velocity (Fig. 3.2g) is identical for all simulations. Longshore velocity ($\overline{v}$, Fig. 3.2h) from RS2D is strongest at $x\sim$ 300 m, which also corresponds to the location of maximum $\overline{v}$ derived from the analytical solution (Eqn. 3.49); however this location is slightly offshore that of maximum $\overline{v}$ estimated using the VF approach. The overall $\overline{v}$ cross-shore structure slightly differs between the methods, with the analytical solution giving the largest gradients around the maximum point. This difference is mainly due to horizontal viscous mixing in the RS_{2D} solution while for the VF approach this is attributed to horizontal advection and vortex force (see below discussion on momentum balance).

In the barred beach simulations (see Sec. 3.4.2), ζ^c from RS_{2D} (Run 1) and VF (Run 2, no wave rollers/wave mixing) show differences at the bar-crest location and further inshore at the shoreward boundary. These locations correspond to areas with high velocity shear in the cross-shore current profiles (Fig. 3.9a). At these locations the Bernoulli head (Eqn. 3.5) contribution becomes important (see Fig. 3.11c) and modifies the total pressure gradient force, which in turn modifies the ζ^c values. It is important to point out that the radiation stress divergence term is of the same order as the quasi-static pressure gradient (see cross-shore momentum balance) and it cannot resolve wave-averaged effects like the Bernoulli head (see Lane et al., 2007).

The Eulerian, depth-averaged longshore simulated velocities (Fig. 3.5d) using RS_{2D} and VF (with no rollers, i.e., α_r=0, Run 2) differ significantly in terms of cross-shore structure, maximum velocity and location of peak flow. These differences are better explained by the cross-shore variation of the depth-averaged longshore momentum balance terms.

The depth integrated momentum balance for a $\mathrm{RS_{2D}}$ based implementation is (see Warner et al., 2008a):

$$\begin{aligned}&\underbrace{\frac{\partial\left(D\overline{U_\alpha^l}\right)}{\partial t}}_{\text{ACC}}+\underbrace{\frac{\partial\left(\overline{U_\alpha^l}D\overline{U_\beta^l}\right)}{\partial x_\beta}}_{\text{HA}}-\underbrace{fD\overline{U_\beta^l}}_{\text{COR}}=\\&\underbrace{-D\frac{\partial p}{\partial x_\alpha}}_{\text{PG}}+\underbrace{\tau_{s\alpha}}_{\text{SStr}}-\underbrace{\tau_{b\alpha}}_{\text{BStr}}-\underbrace{D\frac{\partial\overline{S_{\alpha\beta}}}{\partial x_\beta}}_{\text{RAD}}\end{aligned}\tag{3.54}$$

where, the subscripts α and β represent the horizontal coordinates, the superscript l denotes Lagrangian mean flows, and the overbar indicates depth averaged values. $\overline{U_\alpha^l}$ and $\overline{U_\beta^l}$ are depth-averaged Lagrangian mean velocities; D is the total water depth, f is the Coriolis parameter, p is the total barotropic pressure, $\tau_{s\alpha}$ and $\tau_{s\beta}$ are surface and bottom stresses, respectively, and $\overline{S_{\alpha\beta}}$ is the depth-averaged radiation stress.

In a similar manner, simplified equations for the VF approach can be obtained from Eqns. 3.12 and 3.13 after removing the curvilinear terms, body forces, horizontal and vertical mixing and using Cartesian coordinates. Adding together the Coriolis and Stokes-Coriolis forces, moving the horizontal vortex force to the left hand side of the equation and vertically averaging, the VF simplified momentum balance equation becomes:

$$\begin{aligned}&\underbrace{\frac{\partial\left(D\overline{U_\alpha}\right)}{\partial t}}_{\text{ACC}}+\left[\underbrace{\overline{\frac{\partial}{\partial x_\beta}(u_\alpha u_\beta)+u_\alpha\left(\frac{\partial u_\alpha^{St}}{\partial x_\alpha}+\frac{\partial u_\beta^{St}}{\partial x_\beta}\right)}}_{\text{HA}}\underbrace{-\overline{u_\beta^{St}\left(\frac{\partial u_\beta}{\partial x_\alpha}-\frac{\partial u_\alpha}{\partial x_\beta}\right)}}_{\text{HVF}}\right]-\underbrace{fD\overline{U_\beta^l}}_{\text{COR}}=\\&\underbrace{-D\left.\frac{\partial\overline{\phi^c}}{\partial x_\alpha}\right|_z}_{\text{PG}}+\underbrace{\tau_{s\alpha}}_{\text{SStr}}-\underbrace{\tau_{b\alpha}}_{\text{BStr}}+\underbrace{D\overline{\mathcal{F}^{w\xi}}}_{\text{BA}}\end{aligned}\tag{3.55}$$

where, $\overline{U_\alpha}$ is the depth-averaged Eulerian mean velocity; u_α and u_β are the three-dimensional Eulerian mean velocities; u_α^{St} is the three-dimensional Stokes velocity; $\overline{\phi^c}$ is the vertically-integrated geopotential function (Eqn. 3.14), and $\overline{\mathcal{F}^{w\xi}}$ is the vertically integrated non-conservative wave forcing. It is important to note that the

VF based model solves for three-dimensional flows, and the Eulerian mean and Stokes velocity based advective accelerations in Eqn. 3.55 (2nd term in left hand side) are vertically-averaged from their three-dimensional distribution. This is not the case for Lagrangian advection (2nd term in left hand side of Eqn. 3.54) in the RS_{2D} based model, where the term is obtained as a function of depth-averaged Lagrangian mean flows.

For the planar beach case (see section 3.1), the vertically-integrated cross-shore momentum balance in the cross-shore direction using VF suggests a balance between PG and BA, while the RS2D results show a balance between PG and divergence of radiation stress (RAD) (Eqns. 3.54 and 3.55) (Figs. 3.19a and 19b). In the shoaling region (800 m > x > 500 m) for the VF approach, the quasi-static pressure gradient (P_{qsx}, Eqns. 3.7 and 3.14), a wave-induced effect, balances the Eulerian pressure response (P_{cx}, Eqn. 3.50, see Fig. 3.4c), which leads to a wave set-down. The total pressure gradient which is calculated as the sum of the individual components (Eqn. 3.49) therefore becomes zero only in the shoaling region (i.e., x > 500 m, see Fig. 3.19a). On the other hand, in the RS_{2D} approach the wave-averaged effect is represented only by the RAD term (Fig. 3.19b) and it is balanced by the cross-shore pressure gradient (PG, only Eulerian pressure response, see Eqn. 3.54; Fig. 3.19c). As the wave energy density changes (i.e., increase during wave shoaling and decrease during wave breaking in the surf zone) the gradient of radiation stress follows these changes obtaining positive values in the shoaling region (i.e., x> 500 m, Fig. 3.18b) which change to negative values inside the surf zone. The positive contribution of radiation stress gradient is balanced by a negative pressure gradient forcing (Fig. 3.19b) and therefore it can be considered representing the forces equivalent to the quasi-static pressure gradient (P_{qsx}, Fig. 3.4c) in the VF representation.

The cross-shore distribution of the longshore momentum balance terms BStr and BA in the VF approach are similar and almost mirror images of each other (Fig.

3.19c). A similar relation is found for the HA and HVF terms although both of them change signs at the location of maximum longshore velocity. However, HA and HVF do not add to exactly zero, with a positive sum seaward of point of maximum v and a negative sum landward of maximum v (Fig. 3.19c) These differences in the cross-shore distribution of HVF and HA leads to a decrease in BStr seaward of maximum v and an increase landward of maximum v, and a corresponding landward shift of the cross-shore profile of longshore velocity. Though the imbalance of HVF and HA may seem to play a minor role in here, in the barred beach case these advective accelerations are important as they modify the cross-shore structure of longshore momentum balance (see below). The RS_{2D} model implements Lagrangian averaging and a part of vortex force is accommodated in the HA term (2nd term in Eqn. 53); thus the only balance observed in this case is between BStr and RAD (Fig. 3.19d).

For the barred beach case (see section 3.2) the cross-shore momentum balance terms outside the surf zone are zero for both VF and RS_{2D} approaches (Figs. 3.20a and b) as no shoaling takes place in this case (see Fig. 3.5a). Within the surf zone, the major balance is between PG and BA for the VF approach and PG and RAD, for the RS_{2D} approach.

The VF and RS_{2D} models suggest major difference in the contribution of dominant terms in the longshore momentum balance for the barred beach. The HVF and HA terms have similar cross-shore structure but different magnitude in the surf zone (Fig. 3.20c). The HVF term becomes significant in the vicinity of the bar, and it has the same structure and order of magnitude (but of opposite sign) as the BA term. On the contrary, the RS_{2D} model still suggests a balance between BStr and RAD (Fig. 3.20d) and zero contribution from HA because the depth-averaged Stokes and anti-Stokes flow (Eulerian mean flow) are of opposite sign and same cross-shore structure. This makes the Lagrangian mean flow ($\overline{U_\alpha^l}$) zero in Eqn. 3.54, leading to no contribution of HA. This is not the case for the vertically-integrated terms from the VF simulations.

In there, although the vertically-averaged Stokes and Eulerian mean cross-shore flows balance each other (i.e., $\overline{u_\alpha^{St}} = -\overline{u_\alpha}$), their vertical structure are significantly different (e.g., see Figs. 3.2 and 9). This difference in structure creates an inequality in the contribution of vertically integrated horizontal advection and vortex-forces (i.e., assuming alongshore uniformity in Eqn. 3.55, $\overline{\frac{\partial(u_\alpha u_\beta)}{\partial x_\beta}} \neq \overline{u_\beta^{St}\left(\frac{\partial u_\beta}{\partial x_\alpha}\right)} + \overline{u_\beta\left(\frac{\partial u_\beta^{St}}{\partial x_\beta}\right)}$, see Fig. 3.20c), which in the present case manifests itself in the form of an inshore shift of the whole longshore flow pattern.

3.6 Summary and Conclusions

The wave-current coupling component of the three-dimensional circulation model ROMS (a public domain model) has been updated with the vortex force formalism presented by MRL04 and U10 and enhanced with a GLS mixing scheme. The modeling system has been applied to study four test cases including littoral velocities in a synthetic planar and a natural, barred beach due to obliquely incident waves, complex flow fields in a synthetic barred beach with rip channels, and validated against undertow profiles in an inner-shelf setting.

The model results for a planar beach show qualitative agreement to laboratory results and field measurements. Simulations for the DUCK' 94 experiment provided close agreement to measured cross-shore and longshore velocity profiles by Garcez-Faria et al. (1998, 2000). Normalized rms error analysis suggests that nonlinear processes like wave rollers and wave-induced mixing are important. Recent studies by Ribas et al. (2011) show that the wave rollers can be important in the evolution of crescentic bars. In this study we used constant values for α_r and $c_{\epsilon w}$ to account for the portion of energy responsible for creation of roller energy, and to identify the portion of wave dissipation responsible for turbulent mixing. It has been shown (Apotsos et al., 2007) that both these processes can be influenced by local beach profile, water depth, wave height, percentage of wave dissipation etc. It is recommended that

instead of using constant values for α_r and $c_{\epsilon\omega}$ over the entire surf zone, spatially varying non-dimensional quantities should be adopted. These should be a function of local cross-shore position and instantaneous wave parameters (see Cambazoglu and Haas, 2011).

Momentum balance analysis shows a primary higher order balance between quasi-static pressure gradient and breaking acceleration in the cross-shore direction, while in the longshore a balance is achieved between bottom stress, breaking acceleration, horizontal advection and horizontal vortex forces. The contribution of vortex force has not been explicitly identified in studies based on radiation stress approach, but results from a depth-averaged, Lagrangian, radiation stress based model (Warner et al., 2008a) suggest that the effect of the vortex force term is implicitly included within the horizontal advection. It is also important to note that when the vertical structure of Stokes and Eulerian mean velocity are different, the contribution of vortex force is not completely balanced by horizontal advection and this can change the magnitude and cross-shore location of longshore velocity, as is observed for the DUCK' 94 simulations.

The simulation for nearshore barred morphology with rip channels clearly demonstrates the ability of the model to reproduce the circulation patterns that have been observed in laboratory studies (Haller et al., 2002; Haas and Svendsen, 2002). Furthermore, within and outside the rip channel area, flow vorticity interacts with the wave-induced Stokes drift leading to strong alongshore contribution of vortex force, which is balanced by the pressure gradient term. The simulated profiles of undertow for conditions outside the surf zone closely agree with measured flows at MVCO. Furthermore, the shape of the profiles varies as a function of vertical viscosity as suggested by Lentz et al. (2008).

Overall, the method of including the surface gravity waves through VF formalism leads to a clear separation of conservative and non-conservative contribution in

the momentum balance equations. The conservative processes are important outside the surf zone, while within the surf zone wave breaking induced flows dominate the momentum balance. This delineation of conservative and non-conservative wave forcing allows implementation of the VF formalism as a tool to evaluate flow fields both within inner shelf and surf zone environments. This application is a significant step in three-dimensional modeling of wave driven flows providing an alternative to models based on the RS approach (see Wang and Chen, 2010; Sheng and Liu, 2011; Kumar et al., 2011a). The VF representation as presented in this paper has been used to study wave-current interaction in a tidal-inlet along with validation against measurements (Olabarrieta et al., 2011) and simulations under a variety of environments are underway.

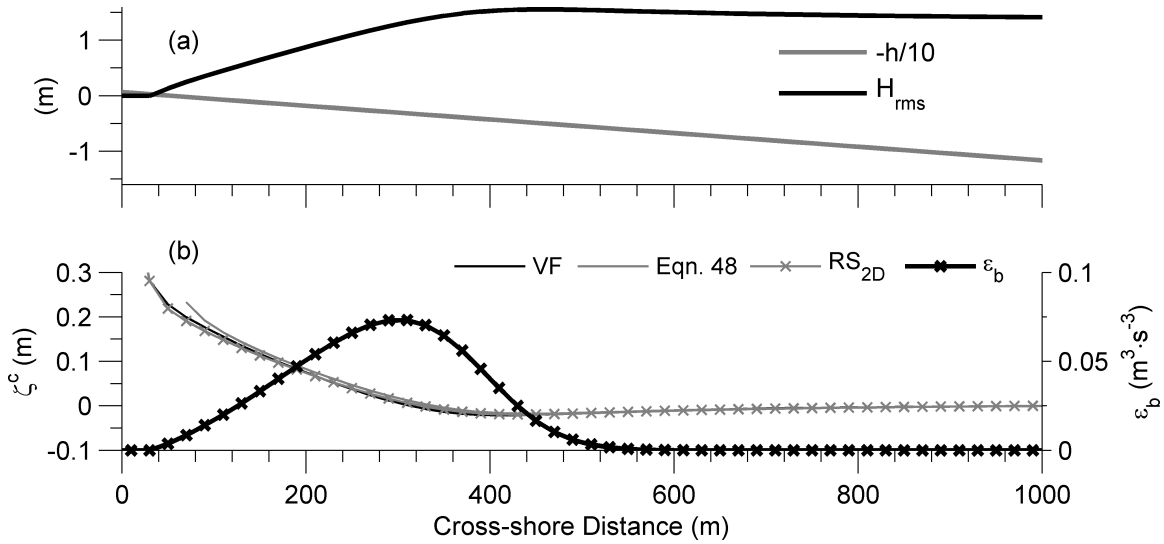

Figure 3.1: Obliquely incident waves on a planar beach simulated using the VF, the RS_{2D} model and analytical solution (see Eqn. 3.49). Cross-shore distribution of (a) root-mean-square wave height (H) and water depth (h); (b) sea surface elevation, ζ^c and depth-induced wave dissipation (ϵ_b).

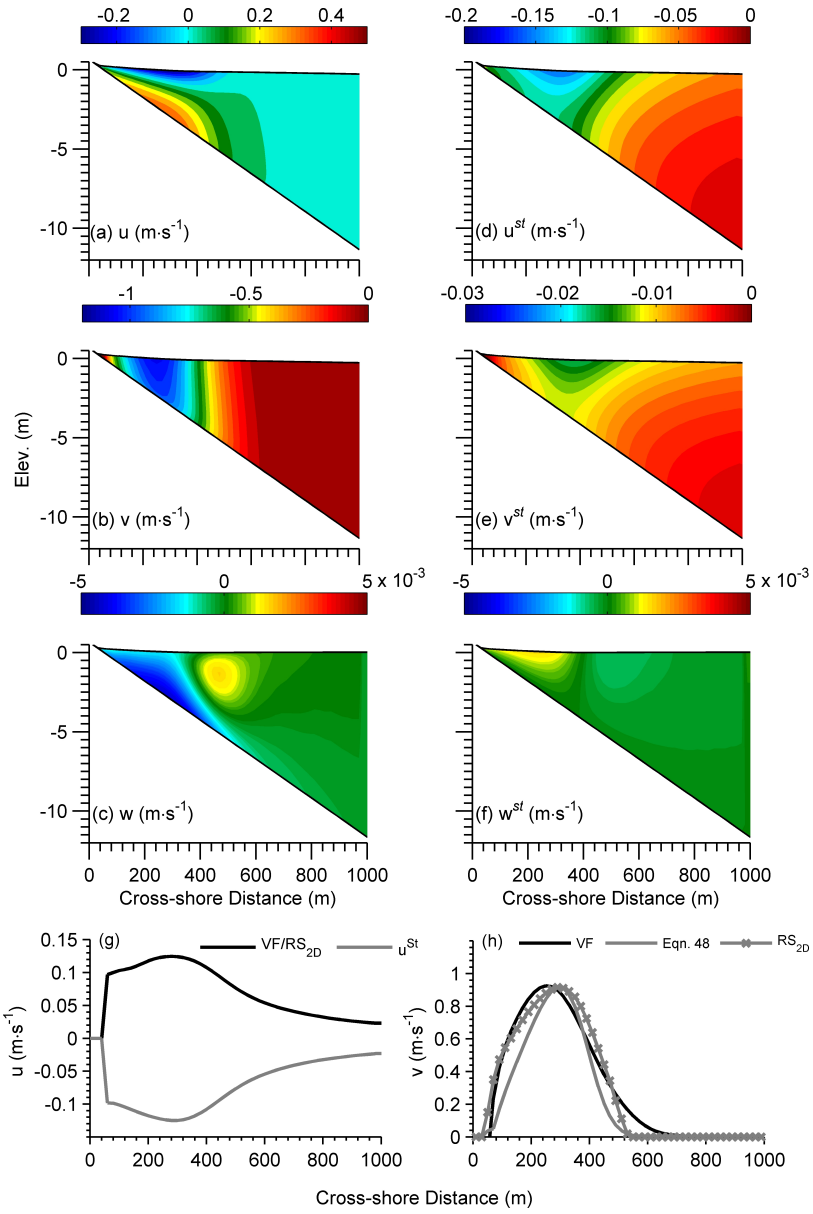

Figure 3.2: Cross-shore sections of Eulerian (a, b and c) and Stokes (d, e and f) velocities from the VF model. (a) cross-shore (u); (b) longshore (v); and (c) vertical (w) Eulerian velocities. (d) cross-shore (u^{st}); (e) alongshore (v^{st}); (f) vertical (w^{st}) Stokes velocities; Cross-shore distribution of (g) depth-averaged, cross-shore Eulerian velocity ($\overline{u}$) and Stokes velocity ($\overline{u^{St}}$); and (h) depth-averaged, alongshore ($\overline{v}$) Eulerian velocity for obliquely incident waves on a planar beach simulated using the VF, the RS_{2D} model and analytical solution (see Eqn. 3.49).

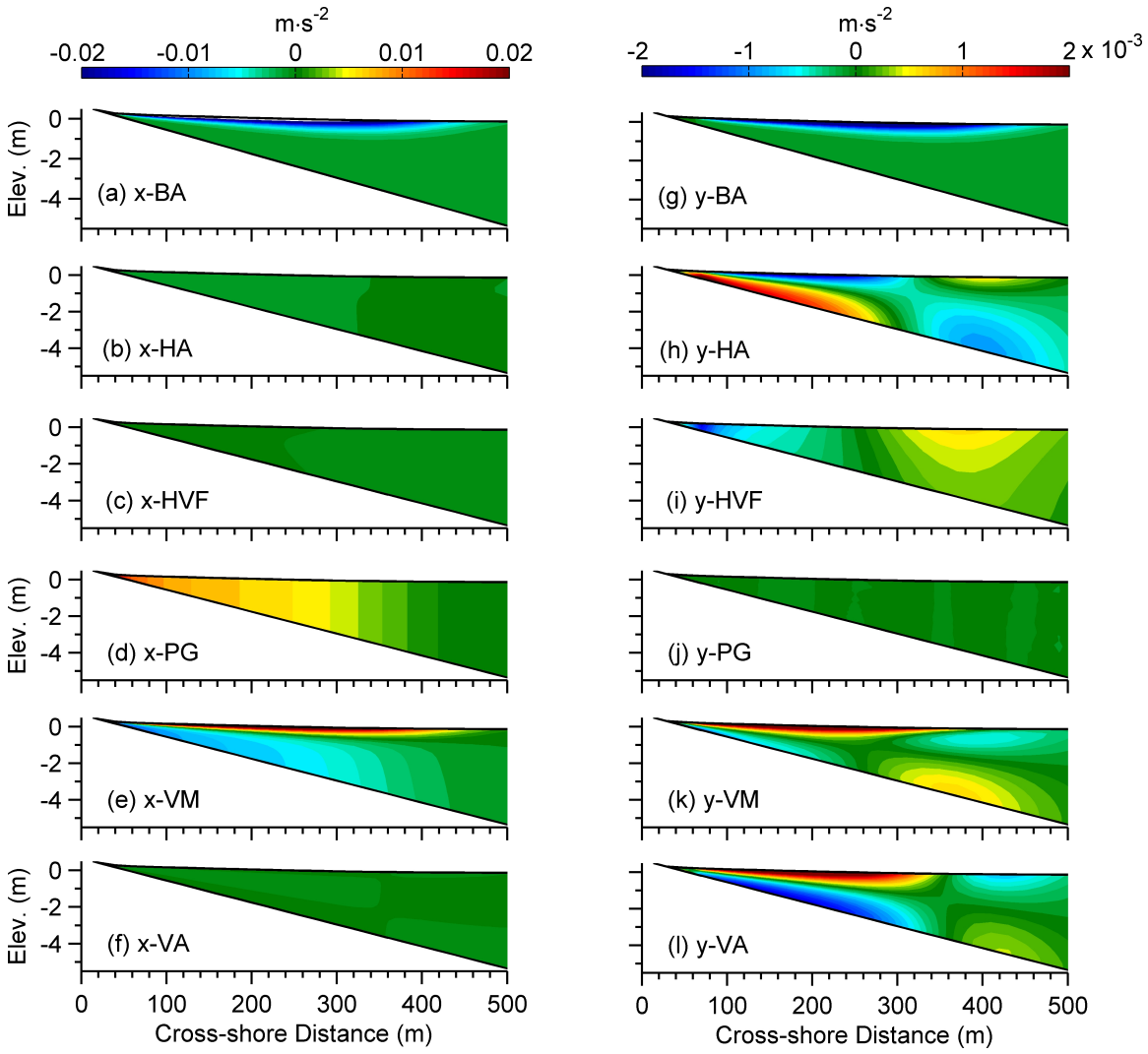

Figure 3.3: Vertical and horizontal cross-shore distribution of the various cross-shore (x) and longshore (y) momentum balance terms. Cross-shore terms: (a) x- breaking acceleration (x-BA) ; (b) x-horizontal advection (x-HA); (c) x-horizontal vortex force (x-HVF); (d) x- pressure gradient (x-PG); (e) x- vertical mixing (x-VM); and (f) x-vertical advection (x-VA); Longshore terms: (g) y- breaking acceleration (y-BA) ; (h) y-horizontal advection (y-HA); (i) y-horizontal vortex force (y-HVF); (j) y-pressure gradient (y-PG); (k) y- vertical mixing (y-VM); and (l) y-vertical advection (y-VA)term.

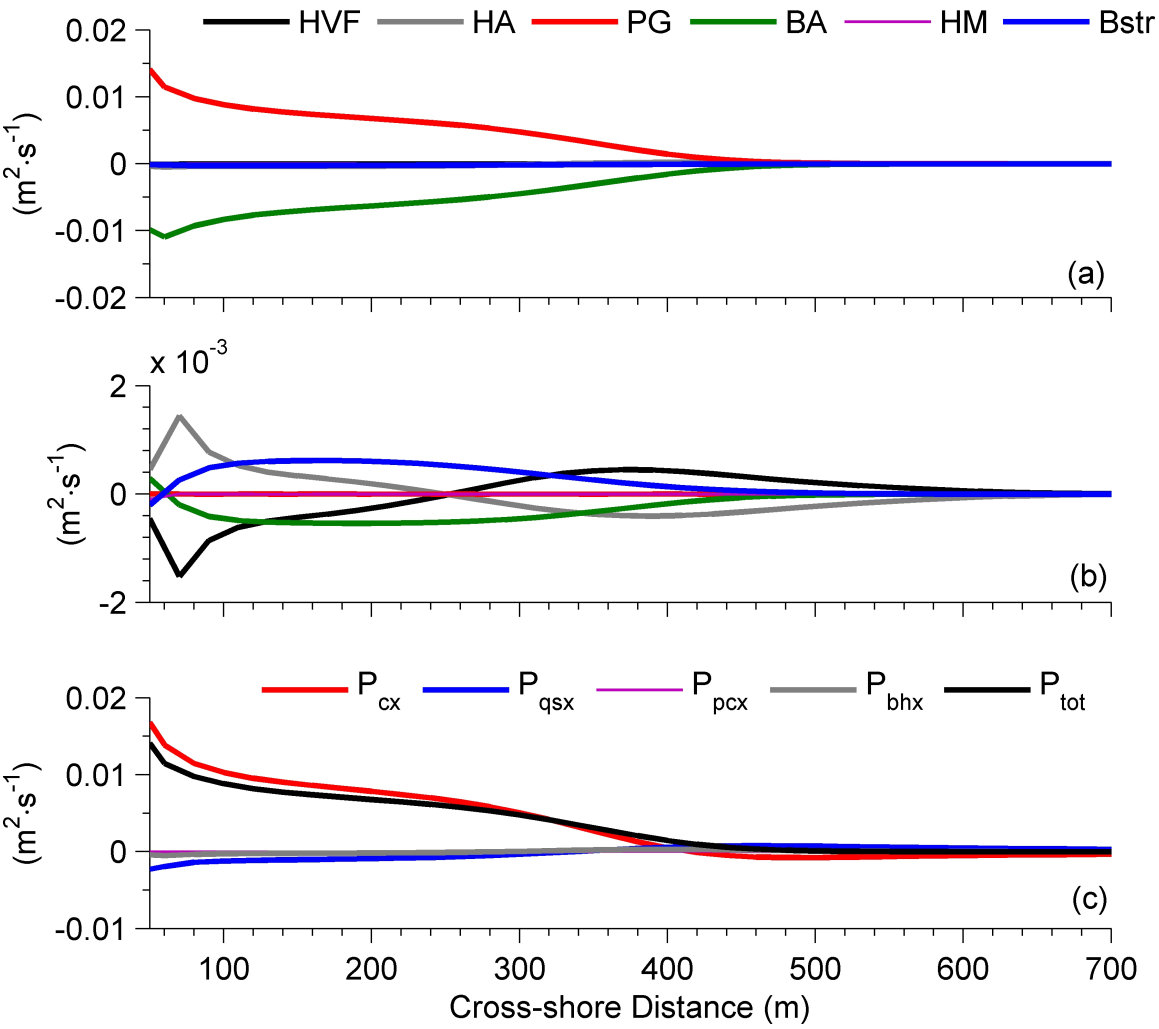

Figure 3.4: Cross-shore variation of depth-averaged (a) cross-shore; (b) longshore momentum balance terms; and (c) decomposed PGF terms in cross-shore as described in Eqn. 3.50.

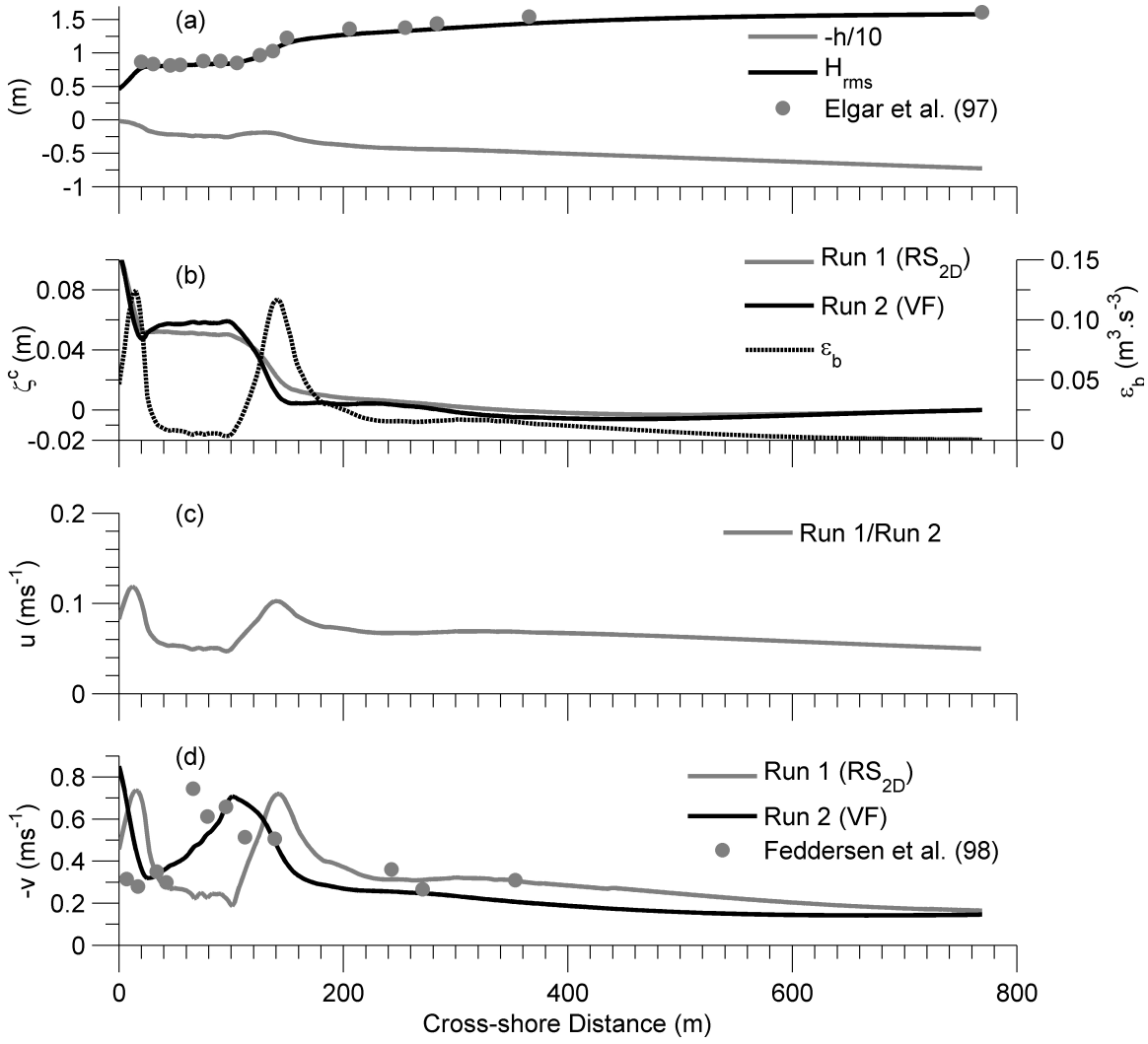

Figure 3.5: Obliquely incident waves on a barred beach simulated using the VF model (no roller model, i.e., Run 2) and the RS_{2D} (Run 1) model (see Table 3.3). Cross-shore distribution of: (a) root mean square wave height (H) from SWAN (solid black line), observed wave height (from Elgar et al., 1997; grey circles) and water depth (h). (b) Sea surface elevation (ζ^c) and depth-induced wave dissipation (ϵ_b). (c) Depth-averaged, cross-shore Eulerian velocity, ($\overline{u}$). (d) Depth-averaged, longshore Eulerian velocity ($\overline{v}$) along with observed velocity (from Feddersen et al., 1998; grey circles).

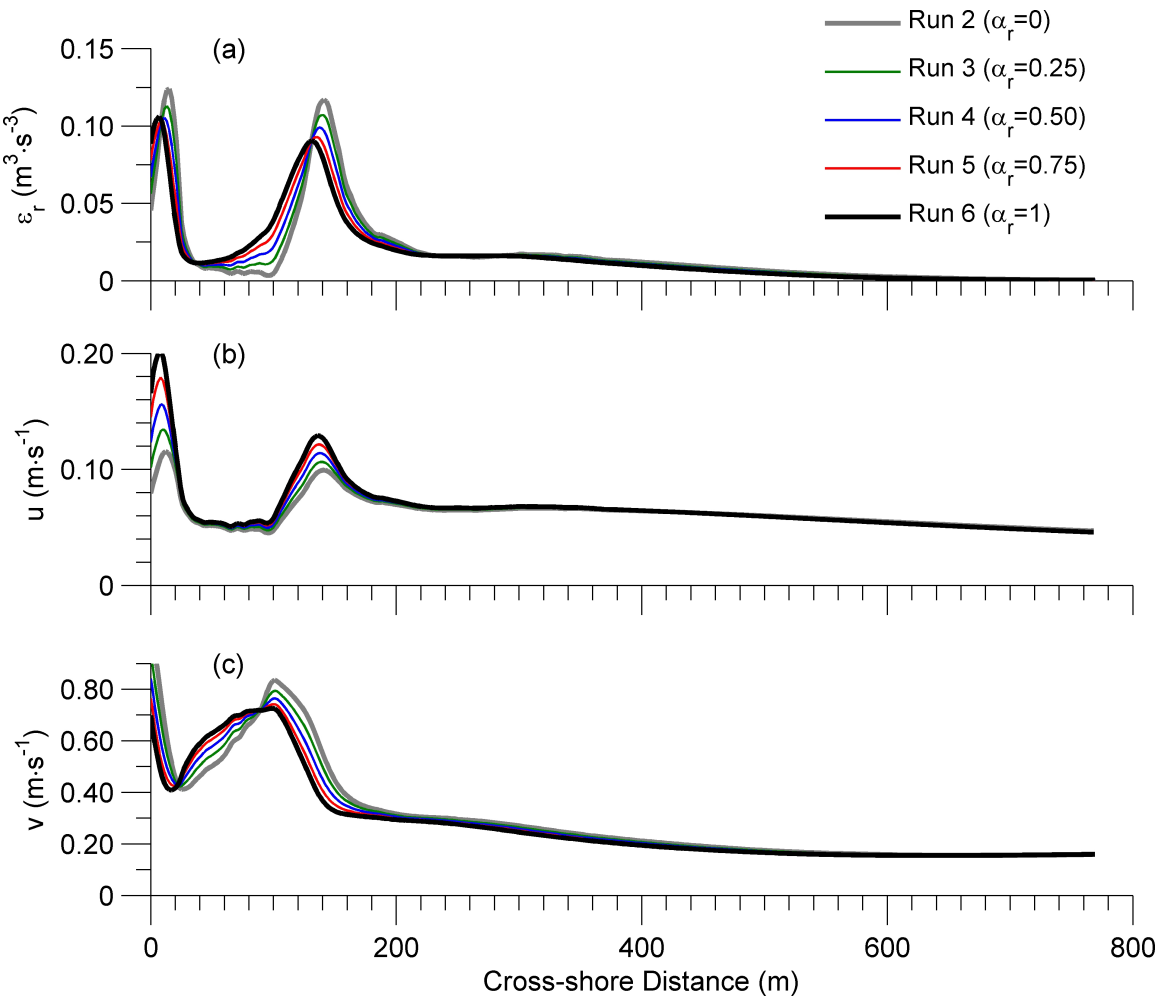

Figure 3.6: Cross-shore variability of (a) total dissipation (breaking + roller dissipation) and depth-averages of three-dimensional (b) cross-shore, $\overline{u}$ and (c) longshore velocity, $\overline{v}$ estimates, for different values of α_r (Runs 2-6, Table 3.3).

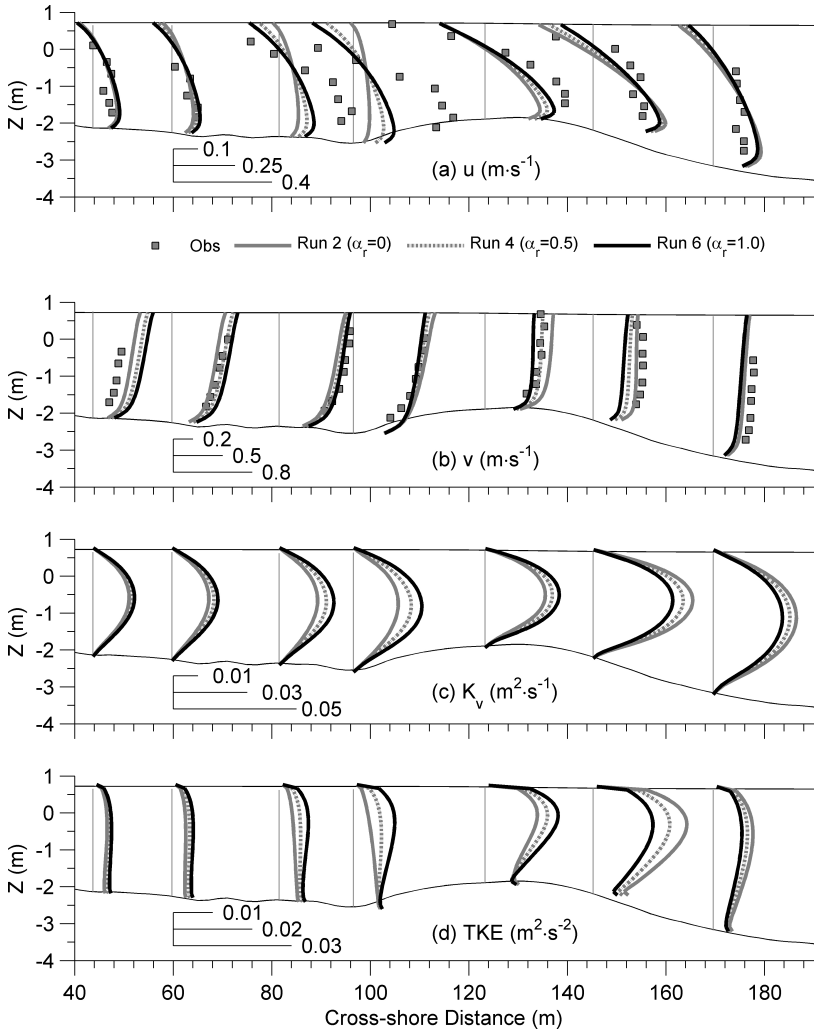

Figure 3.7: Comparison of model results (Runs 2, 4 and 6; i.e., VF model with α_r=0, 0.5 and 1, respectively) with observed vertical profiles (grey squares) of cross-shore (a) and longshore (b) velocities. Vertical grey lines indicate profile measurement locations and zero value for each profile (Data from Garcez-Faria et al. 1998; 2000). Vertical structure of eddy viscosity (c), K_v and turbulent kinetic energy (d), TKE from model simulations at the same cross-shore locations as the velocities.

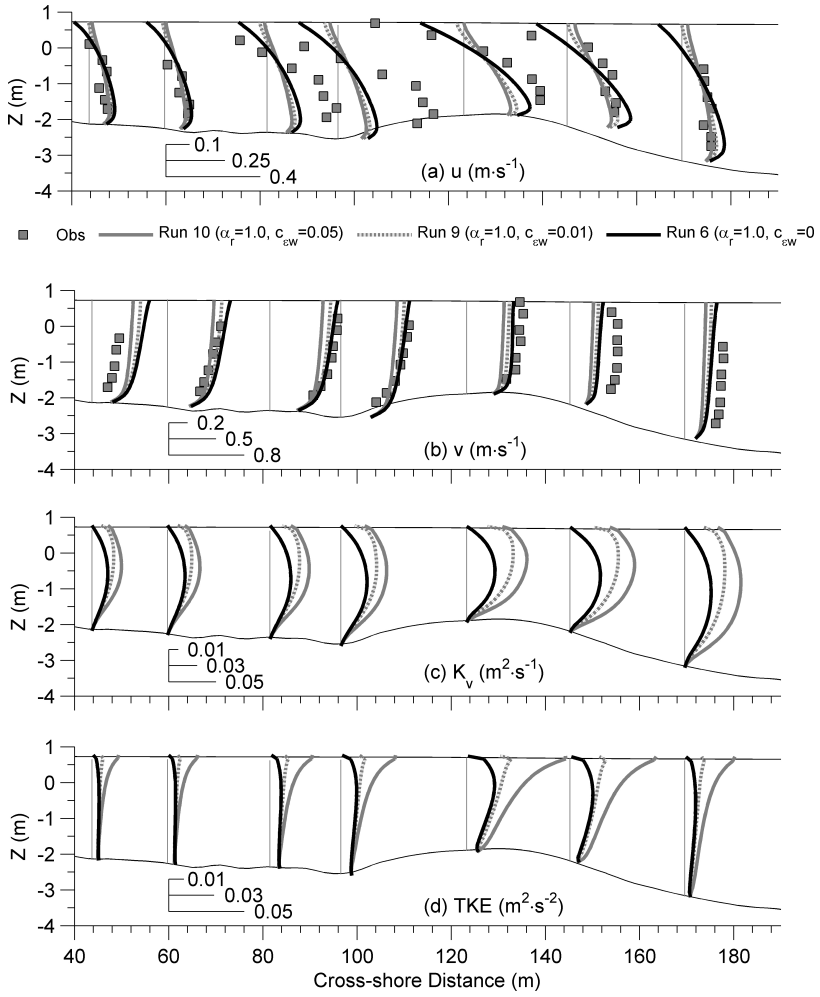

Figure 3.8: Comparison of model results (Runs 6, 9 and 10; VF model with rollers, α_r=1 and wave-induced mixing with $c_{\epsilon w}$=0, 0.01 and 0.05, respectively) with observed vertical profiles (grey squares) of cross-shore (a) and longshore (b) velocities. Vertical grey lines indicate profile measurement locations and zero value for each profile (Data from Garcez-Faria et al. 1998; 2000). Vertical structure of eddy viscosity (c), K_v and turbulent kinetic energy (d), TKE model simulations at the same cross-shore locations as the velocities.

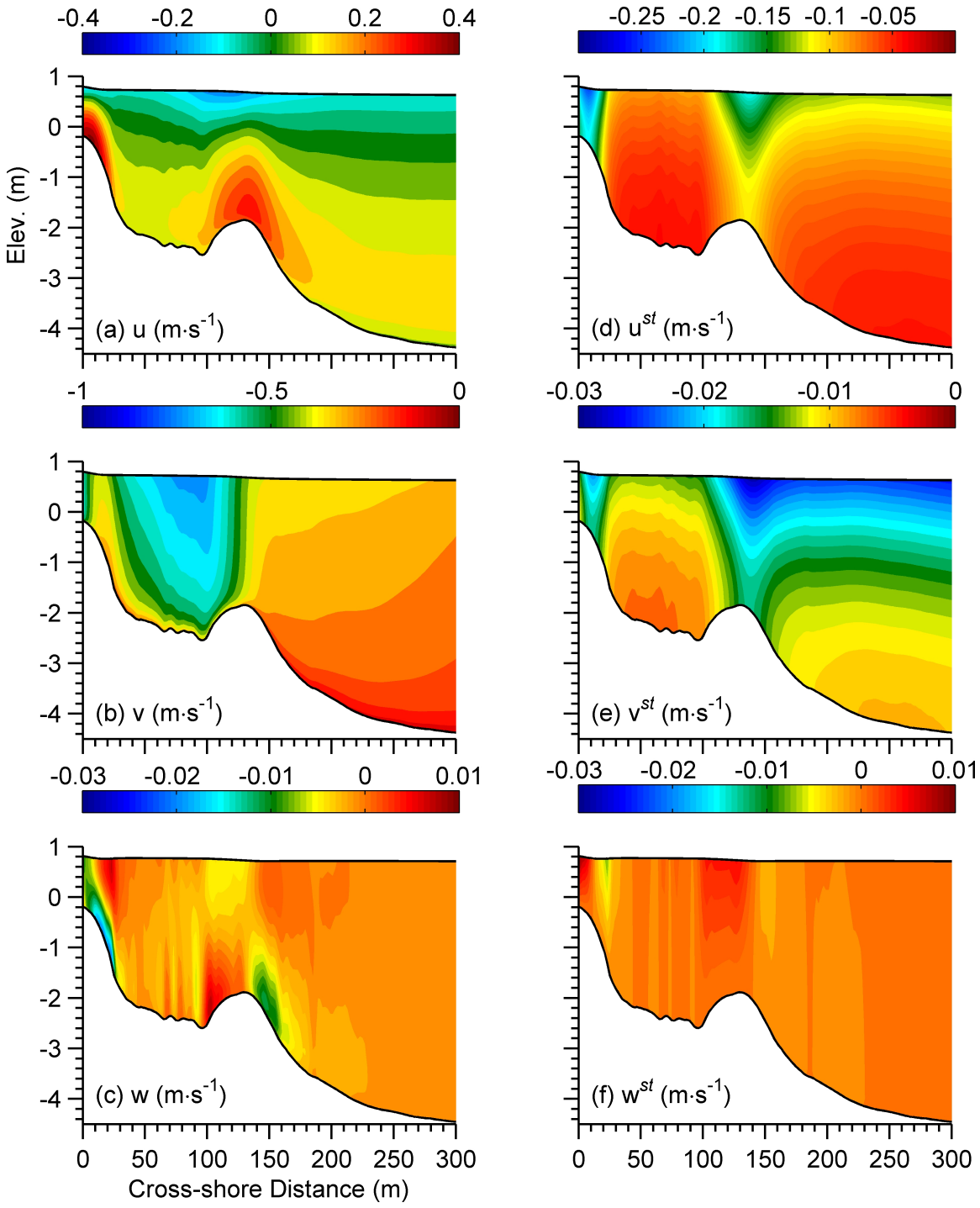

Figure 3.9: Cross-shore sections showing horizontal and vertical variability of Eulerian and Stokes velocity components for Run 6 (VF model with wave rollers, α_r=1 and no wave mixing). (a) cross-shore (u); (b) longshore (v); and (c) vertical (w) Eulerian velocities; (d) Cross-shore (u^{St}); (e) longshore (v^{St}); and (f) vertical (w^{St}) Stokes velocity.

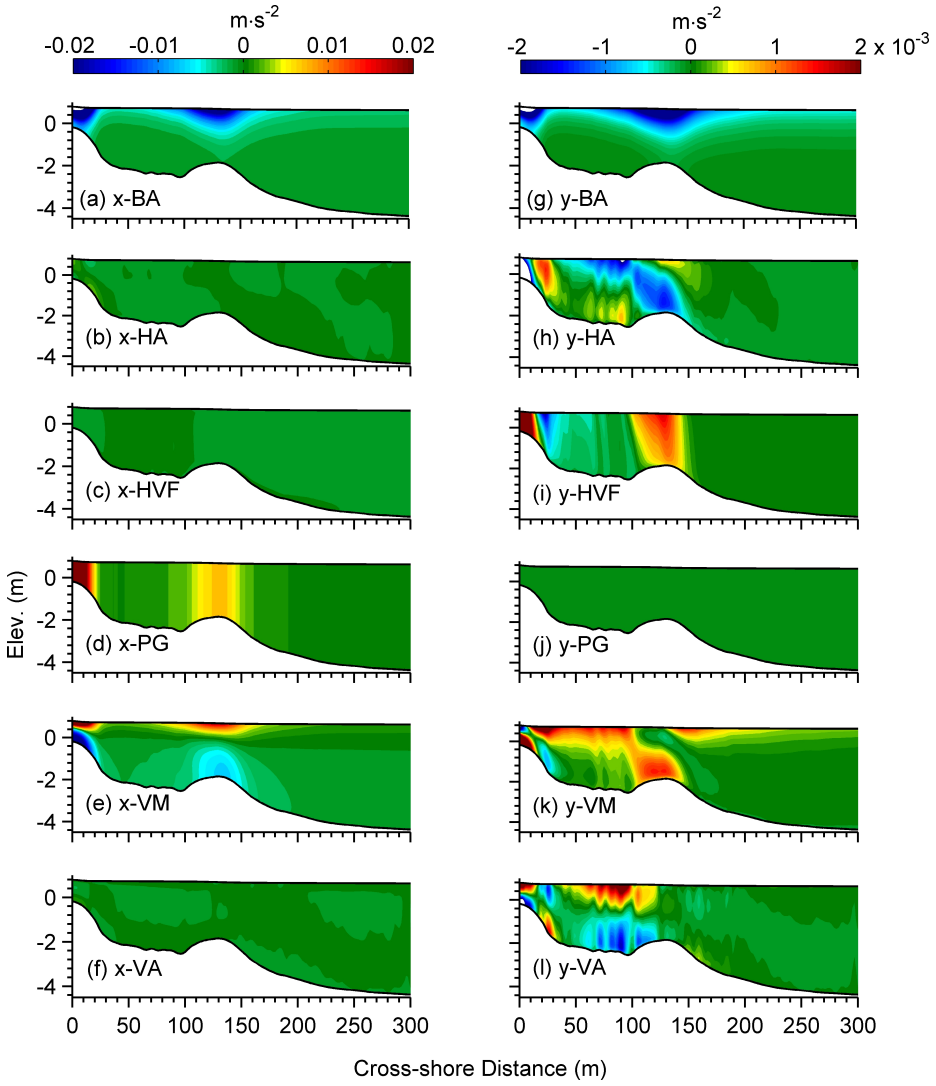

Figure 3.10: Cross-shore and vertical distribution of the terms contributing to the cross-shore (x) and longshore (y) momentum balance for Run 6 (VF model with wave rollers, α_r=1 and no wave mixing). Cross-shore terms: (a) x-breaking acceleration (x-BA) ; (b) Eulerian, x-horizontal advection (x-HA); (c) x- horizontal vortex force (x-HVF); (d) x- pressure gradient (x-PG); (e) x-vertical mixing (VM); (f) x-vertical advection (VA); and alongshore terms: (g) y-breaking acceleration (y-BA); (h) Eulerian, y-horizontal advection (y-HA); (i) y-horizontal vortex force (y-HVF); (j) y-pressure gradient (y-PG); (k) y-vertical mixing (y-VM); and (l) y-vertical advection (y-VA).

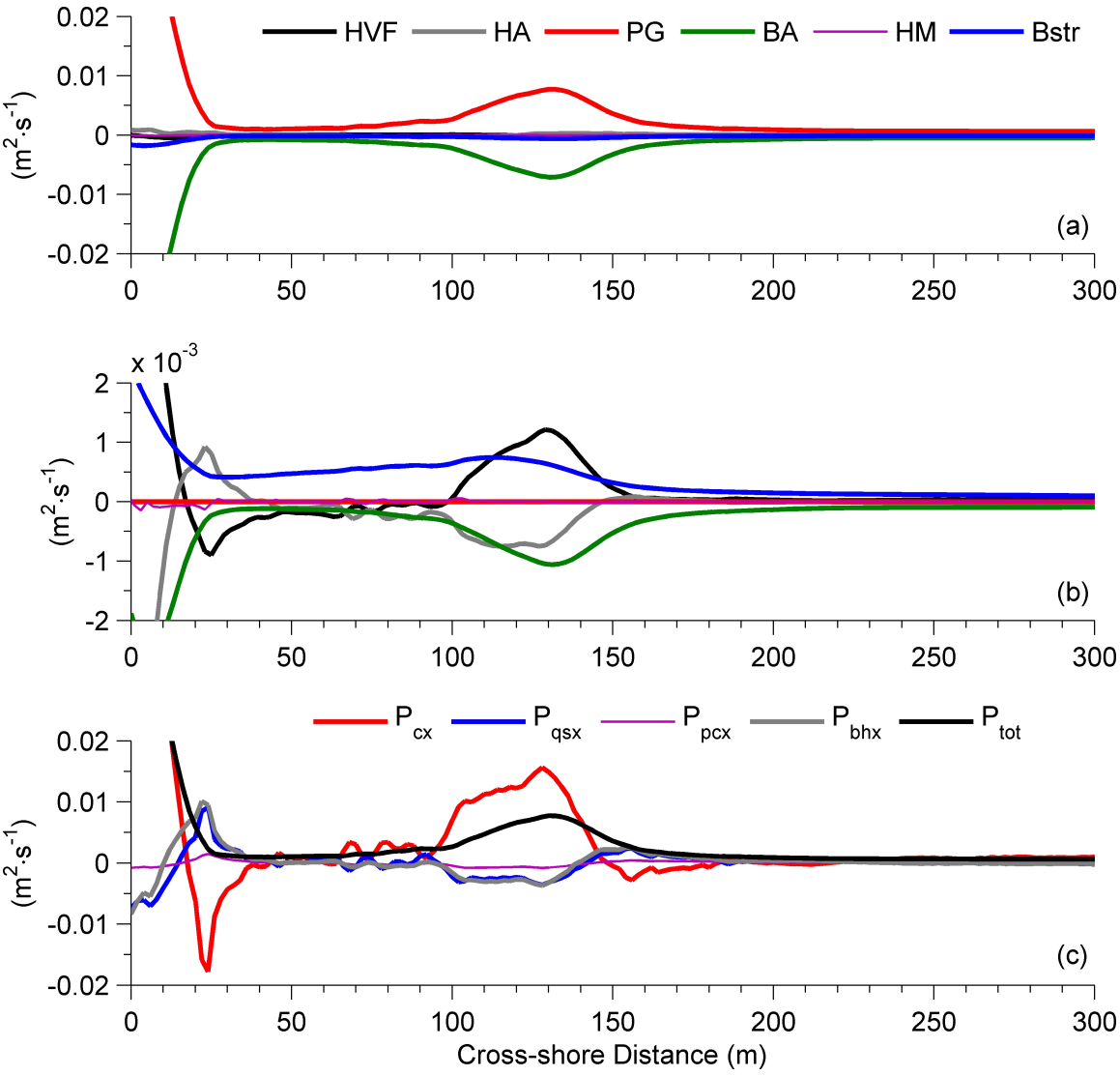

Figure 3.11: Cross-shore variation of depth-averaged (a) cross-shore and (b) longshore momentum balance terms. (c) Decomposed PGF terms in cross-shore as described in Eqn. 49 for Run 6 (VF model with wave rollers, α_r=1 and no wave mixing).

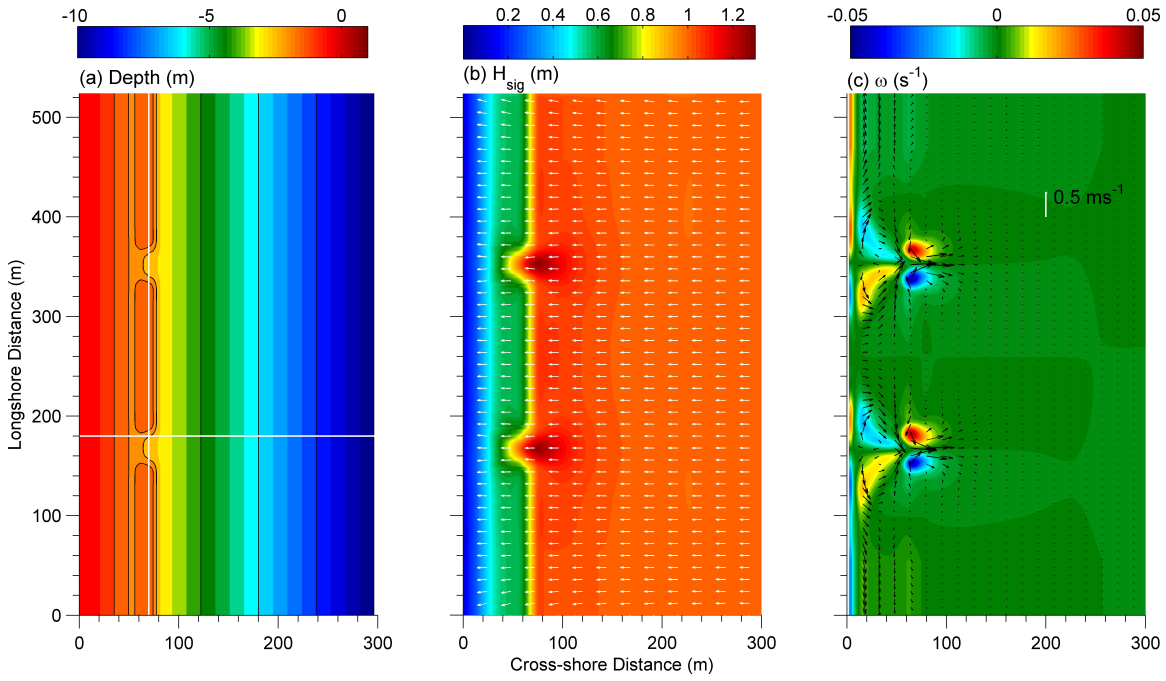

Figure 3.12: Rip channel case. (a) Bathymetric domain; (b) significant wave height (contours) and direction (arrows); and (c) vorticity vector after 1 hour of model simulation. Black arrows in (c) show the depth averaged, Eulerian velocity vector. The white line in (c) shows velocity strength of 0.5 ms^{-1}. The solid white lines in (a) show the transects along which cross-shore and longshore momentum balances are described in Figures 3.15 to 16.

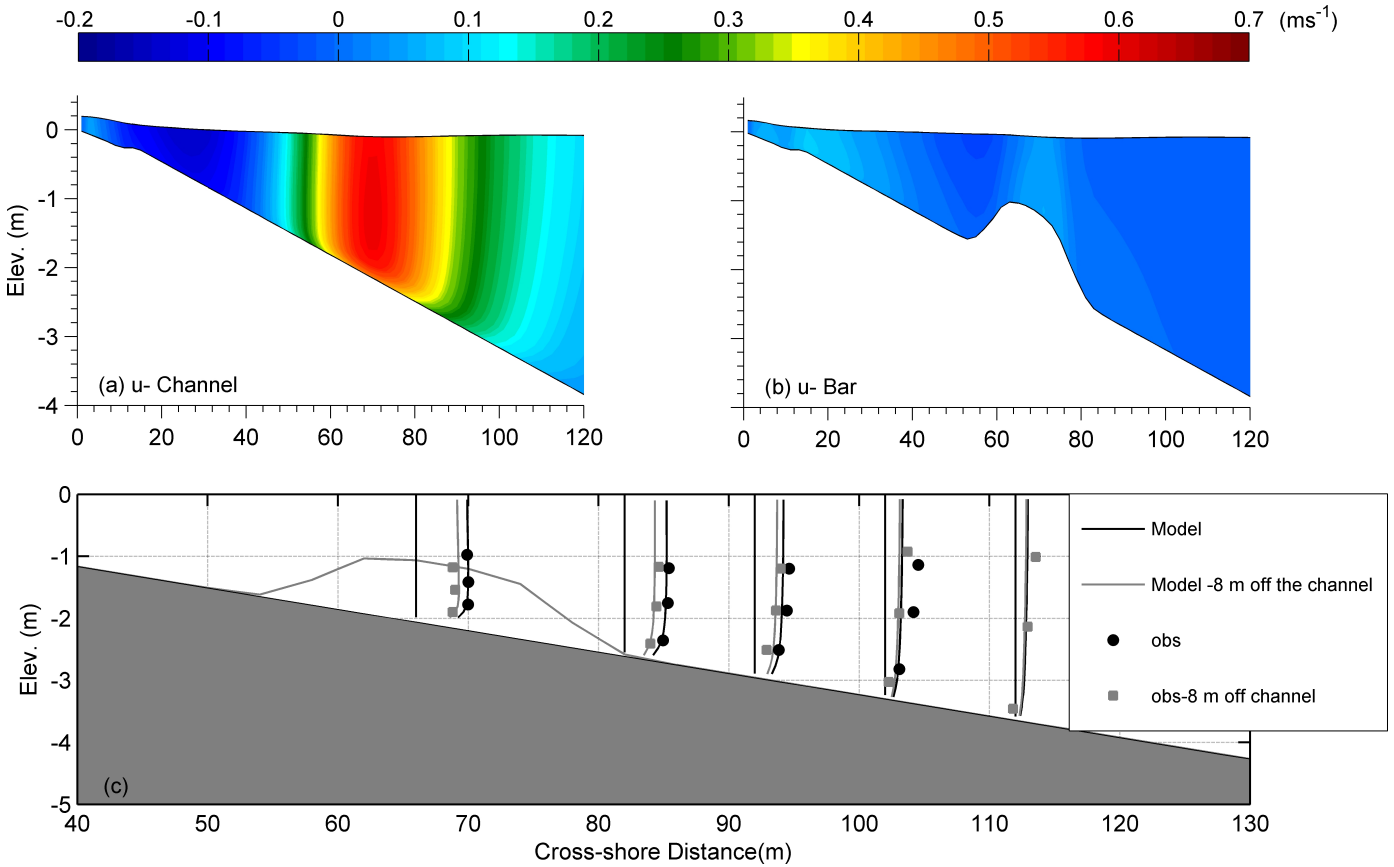

Figure 3.13: Vertical structure of cross-shore Eulerian velocity at (a) the center of rip channel and (b) over the bar. Results derived from VF based model simulations. (c) Comparison of normalized model derived cross-shore velocity with normalized data from Haas and Svendsen, 2002 (key: symbols ■ and ■ and grey and black lines denote data and model results at the center and 8 m off the channel, respectively).

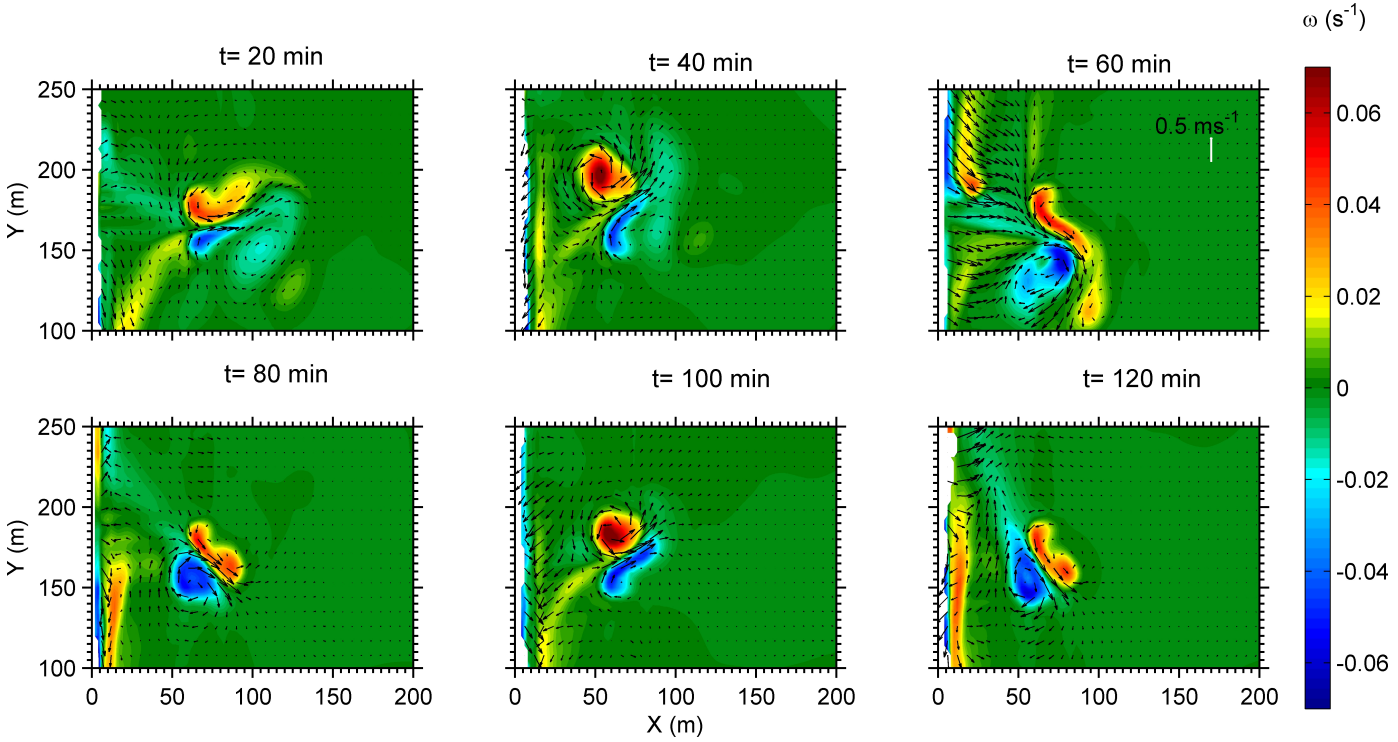

Figure 3.14: Example of unstable rip current conditions simulated using with a linear bottom friction (μ=0.002 m) and a horizontal mixing of 0.05 m^2s^{-1}. Snapshots of vorticity and depth-averaged, Eulerian velocity vector for six different time steps with a time interval of 20 min. Only the computational domain in the vicinity of the rip channel is shown here.

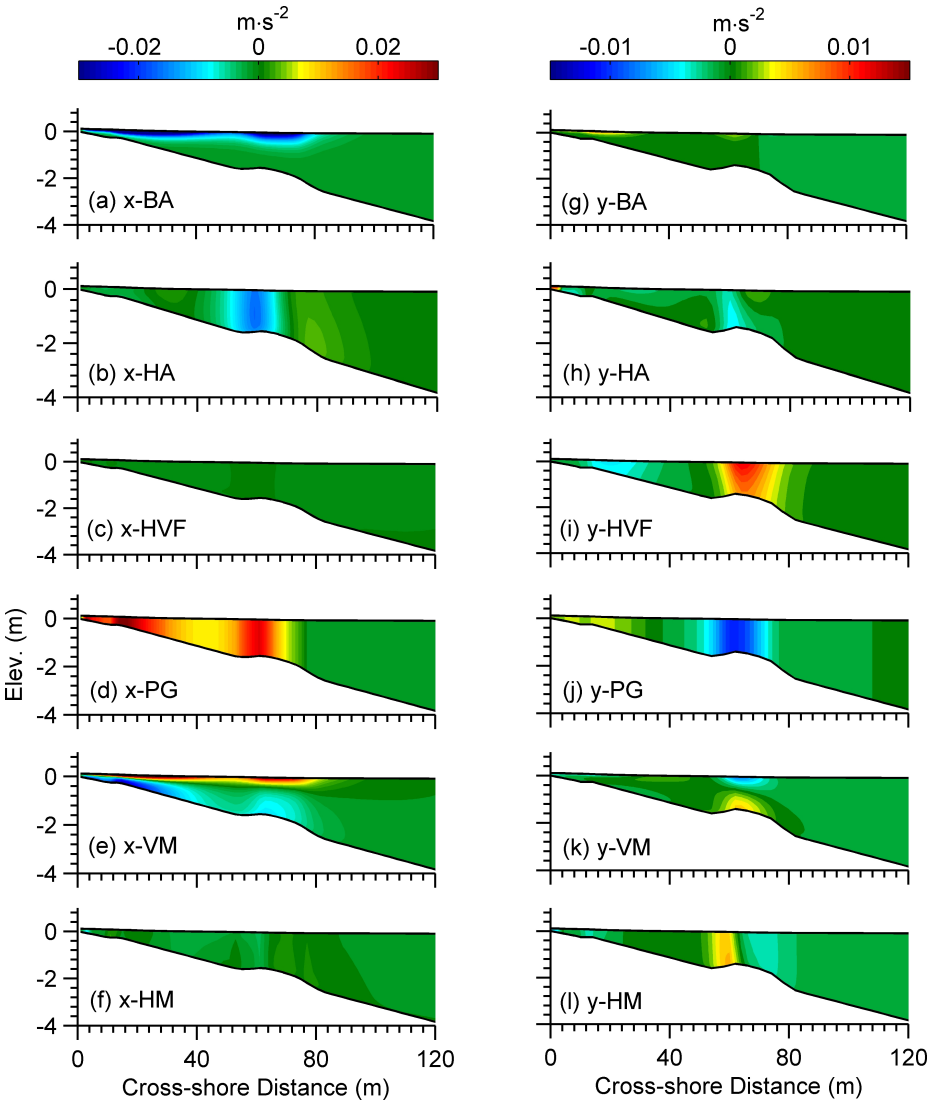

Figure 3.15: Cross-shore distribution of vertical profiles of contributing terms in cross-shore (x)- and longshore (y) momentum balance at y=180m (see Fig. 3.12 for transect location). Cross-shore terms: (a) x-breaking acceleration (x-BA); (b) Eulerian, x-horizontal advection (x-HA); (c) x-horizontal vortex force (x-HVF); (d) x-pressure gradient (x-PG); (e) x-vertical mixing (x-VM); (f) x-horizontal mixing (x-HM); Longshore terms: (g) y-breaking acceleration (y-BA); (h) Eulerian, y-horizontal advection (HA); (i) y-horizontal vortex force (y-HVF); (j) y-pressure gradient (y-PG); (k) y-vertical mixing (y-VM); and (l) y-horizontal mixing (y-HM).

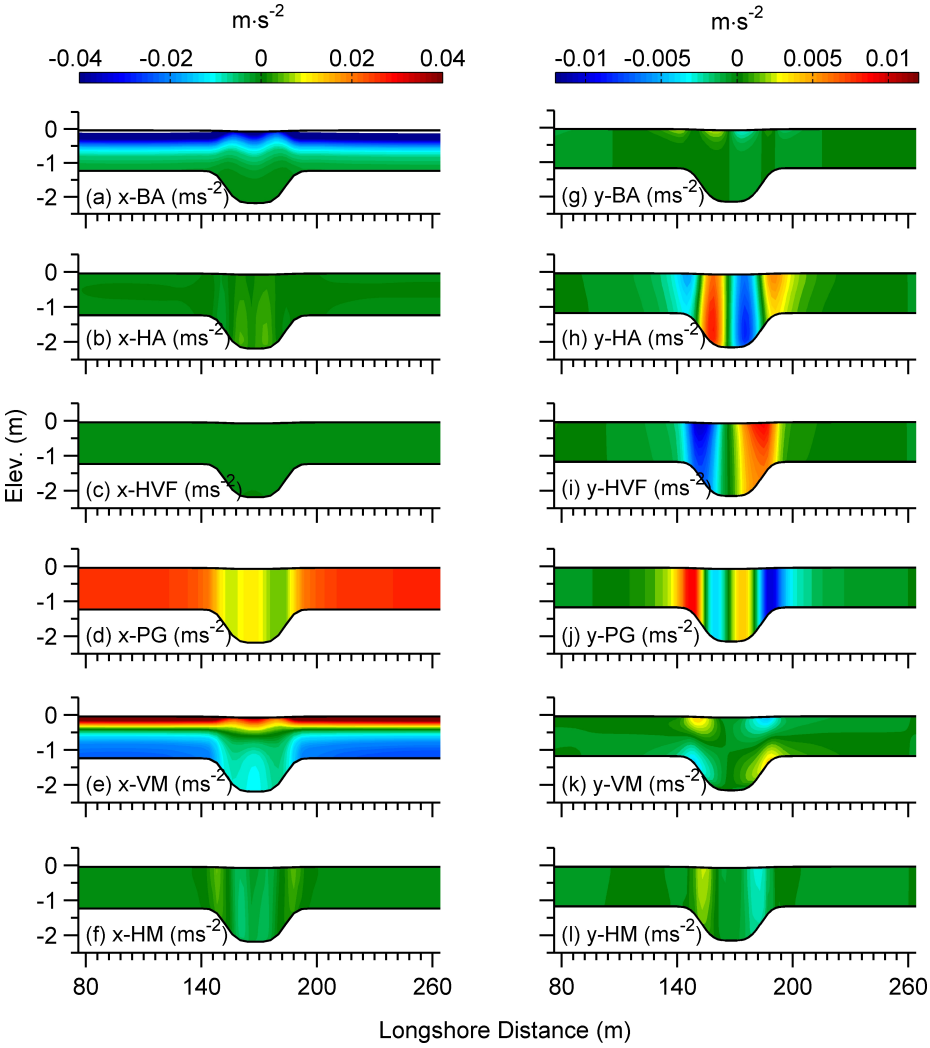

Figure 3.16: Longshore distribution of vertical profile of contributing terms in cross-shore (x) and longshore (y) momentum balance at x=70m (see Fig. 3.12 for transect location). Cross-shore terms: (a) x-breaking acceleration (x-BA); (b) Eulerian, x-horizontal advection (x-HA); (c) x-horizontal vortex force (x-HVF); (d) x-pressure gradient (x-PG); (e) x-vertical mixing (x-VM); (f) x-vertical mixing (x-VM); Longshore terms: (g) y-breaking acceleration (y-BA); (h) Eulerian, y-horizontal advection (y-HA); (i) y-horizontal vortex force (y-HVF); (j) y-pressure gradient (y-PG); (k) y-vertical mixing (y-VM); and (l) y-horizontal mixing (y-HM).

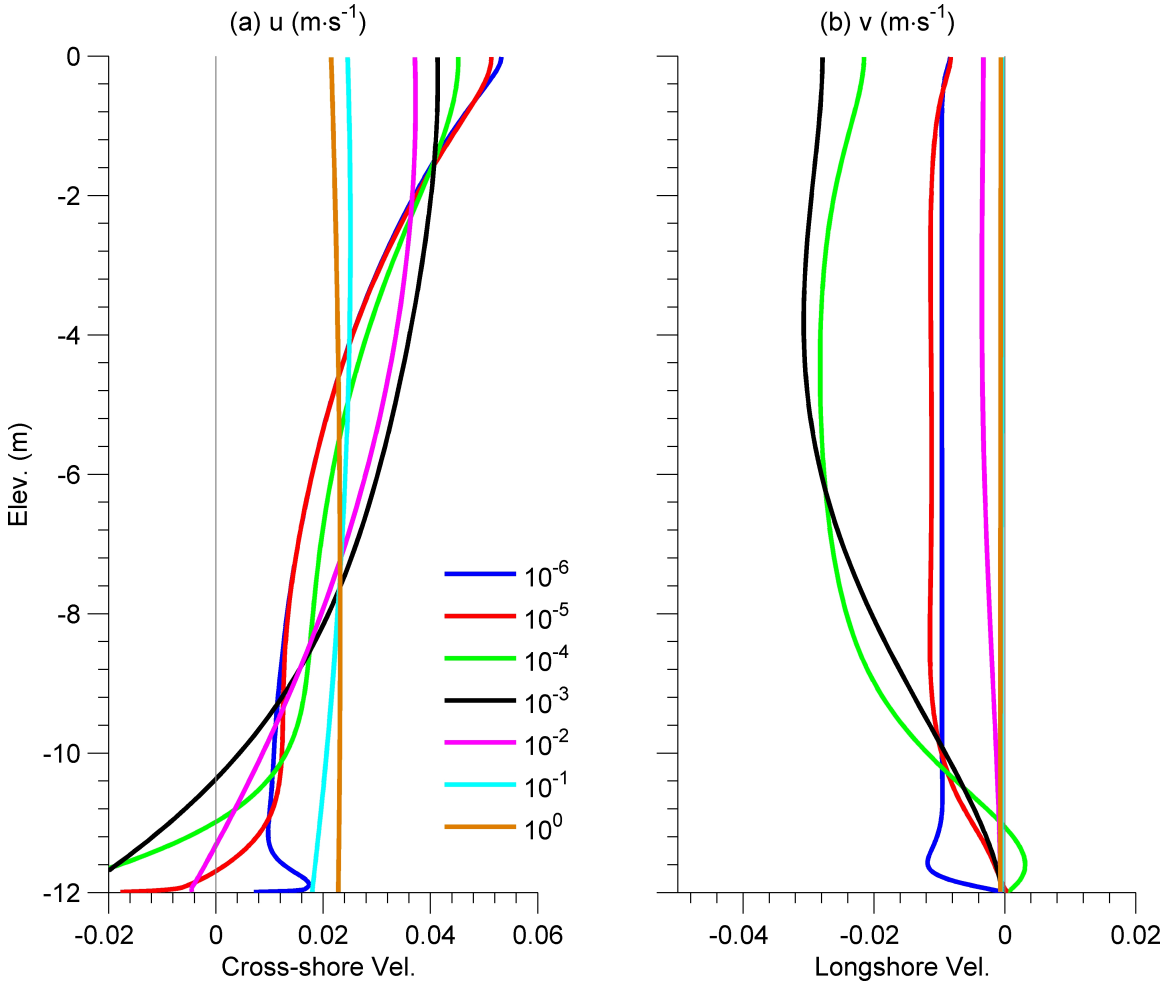

Figure 3.17: Cross-shore (a) and longshore (b) velocity profiles from model simulations with constant vertical viscosity (K_M) values ranging from 10^{-6} to 10^{0} m^2s^{-1}. The model simulations were carried out assuming a normally incident wave with significant wave height of 2 m and wave period of 7 s.

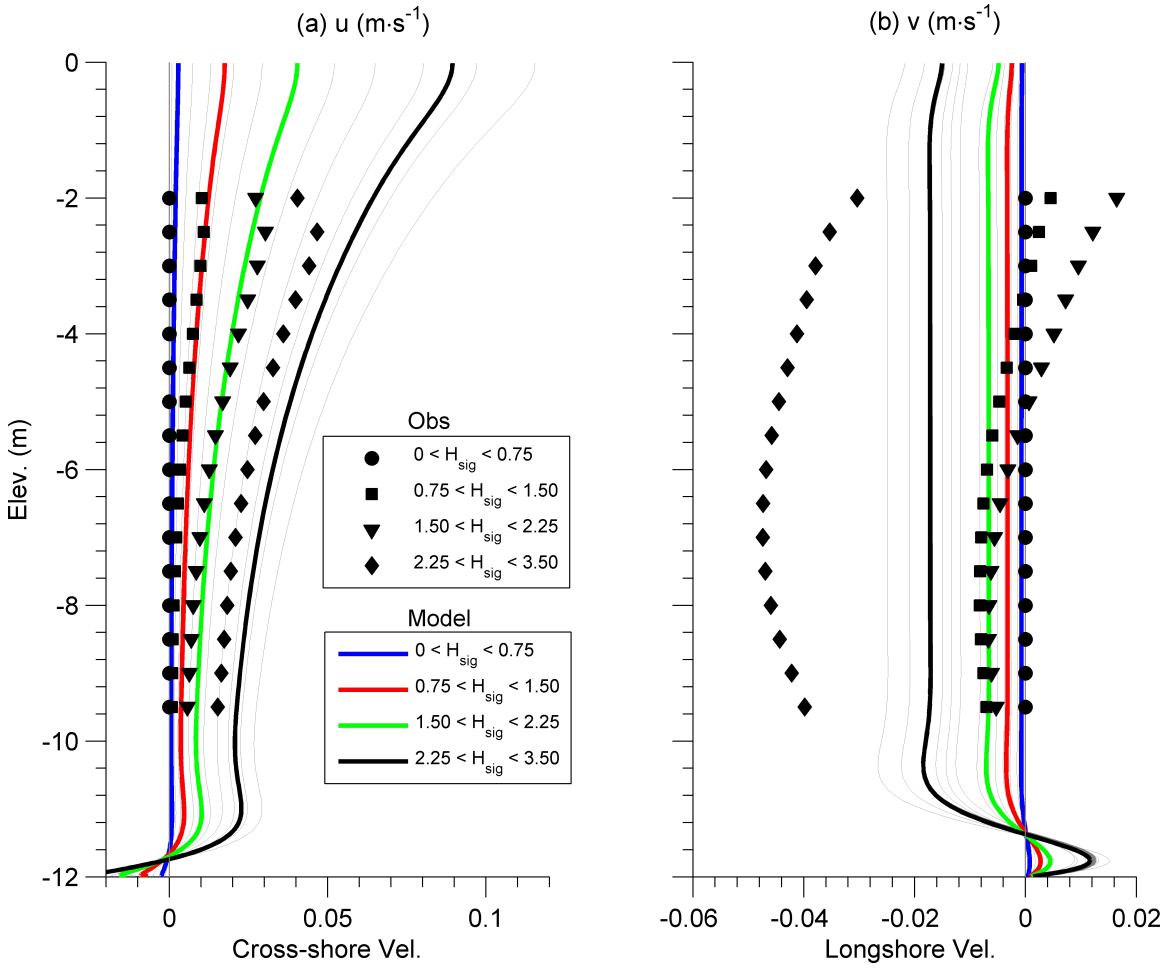

Figure 3.18: Observed (from Lentz et al, 2008) and simulated cross-shore (a) and longshore (b) velocity profiles for different ranges of significant wave height (Hsig). Individual model profiles estimates for wave height values from 0 to 3.5 m with an interval of 0.25 m are shown as thin grey lines while the thicker solid lines show velocity profiles averaged over specific wave height ranges as shown in insert. Simulations were carried out with a constant viscosity of 10^{-5} m^2s^{-1}.

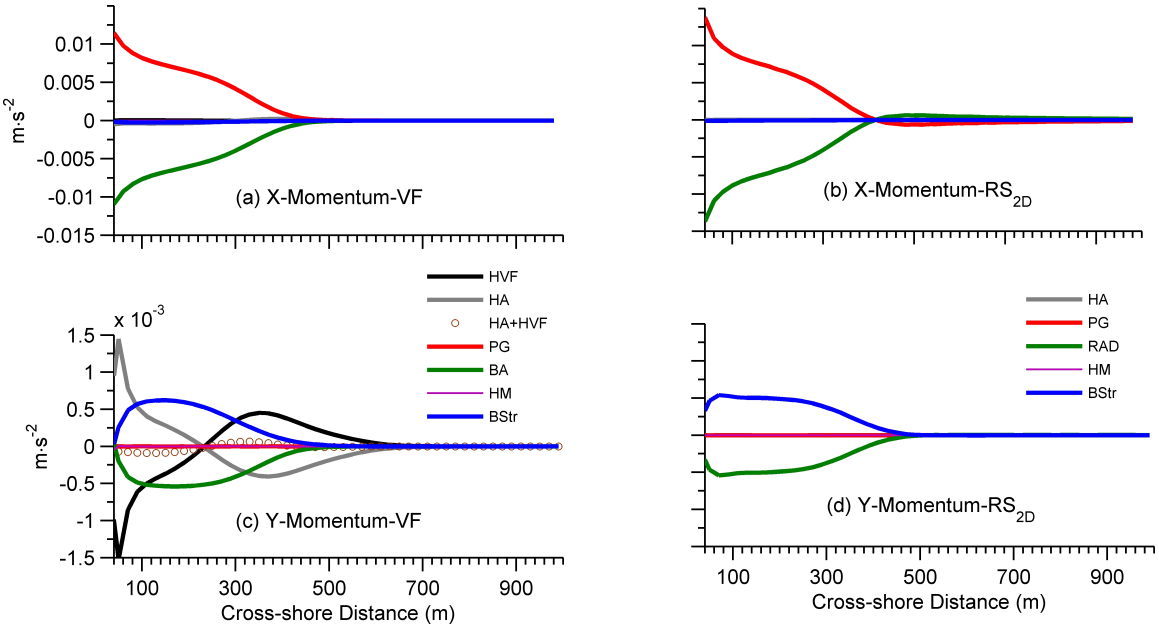

Figure 3.19: Cross-shore distribution of cross-shore (a, b) and longshore (c, d) momentum balance terms from the VF model (a, c) and RS_{2d} (b, d) model simulations for obliquely incident waves on a planar beach (Sec 3.4.1).

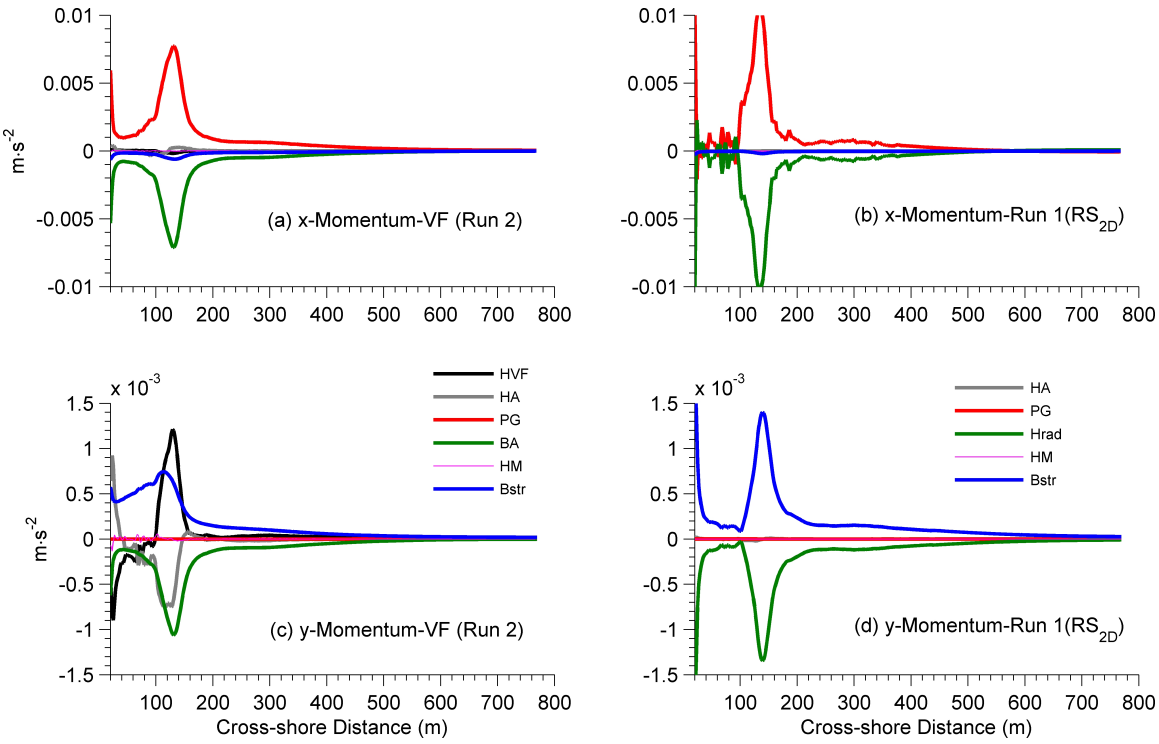

Figure 3.20: Cross-shore distribution of cross-shore (a, b) and longshore (c, d) momentum balance terms from the VF (a, c) and RS_{2D} (b, d) models for obliquely incident spectral waves on a barred beach (Sec. 3.4.2). The VF and RS_{2D} simulation corresponds to Run 6 (VF model with wave rollers, α_r=1 and no wave mixing) and Run 2 (radiation stress model) as described in Table 3.3.

Table 3.1: COAWST options available for the computation of non-conservative wave forces (for details see Sec. 3.2).

VF options in the COAWST Modeling System			
Process	Switch Name	Description	References
Wave Dissipation	WDISS_WAVEMOD	Dissipation from wave model (SWAN)	SWAN Manual
	WDISS_THORGUZA	Wave dissipation using Eq. 3.32	TG86
	WDISS_CHURTHOR	Wave dissipation using Eq. 3.33	CT93
Roller Model	ROLLER_RENIERS	Solve the roller evolution (Eqn. 3.35-38) to calculate roller dissipation	R04 U10
	ROLLER_SVENDSEN	Calculate roller area and roller energy using Svendsen (1984) formulations	S84 W08
Non-conservative forces	WEC_BREAKING	Wave breaking contribution (Eqn. 3.34)	This paper
	WEC_ROLLER	Roller Contribution (Eqn. 3.39)	This Paper
	WEC_WCAP	Whitecapping Contribution (Eqn. 3.30)	This Paper
Streaming	BOTTOM_STREAMING_YU	Calculate wave dissipation due to bottom friction (Eqn. 3.23) and the contribution to momentum balance (Eqns. 3.24-37)	U10
	BOTTOM_STREAMING_XU_BOWEN	Calculate contribution of bottom streaming to momentum balance using Eqn. 3.28	XB94
	SURFACE_STREAMING	Calculate surface streaming contribution to momentum balance using Eqn. 3.29	XB94
Wave induced mixing	TKE_WAVEDISS	Compute TKE contribution due to wave breaking using Eqn. 47, which is implemented as a surface boundary condition (Eqn. 3.45-3.46) to solve GLS model	FT05

Table 3.2: List of the components which constitute the total pressure gradient force (Eqn. 50).

Individual Terms	Description
$\mathcal{P}^{tot}$	Total pressure gradient force. Contribution of both WEC and non-WEC terms
$\mathcal{P}^{c}$	Non-WEC current contribution
$\mathcal{P}^{wec}$	WEC contribution ($\mathcal{P}^{qs} + \mathcal{P}^{bh} + \mathcal{P}^{pc}$)
$\mathcal{P}^{qs}$	Quasi-static response (Eqn. 3.7)
$\mathcal{P}^{bh}$	Bernoulli head (Eqn. 3.5)
$\mathcal{P}^{pc}$	Surface pressure boundary correction (Eqn. 3.9)

Table 3.3: Model configuration for different DUCK' 94 simulations. RS_{2D} refers to simulations conducted using depth-averaged, radiation stress based model, while simulations done using the VF formalism are referred to as VF. α_r is the coefficient which determines the percentage of wave breaking induced dissipation contributing to creation of wave rollers (Eqn. 3.34), while $c_{\epsilon w}$ is the percentage of total dissipation going as turbulent kinetic energy (Eqns. 3.43 and 3.48).

Description of Model Runs for DUCK' 94 Experiment					
Run #	Model Formulation	Effect of Wave Rollers	α_r	Surface TKE	$c_{\epsilon w}$
1	RS_{2D}	OFF	-	-	-
2	VF	OFF	0	OFF	0
3	VF	OFF	0.25	OFF	0
4	VF	ON	0.50	OFF	0
5	VF	ON	0.75	OFF	0
6	VF	ON	1.00	OFF	0
7	VF	ON	0.5	ON	0.01
8	VF	ON	0.5	ON	0.05
9	VF	ON	1.0	ON	0.01
10	VF	ON	1.0	ON	0.05

Table 3.4: Normalized root mean square error $\epsilon_{rms}(j,k) = \left\{ \frac{\sum_{i=1}^{n}(d_{ij} - m_{ijk})^2}{\sum_{i=1}^{n}(d_{ij})^2} \right\}^{0.5}$ for the cross-shore and longshore velocity estimates for DUCK' 94 for various locations across the profile and the different model simulations (Runs 2-10, see Table 3.3). d_{ij} and m_{ijk} represent measured (from Garcez-Faria et al., 1998, 2000) and model estimated velocity values at the 7 cross-shore locations (j) and various elevations (i) above the sea bed (for measurement locations see Fig. 3.10). Station 1 is closest to the shoreline. Numbers in bold typeface indicate minimum values.

Normalized Root Mean Square Error Analysis										
	Run # / Stn #	2	3	4	5	6	7	8	9	10
Cross-shore	1	0.80	0.80	0.80	0.80	0.79	0.88	0.92	0.87	0.92
	2	0.82	0.80	0.77	0.75	0.73	0.83	0.88	0.80	0.86
	3	0.74	0.68	0.62	0.58	0.53	0.69	0.72	0.63	0.67
	4	0.84	0.76	0.71	0.66	0.62	0.76	0.78	0.70	0.73
	5	0.46	0.43	0.41	0.39	0.37	0.65	0.71	0.62	0.69
	6	0.44	0.42	0.40	0.38	0.37	0.42	0.46	0.44	0.48
	7	0.47	0.45	0.43	0.41	0.39	0.25	0.17	0.22	0.15
	Mean	0.65	0.62	0.59	0.57	0.54	0.64	0.66	0.61	0.64
Longshore	1	0.52	0.66	0.79	0.89	0.98	0.65	0.43	0.82	0.59
	2	0.10	0.05	0.08	0.13	0.17	0.07	0.17	0.11	0.10
	3	0.13	0.10	0.07	0.06	0.05	0.13	0.23	0.10	0.19
	4	0.14	0.12	0.11	0.10	0.11	0.10	0.15	0.12	0.16
	5	0.22	0.14	0.08	0.08	0.13	0.08	0.17	0.20	0.30
	6	0.11	0.18	0.25	0.31	0.37	0.33	0.43	0.43	0.53
	7	0.22	0.25	0.27	0.30	0.32	0.33	0.45	0.37	0.49
	Mean	0.21	0.21	0.23	0.27	0.31	0.24	0.29	0.31	0.34

Table 3.5: The RMS error (normalized by the maximum observed value) for the simulated cross-shore velocities for nearshore barred beach with rip channels (sec 3.4.3).

Stn #	RMS Error % Cross-shore Vel.
1	05.8
2	05.3
3	13.1
4	28.3
5	36.0
Overall	12.7

Table 3.6: The RMS error (normalized by the maximum value) for the simulated cross-shore and longshore velocities for wave-induced flows in the inner shelf (sec 3.4.4).

	RMS Error(%)	
Wave Ht. Group	Cross-shore Vel.	Longshore Vel.
$0 < H_{sig} < 0.75$	NA	NA
$0.75 < H_{sig} < 1.5$	21.4	52.0
$1.5 < H_{sig} < 2.25$	34.3	48.9
$2.25 < H_{sig} < 3.50$	48.4	83.2
Overall	11.3	29.5

Chapter 4

A Methodology for the Prediction of Rip Currents using a three-dimensional Numerical, Coupled, Wave-Current Model[1]

[1]This chapter has been published as "Voulgaris G., Voulgaris, G., N. Kumar and J.C. Warner, 2011. Chapter 5: Methodology for Prediction of Rip Currents Using a Three-Dimensional Numerical, Coupled, Wave Current Model. In: Rip Currents: Beach Safety, Physical Oceanography, and Wave Modeling. Editor(s): Stephen Leatherman, Florida International University, Miami, FL, USA; John Fletemeyer, pp. 87-106. See Appendix A for more details.".

Abstract

Rip currents are well known hazards for beach goers and swimmers. Over 80 % of all surf zone rescues are attributed to rip currents. Forecasting systems currently used to predict rip currents are empirical in nature and do not take into account bottom morphology, even though the bathymetry is a major reason for rip current formation. Ideal forecasting systems require information on, or prediction of 3-D nearshore bathymetry. However this is extremely difficult and not feasible at present. In order to overcome this limitation a new method for predicting rip current and nearshore hazard probability has been developed that combines existing historical bathymetric data and hydrodynamic numerical modeling.

Empirical Orthogonal Function (EOF) analysis on time series of historical beach profile data is used to provide the mean profile, bar height, and cross-shore bar location. These parameters in turn are used to construct the alongshore barred beach profile. The profile is then modified to be interrupted by rip channels. The widths of these rip channels and their ratio to rip current spacing and surf zone width are determined from scales found in the literature. This kind of two dimensional beach profile is called Longshore Bar Trough (LBT) morphology and channels in the bar facilitate rip current formation. This morphology is used as an input to a three dimensional numerical system consisting of a circulation (ROMS) and wave propagation (SWAN) model that are coupled. This system has been successfully compared to analytical and laboratory results for rip currents.

A case study based on this technique is presented and discussed for Duck, NC, the site of the US Army Corps of Engineering, Field Research Facility (FRF). Information derived from the model output determines probability of rip current occurrence and the expected strength. Worst case scenarios can also be generated by modifying rip channel width and current spacing parameters in the LBT morphology.

4.1 Introduction

Rip currents constitute one of the most commonly occurring hazards in the nearshore that threaten the lives of the unaware public using the coastal zone recreationally. Society responds to this danger through a number of measures that include: (i) the deployment of trained lifeguards; (ii) public education for the hidden hazards of the nearshore; and (iii) establishing warning systems. In the U.S. the National Oceanic and Atmospheric Administration (NOAA) has teamed with the U.S. Lifesaving Association (USLA) to undertake outreach activities aimed at informing the public about the hazards of rip currents. In addition, the National Weather Service (NWS) has established the Coastal Weather Forecast (CWF) and the Surf Zone Forecast (SRF) that are produced by local Weather Forecast Offices (WFO). The CWF is produced by all WFOs and used by emergency managers, media and the general public for planning purposes to support and promote safe transportation across the coastal waters. The Surf Zone Forecast (SRF), on the other hand, is not mandatory and its issuance is determined by regional policy, customer and partner needs (NOAA, 2004). NOAA (2004) states that SRF has been established in recognition of the fact that such forecast:... *"provides valuable and life-saving information, pertaining to hazards in the surf zone, to the beach front community, including the general public, and providers of beachfront safety services, such as lifeguards"*. Even if a WFO does not issue an SRF they might elect to provide rip-current information within a CWF using a three-tiered text qualifier: Low, Moderate and High Risk (see NOAA, 2004, page 17).

Currently, rip current forecasting is based on predictive indices, which in turn, are based on statistical correlations between rip current related rescues and information on wave and wind conditions. Lushine (1991) developed the first index for South Florida (the Lushine Rip Current Scale or LURCS). This index is an empirical

forecasting technique that utilizes wind direction and speed, swell height, and timing of low tide to predict rip current danger. This index was later modified by Lascody (1998) for use in east central Florida (the ECFLS LURCS). The modification included the addition of the swell period and a slight modification of the tidal factor. Engle et al. (2002) used lifeguard rescue logs from Daytona Beach Florida, and found that the frequency of rip current rescues increased during shore normal wave incidence and during mid-low tidal stages. Engle et al. (2002) removed the wind speed and direction information from the rip current risk prediction index and added tidal stage and wave direction. Their prediction index (modified ECFLS LURCS index) is a numeric one that assigns different weights to different wave parameters. The total value can vary from 0 to 12 indicating low (value 0) to very high (value 12) rip current risk.

Engle et al. (2002) noted that use of correlations between rescue and environmental conditions are not reliable means of determining rip danger. Beach attendance reduces with increased wave energy (or bad weather) and as such the statistical samples are biased if not normalized by the total population visiting the beach. In addition, fatalities or rescues caused by factors other than rip currents (e.g., swimming competence level, alcohol consumption, medical reasons, longshore current strength, etc.) are not accounted with this approach. This leads to all beach rescues being attributed to rip currents, thus biasing the statistics. Also, the rip prediction indices do not include information on beach morphology (i.e., alongshore bar, ridge and runnel morphology, etc.) although scientific evidence suggests that rip currents are related to the presence of longshore bars (e.g., Haller et al., 2002; Aagaard et al., 1997; Wright and Short, 1984; Sonu, 1972). It can be argued that beach morphology is included indirectly, since the statistical correlations are based on data for a particular beach with a particular morphology. This argument although valid, reinforces the fact that the risk index developed strongly depends on the local characteristics and its use in other locations with potentially different morphology might lead to inaccurate

forecasts. Despite its empirical nature, the above-described rip current hazard index relies on information on wind and wave conditions, two important physical forcings that contribute to rip-current generation.

Currently NWS provides weather (wind) forecasting for the coastal areas. Wave forecasts on the other hand provided by NOAA's National Center for Environmental Prediction (NCEP) are limited in resolution (1.25^o x 1° and 0.25^o x 0.25^o for the global and western north Atlantic, respectively) and do not resolve either nearshore bathymetry or coastline variability that can modify nearshore wave dynamics significantly. Wave forecasting models with increased resolution have been implemented locally by a limited number of NWS Weather Forecast Offices, including Eureka, CA, Wakefiled VA, Newport Morehead City and Wilmington, NC (Devaliere et al., 2009; Willis et al., 2010) that improve the predictive capability within the middle and inner shelf. However, no forecast is being provided for inside the surf zone. Allard et al. (2008) presented a methodology for predicting longshore currents using commercial software (DELFT-3D) in a depth-averaged mode, but it suffered from lack of information on bathymetry and it did not address the issue of rip-currents directly. This contribution attempts to fill this gap by incorporating the latest developments of nearshore hydrodynamics and numerical modeling, using a public domain 3-D code, toward the development of a quantitative rip-current prediction tool.

4.2 Background on Rip Current Development

As the waves travel in the nearshore they get modified through refraction, diffraction, dissipation, and shoaling processes, but can also gain energy through the local wind forcing (Kinsman, 1965; Lavrenov, 2003). In very shallow water depths, wave heights tend to be controlled by the local water depth through the process of wave breaking. The excess of momentum due to the presence of waves (Radiation Stress, Longuet-Higgins and Stewart, 1964) is generally conserved until the breaking point. At this

point the energy gets expended and wave-induced currents are generated. In the nearshore, two wave-induced current systems are described (Komar,1998): (1) alongshore currents generated by obliquely approaching waves and (2) a cell circulation system (Shepard and Inman, 1950) that occurs when the incident angle of the waves is small, and usually is responsible for the generation of rip-currents. The latter circulation system consists of: (a) onshore transport of water; (b) longshore currents that are confined within the surf zone and carry water toward the rip (feeder currents); (c) the rip neck, a fast-flowing current that extends from the point of confluence of the two opposing feeder currents and transport water through the surf zone; and (d) the rip head, which is the region of decreasing velocity seaward of the surf zone.

Rip currents are an integral part of the cell circulation system. They are jet-like and directed seaward with speeds that can reach up to 2 ms^{-1} under extreme conditions (Short, 1985) but with typical values 0.5 to 1 ms^{-1}. They are usually associated with intermediate (Wright and Short, 1984) type beaches with a bar/channel morphology (e.g., Sonu, 1972), although theories have been presented (e.g., Murray et al., 2003) suggesting that rip currents can also occur on alongshore-uniform beaches as self-organized features ("flash rips").

The ability to model nearshore circulation and rip-currents improved through the introduction of the concept of radiation stress by Longuet-Higgins and Stewart (1964). According to this theory, shoreward of the wave breaking zone, mean sea level increases (wave set-up), generating a pressure gradient that balances the gradient due to radiation stress. Assuming laterally uniform nearshore morphology, if the waves approach the coastline at an angle, then the alongshore component of the excess of momentum drives alongshore currents that flow parallel to the coastline (Longuet-Higgins, 1970; Thornton, 1970). Their strength depends greatly on their angle of approach and wave breaking height. Under large angles of approach, longshore current velocities can exceed 1 ms^{-1} and can be dangerous for swimmers, especially

children. These currents have been studied extensively since they are responsible for transporting sediment in the alongshore, causing coastal erosion. It is generally agreed that breaking waves stir the sediment (e.g., Voulgaris and Collins, 2000) and the longshore current transports it along the coast (e.g., Voulgaris et al., 1998; 1996). An alongshore gradient of this longshore sediment transport is responsible for the development of erosional and/or accretional parts along a coastline.

Overall, higher waves will create a higher set-up (Bowen, 1969) and a lateral variation in the wave height will create a lateral variability in the wave set-up, developing an alongshore pressure gradient (Dalrymple, 1978; Bowen,1969) that can drive longshore (feeder) currents from areas of high waves toward to areas of low wave height. Lateral variation in wave height can be caused by offshore bathymetric changes that lead to areas of wave convergence (high waves) and divergence (low waves), as is the case for the rip currents found at La Jolla, CA, where rip currents are developed by a longshore variation of wave breaker heights caused by wave refraction over offshore submarine canyons (Shepard and Inman, 1950). In areas with relative uniform offshore bathymetry (as on the south Atlantic Bight and the Carolinas), variation in the alongshore wave height can be caused by variability of the alongshore bar or by the superposition of different wave trains coming from different directions (e.g., Dalrymple, 1975; Dusek et al., 2011) or due to wave group forcing (e.g., Long and Özkan-Haller, 2009). Mei and Liu (1977) demonstrated analytically how alongshore varying surf zone bathymetry could cause longshore pressure gradients. These types of rip currents are common in barred beaches where channels interrupt the continuity of the alongshore bar. Additionally, rip current circulations can be created through a feedback mechanism in which the initial wave height variation causes an incipient rip current to form that in turn interacts with the wave field feeding more energy into the circulation system (e.g., Iwata,1976; Murray et al., 2003).

Independent of the initial conditions it is generally agreed that the rip-currents are maintained and persist because of topographic depressions (rip channels) within the surf zone. However, because the location of the rip channels varies in space and time it has been very difficult to obtain accurate field data. Haller et al. (2002) presented experimental laboratory data of nearshore circulation on a barred beach with rip channels that showed that the presence of gaps in longshore uniform bars dominate the nearshore circulation system for both normal and obliquely incident waves. The SHORECIRC nearshore circulation model was used by Haas et al. (2003) to accurately simulate the rip currents observed by Haller et al. (2002) suggesting that SHORECIRC is an adequate tool to simulate bathymetrically controlled rip currents and other 3-D flows in the nearshore.

In realistic situations, the tide might modulate rip current activity directly by modulating local water depth and indirectly through modulation of the incident wave field. Brander and Short (2001) presented data from an Australian beach with a tidal range of 1.6m and medium energy wave activity. They showed that rip current velocity is inversely proportional to the water depth and is modulated by the tide resulting in stronger rip current speeds at low tide conditions. Similar dependence of rip current velocity on tidal stage was shown by Brander (1999) who demonstrated that the velocity of rips is proportional to the cross-sectional area of the rip channel. Also, the same investigator noted that rip currents occur in intermediate type (Wright and Short, 1984) beaches especially during the decreasing end of a highly energetic event. This dependence of rip currents and tidal stage is also reflected on the modified ECFLS LURCS Index of Engle et al. (2002).

4.3 Objectives

The objective of this study is to design a physics based nearshore hazards forecasting system that can provide quantitative values of rip current aspects (current speed,

relative density and location offshore) that can be used with confidence to compute rip current risk indices by authorities charged with public safety. The methodology needs to depend on sound physical principles, being transferable to different locations so that it can be adaptable for different morphologies found in different sites. At this juncture it should be noted that the proposed prediction system, does not allow for the prediction of exact location and timing of a rip current as this is impossible at present. The only exception to this will be the case of fixed bathymetry (i.e., vicinity of terminal groins, or narrow passages through rocks etc). Instead, this approach aims at providing the quantitative predictions of the severity of the rip current hazard to allow for a better management of the beaches and an optimized deployment of professionals charged with life rescue.

In particular our methodology aims at: (1) providing quantitative values of risks (current speed, relative location offshore, density of rip currents etc.) in three dimensions; (2) account for the specificities of the particular site as these are expressed through the historic morphology; and (3) providing solid physical parameters that can be incorporated into a more comprehensive risk index that could include sociological parameters (i.e., beachgoer attitudes, levels or swimming competence etc). Finally we argue that this information must be part of a more comprehensive decision management tool operated by experts in beach management and sea rescue.

4.4 Methodology

The methodology for a rip-current prediction system consists of the application of a suite of numerical models and appropriate bathymetric and offshore boundary conditions which are described in the following sections. In particular, a coupled 3-D circulation and wave propagation model are used to predict nearshore circulation and assess the potential for rip current development. The biggest unknown in the devel-

opment of the prediction system is the nearshore bathymetry and a methodology is presented that deals with this unknown.

4.4.1 Circulation Modeling

ROMS is a three dimensional, free surface, bathymetry following numerical model, which solves finite difference approximations of the Reynolds Averaged Navier Stokes (RANS) equations using hydrostatic and Boussinesq approximations with a split-explicit time stepping algorithm (Shchepetkin and McWilliams, 2005; 2009). ROMS provides choices of model components like advection schemes (second, third and fourth order), turbulence closure models (e.g., Generic Length Scale mixing, Mellor-Yamada, Brunt-Väisälä frequency mixing, user provided analytical expressions, K-profile parameterization), boundary conditions etc.

ROMS has undergone modifications for use in nearshore environment that incorporate the methods described in Mellor (2003) and Mellor (2005). Haas and Warner (2009) compared the performance of ROMS to a quasi 3D model (SHORECIRC) for obliquely incident wave induced current on a gently sloping beach and also for generation of rip currents. The wave information required for calculating wave induced radiation stress was obtained by coupling ROMS to SWAN (obliquely incident wave case) and to a monochromatic wave driver REF/DIF (rip current circulation case). Following the remarks of Ardhuin et al. (2008) on Mellor's (2003; 2005) implementation of depth-dependent radiation stress equations, Mellor (2008) produced an updated formulation that was coded into ROMS and evaluated against analytical solutions for rip-current flows by Kumar et al. (2011). This updated coupled model also has been modified to include a vertical distribution of stresses that is more appropriate for sigma coordinates in very shallow waters (see Kumar, 2010; Kumar et al., 2011). The updated model was tested through simulations of several cases that include: (a) obliquely incident spectral waves on a planar beach; (b) alongshore variable offshore

wave forcing on a planar beach; (c) alongshore varying bathymetry with constant offshore wave forcing; and (d) nearshore barred morphology with rip-channels. A number of quantitative and qualitative comparisons to previous analytical, numerical and laboratory data showed that the updated model more accurately replicates surf zone recirculation patterns (onshore drift at the surface and undertow at the bottom) as compared to the previous versions.

4.4.2 Wave Propagation Model (SWAN)

Several numerical models are available for the description of wave transformation across arbitrary bathymetry, including phase resolving and phase averaged models. Phase resolving models can accurately predict the free surface displacement due to the wave field, but are computationally demanding and not practical for forecasting scenarios. Phase averaged models compute wave statistics such as wave height and period and are more practical for forecasting. Monochromatic phase averaged models typically overestimate focusing due to bathymetric rises, while spectral models are much less sensitive in this regard. A spectral model including wind forcing is preferred in some locations because the wind can provide a strong influence on nearshore wave conditions as is the case for the Carolinas and the east coast in general (Austin and Lentz, 1999). As such, the SWAN model (Booij et al., 1999; Ris et al., 1999) has been chosen to meet project needs. Input to the model consists of a bathymetric grid, a description of the incident wave conditions (measured spectra in this application) wind and mean current velocity fields. Output provides comprehensive parameters of significant wave height, mean wave length, peak and mean surface period, mean bottom period throughout the model domain. The model simulates shoaling, wave refraction due to both bathymetric features and mean currents, energy input due to winds, energy loss due to white-capping, bottom friction, and breaking. This model is comprehensive, widely used and has been compared favorably to a variety

of different data sets and analytical solutions. The same model has been setup for predicting nearshore waves for North Carolina (WFOs of Newport/Morehead City and Wilmington (Willis et al., 2010) and is planned to be implemented in FL by the Melbourne WFO (Lascody, pers. com). Wave setup and non-stationary boundary conditions are included in the model.

4.4.3 Bathymetric Domain

The accuracy of any numerical modeling application can depend on the accuracy of the boundary conditions, initial conditions, forcings, and the bathymetry used to construct the grid domain. The latter can change rapidly, especially in the very shallow waters of the nearshore. In case of fixed coastline areas (i.e., rocky coasts, jetties, concrete piers etc) the bathymetric domain can be considered constant and could be easily defined from existing charts or a bathymetric survey. However, in natural beach environments, the beach morphology can change rapidly in response to wave forcing. Although, technologies emerge that might be able to provide remote assessment of the nearshore beach morphology (e.g., microwave radars, McNinch, 2006) these are still experimental and not available for routine use. However, a rigorous analysis of existing beach profile data, routinely collected as part of beach monitoring projects can be incorporated in the design of synthetic model domains suitable for a particular location. For the case of barred morphologies, the bathymetric problem consists of defining the mean bathymetric profile, location and dimensions of the alongshore bar, the rip-channel width and the rip-channel spacing.

In the approach presented here, a synthetic bathymetric setup is created based on the local characteristics of the region of interest. Historical nearshore surveys can be utilized to construct "averaged" and extreme "rip favorable" beach profiles. Such survey data describe the beach profile shape across the beach out to a predetermined water depth. Such profiles from each benchmark and location can be analyzed using

empirical orthogonal analysis (EOF) analysis (Aubrey, 1979; Gao et al., 1998) as described below.

For a beach profile monitored n times at m cross-shore locations, a correlation matrix M $(m \times n)$ with the elements h (x,t) can be created where, x is the cross-shore location, t is the time, and h is the elevation above the sea bed. The two square matrices formed using M are:

$$A = \frac{1}{(m \times n)}\left(MM^T\right); B = \frac{1}{(m \times n)}\left(M^T M\right) \tag{4.1}$$

where M^T is the transpose matrix of M. Matrix A has a dimension of m x m and possesses m eigenvalues (e) and eigenfunctions (λ) such that:

$$Ae^i = \lambda e_i \tag{4.2}$$

and

$$Bc^j = \lambda c_j \tag{4.3}$$

where c is temporally related eigenfunction

Aubrey (1979) has shown that only the highest 3 eigenvalues (λ_1, λ_2, λ_3) and their associated eigenfunctions (e_1, e_2, e_3; c_1, e_2, e_3) explain the majority (> 90 %) of the variance representing beach profiles. The bed elevation (h) at the location, x and time, t can be re-constructed using:

$$h(x,t) = a_1 e_1(x,1) \times c_1(t,1) + a_2 e_2(x,1) \times c_2(t,2) + a_3 e_3(x,1) \times c_3(t,3) \tag{4.4}$$

where a is the normalizing factor, $a = (\lambda mn)^{0.5}$. In this paper only spatial eigenfunctions (e_1, e_2 and e_3) are utilized. The first eigenfuction (e_1) from the analysis is interpreted to represent the mean profile while the second (e_2) and third (e_3) eigenfunctions are correlated to the bar topography. The second eigenfunction typically shows a large maximum that is correlated to the location of the summer berm and a minimum in the area of the offshore bar, while the third eigenfunction shows a broad maximum that is correlated to the location of the low-tide terrace.

Thus the analysis of historical data can provide a measure of the mean beach profile, the location, and the dimensions of the bar. Synthesis of data collected from field studies of rip currents indicate a distinct scaling of rip channel spacing (L) with surf zone width (X_c) and channel width (L_t) respectively. The ratio of channel spacing over surf zone width has been found to be 2.7 to 4 and 1.5 to 8 by Haller et al. (2002) and Huntley et al. (1992), respectively. On the other hand rip-channel spacing appears to be 5 times the channel width (Haller et al, 2002; Brander and Short, 2001; Aagard et al, 1997).

Based on the above scaling a nearshore bathymetric model domain can be developed that consists of the following composite beach profile configurations: (i) alongshore uniform beach morphology equivalent to the mean profile (open lateral boundary conditions); (ii) alongshore uniform beach profile consisting of the mean profile plus the bar with a height as revealed by the EOF analysis (open lateral boundary conditions); (iii) alongshore variable beach profile consisting as in (ii) with a channel interrupting the bar to simulate the potential of rip current development due to bathymetric features. The latter presents the most rip-favorable condition and accurate simulation of the flows for such conditions can provide the risk for rip current development. The scaling presented in the previous paragraph can be used to define the 3-D bathymetric domain. An experimental design for the domain is shown in Fig. 4.1 consisting of a barred beach incised with 2 rip channels. The profile for the barred beach is obtained by superposition of bar information on the mean profile as in (ii). Profile for the rip channel is created by joining a straight line from the bar trough to the starting or end point of the bar crest (see Fig. 4.2c for further details). The rip channel spacing (L) and channel width (L_t) are calculated by exploiting the ratio with surf zone width (X_c), as provided for by previous field and laboratory studies. The transition from the rip channel to barred beach is done using a sinusoidal function.

4.5 Study Case: Duck, NC

As a demonstration of the proposed methodology we present a study that applies to the bathymetry of Duck, NC. The procedure for the development of the rip current prediction tool consists of three distinct steps: (i) Development of the bathymetric domain; (ii) set up of the numerical domain; (iii) numerical simulations; and (iv) rip-current condition prediction for different waves and/or tidal stages.

4.5.1 Development of Morphology

Beach profiles covering a period of 20 years have been analyzed using Empirical Orthogonal function. The data were collected monthly by the Field Research Facility (FRF), NC (http://www.frf.usace.army.mil/bathy-main.shtml). From the analysis of these data using the EOF analysis a beach profile has been created that is decomposed into a mean ($h(x)$) and a bar $h_1(x)$ function. Figure 4.2a shows EOF 1, the mean profile for entire data set, that explains 98.94% of the variance. The second and third EOFs (Figure 4.2b) are the bar and terrace functions that explain 0.40 and 0.26% of the total variance, respectively. This corresponds to 60.6 and 39.3% of the variability found around the mean profile and these EOFs are indicative of the location, width and height of the bar that develops in the study area. The bar width in this case has been defined as the cross-shore distance from bar trough to the bar crest. Identification of the maximum value and its location along the cross-shore profile is used to identify the bar height and location for each time that measurements exist. The most commonly occurring bar distribution pattern can be superimposed on the mean profile to create possible barred beach profiles and further modified to obtain rip channel profile configurations (Fig. 4.2c). A statistical analysis in the form of a joint probability plot of bar height vs. width, bar distance from shoreline vs. bar width and bar distance from shoreline vs. bar height are used to identify the most

common bar configurations that develop in the study site. This analysis incorporates local information such as sediment size and local wave climate and the longer the data base available the more reliable and significant the correlations are. This joint-distribution analysis for Duck, NC is shown in Figure 4.3. It reveals two types of bars being the most common, which not surprisingly correspond to the development of the so called summer and winter profiles, respectively. Quantitatively, these conditions are: (a) bar located 60m from the shoreline, 1.2m height and 70m wide; (b) bar located 120m from the shoreline, with a height of 1.0m and a width of 70m. Using the scaling analysis discussed in the previous section the channel width and spacing is 40m and 200m for (a) and 80m and 400m for (b), respectively.

These bar characteristics can be superimposed on the mean beach profile (see Fig. 4.1, 4.2) and used to develop the bathymetric domain shown in Figure 4 for two bar cases presented in the next section (hereafter called case A and B, respectively).

4.5.2 Model Set-up

For each condition a model domain is constructed with a grid resolution 4m × 4m in the cross-shore and longshore directions, respectively. The setup of this case study includes normal incidence of alongshore uniform wave height on the bathymetric domain.

The domain for Case A is 500 m in the cross-shore and 640 m in the alongshore direction, while for Case B it is 500 m in the cross-shore and 800m in the alongshore direction. Vertically, the domain is distributed in 10 equally distributed layers. Closed boundary conditions are used at the two lateral sides and the shoreline, while gradient (Neumann) boundary conditions have been used at the offshore boundary. A logarithmic bottom friction is used with a roughness length of 0.005 m, a value close to those reported from field studies (e.g., Feddersen et al., 1998).

The wave model (SWAN) is run for the same grid as ROMS. The wave forcing applied at the offshore boundary is directed perpendicular to the domain, has a period of 8 s and a significant wave height of 2 m. The selected period corresponds to the most commonly occurring period at the site as revealed through a joint probability analysis of wave information from the site. The corresponding most common wave height is 1 m. However, in this test case the wave height was increased to represent increased wave conditions. The wave forcing is described by a directional spectrum consisting of 20 frequency bands in the range 0.04 Hz to 1 Hz, and 36 directional bins of 10° each from 0° to 360° with a directional spreading of 6°. The bottom friction used in SWAN is based on the eddy viscosity model of Madsen et al. (1988) with a bottom roughness value of 0.05 m. The modeling system for this case is configured in two way coupling mode where exchange of wave and current information takes place between ROMS and SWAN at a synchronization interval of 15 s. The coupled model system is run for a simulation time of two hours over which the hydrodynamics achieves stability.

4.5.3 Results

The depth-averaged velocities for each case are shown in Figure 4.4 for a simulation with a mean tidal water level. It is characteristic that for each case a rip-cell develops and occupies the region between the bar and the shoreline, with the main rip-current developing over the rip-channel location. Subtle differences are observed between the two cases. In the case A the offshore directed current develops exactly at the location of the rip channel (some 50 m from the shoreline), while in case B, offshore directed flows start developing well inshore of the rip channel, and intensify at the location of the channel. In both cases the depth averaged offshore directed current is approximately 0.5 ms^{-1}.

The vertical distribution of the cross-shore current for the same conditions are shown in Figure 4.5 for locations over the channel and over the bar for case A and B, respectively. It is characteristic that the flow over the bar in either case is much smaller than thru the channel. Maximum offshore velocities occur in the channel and some 1 m and 1.5 m below the sea surface for case A and B, respectively.

The effect of tidal variability is shown through the comparison of simulations at mean, high and low water levels for the same offshore wave conditions(Fig. 4.6 and 4.7) in case A and B. In case A, the rip current strength at high, mean and low water levels are 0.47 ms^{-1}, 0.61 ms^{-1} and 0.66 ms^{-1}, respectively, while for Case B, these velocities are 0.49 ms^{-1}, 0.58 ms^{-1} and 0.65 ms^{-1}. It is characteristic how the rip current strength increases during the low water conditions, exhibiting a clear dependence of wave conditions to tidal stage.

4.6 Discussion

The model has been shown to predict rip-current conditions for a normal wave incidence. Due to space limitations, no example showing the response of the model for waves approaching from different angles or on the sensitivity of the results on the parameterizations used for the development of the bathymetric domain have been included. These are briefly discussed in this section.

Kumar et al. (2011) presented results on the strength of rip currents as function of angle of wave approach. In that work, the development of rip current circulation on an alongshore bar-trough morphology domain was subjected to offshore waves with height of 0.5 m and period of 3.16 s incident at angles 0°, 5°, 10° and 20° with respect to the shore normal. The results showed that as the wave incidence angle increases from 0° to 20°, the angle of exit of the rip current increases with respect to the shore normal. The trend is linear and for angles greater than 20° the current becomes almost parallel to the shoreline. As expected the strength of alongshore

velocity increased as the wave angle of incidence increases, making longshore current a potential hazard for the nearshore. For normal wave incidence primary and secondary circulation cell formation occurs outside the rip channel and close to the shoreline, respectively. The cells are symmetric about the rip channel center with opposite sign of vorticity indicating reverse sense of circulation. With increasing angle of wave incidence, the secondary circulation pattern weakens but the primary circulation pattern is reinforced. At a wave incidence of 10°, the secondary circulation cell close to the shoreline disappears while 20° incidence shows only one circulation cell which is constrained at the original location where primary circulation was observed.

Overall, Kumar et al (2011) showed that rip current velocity at these locations is stronger when wave incidence is at 5° and 10°. Onshore of the channel, maximum offshore directed flow within the channel area occurs for 5° whereas at transects within the channel, rip current velocity is slightly higher for 10° in comparison to 5° incidence. Higher angles of incidence ($> 20^o$) inhibit rip currents due to inertia of alongshore flow. Aagard et al. (1997) observed similar increase in the rip current velocity due to oblique incidence, while Haller et al. (2002) observed an abrupt increase in cross-shore velocity for wave incidence angle of 10° in their test F. The reason for this behavior is suggested to be due to increase in alongshore radiation stress forcing in alongshore direction created by breaking of obliquely incident waves at the bar crest.

To examine the sensitivity of the model to the parameterization of the bar-trough morphology, we carried out runs for case A after changing the width of the channel while all other parameters remained the same. The results of this exercise are shown in Figure 4.8. It is characteristic that the circulation cell that develops increases with increased channel width, implying that more water mass is exiting through the rip-channel. However, since the channel width has also increased, it appears that the

increased mass of water is trying to exit through an increase cross-sectional area so that net the rip current speed seems to be the same (approx. $0.45 ms^{-1}$).

4.7 Conclusions

In this contribution we presented a methodology to utilize existing historical bathymetric surveys and construct realistically based hypothetical bathymetric data sets to represent local bar/trough morphology. The constructed bathymetry provides several scenarios of realistic cases that can be simulated using a public domain, well-tested, physics-based, full 3-D circulation model (ROMS) with a wave propagation model (SWAN) to nowcast and/or forecast surf zone conditions (i.e., development of rip current and actual expected current strength). Such approach can be implemented using existing wave and current forecasting systems for boundary conditions; bottom morphology created from historical beach profile data or remotely sensed morphology (X-Band radar, Images etc.). The derived predictions are based on runs for different variation of morphology as defined by the historical analysis and the highest rip current speeds should be selected for beach management decisions.

An advantage of this approach is that the methodology incorporates site specific characteristics to provide local characterization of the flows. However, the authors recognize and caution that knowing the strength of the rip current does not contribute to the protection from the hazards of rip currents. Instead the goal is for this information to be provided to the beach management personnel for use as a part of a comprehensive decision making tool that includes other parameters such as sociological, beach safety personnel availability etc. One aspect that this tool can contribute significantly is to provide a-priori knowledge of the conditions to be expected to assist planning and optimized deployment of available resources. Finally, prior to implementation as an operational tool, a period of intense evaluation is highly recommended.

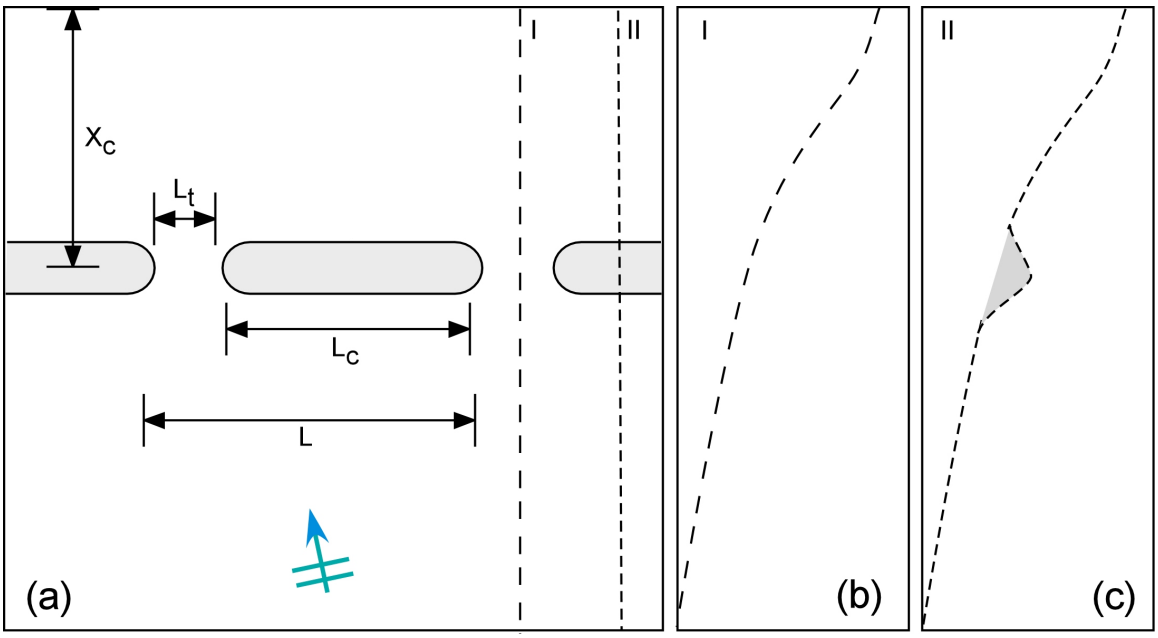

Figure 4.1: Schematic diagram showing the length scales required to construct a bar trough morphology domain to model rip current channel. (a) Plan view; (b) and (c) beach profiles at rip channel and over bar respectively. The bar length (L) will be 3.3 times the length of the surf zone width (X_c) which will be estimated from empirical orthogonal functional (EOF) analysis on time series of beach profile, while the channel width (L_t) will be taken L/5.

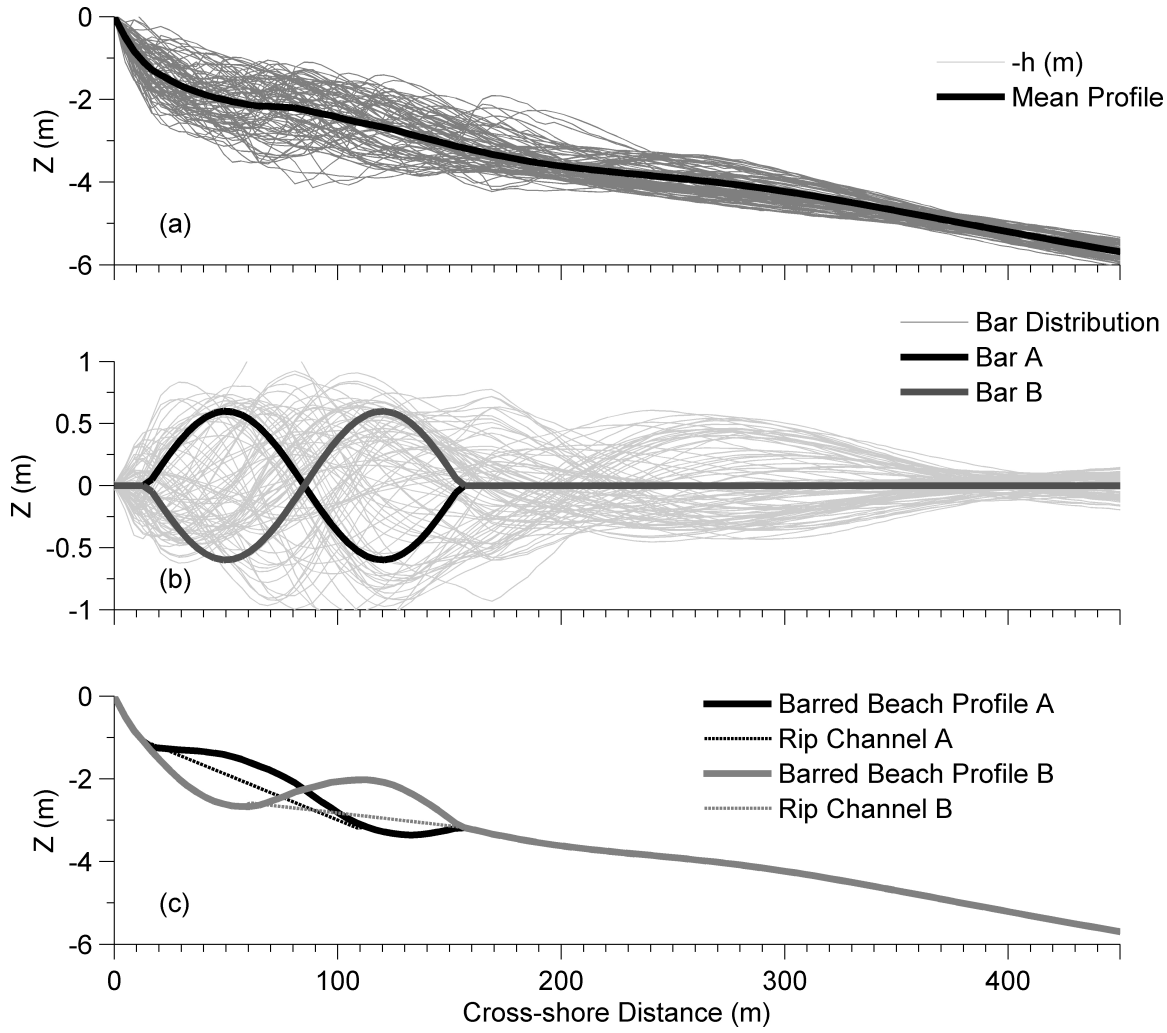

Figure 4.2: EOF analysis of 20 year long, monthly beach profile record at Duck, NC and the creation of a synthetic profile. (a) Individual profiles (grey lines) and mean profile (black line) as obtained by EOF; (b) Cross-shore profile of bar functions obtained from EOF analysis on individual profiles. The solid and dashed lines show two most commonly occurring bar distribution; (c) Solid black and grey lines correspond to the barred beach profiles obtained by adding the mean profile in (a) to bar distribution in (b). The dashed black and grey lines show the rip channel profile obtained by joining a straight line from bar trough to end or beginning of the bar crest for Case A and B, respectively.

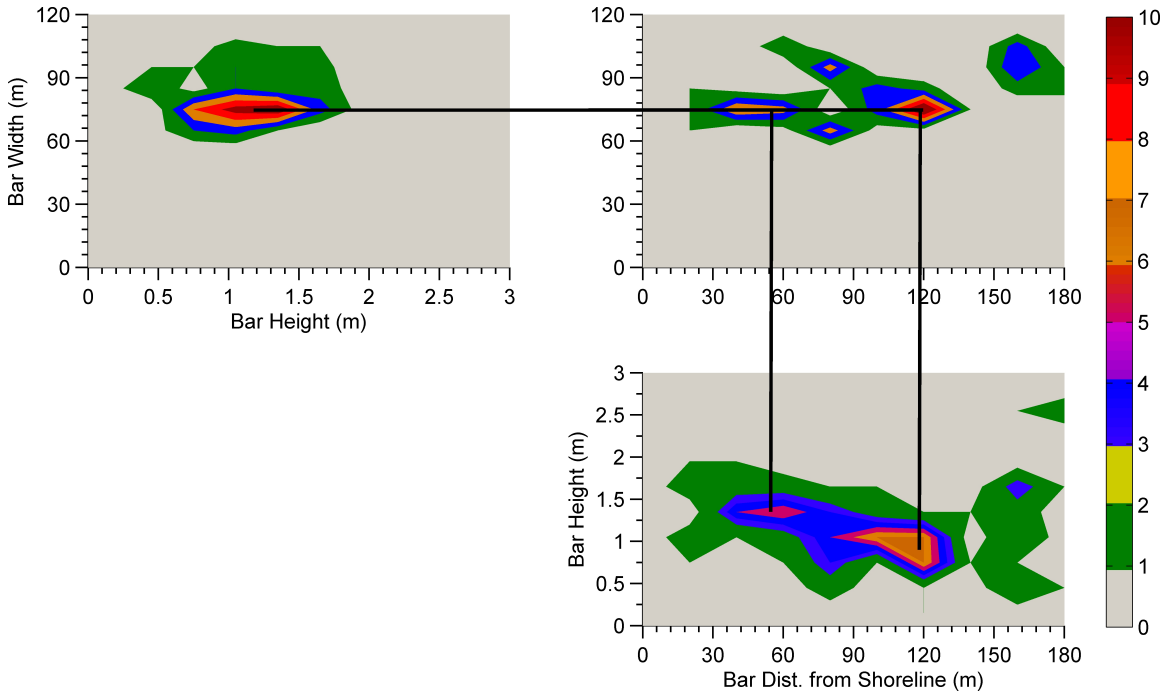

Figure 4.3: Joint probability distribution of bar characteristics (bar width, height, distance from shoreline) for Duck NC. Bar characteristics identified from the EOF analysis (see Fig. 4.2). Note two distinct bars occurring that correspond to typically observed summer and winter profiles.

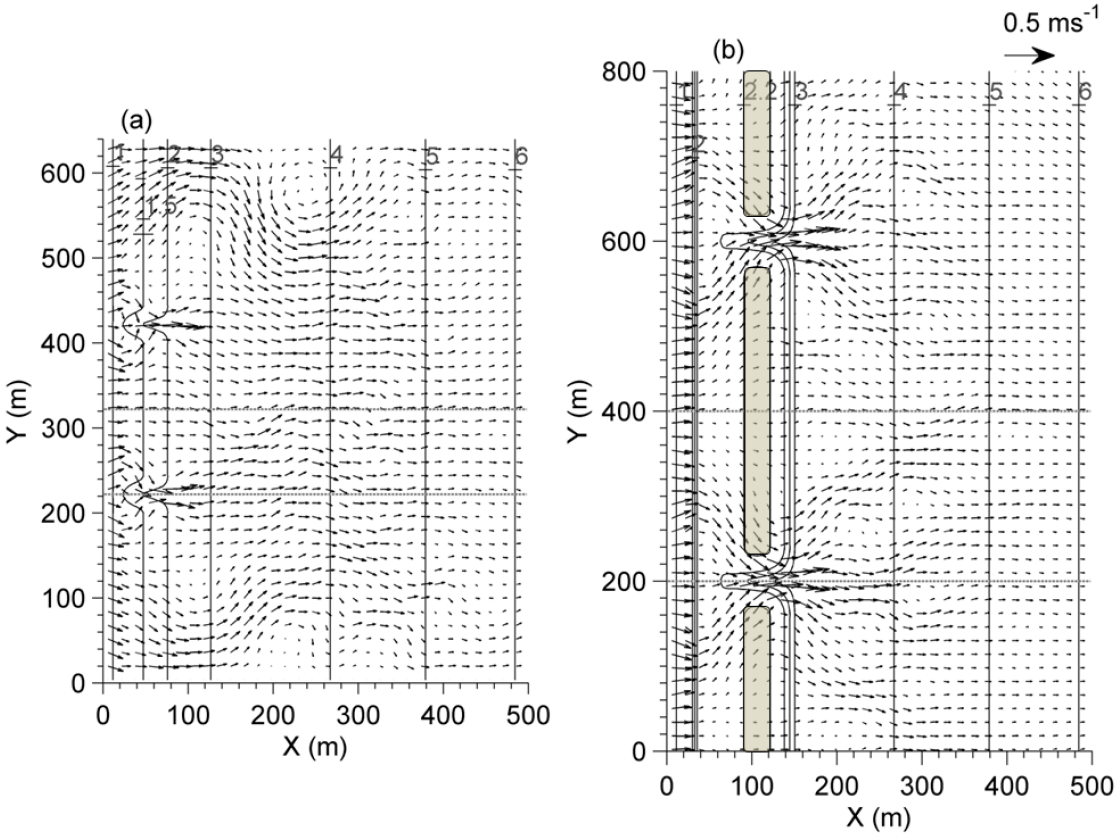

Figure 4.4: Synthetic bar-trough morphology for cases A and B (left and right panels, respectively) and corresponding depth-averaged current vectors for an incoming wave with 2m height, period of 8s, approximately perpendicular to the coastline. The solid white lines show the bathymetry contour, while the black arrows show the direction and magnitude of the flow field. The dashed grey lines indicate location of transects at which the vertical profile of cross-shore velocity are considered in Fig. 4.5, 4.6 and 4.7.

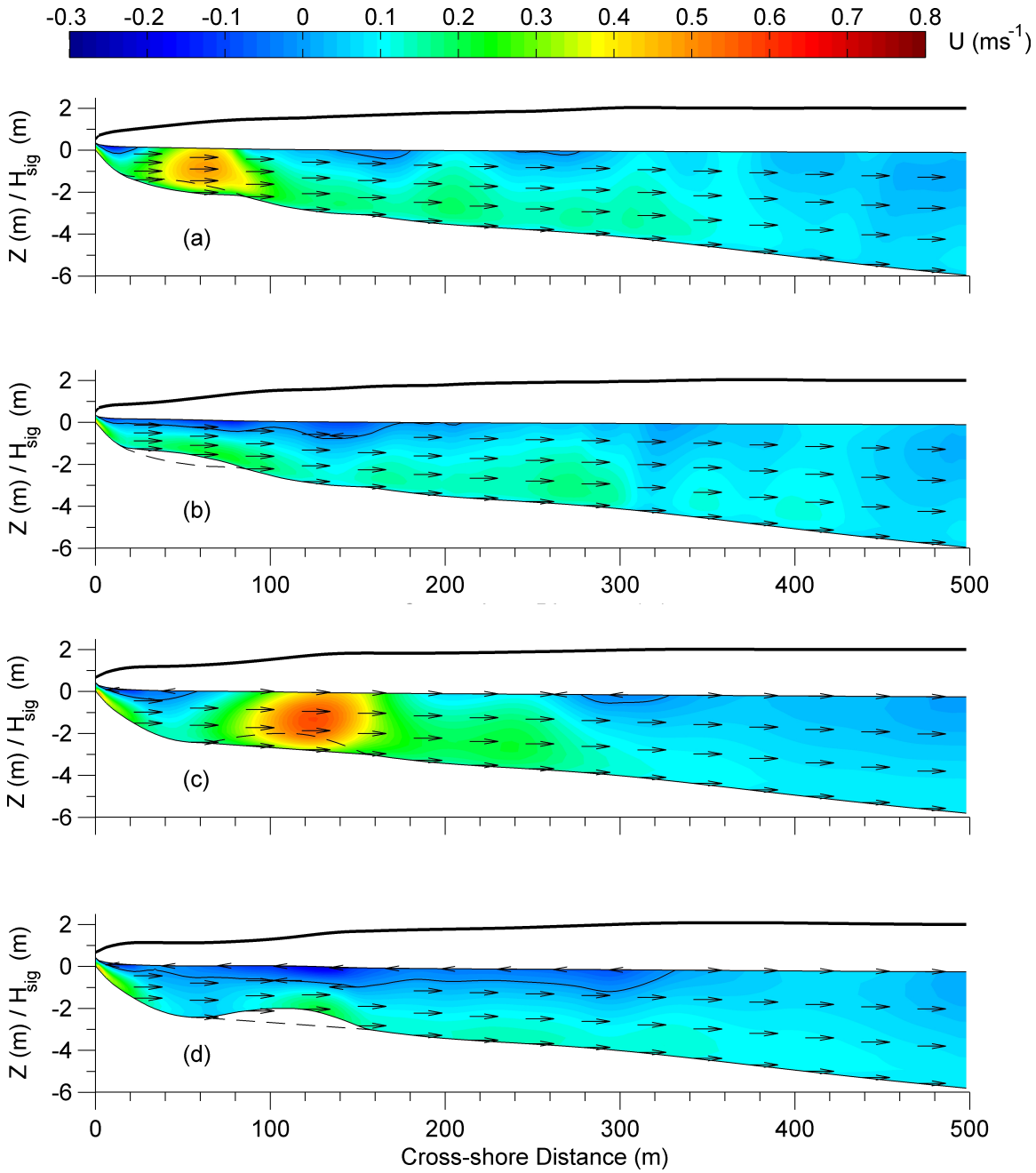

Figure 4.5: Vertical distribution of cross-shore velocity at the center of the rip channel (a and c) and bar (b and d) for bathymetric domain corresponding to case A (a and b) and B (c and d), respectively. Thick black lines show the cross-shore profile of significant wave height. The location of transects is shown in Fig. 4.4.

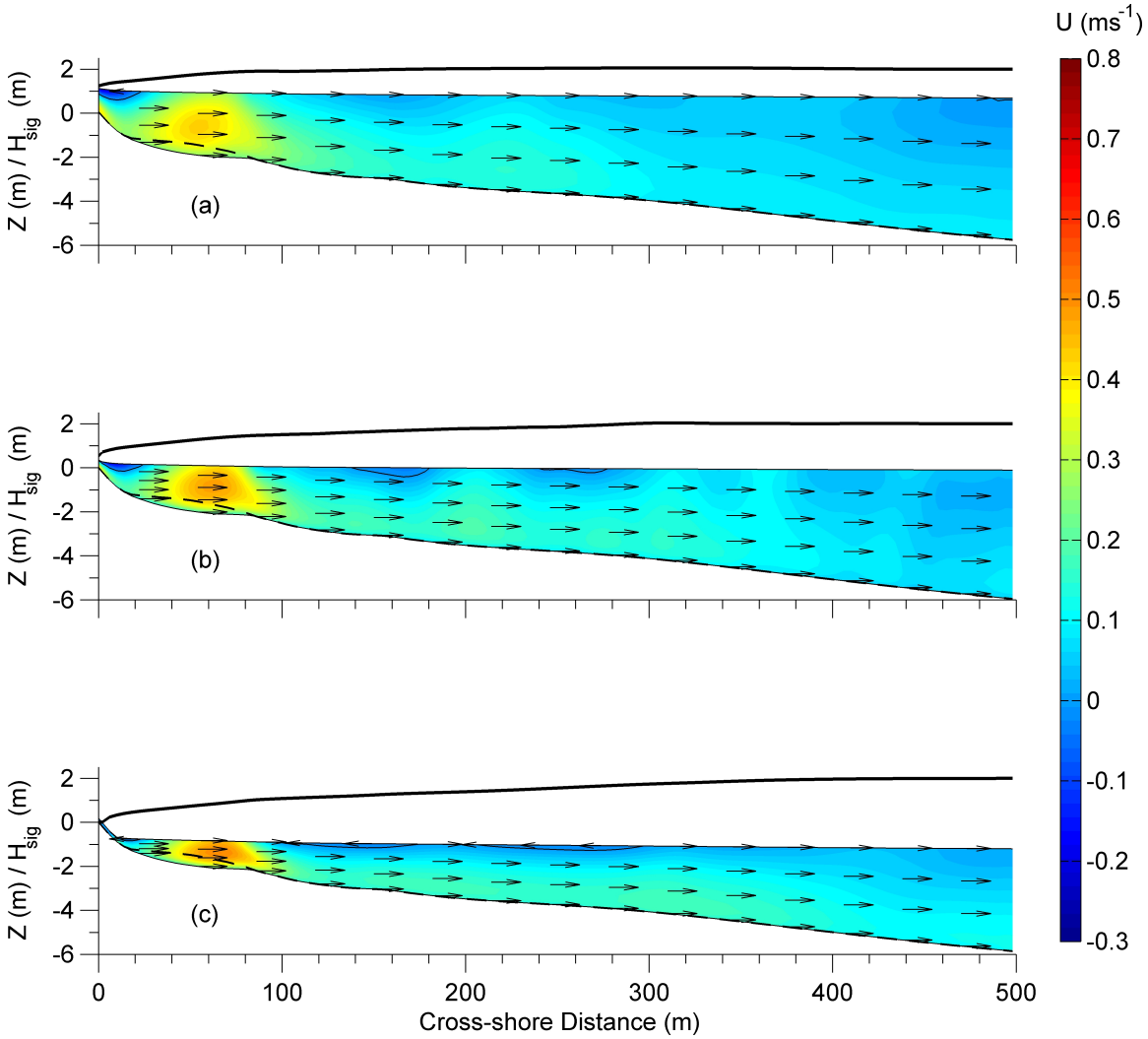

Figure 4.6: Cross-shore velocity (color contours) and significant wave height (black line) distribution along a transect through the rip channel location (case A) for three tidal stages: (a) high; (b) mean and (c) low water levels. Thin black lines represent wave height distribution across the domain as estimated by SWAN. Note how the speed of the rip current increases with decreasing water level, while the offshore location of the maximum rip speed remains the same. The arrow direction indicates direction of flow; while the color contours indicate strength of the current.

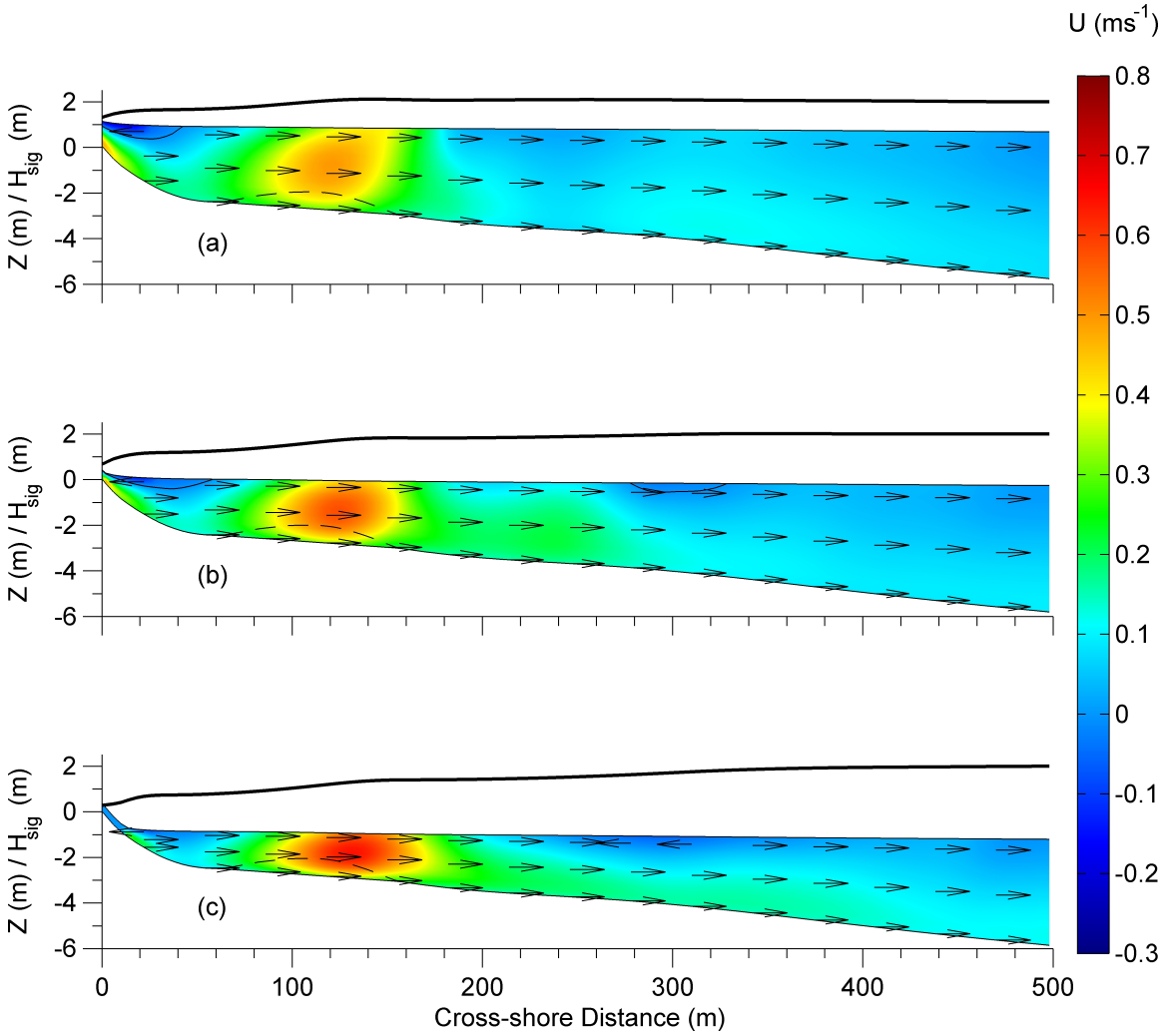

Figure 4.7: Cross-shore velocity (color contours) and significant wave height (black line) distribution along a transect through the rip channel location (case B) for three tidal stages: (a) high; (b) mean and (c) low water levels. Thin black lines represent wave height distribution across the domain as estimated by SWAN. Note how the speed of the rip current increases with decreasing water level, while the offshore location of the maximum rip speed remains the same. The arrow direction indicates direction of flow, while the color contours indicate strength of the current (units in color bar are m/s). The relative location of the bar is shown as a grey line.

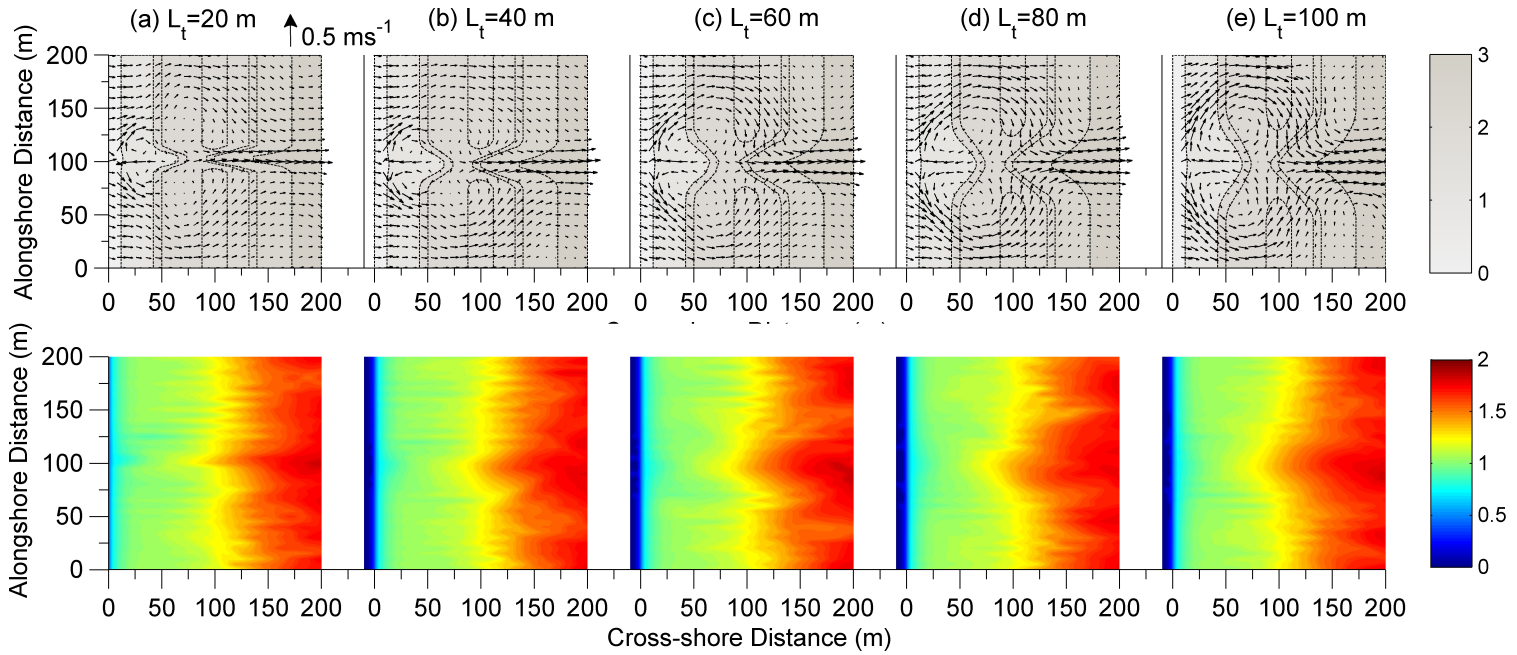

Figure 4.8: Circulation (depth averaged current vector, top row) and significant wave height distribution (bottom row) for the bathymetric domain corresponding to case B but with a varying channel width, (a) L_t=20m; (b) L_t=40m; (c) L_t=60m; (d) L_t=80m; (e) L_t=100m. Note: Only relevant part of the model domain has been shown here.

Chapter 5

Alongshore momentum balance analysis on a cuspate foreland[1]

[1]This chapter is presently in review with Journal of Geophysical Research.

Abstract

Nearshore measurements of waves and currents off Cape Hatteras, North Carolina, U.S.A, are used to investigate depth-averaged subtidal circulation and alongshore momentum balances in the surf and inner shelf region around a cuspate foreland. Data were collected on both sides of the cape representing shorefaces with contrasting shoreline orientation (north-south vs. northwest-southeast) subjected to the same wind forcing. In the nearshore, the subtidal flow is aligned with the local coastline orientation while at the cape point the flow is along the existing submerged shoal, suggesting that cape associated shoals may act as an extension of the coastline. Alongshore momentum balance analysis incorporating wave-current interaction by including vortex and Stokes-Coriolis forces reveals that in deep waters surface and bottom stress are almost in balance. In shallower waters, the balance is complex as nonlinear advection and vortex force become important. Furthermore, linearized momentum balance analysis suggests the vortex force can be of the same order as wind and wave forcing. Farther southeast of Cape Hatteras point, wind and wave forcing alone fail to fully explain subtidal flow variability and it is shown that alongshore pressure gradient as a response to the wind forcing is required to close the momentum balance. Adjacent tide gauge data suggest that the magnitude of pressure gradient depends on the relative orientation of local coastline to the wind vector, and the pressure gradient generation due to change in coastline orientation even at km length scale is analogous to the effect of alongshore variable winds on a straight coastline.

5.1 Introduction

Subtidal, wind driven circulation has been the subject of numerous experimental studies conducted at different nearshore environments along the US coast that include: the Middle Atlantic Bight (MAB) (e.g., Feddersen et al., 1998; Lentz et al., 1999; Lentz, 2001); the inner and mid shelf in Northern and Southern California (Lentz, 1994; Lentz and Winant, 1986); Central Oregon Coast (Kirincich and Barth, 2009); the South Atlantic Bight (SAB) (Gutierrez et al., 2005); and Martha's Vineyard (Fewings and Lentz, 2010). These studies have enhanced our understanding of wind-driven circulation and have identified the most important constituents of the momentum balance equation (see Lentz and Fewings, 2012 for a detailed review).

It is only recently (Lentz et al., 2008; Fewings and Lentz, 2010) that the role of the Stokes-Coriolis force term (Hasselmann, 1970) has been considered in studies of shelf circulation. Vortex force (hereinafter referred to as VF) is another wave related term (Craik and Leibovich, 1976) that represents the interaction between wave-induced mass drift and mean flow vorticity. Although no direct experimental data exist, results from recent modeling studies (Uchiyama et al., 2010; Kumar et al., 2012) have shown that nonlinear advection and VF can be dominant in the nearshore and especially within the surf zone. The contribution of these terms is expected to be more pronounced in regions with complex bathymetric features such as barred beaches and shallow regions with shoals present. Further, the role of VF also becomes important in areas with strong horizontal shear in cross/alongshelf velocity.

Studies of flows around complex coastline configurations such as those found around capes (i.e., McNinch et al., 2000) or over bathymetric features (i.e., Sanay et al., 2007) are limited mainly to tidal time scales. Roughan et al. (2006) and Gan and Allen (2002 a, b) presented work on wind-driven flows around capes, but the focus was mainly on upwelling dynamics in the leeward side of a cape, while transient wind

driven circulation in a region with alongshelf topographic variations was studied by Barth et al. (2005). Capes are characterized by abrupt changes in coastline orientation and a complex bathymetry and their role in subtidal circulation processes is not clear yet. Experimental data from such a location are used in this contribution to reveal some of these interactions of coastline shape, waves and subtidal flow dynamics. In particular, the objectives of this work are to: (a) identify the subtidal circulation pattern in the inner shelf region around a cuspate foreland system with a complex morphology; (b) experimentally assess the role of VF and nonlinear advective acceleration terms in this subtidal circulation; and (c) reveal the response of the surf zone and inner shelf for a non-uniform coastline and complex bathymetry to surface waves and wind fields. In this contribution we present estimates of VF and nonlinear acceleration terms from a combination of in situ data and a simplified momentum balance model, which are compared to wind stress and wave breaking induced acceleration.

First we describe the study area and the data collection procedures in Section 5.2. This is followed with an overview of the hydrodynamic conditions encountered in terms of wave activity and subtidal flows (Section 5.3), while in Section 5.4 the depth-averaged momentum balance is presented. The findings are discussed in Section 5.5 while the final conclusions are presented in Section 5.6.

5.2 Data Collection

Inner shelf hydrodynamic data were collected over the period February 3 to 22, 2010 (Table 5.1) on Cape Hatteras, NC. The study site has a typical cape coastline configuration characterized by abrupt changes in orientation and a complex bathymetry. The coastline is oriented approximately 10° N on the east side (see Figure 5.1), which is re-oriented to 166° N at the Cape Hatteras point, transitioning to an orientation of 120° N farther west. These two sides around the cape point, with distinctly dif-

ferent coastline orientations, are subsequently referred to as the east and south sides, respectively. The bathymetry in the area is complex, consisting of a shoal (Diamond Shoals) that extends from the cape point to some 20km offshore toward the SE (see Figure 5.1d). On the east side and farther away from the shoal, the bathymetric profile (see Transect 1 in Figure 5.1c) reveals a typical barred beach with an inner and an outer bar. The beach slope varies from 0.040 inshore of the inner bar to 0.004 offshore of the outer bar. Farther south and closer to the shoal (see Transect 2 in Figure 5.1c) the bathymetry is more complex due to the presence of obliquely aligned transverse ridges. A transect from Cape Hatteras point along the axis of Diamond shoals (see Transect 3 in Figure 5.1c) reveals a foreshore slope of 0.040 and an irregular bathymetry farther offshore. On the other hand, the south side is characterized by a relatively simple beach profile consisting of a single inner bar (see Transects 4 and 5 in Figure 5.1c). The foreshore slope is 0.030, and reduces to 0.004 farther offshore.

Wave and current data were collected at 13 locations dispersed throughout the area (see Figure 5.1 and Table 5.1). Three of the sites (O1, O2, and O3) were at relatively deeper water depths of approximately 9-10 m. The remaining of the stations were located in the nearshore with 4 of them (N1 to N4) located on the east side, 2 (N11 and N12) on the south side and the remaining 4 stations (N5, N6, N8 and N9) over the shoal itself. The instrumentation consisted of acoustic current meters (Nortek Aquadopp and Teledyne RDI ADCP profilers) programmed to resolve both mean and wave-induced flows by measuring three-dimensional flow velocities (bin size 40 cm) and pressure fluctuations with a sampling frequency of 1 Hz. The type of acoustic instrument for each station, their deployment depth and other details relating to the data collection are listed in Table 5.1. The Aquadopps collected data continuously while the ADCPs were deployed in a burst data collection mode, recording 1,024 data points every hour, centered on the hour. Details of the instrumentation deployment

and other auxiliary measurements not presented in this manuscript can be found in List et al. (2011).

The continuous records from the Aquadopp instruments were divided in 1,024 sec segments centered on 0, 15, 30 and 45 min past the hour. This segmentation resulted in a 24 sec overlap between adjacent segments. ADCP data was already available in bursts of 1024 seconds centered on the hour resulting in simultaneous hourly data from all instruments. Instantaneous pressure (p) and horizontal (u, v) velocities from the bin closer to the sea bed were used to calculate power spectral and cross-spectral densities using Welch's (Welch, 1967) method of spectral estimation using 15 ensembles of 128 data points with 50% overlap. The pressure spectra were converted to sea surface elevation spectra after correcting for pressure attenuation with depth using linear wave theory (Bishop and Donelan, 1987). The sea surface power spectral density and cross-power spectral density values were then used to calculate the wave height, period, direction and directional spreading using the moments method (Herbers et al., 1999). Identification of wave energy and directional characteristics for swell and wind waves was carried out by integrating the wave spectra over the frequency bands below and above 0.1 Hz, respectively.

Mean flows were estimated by averaging the instantaneous flows measured within each 1,024 sec segment. In addition, mean flows from all the bins were linearly extrapolated to the surface and seabed, and then averaged to obtain estimates of depth-averaged mean flows. Finally, these depth-averaged flows were low-pass filtered (Beardsley et al., 1985) to remove tidal and other oscillations occurring at periods less than 33 hours. Meteorological data for the deployment period and offshore wave data were obtained from the NOAA/NDBC Diamond shoals buoy (ID 41025, Figure 5.1b).

5.3 Results

In this section, the filtered, sub-tidal flows and wave data are presented together with the atmospheric conditions prevailing during the data collection period. Data only from sites O2, O1, N5, N6, N9 and N8 are presented because of their relative deployment locations, which are optimal for resolving momentum balance forces in the alongshore direction.

5.3.1 Offshore Conditions

Time series of the offshore meteorological and wave conditions from NOAA Buoy 41025 during the data collection period are shown in Figure 5.2. Three high wave energy events are identified that coincide with the passage of two warm and one cold front systems (Figure 5.2a). The passage of the first warm front system occurred during February 5-7, 2010 (referred to as Event F1), and is characterized by wind speeds in excess of 12 ms^{-1} directed towards the southwest initially and rotating towards the northeast later on (Figure 5.2a). The maximum offshore wave height recorded was 6 m (Figure 5.2b) with periods varying from 5 to 10s (Figure 5.2d). This event was associated with a drop in atmospheric pressure (Figure 5.2e) and an increase in both air and water temperature (Figure 5.2f). This event was followed by a cold front system (Feb. 10-12, 2010, Event F2), with winds from the north/northwest initially, changing to east/southeast later on; the maximum wave height recorded was 3 m. After the passage of this second frontal system, increased wave energy concentrated mainly on the swell wave band (Figure 5.2c) is observed. The two periods (Feb. 7-9 and Feb. 12-13, 2010) when the ratio of swell to sea wave energy is greater than 1.25 are referred to as swell events and denoted with S1 and S2, respectively. The wave height measured at the offshore buoy during these events (Figure 5.2b) varied between 2 and 3 m. The third event (Feb. 15-16, 2010, Event

F3) was due to a warm front similar to event F2 but of reduced intensity. The sea temperature record from the same offshore location appears to respond to fluctuations in the air temperature (Figure 5.2f), suggesting that the 50-60 m isobath is not influenced by warmer Gulf Stream waters, and neither is our study area located farther inshore.

5.3.2 Nearshore Conditions

Time series of mean water depth, root mean square wave height (H_{rms}), peak (T_p) and mean (T_m) wave periods, and mean wave direction (measured clockwise from north) estimated from the data collected at sites O2, N5 and N6, located on the east side of the Cape Hatteras point are shown in Figure 5.3 (left panel). Water depth variation is primarily due to tides (Figure 5.3a1), while the wave height (Figure 5.3b1) varied between 0.5 and 3m for the entire data collection period with the peak wave period (Figure 5.3c1) fluctuating between 5 and15 s. Swell waves (T_p > 10s) approached the shoreline from the northeast (see Figure 5.3d1) while gravity wind waves (T_p < 10s) tended to approach from the east-southeast. During periods of low wave activity (see Feb. 16-22, 2010), both wave height (Figure 5.3b1) and direction (Figure 5.3d1) show a tidal modulation, revealing the influence of wave refraction and depth-limited leakage of wave energy over the shoal.

The most energetic wave events in the records are associated with the passage of the first warm front (event F1) and the swell event S1. During event F1, negligible cross-shore variability in wave height is observed between stations O2, N5 and N6, while the wave height reduces substantially as it approaches the shore during event S1 (Figure 5.3b1). The dissipation of wave energy per unit distance from site O2 to N5 is three orders of magnitude higher than typical dissipation rate of swell waves due to bottom friction (e.g., Herbers et al., 2000), suggesting wave breaking between these sites primarily occurs due to depth limited wave breaking. The wave forcing

during other frontal passages (event F2 and F3) were similar to event F1, but less energetic when compared to event F1.

In contrast to the conditions recorded on the east side, on the south side (Figure 5.3, right column) smaller wave heights were measured (0.5 to 2.5m) with peak wave periods ranging from 5 to 15 s. The general wave direction (Figure 5.3d2) was consistently from the southwest for all events with the highest wave conditions recorded during event F1 (Feb. 5-7, 2010). A similar but weaker response is seen during the passage of the other two fronts (Feb. 10-12 and 15-16). Interestingly, in this (south) side, swell height during events S1 and S2 was small (Figure 5.3b2) while mean swell direction varied from south to southwest. The tidal modulation of swell direction on the south side suggests refraction of swell waves around the shoal. This combined with dissipation due to bottom friction and depth limited wave breaking over the shoal, leads to a significantly reduced swell height when compared with that recorded on the east side for the same events.

5.3.3 Subtidal Flows

Synoptic Flows

The low pass filtered wind stress exhibits large variability (Figure 5.4) around its mean value, with the principal axis of the variance ellipse being almost perpendicular (120°) to the coastline on the east side and almost parallel to the coastline orientation further west of the Cape Hatteras point. The strongest flows were measured at site N6 with a southward mean direction. The principal axes of the subtidal flow variance ellipses at sites O3, N1, N2, N3, N4 and O2 are parallel to the local coastline orientation (Figure 5.4); at sites N5 and N6 the ellipse is rotated and aligned with the local bathymetric contours that define the orientation of the shoal itself (see Figure 5.4). Also, the eccentricity of the ellipses in these sites decreases, indicating the existence of some cross-shoal flows. Furthermore, it is worth noting that the mean flows at N1,

N5 and N6 do not align with the major axis of the subtidal ellipse possibly due to bathymetric rectification.

On the south side, the variance ellipses are aligned to the local coastline orientation away from the shoal (i.e., sites N11 and N12), while at sites O1, N8 and N9, the orientation of the principal axis becomes parallel to the bathymetric contours. The mean flows at all sites on the south side are obliquely oriented to the ellipse semi-major axis with the exception of site N11.

In order to examine the balance of the wind and hydrodynamic forces, the depth-averaged subtidal flow and wind vector components are rotated into two local coordinate systems corresponding to the respective local coastline orientations (10° and 166° N) for the east and south sides, respectively (see Figure 5.4). In each one of these new coordinate systems positive cross-shore velocity values indicate offshore directed flows while positive alongshore velocities indicate northeastward flow at the east side and southeastward flow at the south side. Correlation coefficients (r) between the alongshore and cross-shore components of wind stress and measured flow (subsampled with a decorrelation time scale of 33 hours, see section 5.4.2) for each site are presented in Table 5.2.

Local cross-shore wind stress shows a negative correlation with alongshore flows on both sides of the cape with those on the south side being larger (-0.67 to -0.77) than those on the east side (-0.29 to -0.51, not significant at 95% CI). On the other hand, local alongshore wind stress is highly (0.83 to 0.90) and moderately (0.54 to 0.63) correlated with alongshore flows on the east and south sides, respectively. Correlation of the wind components with the cross-shore flows is generally variable with strong and statistically significant correlations (see Table 5.2) found only for site N8.

In the east side, at sites O2, N5 and N6 the alongshore flow responds to the alongshore wind stress with a small time lag (~1 hour) during all events (Figs. 5.5a1 and b1). The highest alongshore and cross-shore current speed were measured during

events F1 and S1 (Figs. 5.5b1 and c1), while the flow response was weaker for all other events. In the south side, although the highest alongshore wind stress occurs during event F1, the subtidal response of the alongshore flow (at sites N9 and O1) is relatively weak (< 0.2 ms^{-1}) and with a direction opposite of that of the wind (Figure 5.5b2). Alongshore current velocities at site N8 are of the same magnitude as those at site N9 but they are directed towards the northeast. For events F2 and F3 the data from sites O1, N9 and N8, show a direct response of the alongshore flows to the wind stress, while cross-shore flows are usually negligible except at site N8 during event F2 (Fig 5b2).

Overall, circulation on the east side of Cape Hatteras point appears to be driven primarily by wind stress, while on the south side wind stress alone does not seem to be adequate to explain the observed circulation. These flows are further examined through a depth-averaged, alongshore momentum balance analysis which is presented next.

5.4 Momentum Balance Analysis

The goal of this section is to identify the drivers of observed circulation patterns on both east and south side of Cape Hatteras using a depth-averaged form of the momentum balance equations presented in Kumar et al. (2012). In comparison to Lentz et al. (1999), these equations contain two more terms: (a) Stokes-Coriolis force (effect of Earth's rotation on surface gravity waves) and (b) the horizontal component of vortex force (interaction between Stokes drift and mean flow vorticity). In its full flux form the depth-averaged alongshelf momentum balance equation can be written

as:

$$\underbrace{\frac{\partial \overline{v}}{\partial t}}_{\text{LA}} + \underbrace{f\overline{u}}_{\text{CA}} + \underbrace{f\overline{u^{St}}}_{\text{SC}} + \underbrace{\frac{1}{h}\frac{\partial}{\partial x}\left(\int_{-h}^{0}(uv)\,dz\right) + \frac{1}{h}\frac{\partial}{\partial y}\left(\int_{-h}^{0}(vv)\,dz\right)}_{\text{HA}} + \underbrace{\frac{\overline{u^{St}}}{h}\left\{\frac{\partial}{\partial y}\left(\int_{-h}^{0} v dz\right) - \frac{\partial}{\partial x}\left(\int_{-h}^{0} u dz\right)\right\}}_{\text{VF}} + \underbrace{\frac{\tau_{by}}{\rho_o h}}_{\text{BS}} = \underbrace{\frac{-1}{\rho_o}\frac{\partial p}{\partial y}}_{\text{APG}} + \underbrace{\frac{\tau_{sy}}{\rho_o h}}_{\text{SS}} - \underbrace{\frac{-1}{\rho_o h}\frac{\epsilon_b k_y}{\sigma}}_{\text{BA}} \tag{5.1}$$

where u and v are the cross-shore and alongshore subtidal velocity components with the overbar denoting depth averaging; z is the elevation above mean sea level; h is water depth; f is the Coriolis parameter (=8.43×10-5 s^{-1}); and ρ_o is the reference density (=1,024 $kg{\cdot}m^{-3}$).

In this study the various terms of equation (5.1) are estimated using data from Sites O2, N5, N6, O1, N9 and N8. Estimation of the nonlinear (NA) and VF terms require the calculation of gradients in the cross-shore (x) and alongshore (y) directions. Although cross-shore gradients were estimated (see Section 5.4.1), the instrument layout did not allow us to obtain reliable alongshore gradients for the majority of the sites. However, a comparison of depth-averaged alongshore velocities between site pairs (O2, O3) and (N3, N5) did not reveal any substantial alongshore gradient and therefore we have assumed that these terms are negligible. In addition, due to low resolution of the pressure sensors installed on the acoustic sensors no accurate pressure gradient terms could be estimated, thus we elected to omit these terms as well. These assumptions allow us to simplify equation (5.1) to:

$$\frac{\partial \overline{v}}{\partial t} + f\overline{u} + f\overline{u^{St}} + \frac{1}{h}\frac{\partial}{\partial x}\left(\int_{-h}^{0}(uv)\,dz\right) + \frac{\overline{u^{St}}}{h}\left\{\frac{\partial}{\partial y}\left(\int_{-h}^{0} v dz\right)\right\} + \frac{\tau_{by}}{\rho_o h} = \frac{\tau_{sy}}{\rho_o h} - \frac{-1}{\rho_o h}\frac{\epsilon_b k_y}{\sigma} \tag{5.2}$$

5.4.1 Calculation of alongshore momentum balance terms

The local acceleration term $\partial\overline{v}/\partial t$ is calculated using a forward differencing scheme although usage of a central differencing method did not provide any different results

from what is shown here. The Coriolis acceleration is obtained as a product of Coriolis parameter and subtidal, depth-averaged cross-shore currents.

Wind stress is estimated using the wind data from NOAA-NDBC Diamond shoals buoy (see location in Figure 5.1b) utilizing the neutral drag law of Large and Pond (1981) after correcting for the elevation of the wind sensor above the sea surface and accounting for the influence of waves (Large et al., 1995). It is assumed that the wind velocity remains uniform over the entire study area as the vector correlation between winds measured at Diamond Shoals and Oregon Inlet some 90 km away (see Figure 5.1b) was found to be 1.56 (Crosby et al., 1993).

Bottom stress is estimated using the method of Styles and Glenn (2002) that accounts for enhanced roughness due to the presence of waves, a process which becomes important in shallower inner shelf waters as is the case in here. The Stokes-Coriolis force term was estimated using a depth-averaged Stokes velocity derived from the directional wave properties estimated from the wave measurements at each site using:

$$\overline{\mathbf{u^{St}}} = \frac{gH_{sig}^2}{16ch}\hat{\mathbf{k}} \tag{5.3}$$

where, H_{sig} is the significant wave height, g is the acceleration due to gravity, c is the phase speed of wave, h is the water depth and $\hat{\mathbf{k}}$ is the unit wave vector.

When no data with high spatial resolution are available the NA and VF terms can be estimated assuming a no flux condition at the coastline as in Fewings (2007) and Kirincich and Barth (2009). This method assumes that the alongshore and cross-shore velocities decrease monotonically from the most inshore measurement site to the no flux point at the coastline and as such is highly sensitive to location of the inshore station in relation to the coastlines and the shape of the bathymetric profile. Shoaling waves and surf zone dynamics suggest the existence of a maximum in longshore currents (and associated flux) inside the surf zone which is missed if the inshore station is farther offshore. In order to identify that maximum velocity and obtain a better approximation of the NA and VF terms, a linearized alongshore

momentum balance equation is used to calculate cross-shore distribution of depth-averaged alongshore velocity ($\overline{v}$, see Sec 5.5.3). This basic equation does not consider the NA and VF terms while bottom stress is approximated as a linear drag. This method assumes that wave breaking induced acceleration (obtained from a third generation wave propagation model Simulating Waves Nearshore, Booij et al., 1999, Sec 5.5.3) and wind stress are the only forcing terms.

The VF term is calculated from the simplified model as the product of the depth-averaged, cross-shore Stokes drift obtained from the wave parameters (equation (5.3)) and cross-shore gradient of depth-averaged alongshore velocity ($\overline{u^{St}}\partial\overline{v}/\partial x$), while NA is approximated at each site as the product of measured depth-integrated cross-shore velocity and the estimated cross-shore gradient of depth-averaged alongshore velocity ($\overline{u}\partial\overline{v}/\partial x$). At this point we should mention that these estimates have similar magnitude as those obtained directly from field observations assuming no flux conditions at the coastline (not shown here).

Finally, following Lentz et al. (1999) the breaking acceleration term shown in equation (5.2) is estimated from the directional wave properties measured at each site using the wave dissipation model of Church and Thornton (1993):

$$\epsilon_b = \frac{3\sqrt{\pi}}{16}\rho_o g \frac{B_b^3 f_p}{D} H^3 \left[1 + tanh\left\{8\left(\frac{H_{rms}}{\gamma_b D}\right)\right\}\right]\left[1 - \left\{1 + \left(\frac{H_{rms}}{\gamma_b D}\right)^2\right\}^{\frac{-5}{2}}\right] \tag{5.4}$$

which is subsequently used to estimate the breaking acceleration:

$$BA = \frac{1}{\rho_o h}\frac{\epsilon_b k_y}{\sigma} \tag{5.5}$$

where, H_{rms} is the root mean square wave height; f_p is the wave frequency; σ is the angular frequency ($2\pi f_{\mathrm{p}}$); k_y is the alongshore component of wavevector ($\mathbf{k}$); g is the acceleration due to gravity. B_b (= 0.72) and γ_b (=0.24 to 0.40) are empirical parameters (e.g., Chen et al., 1997) that depend on beach profile type and wave conditions. Using this method, wave breaking conditions were identified during the periods Feb. 7-9 and 5-7, 2012 for the east (sites N5 and N6) and south (site N8)

sides respectively (Figs. 5.6b1 and 6b2), with γ_b values ~ 0.30. When wave breaking is not evident, the breaking acceleration term is set to zero.

5.4.2 Depth-averaged, simplified alongshore momentum balance

The time-series of the momentum balance terms shown in equation (5.2) are displayed in Figures 5.6 and 7 for both east and south sides. Considering that the mean values of most of these terms are close to zero, their standard deviation (see Table. 5.3) provides an indication of the term's relative importance. Overall, bottom stress (BS), surface stress (SS), breaking acceleration (BA), nonlinear advective acceleration (NA) and vortex force (VF) have high standard deviation values, while the contribution of local (LA), Coriolis (CA) and Stokes-Coriolis (SC) acceleration is smaller, except at site N5 where VF is of the same order as LA, CA and SC.

The temporal and spatial variability of the alongshore momentum balance terms provide some additional insights on the response of the shelf during this experiment. Both the LA (Figs 5.7a1 and a2) and CA (Figs 5.7b1 and b2) terms show the expected variability in response to wind and wave forcing. The Stokes-Coriolis term (Figs. 5.7c1 and c2) becomes important during both front and swell events due to increased wave activity. In deeper waters (e.g., site O2), its magnitude is similar to Coriolis acceleration during swell events. The NA and VF terms, both become important only during the first front (event F1) and swell event S1 (see Figs. 5.7d1, e1, d2 and e2). The magnitude of these latter terms is higher at sites N6 and N8 than at sites N5 and N9 while the NA term is usually slightly greater than VF.

A re-arrangement of the terms in equation (5.2) into forcing and response ones allows us to examine the two groups separately. Although there is no strict definition of "forcing" and "response", in here we define as forcing the terms that can drive flow (i.e., terms that do not depend on velocity, i.e., wind and waves). The remainder terms that depend on velocity (alongshore or cross-shore) are considered to represent

the response of the system to the forcing. It should be noted that since part of NA can be balanced by VF (see Figs. 5.7d1, 5.7d2, 5.7e1 and 5.7e2, and Kumar et al., 2012), in this analysis, the NA and VF terms are added together and their sum is treated as a single term.

Initially the correlation between the SS (representing forcing) and BS (representing response) terms is estimated. Subsequently, the breaking acceleration (BA) term is added to SS and then compared against BS. If the correlation between forcing and response improves, then BA is retained as a forcing term, alternatively is rejected. After identifying the terms constituting the forcing, the same method is followed for the response with each term being added to BS and retained only if it contributes to increasing the correlation between the net forcing and response terms. The correlation coefficient (r) estimates in this analysis have been corrected for the decorrelation time of our data. Using Garrett and Toulany (1981, their equation 8.1) we estimated a wind forcing decorrelation time scale ~ 20 hrs. However, being conservative and considering that all data presented in this study have been low-pass filtered, we elected to adopt the filter's cut-off period (33hrs) as the appropriate decorrelation time scale. This assumption makes the number of independent data points to vary from 12 (for the shorter deployment site N8) to 33 for the longer deployment site (i.e., site O2). The critical correlation coefficient to determine if the correlation obtained is significant ($\neq 0$) at 95 % confidence interval are 0.56 and 0.33 for a sample size of 12 and 33, respectively.

The analysis of estimating forcing and response terms is conducted for both sides and the results are listed in Tables 4 and 5 for the forcing and response, respectively, while a description per site is presented in the following 2 sub-sections.

East Side

At site O2 (depth ~ 10 m), the major balance is between surface stress (SS) as forcing and bottom stress (BS), Stokes-Coriolis (SC) and Coriolis Acceleration (CA) as response which correspond to a correlation of $r = 0.79$. A regression between the forcing and the sum of the response terms (BS+SC+CA) reveals of slope close to 1 (see Table. 5.6), with BS dominating the response (Figure 5.8a1).

In shallower water depths (depth ~ 6 m, site N5), the bottom stress is moderately correlated to surface stress (r=0.50, see Table. 5.4) but when breaking acceleration is added to the surface stress, the correlation improves ($r = 0.83$, see Tables 4 and 5). Addition of the smaller in magnitude VF, NA and SC terms at site N5 in the response group (see Figs. 5.7c1, d1 and e1) slightly improves the correlation providing a correlation coefficient between force and response of 0.86 and a slope of 1.0 (Table. 5.6) suggesting that BS+VF+NA+SC ≈ BA+SS (Figure 5.8b1). The same balance is identified for even shallower waters (i.e., 5 m, at site N6, see Tables 5 and 6 and Figure 5.8c1).

Overall, on the east side of the cape, the shallower parts of the inner shelf respond to forcing provided by both wind (SS) and waves (BA). These two forcing parameters are usually interrelated during periods of storm activity like the frontal events identified in here, but in the case of swell waves this is not the case. The response is exhibited mainly through bottom stress (BS), nonlinear advective acceleration (NA) and vortex force (VF) (also see Sec. 5.5.3). In deeper waters (~10 m) the surface and bottom stress almost balance each other.

West Side

Unlike the east side, the alongshore momentum balance on the south side is more complex. At site O1 (water depth ~ 9 m) surface and bottom stresses (Figs. 5.6a2 and 7f2) are strongly correlated (r=0.90, Table 5.4). Adding LA to BS as a response

term (Figure 5.7a2) reduces this correlation, while adding CA and SC (Figs. 5.7b2 and 7c2) marginally improves r to 0.91 (Table 5.5). The slope of the regression line of forcing (wind stress only) and response defined as the sum of bottom stress and Coriolis acceleration is only 0.5 (Table 5.6), indicating that additional terms are needed to close the balance.

At shallower water depths (i.e., 6.5 m, site N9), both VF and NA (Figs. 5.7d2 and e2) have the same magnitude as BS but do not correlate to surface stress (SS). The highest correlation (r=0.33, not significant at 95% CI, see Table 5.5) and regression slope (m = 0.20, Table 5.6) are obtained only when we include CA (Figure 5.7b2), BS (Figure 5.7f2) and SC (Figure 5.7c2) as response to the surface stress (SS) forcing (Figure 5.6a2). Similar results are obtained for site N8 where response (BS) and forcing (SS+BA) correlate with a coefficient of 0.68 while the regression slope between them is only 0.5.

Unlike the north side, the momentum balance is not closed on the south side as clearly demonstrated by the low regression slopes and correlation coefficients obtained. Furthermore, it is worth noting that at times forcing acts in a direction opposite to what it should be expected from the response (Figs. 5.8a2, b2 and c2).

5.5 Discussion

The discussion is divided into two sections that attempt to: (a) explain the inability to close the momentum balance on the south side of Cape Hatteras and investigate the relation of this with coastline orientation; and (b) identify the importance of the vortex force term in relation to wave forcing and wind stress.

5.5.1 The effect of coastline orientation

As shown in section 5.4.2 we were not able to close the alongshore momentum balance on the south side of Cape Hatteras, suggesting the existence of additional forcing that

has not been captured by our analysis. One possibility is pressure gradient that was not considered in the analysis. Although, this term was not found to be important on the east side, we hypothesize that pressure gradient can play a role on the south side. This hypothesis is explored using a linearized form of the momentum balance equation that can be used to estimate the magnitude of a pressure gradient (PG) term that could close the balance. The alongshore momentum balance equation (equation (5.2)) is modified so that the PG term is now included and linearized by expressing the bottom stress through a linear bottom drag parameterization (e.g., Lentz and Winant, 1986) so that:

$$\frac{\partial \overline{v}}{\partial t} + f\overline{u} + f\overline{u^{St}} + \frac{1}{h}\frac{\partial}{\partial x}\left(\int_{-h}^{0}(uv)\,dz\right) + \frac{\overline{u^{St}}}{h}\left\{\frac{\partial}{\partial y}\left(\int_{-h}^{0} v dz\right)\right\} + \frac{r\overline{v}}{h} = -g\frac{\partial \eta}{\partial y} + \frac{\tau_{sy}}{\rho_o h} - \frac{-1}{\rho_o h}\frac{\epsilon_b k_y}{\sigma} \tag{5.6}$$

where r is the linear bottom drag coefficient for depth-averaged flows, h is the mean water depth, η is the sea surface elevation and g is the acceleration due to gravity. In section 5.4.2 we showed that both LA and CA are an order of magnitude smaller than the dominant terms (see Figure 5.7a2, b2), while NA and VF do not correlate with the observed forcing terms on the south side. On the basis of these findings, we can further simplify equation (5.6) by ignoring these terms and solve for mean velocity:

$$\overline{v_o} = T_f\left[-g\frac{\partial \eta}{\partial y} + \frac{\tau_{sy}}{\rho_o h} - \frac{-1}{\rho_o h}\frac{\epsilon_b k_y}{\sigma} - f\overline{u^{St}}\right] \tag{5.7}$$

where T_f, a representation of a frictional time scale, is defined as h/r and $\overline{v_o}$ is the observed flow. equation (5.7) will be valid for our velocity measurements if all the forcing terms (i.e., BA, SS and pressure gradient term) are responsible for the observed flows. Ignoring the PG term and considering a balance between dominant forcing and response terms as exhibited through the correlation analysis (Sec. 5.4.2),

we can estimate an equivalent velocity ($\overline{v_e}$) such that:

$$\overline{v_e} = T_f \left[\frac{\tau_{sy}}{\rho_o h} - \frac{-1}{\rho_o h} \frac{\epsilon_b k_y}{\sigma} - f\overline{u^{St}} \right] \tag{5.8}$$

where $\overline{v_e}$ represents the magnitude of the flow that should had developed using the measured BA and SS forcing terms alone assuming that pressure gradient was not important. Combining equations (7) and (8), the PG term required to produce the observed flow ($\overline{v_o}$) can be estimated by:

$$-g\left(\frac{\partial \eta}{\partial y}\right) = \frac{\overline{v_o} - \overline{v_e}}{T_f} \tag{5.9}$$

Using equations (7) to (9), time series of the equivalent velocity (Figure 5.9a) and PG term (see Figure 5.9b) were estimated for sites O1 and N9. The linear bottom drag coefficient (r) value was obtained by regression analysis where the measured depth averaged velocity ($\overline{v_e}$) at each site was regressed against the bottom stress values derived using the Styles and Glenn (2002) model (see section 5.4). The estimated PG time series (Figure 5.9b) is always directed opposite to the local alongshore wind forcing (Figure 5.9b). These results suggest that the estimated pressure gradient could potentially be the response to the wind forcing that was missing from our analysis, although further verification is needed.

The south side of the study area is part of Raleigh Bay, a cuspate foreland system very similar in geometry and orientation as Onslow and Long Bays that are located farther south (see Figure 5.10a). Assuming a coherent wind system (vector correlation of winds measured at Diamond Shoals to Cape Lookout and Frying Pan Shoals is 1.81 and 1.60, respectively), the pressure gradients developed in between these bays must be of similar magnitude and orientation. Using this analogy, three months of subtidal pressure gradients term ($-g\partial\eta/\partial y$) calculated from the sea surface records of two tide gauges in Onslow Bay (Beaufort, NC and Wrightsville Beach, NC, see Figure 5.10a) is compared to the subtidal wind stress from the NOAA buoy at Frying Pan Shoals. The estimated PG term from Raleigh Bay (Figure 5.10b) shows similar variability as

the wind stress component parallel to large scale shoreline (~ 60° clockwise North, see Figure 5.10a) with a correlation coefficient (r) of -0.84. When the winds are directed toward the northeast, the PG term is negative suggesting the potential of flow towards the southwest, (i.e., opposite to direction of the wind), especially during relaxation periods. Furthermore, the magnitude of this term (Figure 5.10b) is of the same order (Fig, 9b) as that estimated using equations (7) to (9) confirming our hypothesis that this magnitude of pressure gradient is required to close the momentum balance on the south side.

In a similar manner, the generation of pressure gradient on the east side of Cape Hatteras and farther away from the measurement location is examined using the subtidal sea surface elevation records from the two nearest oceanic tide gauges located in Chesapeake Bay, VA and Duck, NC (Figure 5.10a). The pressure gradient is again compared to the same wind forcing, with the alongshore component being appropriately defined using the shoreline orientation (~ 25° counterclockwise from North, see Figure 5.10a) at this region. The PG term (Figure 5.10c) is of the same order of magnitude as that obtained on the south side and it is strongly correlated to local alongshore wind stress (r = -0.68). A more appropriate comparison of the response (i.e., pressure gradients) to forcing (i.e., alongshelf wind stress) for the two different locations requires normalization of the terms. The ratio of variances of the local (i.e., per side) subtidal alongshore wind stress and that of the pressure gradients from each side ($\sigma^2(PG)/\sigma^2(\tau_{wy})$) provides such a normalization and as we can see in Figs. 5.10b and c the ratios are almost identical (1.59 and 1.54 for the remote south and east sides, respectively) implying the generation of the same pressure gradient for the same magnitude of alongshelf wind stress.

The analysis presented above suggests that the pressure gradient acting as a response to alongshore wind forcing within the cuspate embayment on the south side is of the same order as that observed for the straight coastline on the remote east

side. Nonetheless, unlike the south side, the momentum balance analysis on the near-field east side (i.e., at sites O2, N5 and N6, in the vicinity of the cape) is almost closed without the need for inclusion of pressure gradient. Upon closer examination we can note that the near-field, local coastline orientation at this area is different (larger) than that of the remote straight coastline farther east (i.e., from Duck, NC to Chesapeake Bay, VA, Figure 5.10a). The relative difference in coastline orientation between these two parts of the coastline is approximately ~ 35°. This is a large enough change in coastline orientation that can lead to significant differences in alongshelf wind stress magnitude capable of explaining the differences in relative magnitude of pressure gradient contribution on the two sides of the cape. This analogue is similar to that presented by Crèpon and Richez (1982) and Crèpon et al. (1984) for transient upwelling generated by wind forcing and variability in the coastline. At this point we should note that there is a small possibility that the pressure gradient estimated on the east side (Figure 5.10c) is partially balanced by the nonlinear advective acceleration (see equation (5.1)) which was not included in this study, something that we cannot verify with our data at present. Additional field observations or numerical modeling is required to further investigate this issue.

5.5.2 The role of Vortex Force

The observations presented in Section 5.4 provide some evidence regarding the importance of the VF and nonlinear advective acceleration terms in the alongshore momentum balance. This is further explored in here using a wave propagation model forced with the observed wind stress.

The wave propagation model Simulating WAves Nearshore (SWAN, Booij et al., 1999) was set up on an alongshore uniform bathymetric domain with a bathymetry similar to that observed on the profile that passes through sites N5 and N6 (Figure 5.11a). The model was driven with the measured wind stress, sea surface variability

and offshore directional wave characteristics (height, peak period, mean direction and directional spreading) as measured at Site O2. The results (i.e., cross-shore distribution of wave height, period, wave length, direction and depth-limited dissipation) were then used to determine the breaking acceleration term (see, equation (5.5)).

Considering only alongshore wind stress and breaking accelerations as the forcing terms, and a cross-shore variable linear drag (Figure 5.11a), equation (5.6) is solved to obtain the cross-shore and temporal variability of the alongshore velocity. NA and VF terms are not accounted for, in this analysis, and it is expected that the velocity structure obtained might differ from the measurements, especially during periods when the NA and VF terms were found to be important in the momentum balance analysis (Sec. 5.4). The cross-shore component of Stokes drift is obtained from the SWAN results using equation (5.3), while the VF is determined as the product of Stokes drift and the cross-shore gradient of depth-averaged alongshore velocity.

The velocity predicted using equation (5.6) (Figure 5.11e) shows similar variability and magnitude to that observed at sites O2, N5 and N6, thus providing some confidence in this simplified analysis. The estimated breaking acceleration becomes significant during the periods corresponding to the passage of the front systems (events F1 and F2), and the swell dominated periods S1 and S2 (Figure 5.5.11d). During these wave-dominated events, cross-shore variability in breaking acceleration is present due to depth-limited breaking that occurs over the shallow areas of the nearshore bar. This is followed by a region of limited wave breaking and subsequently wave breaking commences again in shallower water depths. It is further established that in deeper water the magnitude of breaking acceleration forcing is of the same order as that of wind stress and becomes more important with decreasing water depth. The variability of the modeled breaking acceleration resembles that calculated from the measurements. In deeper waters (~ 10m, e.g., site O2) wave breaking acceleration is not present and wind stress is the dominant term, while in shallower waters (e.g.,

sites N5 and N6), breaking acceleration is an order of magnitude higher than wind stress.

The modeled VF estimates (Figure 5.11f) are important at all instances when wave breaking occurs, as this forcing mechanism leads to formation of a cross-shore gradient in the alongshore velocity and thus an increase of horizontal shear ($\partial\overline{v}/\partial x$). The cross-shore variability of VF is similar to that of breaking acceleration and alongshore velocity, however, at locations with local maxima in alongshore velocity the VF term becomes zero ($\partial\overline{v}/\partial x$=0). Maximum VF usually occurs around the bar and at locations with strongest cross-shore gradient in alongshore current. In deeper waters, VF (Figure 5.11f) is similar in magnitude to wind stress (Figure 5.11b).

Overall, this simplified analysis suggests that in the transition zone between inner shelf and surf zone, even under moderate wave breaking, the role of VF term may be important and should be included. This might be particularly the case in locations where the alongshore component of the wind stress is reduced so that alongshore pressure gradients due to wind might not be as important as it appears to be the case for the near-field, east side of Cape Hatteras. Inside the surf zone the balance can be more complex than traditionally described and the breaking acceleration can be balanced by the sum of bottom stress, nonlinear acceleration and VF (Figure 5.12), something also shown numerically using wave-current interaction 3-D models (Kumar et al., 2012; Uchiyama et al., 2010). The transition (shoaling) zone between inner shelf and surf zone is an area that has not been thoroughly investigated at subtidal time scales. Our results indicate that in this region depending on the bathymetry, VF might be as important as bottom stress and wind stress.

We should emphasize that the estimates of both VF and nonlinear advective acceleration presented in here are the results of a simple model. Since the time series length and cross-shore instrumentation density does not allow us to further evaluate

the importance of our findings; a longer experiment with higher spatial resolution is recommended to address these issues.

5.6 Summary and Conclusions

We presented wave and sub-tidal circulation data collected within the surf and inner shelf regions around the Cape Hatteras point, North Carolina, an area with complex morphology and abruptly changing shoreline orientation. Despite the short length of the time series, the winter season events identified and analyzed in here represent typical synoptic weather fronts in the South Atlantic Bight (e.g., Austin and Lentz, 1999; Warner et al., 2012), which is dominated by strong wind and wave forcing along with well mixed conditions. An important aspect of our work is the inclusion of Stokes-Coriolis (physically representing the influence of Earth's rotation on surface gravity waves) and vortex force (interaction between wave-induced mass drift and the mean flow vorticity) terms in the momentum balance analysis.

Our analysis has shown that: Mean subtidal flows are parallel to the local coastline orientation on either side of the Cape Hatteras point, while in Diamond shoals the flows are directed along the shoal, suggesting that the shoals possibly act as an extension of the coastline, regulating flow between the east and the south side of the cape. We believe these results are applicable to all coastlines with similar geometries systems (e.g., Cape Lookout, NC and Cape Fear, NC) in the South Atlantic Bight.

In the absence of wind stress (i.e., swell dominated events) the Stokes-Coriolis term is as important as Coriolis acceleration term, as was also shown in Lentz et al. (2008) and it should not be neglected. Only under wind forcing when only locally generated, gravity waves are present and in the absence of swell forcing, Coriolis acceleration becomes the dominant term relative to Stokes-Coriolis term (also see Fewings and Lentz (2010)).

Pressure gradient generated as a response to spatially uniform wind forcing within a region with varying coastline orientation is hypothesized as a possible contribution to close the momentum balance on the south side of Cape Hatteras (Section 5.1). The magnitude of this pressure gradient is contingent upon the relative angle of local coastline to the wind velocity vector. It can be further argued that for a constant wind field, the effect of coastline orientation in nearshore sub-tidal flows can be explained using an analogue of a spatially varying alongshelf wind stress even at scales of few kms (i.e., similar to Crèpon and Richez, 1982).

In shallower waters the momentum balance is complex and a balance is achieved between bottom stress, breaking acceleration, nonlinear advection and vortex forces, as it has been also shown in three-dimensional modeling studies (Uchiyama et al., 2010; Kumar et al., 2012). In the transition zone between inner shelf and surf zone, in the presence of strong along/cross-shore shear, the vortex force term can be of the same order as the wind stress, suggesting a need to include the former term in any study dealing with the flows and exchange between surf zone and inner shelf.

Despite the limitations, we minded the available data to the depths possible to identify the significant processes responsible for flow conditions around the Cape Hatteras point. This work has provided important glimpses on the role of coastline orientation in the development of subtidal circulation under wind and wave forcing. However, the coupling of observational data and numerical models can lead to better understanding of the hydrodynamic processes including the effect of Vortex and Stokes-Coriolis force.

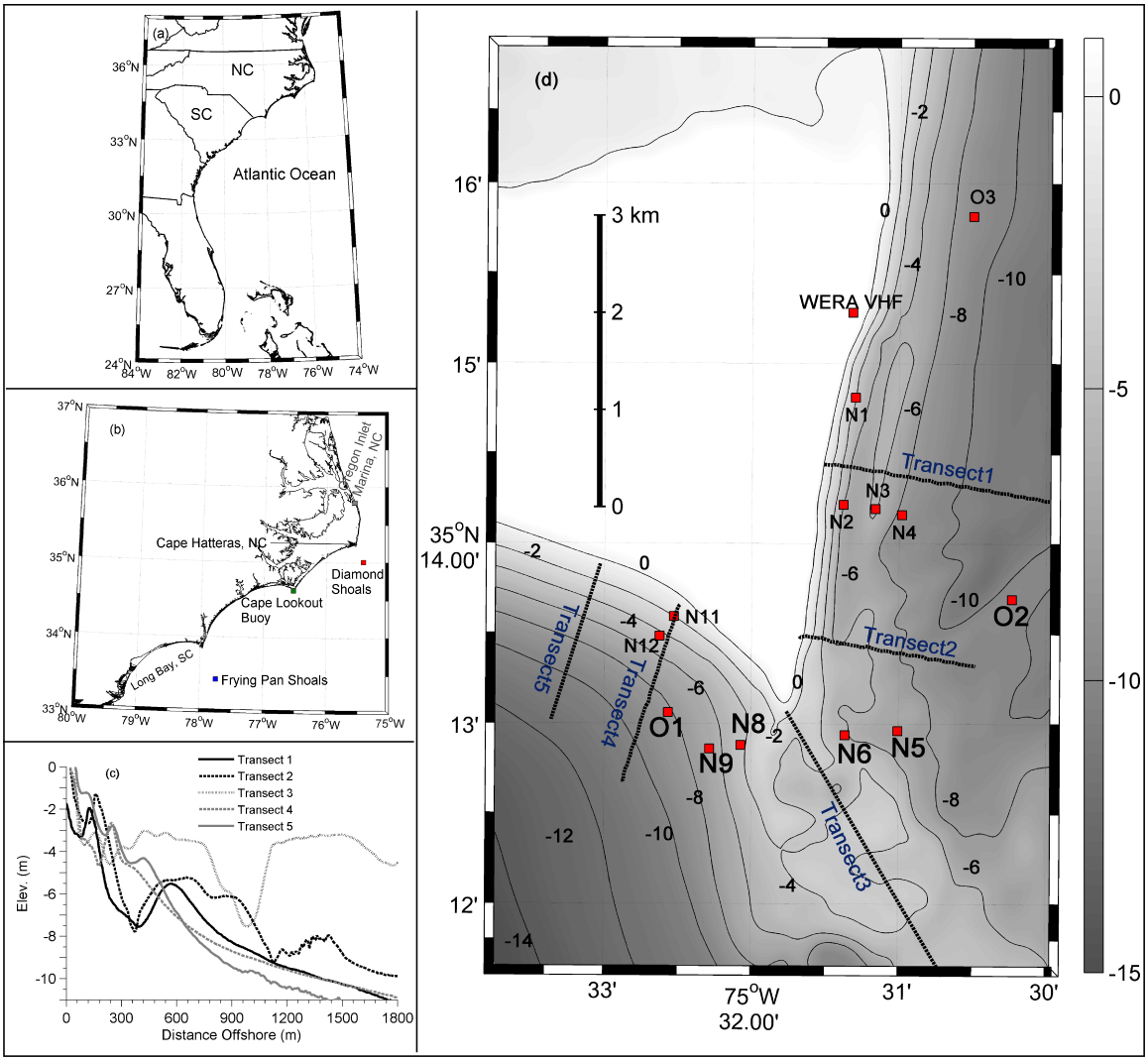

Figure 5.1: Map showing the study area (Cape Hatteras, NC), the nearshore bathymetry and data collection sites. Bathymetry contours shown are in m. The prefix "N" and "O" in the station names suggest nearshore (mean water depth less than 8 m) and offshore sites, respectively. The stations used in the analyses are shown with a larger font. Solid black lines are the transects along which the beach profiles are provided in (c). The location of the NOAA Diamond Shoals buoy is shown in (b).

Table 5.1: List of instruments deployed around Cape Hatteras point during February, 2010. Key: AQD: Nortek aquadopp, ADCP: Teledyne RD Instruments acoustic Doppler current profiler.

Site	Instrument Type	Mean Water Depth (m)	Height above bed of first bin (m)	Deployment duration (days)
N1	AQD	4.65	0.4	17
N2	AQD	7.01	0.4	17
N3	AQD	6.01	0.4	18
N4	ADCP	8.76	1.6	18
N5	ADCP	6.13	0.64	20
N6	AQD	4.65	0.4	20
O2	ADCP	10.69	0.64	45
O3	ADCP	10.01	0.64	45
N8	AQD	5.29	0.4	19
N9	ADCP	6.58	0.64	19
N11	AQD	5	0.4	20
N12	AQD	3.47	0.4	20
O1	ADCP	8.91	0.64	18

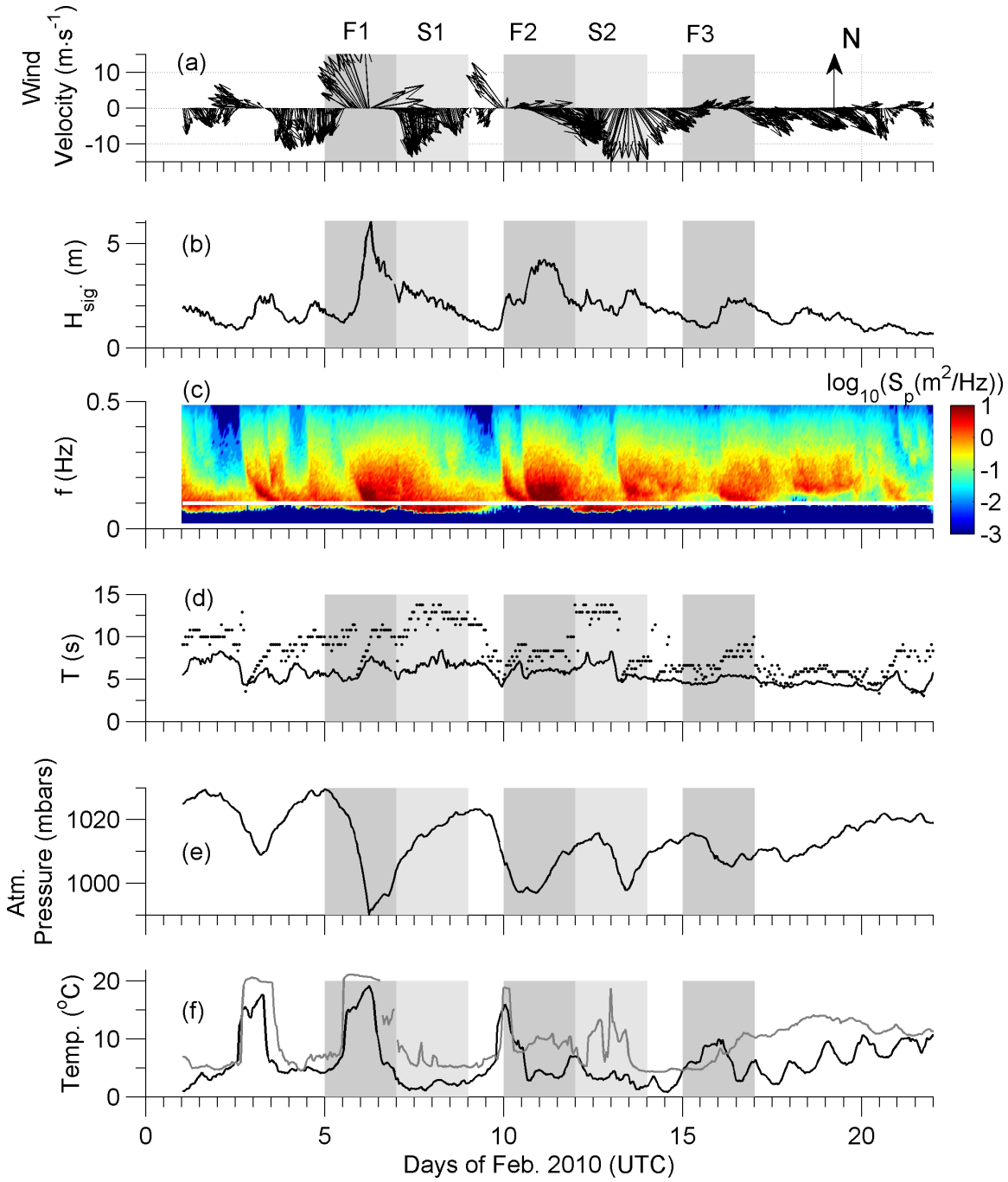

Figure 5.2: Meteorological and wave data from the Diamond Shoals buoy (NOAA/NDBC Station ID: 41025) for February, 2010. Time series of (a) wind velocity vector in oceanographic convention; (b) significant wave height; (c) surface wave spectrum (m^2/Hz). The 0.1 Hz cut-off used to separate sea and swell frequencies is also shown; (d) peak (black dots) and mean (solid black line) wave period); (e) Atmospheric pressure (solid black line); and (f) air (black) and water (gray) temperature. Dark gray shaded areas correspond to passage of synoptic meteorological fronts, and light gray shaded regions are the swell events.

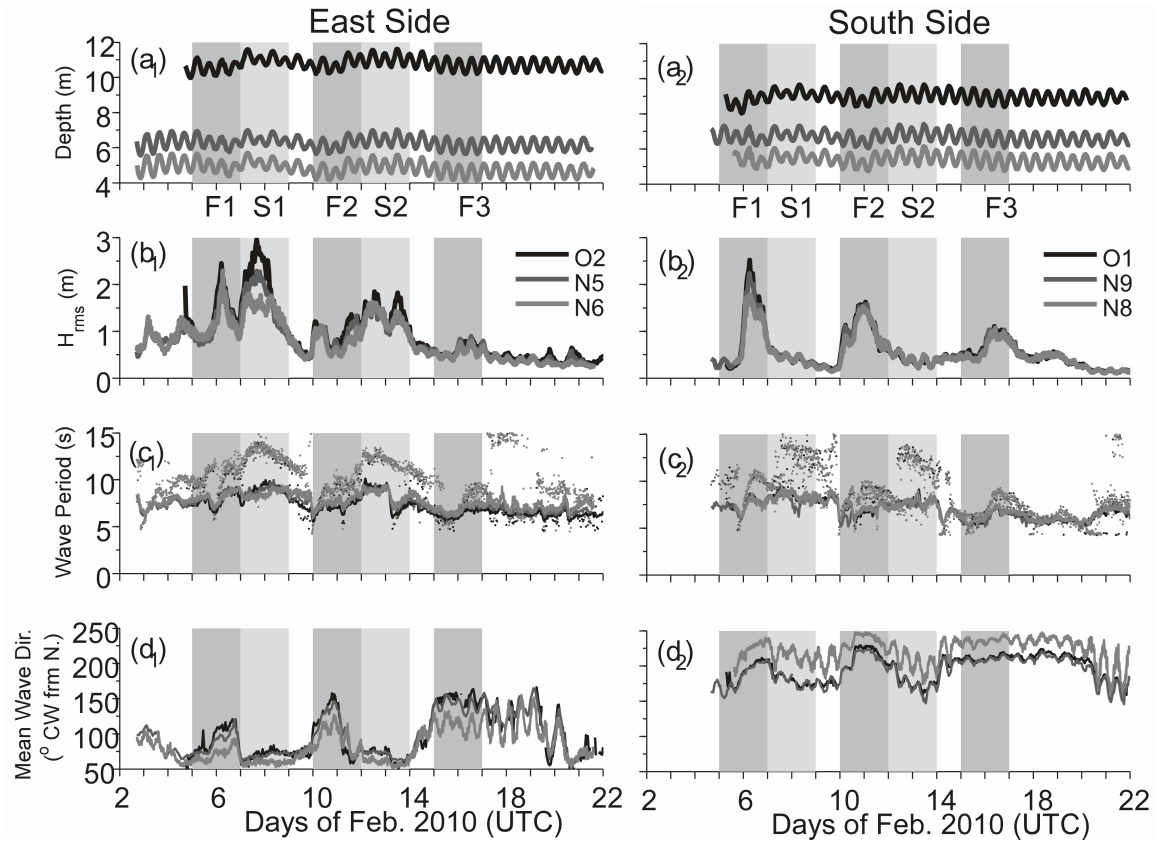

Figure 5.3: Time series of (a) water depth, (b) root mean square wave height, (c) Peak (dots) and mean (solid) wave period, and (d) mean wave direction (°N) for the east (left panel, subscript 1) and south sides (right panel, subscript 2), respectively. The shaded areas indicate periods of frontal passage (dark gray shade) and swell events (light gray shade) as in Figure 5.2.

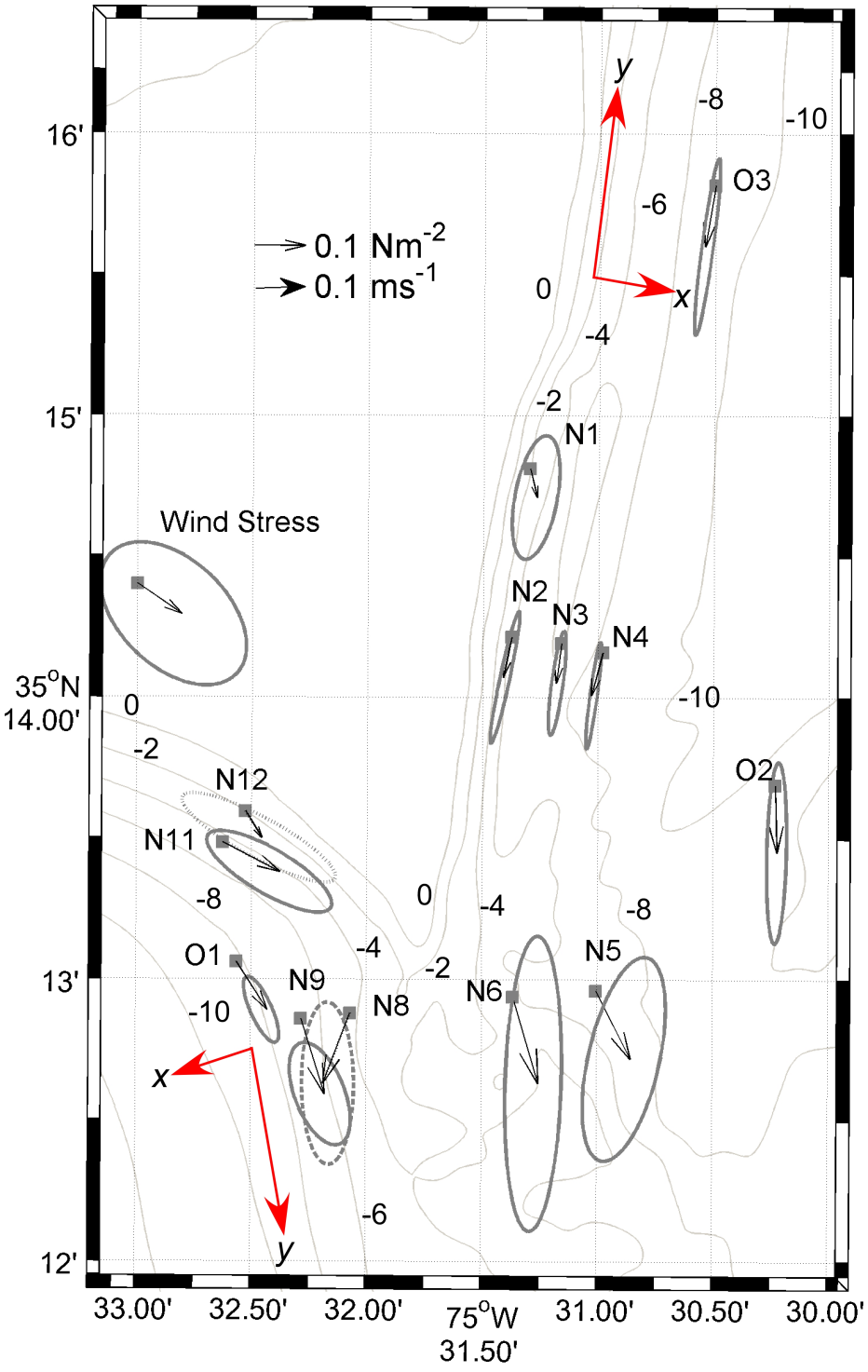

Figure 5.4: Synoptic description of wind forcing and depth-averaged subtidal currents described by their mean (black arrows) and vector variance ellipses for the full period of data collection for each site (see Table 5.1). The local coordinate (x, y) systems used at each side are also shown.

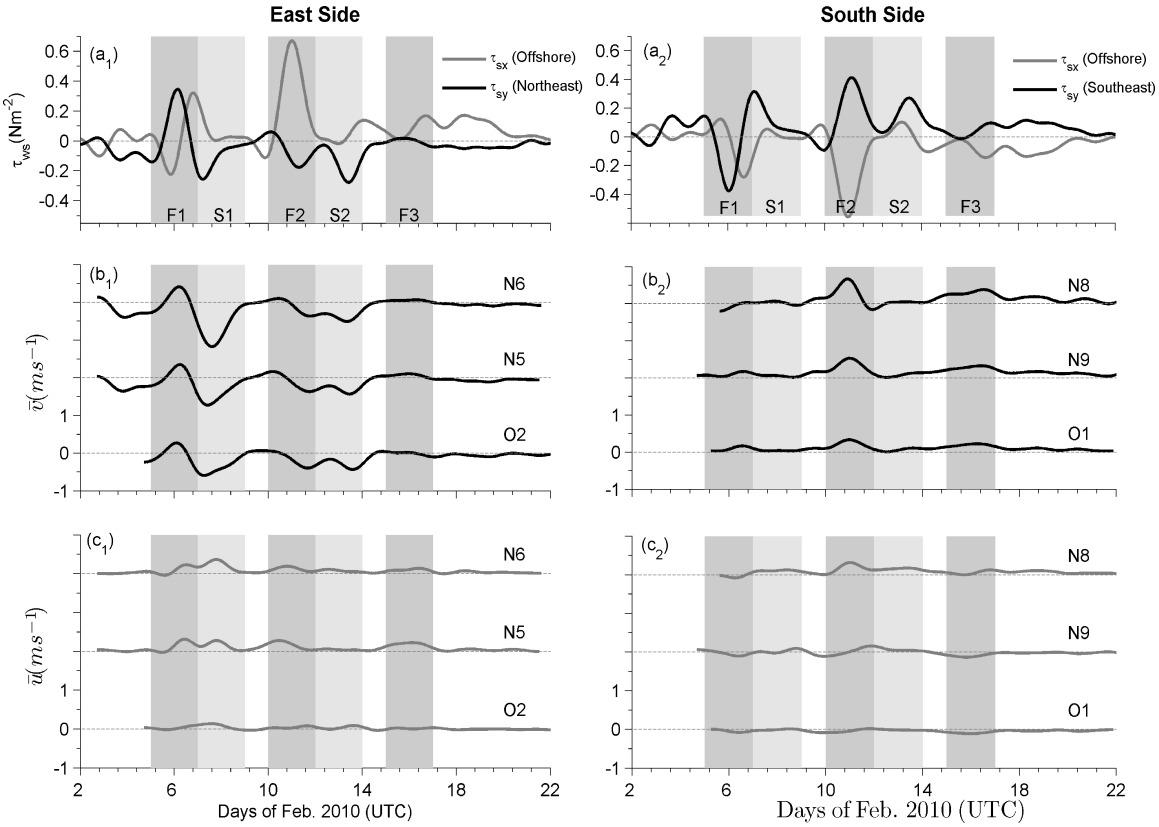

Figure 5.5: Time series of local (a) subtidal alongshore (solid black) and cross-shore (solid gray) wind stress; (b) alongshore ; and (c) cross-shore currents on the east (left panel, subscript 1) and the south side (right panel, subscript 2). The vertical scale in (b) and (c) is shifted vertically for each station for clarity. Dark and light gray shaded regions correspond to the periods of frontal passage and swell events, respectively. The coordinate systems for the east and south sides are shown in Figure 5.4.

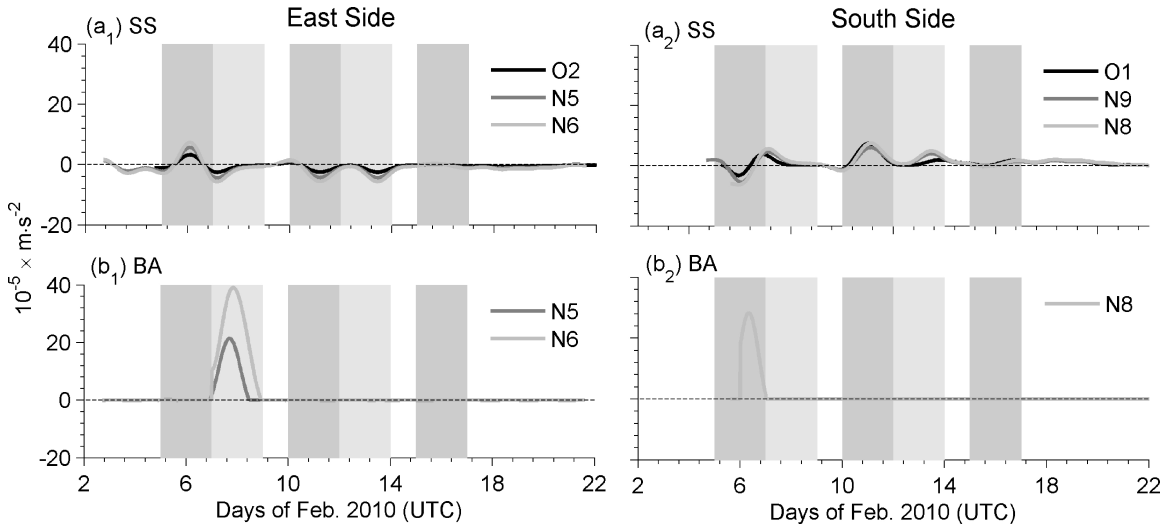

Figure 5.6: Time series of low-pass filtered (a) surface stress, (b) breaking acceleration for the east (left panel, subscript 1) and south (right panel, subscript 2) sides No depth-limited wave breaking was observed a site O2, O1 and N9 during the deployment period.

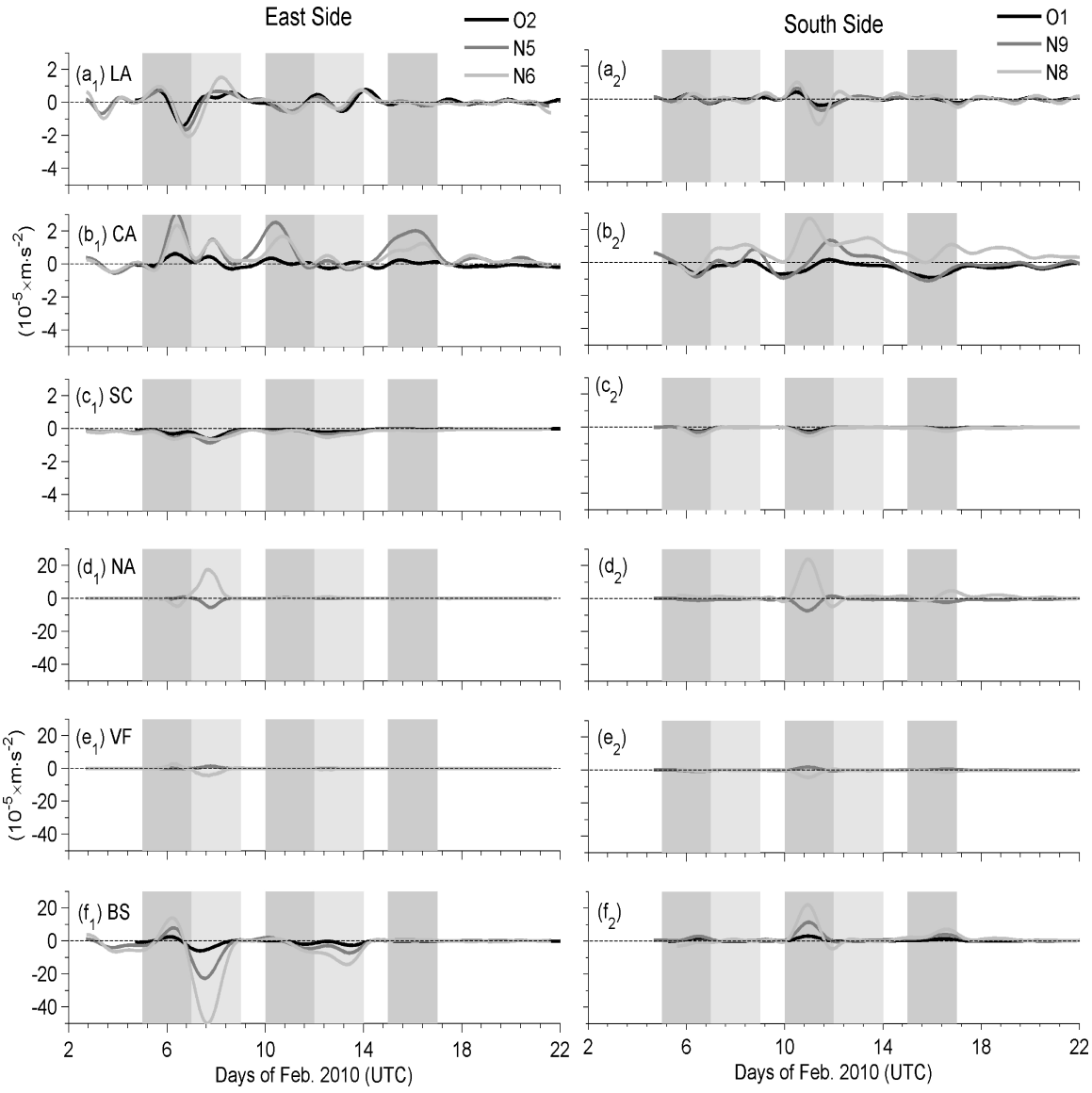

Figure 5.7: Time series of low-pass filtered response terms in depth-averaged alongshore momentum balance (equation [2]) for the east (left panel, subscript 1) and south (right panel, subscript 2) sides and for different sites (see key). (a) Local Acceleration; (b) Coriolis acceleration; (c) Stokes-Coriolis force; (d) Nonlinear Advective Acceleration; (e) Vortex Force and (f) Bottom stress. Please note that the vertical scales in d, e and f, are 10 times the vertical scale in a, b and c.

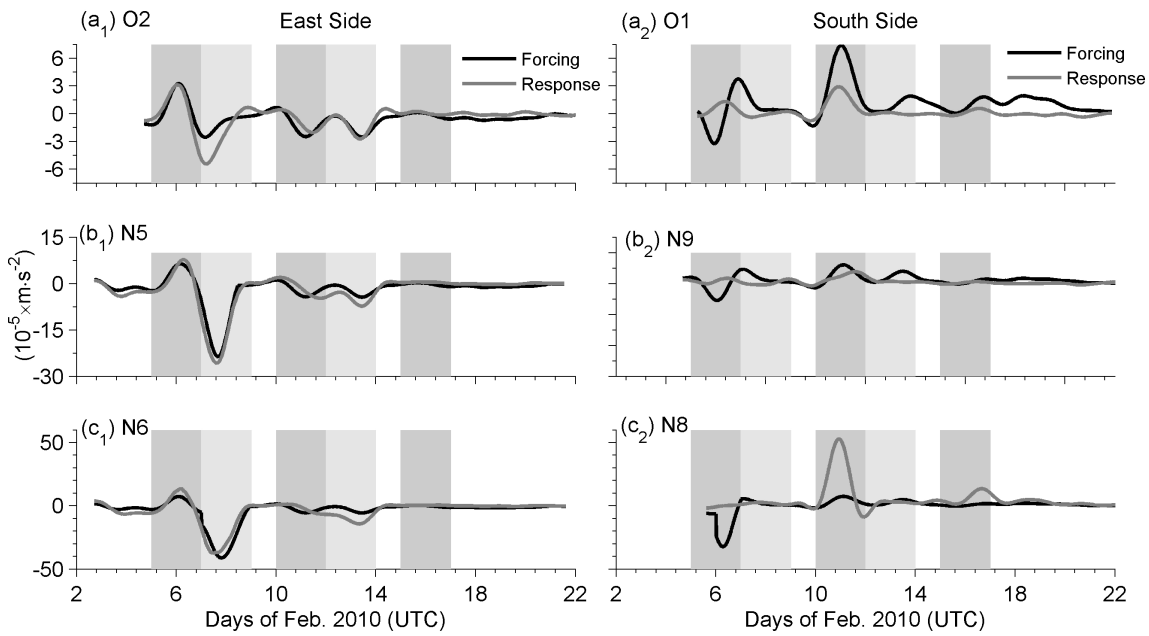

Figure 5.8: Time series of response (gray) and forcing (black) terms at north (left panel, subscript 1) and west (right panel, subscript 2). The relevant forcing and response terms at each site are listed in Tables 4 and 5. Note the different vertical scales used.

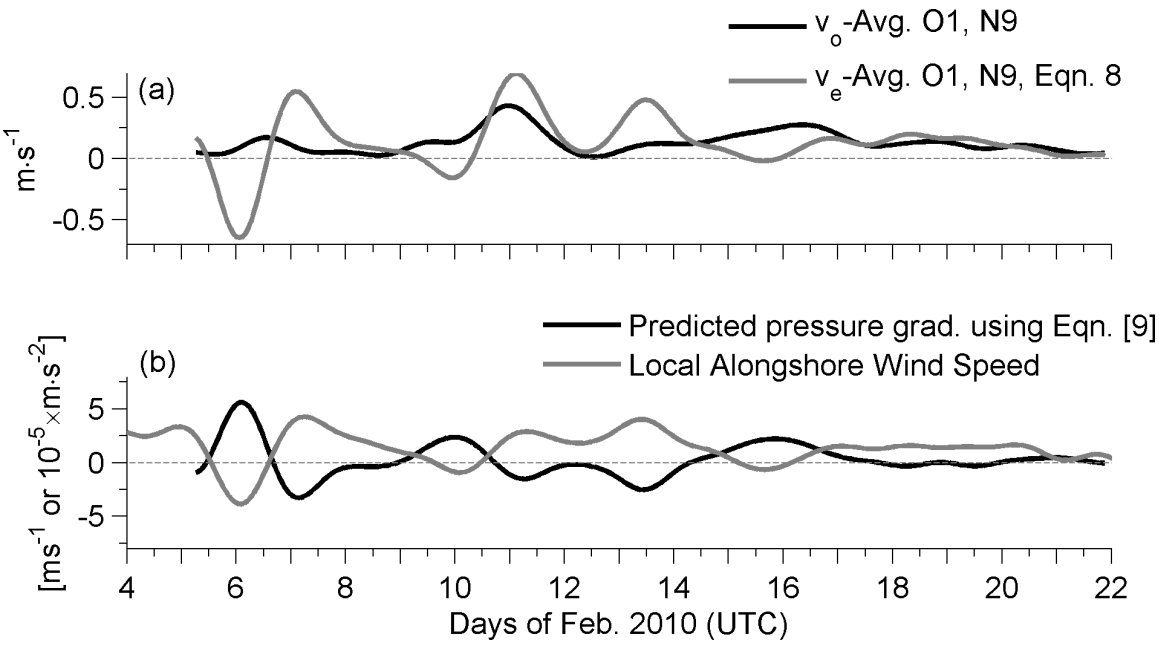

Figure 5.9: Time series of (a) average (between Site O1 and N9) observed (black) and predicted (gray) alongshore velocity (ms-1); (b) predicted (black) pressure gradient terms and local alongshore wind speed from NOAA-NDBC Diamond shoals buoy (for definition of local coordinate system see Figure 5.4).

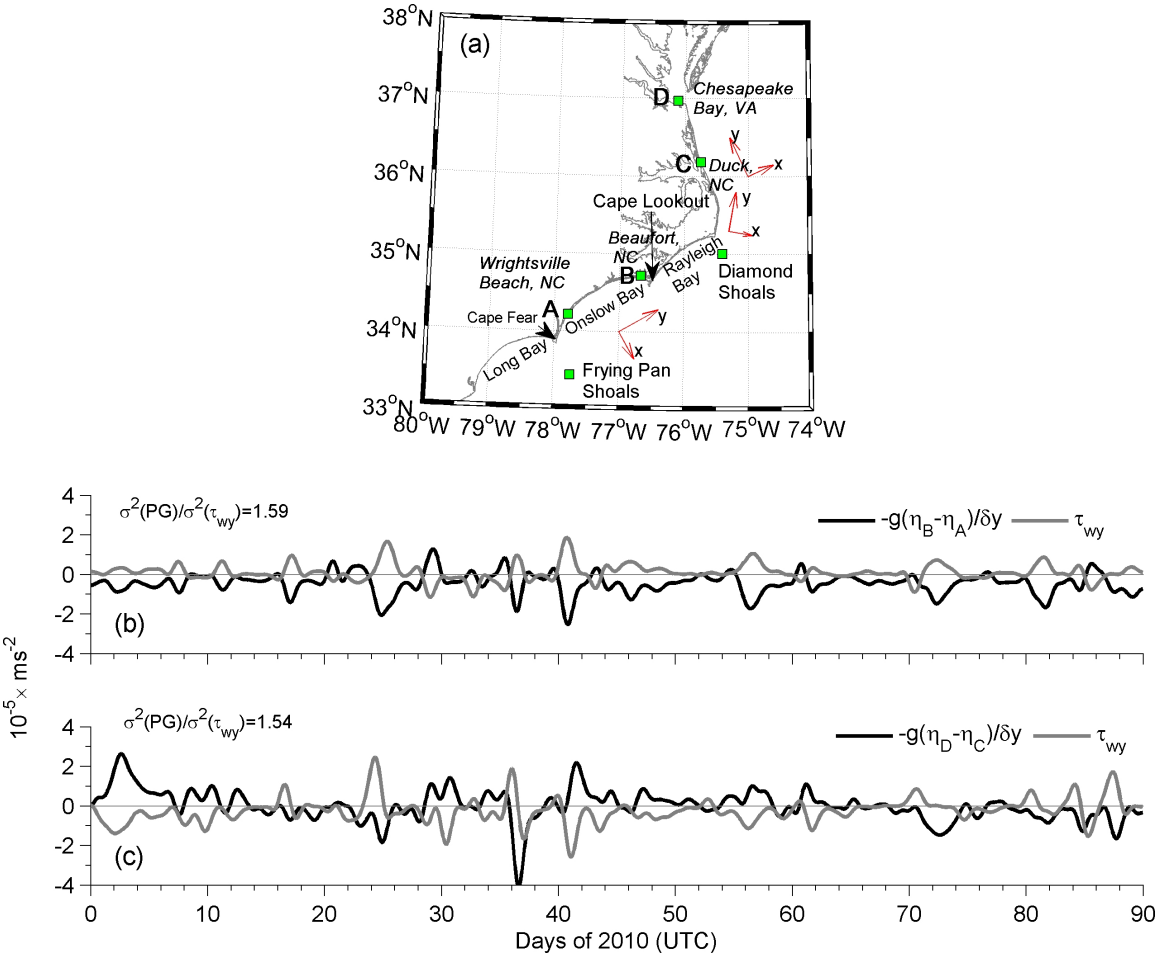

Figure 5.10: (a) Map of the South and Mid Atlantic Bight showing the cuspate shapes of coastlines from Long Bay, (SC) to Cape Hatteras point (NC). The locations of NOAA tide gauges used to estimate pressure gradients are shown as squares. The three different coordinate systems used for determining local alongshore and cross-shore components of wind velocity for different regions of the coastline are shown in red. (b) Time series of low-pass filtered pressure gradient term, $-g\partial\eta/\partial y$ (black) between Wrightsville Beach (location A) and Beaufort, NC (location B), and low-pass filtered alongshore (gray) wind velocity from Frying Pan Shoals, (c) Same as in (b) but the pressure gradient is estimated between Duck, NC (location C) and Chesapeake Bay, VA (location D) , and the along coastline wind velocity is estimated using the local coastline orientation between the tide gauges.

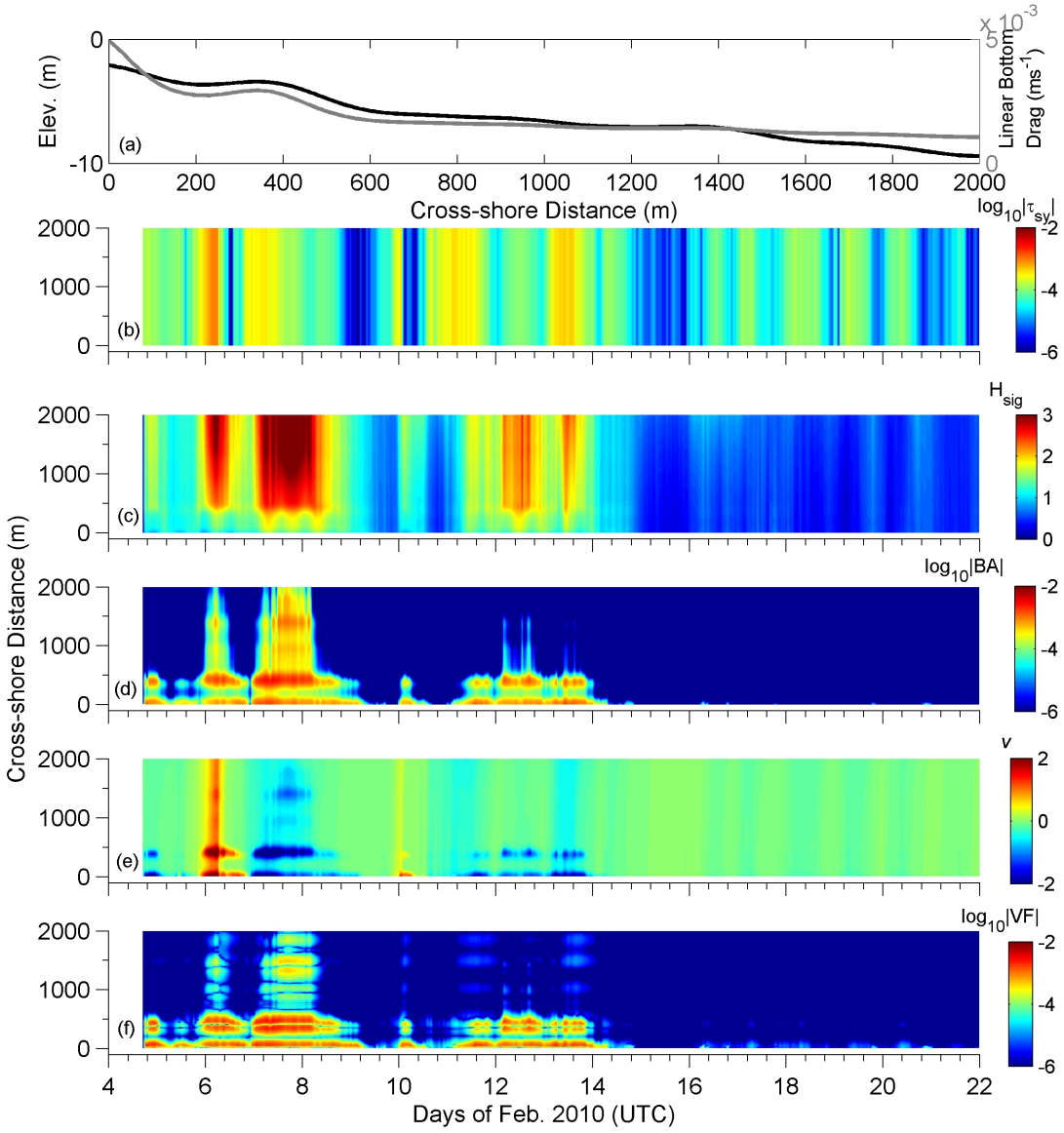

Figure 5.11: Cross-shore distribution of (a) Linear bottom drag coefficient (black) and water depth (gray); Color shading of (b) absolute value of wind stress (m^2s^{-2}); (c) significant wave height (m); (d) absolute value of breaking acceleration (m^2s^{-2}); (e) alongshore current (ms^{-1}); and (f) vortex force (m^2s^{-2}) showing spatial (along y-axis) and temporal (along x-axis) variation. Log scale is used for (b), (d) and (f).

Table 5.2: Correlation coefficient (r) between wind stress and local alongshelf (v) and cross-shore (u) velocity components. r values in italics are not significant at the 95% confidence level.

Local Wind Stress	Site					
	East Side			South Side		
	O2	N5	N6	O1	N9	N8
	u,v	*u,v*	*u,v*	*u,v*	*u,v*	*u,v*
τ_x	0.20, -0.51	-0.42, -0.41	-0.20, -0.26	0.04, -0.82	-0.22, -0.83	-0.84, -0.78
τ_y	-0.46, 0.90	0.37, 0.87	-0.20, 0.83	0.10, 0.63	0.36, 0.58	0.79, 0.54

Table 5.3: Standard deviation of local alongshore depth-averaged momentum balance terms. No values are shown for terms/site combinations which could not be calculated. All units in 10^{-6} ms^{-2}.

Term	*East*			*South*		
	O2	N5	N6	O1	N9	N8
Local Acc. (LA)	3.3	4.2	5.8	1.5	2.1	3.6
Coriolis Acc. (CA)	2	8.4	5.8	2.7	5.3	6
Stokes-Coriolis Acc. (SC)	1.2	1.9	1.8	0.7	0.9	1.4
Nonlinear Acc. (NA)	-	10.7	48.5	-	13.7	44.9
Vortex Force (VF)	-	1	24.9	-	3.9	8.7
Bottom Stress (BS)	14	50.6	108.8	6.7	23.1	43.9
Surface Stress (SS)	8	17.4	22.4	17.2	18.8	23.8
Breaking Acc. (BA)	0	39	157. 8	0	0	49.6

Table 5.4: Correlation coefficient (r) between bottom stress (BS) and forcing terms of depth-averaged momentum balance.r values in italics are not significant at the 95% confidence level. Key: SS = surface stress; BA = breaking acceleration.

Site		Response	Forcing	
			SS	SS+BA
East	O2	BS	0.74	-
	N5	BS	0.5	0.83
	N6	BS	*0.33*	0.88
South	O1	BS	0.91	-
	N9	BS	*0.11*	-
	N8	BS	0.63	0.68

Table 5.5: Correlation coefficient (r) between forcing and response terms of depth-averaged momentum balance.r values in italics are not significant at the 95% confidence level. Bold typeface values represent the maximum correlation coefficient value for given combination of forcing and response terms. Key: BA= Breaking acceleration; NA= Nonlinear advective acceleration; VF= Vortex Force; SS= Surface Stress; BS= Bottom Stress; LA=Local Acceleration; and SC= Stokes-Coriolis term.

Site		Forcing Terms	Response Terms					
			BS	BS+SC	BS+SC+ CA	BS+SC+ CA+LA	BS+SC+ CA+LA+ [NA+VF]	BS+SC+ [NA+VF]
East	O2	SS	0.74	0.76	**0.79**	0.78	-	-
	N5	SS+BA	0.83	0.84	0.76	0.75	0.75	**0.86**
	N6	SS+BA	0.88	0.89	0.87	0.85	0.84	**0.92**
South	O1	SS	0.9	0.89	**0.91**	0.9	-	-
	N9	SS	*0.11*	*0.09*	***0.33***	*0.25*	*0.21*	*0.03*
	N8	SS+BA	0.68	0.68	**0.71**	0.7	0.67	0.65

Table 5.6: Slope (m) and intercept (c) for the relation [R=mF+c]. F is the forcing term determined from Table 5.4 to have maximum correlation to the response term (R). 95% confidence interval for m and c are shown. On using the algorithm of Krystek and Anton (2007) instead of using a standard linear regression technique, and assuming 50% uncertainty in both forcing and response terms, only slightly modifies the regression coefficients and slopes shown here.

Site Name	m	c ($\times$ 10^{-5} ms^{-2})
O2	1.1±0.3	-0.01±0.3
N5	1.0±0.4	-0.3±1.1
N6	1.1±0.1	-0.4±1.2
O1	0.5±0.1	-0.4±0.2
N9	0.2±0.4	1.0±1.1
N8	0.5±0.4	4.4±2.7

Chapter 6

Modeling the inner-shelf and surf zone flow dynamics around a cuspate foreland using coupled wave-current interaction model

Abstract

A coupled wave-current interaction modeling system is used to simulate inner shelf and the surf zone circulation pattern and wave field from February 1 to March 20, 2010 around the Cape Hatteras point, a cuspate foreland characterized by a shallow shoal complex extending seaward and shorefaces with contrasting shoreline orientation. The model simulated bulk wave parameters and frequency spectrum are in good agreement to measurements in open ocean, inner shelf and within the surf zone. Likewise, simulated subtidal alongshore flows compare well with vertical profile of measured local alongshore flows at point locations within and around the shoal complex. The spatial gradients in flow are also captured correctly as revealed by comparison against Lagrangian mean surface currents from a VHF radar system. Analysis of flow patterns suggests that during sustained south/southwestward directed winds, a gyre like formation occurs on the leeward (south) side of the cape. Local alongshore momentum balance implies that wind stress and the pressure gradient term are in balance on the south side. On the east side of Cape Hatteras point, the pressure gradient is almost always in the same direction as the wind stress and their sum is balanced by the bottom stress. During wave breaking events, both nonlinear advective acceleration and vortex force terms become relatively important, while pressure gradient is generated perpendicular to the shoal axis to balance the contribution of wave breaking, a behavior similar to that observed for wave breaking near a coastline. Finally, the mean, subtidal, depth-averaged flow is found to be substantially stronger than the tidal residual flow and may play a more dominant role in short term shoal building process.

6.1 Introduction

Cross-shore movement of material (sediment, pollutants, sewage, nutrients etc.) from the surf zone to the inner and mid-shelf and vice versa is an important process that affects the nearshore environment and is of great societal interest. Changes in shoreline orientation within a region can alter the magnitude of local cross-shelf transport. Cuspate shorelines are typical examples where shoreline orientation can change up to 90° within a region. Such shorelines are ubiquitous along the US coastline, with cuspate forelands being one of the most dominant configurations [Komar, 1998]. Along the SE USA, from the northern part of South Carolina to Cape Hatteras, North Carolina the coastline is characterized by an extended cuspate foreland system consisting of three embayments (Long Bay, Onslow Bay and Rayleigh Bay, see Figure 6.1). This coastline configuration plays a dominant role in shaping both wind and wave-driven circulation patterns. Although a number of studies have attributed various circulation patterns to coastline configuration [e.g., Gutierrez et al., 2006; Sanay et al., 2007] no specific studies have been carried out to study this effect in detail, especially in the South Atlantic Bight (SAB).

The largest contrast in circulation is usually expected to be present at the cuspate foreland that divides to adjacent coastal embayments. Kumar et al. [2013] described the circulation patterns around Cape Hatteras using in-situ measurements of waves and currents from 13 locations around the cape distributed in both the east and south side of the Cape Hatteras point (see Figure 6.1). The two sides of the cape represent shorefaces with contrasting shoreline orientation (north-south vs. northwest-southeast) subjected to the same wind forcing.

Analysis of these point measurements in form of a simplified alongshore momentum balance revealed a dominant balance between wind and bottom stress in deeper waters (~ 10m) of the east side, while a more complex balance involving wind stress,

wave breaking induced forcing, nonlinear advective acceleration, bottom stress, and vortex force was estimated for shallower waters (~ 5 m). On the south side of Cape Hatteras, a linearized momentum balance analysis suggested the development of a pressure gradient as a response to the wind stress. It was also suggested that changes in local coastline orientation can alter the magnitude of the pressure gradient as a function of the relative angle of wind stress and coastline orientation.

Even though the analysis of Kumar et al. [2013], hereafter referred to as K13, provides a comprehensive idea of flow and momentum balance dynamics, some pertinent questions could not be answered due to limited spatial resolution of the in situ, point measurements, and only the application of a numerical model verified by in situ data could answer. In particular:

(a) What is the flow exchange between the two sides of a shoal usually associated with a cuspate foreland? (b) What is the relationship between local pressure gradient and wind forcing at either side of a cuspate foreland and how does this change in the cross-shore? (c) What is the exact balance of pressure gradient, nonlinear advective acceleration and vortex force in the inner shelf and the surf zone on the leeward side of the cape; and finally (d) what is the large scale response of a cuspate foreland systems to varying wind and wave forcing?

These queries form the objectives of this study, and are addressed using Cape Hatteras as a case study and through the application of a three-dimensional coupled wave-current interaction modeling system that incorporates both the conservative (in form of vortex force) and non-conservative (wave breaking) wave forcing in categorizing the flow dynamics. Most of the previous similar modeling studies [e.g., Gan and Allen, 2002ab; Costelau and Barth, 2007] do not account for the effect of waves.

In the next section we describe the site used as a case study for this work. This is followed by a description of the model suite used in the simulations, the model setup, study site and experimental data collected (Section 3). The application of the

model and its validation with the field observations are presented in section 4, while the results of the simulations are described in section 5. Discussion from the findings is provided in section 6, followed by conclusions.

6.2 Site Description

The surf zone and inner shelf region around Cape Hatteras, NC is characterized by abrupt changes in coastline orientation from 10° N on the east side (see Figure 6.1) to 166° N at the Cape Hatteras point, transitioning to an orientation of 120° N farther west. The bathymetry in the area is complex, consisting of a shoal complex (Diamond Shoals) that extends from the cape point to some 20km offshore toward the SE (see Figure 6.1b). Gulf Stream grazes along the narrow shelf break (50-60 m isobath) south of Cape Hatteras before disassociating from the continental shelf [Savidge and Bane, 2001]. The existence of horizontal and vertical stratification, especially during summer season adds to the complexity of the region. In addition, interaction of cooler waters from the MAB and warmer, saline waters of the SAB; and the cross-shore transport of alongshore convergent flows occurs around the Cape Hatteras region [Savidge and Bane, 2001; Churchill and Gawarkiewciz, 2012].

In terms of meteorological conditions, analysis of data from the NOAA/NDBC Diamond shoals buoy (ID 41025, Figure 6.1b) shows that the wind climatology consists mainly of winds that are directed to the northeast or south/southwest with magnitude varying from 4 to 14 ms^{-1} (see Fig. 6.2a). This wind climatology agrees with the pattern suggested by Austin and Lentz [1999] whereby the southeast US is predominantly influenced by the passage of low pressure synoptic meteorological fronts

The offshore wave climate as revealed through the joint probability distribution of significant wave height (H_s) and peak period (T_p, Fig. 6.2c) from 5 years of data at Diamond shoals buoy shows a significant wave height that typically varies between

0.5 and 3m with periods between 4-14 seconds. It is evident that Diamond shoals is influenced by swell waves in addition to the locally generated wind waves ($T_p < 10$s).

6.3 Model Description and Set-Up

In this study we use the Coupled Ocean Atmosphere Wave and Sediment Transport (COAWST) modeling system, which is a collection of open-source, public domain modeling components that have been customized to investigate processes in the coastal ocean pertaining to oceanic circulation, wave propagation, atmospheric boundary layer and sediment transport [Warner et al., 2010]. This modeling system has been recently updated with a wave-interaction module based on vortex force formalism [Kumar et al., 2012], and has been successfully applied to a variety of applications including the study of wave-current interaction in the surf zone [Kumar et al., 2011a, 2011b] and in a tidal inlet [Olabarrieta et al., 2011]; atmospheric-ocean-wave interactions under hurricane forcing [Olabarrieta et al., 2012]; and sediment dispersal in shallow semi-enclosed basins [Sclavo et al., 2013].

The circulation model used in the COAWST modeling system is the Regional Ocean Modeling System (ROMS), a three-dimensional, free surface, topography following numerical model, which solves finite difference approximation of Reynolds Averaged Navier Stokes (RANS) equations using hydrostatic and Boussinesq approximation with a split explicit time stepping algorithm [Shchepetkin and McWilliams, 2005, Haidvogel et al., 2008 and Shchepetkin and McWilliams, 2009]. ROMS includes several options for several model capabilities, such as various advection schemes (second, third and fourth order) and turbulence closure models (e.g., Generic Length Scale mixing, Mellor-Yamada, Brunt-Väisälä frequency mixing, user provided analytical expression and K-profile parameterization). Currently there are four variations of ROMS-family codes, and the COAWST system uses a version based on the Rutgers University ROMS which was first introduced by Haidvogel et al. [2000].

The wave-current interaction algorithm within the ocean circulation model has been updated on the basis of a vortex force formalism method. This method allows for distribution of wave-induced effect as conservative and non-conservative forces, where the former is characterized by a vortex force (physically represented as the interaction between wave-induced mass transport and mean flow vorticity), quasi-static pressure adjustment and a Bernoulli head [McWilliams et al., 2004]. The non-conservative forcing is divided into depth-limited wave breaking induced acceleration, wave-roller acceleration, bottom and surface streaming, and enhanced turbulence due to wave breaking [Kumar et al., 2012].

In this application, ROMS has been configured for two-way grid refinement process [Warner et al., 2010]. A parent grid encompassing the region of interest was first generated and subsequently a higher resolution (child) grid was defined with 5 times higher resolution. The two way grid refinement process allows transfer of boundary information of prognostic variables (velocity, sea surface, temperature, salinity and concentration) from the parent to the child grid, while high resolution prognostic variable information from the child grid is averaged on to the parent grid. The ratio of time stepping between the two grids can be same as the ratio of their grid resolutions. The parent grid on finishing one baroclinic (slow) time step provides boundary information to the child grid, while during this period the child grid takes 5 baroclinic time steps to reach at the same time level as the parent grid, followed by transfer of interpolated values of prognostic variables to the parent grid. In cases with multiple child grids, this process of subsequent reduction in baroclinic time stepping continues. More details for two way grid refinement are provided in Warner et al. [2012].

The wave propagation model used in COAWST is Simulating WAves Nearshore [SWAN, Booij et al. 1999; Ris et al., 1999], a third generation, spectral, phase averaged, wave propagation model, which conserves the wave action density. Inputs

to SWAN consists of a bathymetric grid, incident wave conditions at the boundary, wind and mean current velocity fields, while the output provides significant wave height, mean wave length, peak and mean surface period, and mean bottom period. The model simulates shoaling, wave refraction due to both bathymetric features and mean currents, energy input due to winds, energy loss due to white-capping, bottom friction, and depth-limited breaking.

In this study SWAN is used in a two-way coupling mode, allowing for interaction with the circulation model. SWAN receives information about sea surface elevation, bathymetric change, and a circulation field from ROMS to determine the effect of currents and total water depth on wave propagation. In turn, ROMS receives information on surface and bottom wave parameters (height, orbital velocity, period, wavelength and direction), wave dissipation due to bottom friction, wave breaking, and whitecapping, which is used to estimate the conservative and non-conservative wave -induced processes. This exchange of information between the circulation and wave models occurs at user defined intervals in a two-way coupling scenario. A detailed discussion about model coupling can be found in Warner et al. [2008a; 2008b]. The SWAN model used within the COAWST modeling system is capable of one-way grid refinement, which is described in more details in Warner et al. [2010].

6.3.1 Domain and Grid Nesting

We use three nested grids to resolve the flow dynamics and wave propagation around the Cape Hatteras point. Each grid is designed so as to be able to resolve a variety of processes ranging from outer continental shelf scales to inner-shelf and surf zone circulation. The largest (parent) grid has a resolution of 2,000m, and extends from Myrtle Beach, SC in the southwest to the New Jersey Bight in the northeast. The maximum water depth within this grid is ~ 3,000m (Fig. 6.3a). It is important to point out that the parent grid chosen here does not resolve the Gulf Stream dynamics.

Nonetheless, during the data collection period no effect of Gulf Stream was evident within the study region. The parent grid is nested to an intermediate grid (Figure 6.3b) with a resolution of 400 m that encompasses the area from Beaufort, NC to Duck, NC. The maximum water depth within this domain is ~ 800m. Finally, this intermediate grid is nested to a very high resolution child grid (Fig. 6.3c) that covers the area from the southwest of the Hatteras Bight to farther northeast of Cape Hatteras point. The resolution is 80 m and the water depths included are smaller than 50m. In all the grids, 16 sigma layers are used with higher resolution close to the surface and the bed.

In this study, same grids are used for both the circulation and the wave propagation models. Wetting and drying of the computational domain due to tidal variability is taken into account by activating this option in ROMS. The minimum depth for wet/dry criterion is set to 1 m.

The baroclinic time steps used in the circulation model for the parent, intermediate and child grid domains are 150, 37.5 and 18.75 s. respectively. For the wave propagation model the corresponding values are 300, 150 and 75 s. Exchange of information between the wave and circulation model occurs every 20 minutes.

The bathymetry used for the child grid (Fig. 6.3c) was generated using a combination of bathymetric field surveys conducted during the experiment, and a LIDAR bathymetric survey conducted in October 2009. These information were augmented with depth information obtained using microwave X-band radar [McNinch, 2007]. The bathymetric information for the intermediate grid (Fig. 6.3b) is a combination of bathymetry data from the NOAA coastal relief model, and the high resolution bathymetry from the child grid. Finally, bathymetry for the parent grid (Fig. 6.3a) was created using bathymetry from the intermediate grid and ETOPO 1 data set.

6.3.2 Forcing, Initial and Boundary Conditions

Atmospheric forcing to the circulation model included wind velocity, longwave and shortwave radiation flux, atmospheric pressure, air temperature, precipitation and relative humidity. These parameters were obtained from the North American Regional Reanalysis (NARR) database which contains data with spatial resolution of approximately 32 km and a time step of three hours.

Boundary conditions for barotropic tides were derived from the ADCIRC [Mukai et al., 2001] tidal database for the northeast Atlantic Ocean. This database includes water levels and current velocity phases and amplitudes of the M2, S2, N2, K2, O1, K1, Q1, and P1 tidal constituents along the east coast of the US.

The prognostic variables (sea surface height, velocity, temperature and salinity) within the hydrodynamic model were initialized by interpolating information from the HYbrid Coordinate Modeling System (HYCOM), available with a spatial resolution of $1/12^{\circ}$.

The lateral boundary conditions for free surface, barotropic (depth-averaged) and baroclinic (three-dimensional) velocities, and temperature and salinity were set as follows. We used a Chapman boundary condition [Chapman, 1985] for sea surface elevation, which assumes all outgoing signal leaves at a shallow water speed. This condition together with a Flather boundary condition [Flather, 1976] is used to radiate out tidal and wind driven barotropic (depth-averaged) flows. Standard radiation boundary condition [Raymond and Kuo, 1984] was used for baroclinic (three-dimensional) velocities. Finally, temperature and salinity fields, and baroclinic velocities were nudged to climatology information obtained from the HYCOM model with a 1 day nudging coefficient at the boundary points, linearly decreasing to no nudging at locations 40 km (20 grid points) away from the northern, southern and the eastern boundary.

The bottom friction parameterization used for this study accounts for wave-current interaction within the bottom boundary layer and is described in details in Warner et al. [2008a]. The physical roughness length associated with grain size (skin friction) was used to estimate the kinematic bottom stress due to pure waves and currents, and for calculating eddy viscosity profiles. The grain size used for the smallest grid (0.2 mm) is representative of the average grain size measured during the experiment. As an approximation, same grain size is used for larger grids as well. This constraint does not change the flow circulation pattern in the parent grid in comparison to flows obtained from a bottom friction parameterization based on logarithmic layer prescribed through a bottom roughness length. Vertical turbulence mixing was parameterized using the k-ϵ Generic Length Scale momentum turbulence closure submodel [Umlauf and Burchard, 2003; Warner et al., 2005] and a background vertical viscosity of 5×10^{-6} ms^{-2}.

6.3.3 Forcing Conditions for the Wave Module

Wind field from NARR was used to force the wave propagation model. Wave field information at the open boundary of the parent grid (Fig. 6.3a) can be provided using either bulk wave parameters (significant wave height, peak/mean period, mean direction and directional spreading) or the complete frequency-directional wave spectrum. The former methodology is usually preferred [e.g., Olabarrietta et al., 2012] due to relative ease in obtaining the bulk wave parameters from archived WaveWatch III data (resolution ~ 3.33 km), which is used by the SWAN model to create a Joint North Sea Wave Propagation JONSWAP, Hasselmann et al., 1973) spectrum. One of the deficiencies of this approach is possible concentration of wave energy in the sea or the swell band depending on the wave period estimated for the entire spectrum. In addition, at any given moment more than one spectral peak may occur within the wave spectrum.

WaveWatch III hindcast reanalysis is also available as partitioned data where the two-dimensional wave spectrum is separated and stored as partitions by identifying the different peaks in the spectrum. These data can be used to create a two-dimensional (frequency-directional) ocean wave spectrum, by individually creating a JONSWAP spectrum with cos^{2s} directional distribution [e.g., Kuik et al., 1988] for each wave partition, and then summing up all individual directional partition-based spectra to create a single 2-D ocean wave spectrum. A MATLAB routine for creating two-dimensional wave spectrum from partitioned WaveWatch III data is provided in Appendix 1.

In this study, two simulations were conducted by providing wave forcing information in the form of (a) bulk wave parameters; and (b) two-dimensional wave spectrum from partitioned data. Simulated bulk wave parameters and frequency wave spectrum are compared to observations at site O2 (Fig. 6.1). During strong wave conditions (February 1-13, 2010), both approaches yield similar wave spectrum (Figs. 6.4b and c) in comparison to field observations (Fig. 6.4a). However, for weak wave conditions (February 13-21) the second method (spectral input) based simulation (Fig. 6.4b) is in better agreement with the observed spectrum. It is also evident that at certain times (February 18, 26, March 1 and 15) higher wave energy is observed in the swell band when forcing is provided through bulk wave parameters (Fig. 6.4c). This discrepancy is exhibited in form of sudden sharp peaks in the wave height time series (Fig. 6.4d). The model skill (using Brier Skill, Ganju et al., 2011) for comparison between measured and simulated significant wave height is high (S~0.8) for spectral wave input and comparatively low (S~0.6) for bulk wave parameter input. Also, comparison between observed and simulated mean wave direction (Fig. 6.4e) reveals a superior skill for spectral wave input (S~0.3) vs. bulk wave parameter input (S~ -0.9). Similar improvement in model performance is manifested at other measurement sites, and offshore buoy locations (not shown here) when using a spectral wave input. In

rest of this manuscript we use the wave parameter results obtained from simulation with forcing as spectral wave input.

6.4 Model Validation

In this section, model calculated hydrodynamic parameters (wave height, peak period, mean period, mean wave direction, frequency wave spectrum, depth-averaged and vertical profile of subtidal flows) are compared to field observations from a combination of offshore buoys, acoustic current meters, and VHF WERA radar measurements which are briefly described in the next section. The model skill is evaluated using two parameters: (a) correlation coefficient (r) and (b) Willmott skill score [Willmott et al., 1981], which is defined as:

$$S = 1 - \frac{\sum |X_{Model} - X_{obs}|^2}{\sum \left(|X_{Model} - \overline{X_{obs}}| + |X_{Obs} - \overline{X_{obs}}| \right)^2} \tag{6.1}$$

where, X is a prognostic variable being compared with a time mean $\overline{X}$. Perfect skill is denoted by S=1, while S=0 suggests complete disagreement. The Willmott skill score has been previously used to evaluate the performance of the COAWST modeling system in Willapa Bay [Olabarrietta et al., 2011]; ROMS simulations in Hudson Bay Estuary [Warner et al., 2005] and Columbia River plume study [Liu et al., 2009].

6.4.1 Experimental Data

In this section, hydrodynamic data collected around Cape Hatteras, NC as a part of US Geological Survey sponsored Carolina Coastal Change Processes is presented. These data were used to verify the performance of the model and are presented in detail in Kumar et al (2013).

Hydrodynamic Data

Inner shelf hydrodynamic data were collected over a number of nearshore sites during the period February 3 to 22, 2010. Acoustic current meters were used to measure three-dimensional flow velocities at various heights above the sea bed and hydrostatic pressure fluctuations. The time series collected were used to obtain sea surface power and cross-power spectral densities, wave height, period, direction, directional spreading, mean flows [see Kumar et al (2013) for more details on data reduction]. Three of the sites (O1, O2, and O3) were at relatively deeper water depths of approximately 9-10 m. The remaining of the stations were located in the nearshore with 4 of them (N1 to N4) located on the east side, 2 (N11 and N12) on the south side and the remaining 4 stations (N5, N6, N8 and N9) over the shoal itself.

Surface Currents

In addition to the current profiles measured at distinct point locations, a single station of a Very High Frequency (VHF) beam forming WEllen RAdar (WERA), manufactured by Helzel Messtechnik GmbH, was used to obtain radial surface currents over the area (Voulgaris et al., 2012). The surface radial currents were obtained on a grid 150 × 150m over the area (Fig. 6.1c). Radar coverage extends over the period February 3 to 26, 2010 with an interval of 30 min. The radial velocity estimates were the averages of 14.8 min of continuous radio transmission. More details regarding radar data collection and analysis are presented in Voulgaris et al. [2011].

Meteorological Conditions

Meteorological data for the deployment period and offshore wave data are available from the NOAA/NBC Diamond shoals buoy (ID 41025, Figure 6.1b). During the period of this study, seven synoptic frontal passages are observed over the study area (Figure 6.5). These events are characterized by increased wind speed with sudden

change in wind direction from the southwest to the northeast (Fig. 6.5a), increased wave height (Fig. 6.5b), a sudden drop in the atmospheric pressure (Fig. 6.5d), and an increase in the air and water temperature (Fig. 6.5e). Swell events (T_p > 10s, Fig. 6.5c) were observed after passage of atmospheric fronts.

6.4.2 Wave Model Evaluation

SWAN simulated frequency wave spectrum, significant wave height, mean wave period and direction are compared to measurements from four offshore NOAA-NDBC buoys within the domain of the parent grid (Frying Pan Shoals, Buoy ID 41013; Diamond Shoals, Buoy ID 41025; Delaware Bay, Buoy ID 44009, and Virginia Beach, Buoy ID 44014, see Fig. 6.3a). The simulated wave spectrum has similar, but relatively smoother energy distribution in comparison the observed spectral density (Figures 6.6a-d). The evaluation of significant wave heights (Figures 6.6e-h) and mean periods (Figures 6.6i-l) against measurements shows strong skill (0.9) and correlation (r ≈ 0.8-0.9, Table 1), suggesting that the model simulates the total wave energy field at a high skill. Similarly high skill is found in the simulations of the mean wave direction at FPS and Virginia Beach buoys implying a correct representation of the entire frequency-directional wave spectrum.

The performance of the wave model in the nearshore was evaluated through a comparison of the simulated wave parameters to in situ observations close the Cape Hatteras point (Figures 6.7 and 8). At sites O1, O2 and O3, predicted and measured H_{sig} and T_m (Figures 6.7a and 7b) values are strongly correlated (r > 0.7, see Table 2), and the model skill S is ~ 0.9. On February 8 and 12, when the wave energy is predominantly in the swell band, the simulated wave heights are underestimated at sites O2 and O3, and overestimated at site O1. This finding for the sites O2 and O3 is further corroborated by low swell energy in the modeled frequency wave spectrum (Figure 6.7e). One of the possible reasons for this discrepancy is that SWAN

model treats swell dissipation in similar fashion as depth-limited breaking of sea waves [e.g., Rogers et al., 2003] leading to an increased wave dissipation in the present case. Overestimation of wave height at site O1 is attributed to relatively less wave dissipation over the Diamond shoals, during refraction of swell waves approaching the Cape Hatteras region from the northeast, possibly due to inaccurate bathymetry information.

The skill of the model in simulating mean wave period was found to be fair ($0.5 < S < 0.9$, Table 2). Slight underestimation of wave period was noted during times of low wave energy (Feb. 9-11 and Feb. 17-20), as SWAN predicts higher energy in the wind frequency band in comparison to observed spectral energy. Modeled mean wave direction closely agrees with the observations at sites O1 and O3 ($r \sim 0.7$; $S \sim 0.7$, Table 2), however, for low wave energy conditions the model simulated mean direction at site O2 corresponds to the wind direction during this period, instead of the actual wave direction.

At shallower water sites (sites N5, N6, N8 and N9, water depth < 7m), the modeled wave parameter variability is similar to that previously discussed for sites O1, O2 and O3. At these stations, tidal modulation of wave parameters is evident (Figure 6.8). Model has a high skill (Table 2) in predicting significant wave height and mean period at all the sites. Likewise, the mean wave direction predictions at sites N8 and N9 closely agree with the observations. At sites N5 and N6, the mean wave direction is correctly predicted for most of the data collection period except during low wave energy (Feb. 15-20). It should be pointed that both sites N5 and N6 are close to the Diamond shoals, where the wave field is disorganized due to waves approaching from both the south/southwest and north/northeast. The modeled frequency wave spectrum is smoother but shows similar distribution as the measured spectral energy. Further, it is interesting to note that the presence of tidal variability in spectral energy distribution is correctly simulated by the wave model (Figs. 6.8d and e).

Overall, modeled wave parameters show similar variability as that observed in the measurements. The model has good skill in obtaining the total energy and the distribution of spectral energy as a function of frequency and direction.

6.4.3 Vertical profile and Depth-averaged subtidal flows

The circulation model is evaluated by comparing depth-averaged and vertical distributions of subtidal flows at sites O1, O2, O3 (Fig. 6.9) and sites N5, N6, N8 and N9 (Fig. 6.10). The corresponding model skill and correlations are reported in Table 3.

Model estimated east velocity has similar variability and is strongly correlated to measured flow at site O1, while moderate to poor correlation is obtained for sites O2 and O3, respectively. This behavior is reflected through a decline in model skill from 0.8 at site O1 to 0.4 at site O3 (see Table 3). Further comparison to vertical profile of eastward subtidal flow reveals that during stronger wind and wave conditions, the simulated flow structure is similar to that in the observed flow (Figs. 6.9a and b). On the contrary, during periods of weak winds and wind-induced wave forcing (Feb 8-10; Feb 12), the observed flow has a two layer structure which is not completely captured by the model. This might be due to the fact that the initial stratification conditions used from HYCOM do not resolve inner shelf scale processes. It is also possible that advection of low salinity fresh water [e.g., Rennie et al., 1999] from Chesapeake Bay is advected towards the study area, which modifies the density distribution; a process not captured in this study.

At site O2, the model has a lower skill than that at site O1 at simulating the vertical profile of eastward flow (Fig. 6.9b), although the vertical flow structure is similar to that seen in the data (Fig. 6.9a). Interestingly, the model predicts similar eastward flows at sites O2 and O3 (Fig. 6.9b), although that is not the case in the measurements. It is expected that these differences occur due to local bathymetric

effects around site O3, and the model fails to correctly resolve the velocity structure due to a lack of accurate bathymetric information.

The circulation model shows good agreement to depth-averaged (Fig. 6.9f) and vertical profile of northward velocity (Fig. 6.9d) at sites O2 and O3. From Feb. 15-20, the vertical profile at site O2 has two-layered structure, which is not represented by the model (Fig. 6.9d). Finally, at site O1 the modeled flow is similar but slightly weaker than the observed flows, which is represented by strong correlation ($r \sim 0.7$) and relatively weaker model skill ($S \sim 0.6$) in comparison to site O2 ($S \sim 0.8$, Table 3).

Depth-averaged eastward flow at sites N5, N6, N8 and N9 are in agreement with measured flows (Fig. 6.10e). At certain times, the flows are underestimated at site N5, and overestimated at site N8. Nevertheless, we observe similar temporal variability with high correlation ($r > 0.6$) and model skill ($S > 0.7$) at all the sites expect N8. Similarly, modeled northward depth-averaged flow at all the sites (N5, N6, N8 and N9) is comparable to measured flow (see Fig. 6.10f and Table 3). In addition, comparison of vertical profile of northward subtidal flow also reveals good agreement ($r > 0.5$ and $S > 0.7$, Table 3) to measured values (Figs. 6.10c and d).

In order to quantify the overall model performance at the location of acoustic instrumentation (sites O1, O2, O3, N5, N6, N3, N4, N8, and N9), the model velocities are interpolated for the same duration as that of data collection at an individual site. These interpolated model results are then used to determine the mean flow and variance ellipses for depth-averaged flows and compared to similar analysis conducted for the measurements (Fig. 6.11).

At all the sites but O3, the modeled mean flows have the similar direction as measurements (Fig. 6.11). Moreover, the magnitude of modeled mean flow is similar to the observations at sites O2, O3, N5, N6, N3 and N4, and is underestimated at sites O1, N8 and N9. The modeled variance ellipses (Fig. 6.11) representing variability

around the mean flow are comparable to measured variance ellipses at all the sites except N6, N8 and O3, where the model underestimates the flow variability. Finally, at site N5, measurements suggest that the principal axis of the variance ellipse is parallel to the local bathymetric contour (Fig. 6.11), which is not evident in the modeled variance ellipse.

6.4.4 Time-Space Validation

The model performance over larger spatial scales is evaluated using the VHF radar measured Lagrangian surface currents. The simulated subtidal Lagrangian velocity (sum of Eulerian mean and the Stokes drift) from the sigma layer closest to the sea surface are compared to radar derived radial velocities along two transects aligned in the cross-shore (transect II) and the almost alongshore (transect I) directions with reference to the local shoreline on the east side (see Fig. 6.1b).

Surface cross-shore flows from the radar along transect II suggest an increase in the magnitude of Lagrangian surface flows at locations farther away from the shoreline (Fig. 6.12a). The simulated cross-shore flows (Fig. 6.12a) exhibit a similar spatial - temporal variability for the periods of February 5-15, and February 22 onwards. During the period February 15-22 the simulated cross-shore surface flows are relatively weaker in comparison to the radar derived ones, although they exhibit the same tendency of increased flow strength farther offshore. Model derived surface cross-shore flows are moderately correlated (r= 0.5, Table 4), and the model skill (S) is 0.7.

The model performance in simulating the temporal and spatial variability of the alongshore surface flows is significantly better than that described above for cross-shore flows (Fig. 6.12c and Table. 4). Correlation of the model results with the radar data is moderate (r=0.6) while the model skill is high (S=0.8). Both modeled and radar measured surface flows suggest an increases in the magnitude of alongshore

current near the shoal region. This is partially attributed to a convergence of flows from either sides of the shoal (see Fig. 6.12d), and/or the fact that the water depth rapidly decreases close to the shoal complex leading to an advective flow acceleration.

6.4.5 Spatial Gradient Validation

VHF radar measured and simulated cross-shore gradient of subtidal, cross-shore surface velocity (i.e., $\partial u/\partial x$, Figs. 6.13a and b) and alongshore gradient of alongshore surface velocity ($\partial v/\partial y$, Figs. 6.13c and d) are compared to evaluate the model performance in determining spatial velocity gradients.

Measured $\partial u/\partial x$ (Fig. 6.13a) has substantial spatial and temporal variability in comparison to simulated $\partial u/\partial x$ (Fig. 6.13b). On the contrary, both measured and simulated $\partial v/\partial y$ have relatively uniform spatial distribution (Figs. 6.13c and d). The lack of spatial structure in $\partial u/\partial x$ is partially attributed to the fact that the simulated cross-shore flows only capture part of the actual flow variation in the cross-shore direction, and the temporal-spatial transition is relatively smoother than the observations.

Model skill in simulating velocity gradients as a function of along/cross-shore distance and time are shown in Figs. 6.14a and b. These skills were estimated by using the measured and simulated temporal series for each cross and alongshore location; and spatial distribution in the cross-shore and alongshore transects for each time index. It is evident that model skill is relatively low ($S < 0.4$) for cross-shore flow gradients at most of the cross-shore locations. Only at locations with strong horizontal gradients (4-6 km offshore), the model performance improves. On the contrary, model skill is moderately better in simulating alongshore flow gradients ($S > 0.4$, Fig. 6.14a). At this juncture it is important to point out that the VHF measured cross-shore velocity is weak and can be slightly erroneous especially for periods with negligible wind and wave forcing.

Temporal variation of model skill suggests improvement in model performance (Fig. 6.14b) in simulating alongshore velocity gradients only during periods of strong wind and wave forcing. At all other times the model skill is fair to poor (Fig. 6.14b). On the contrary, relatively high model skill ($S > 0.4$) in simulating cross-shore velocity gradient is obtained for times corresponding to smooth spatial variation.

Overall, our comparisons against static current meters and radar measurements have shown that the model is able to simulate both the temporal and spatial variability of the flow in the transition area between the inner shelf and the surf zone. This is particular the case especially during high wind and wave conditions. Slight differences occur in the simulated vertical distribution of flows especially during weak wind and wave forcing that corresponds to reduced mixing conditions. This discrepancy is expected in the absence of a good control on the initial stratification in the nearshore and lack of high resolution bathymetry within the study area. Nonetheless, it is justified that the model results presented here are accurate enough to be used for identifying the important processes controlling the overall circulation pattern within the study area.

6.5 Results

6.5.1 Circulation Patterns around the Shoal Complex

During the experiment period the study area was influenced by passage of synoptic meteorological fronts on February 5-7, 10-11 and 15-17, 2010. These frontal passages are characterized by strong wind and wave forcing. In addition, strong southwestward directed swell were observed on February 7-8 and 12-13, 2010.

In general, the winds are directed towards the south/southeast for most of the experiment period (Fig. 6.5a). During these periods, model simulated flows suggest southward/southwestward flow on the east side of Cape Hatteras, NC. In the lee

of the cape (i.e., south side), the flows are relatively weak in comparison to those over the shoal complex and on the east side. However, for intermittent eastward/ northeastward directed winds, strong flows are simulated on the south side of the Cape Hatteras point. It is also during these wind conditions that high wave energy induced activity occurs on the south side, while the east side is sheltered. This pattern of wave energy variation is reversed during swell events consisting of waves approaching the study area from the northeast direction.

In order to discern the role of sudden change in shoreline orientation and presence of a shallow shoal complex in modifying the nearshore circulation and wave propagation, we consider six events from the entire time series (see Fig. 6.5 and Table 5) corresponding to (a) south /southwestward directed winds with weak southwestward directed waves (February 4); (b) northeastward winds and strong waves towards the north and northwest direction (February 6); (c) same as in (a) but for strong swell waves propagating towards the southwest (February 7); (d) strong southeastward directed winds and waves (February 11); (e) same as in (b) but with relatively weak wave forcing; and (f) northward directed winds with strong northwestward directed waves. These events provide a comprehensive understanding of the relative role of wind and wave forcing in creating flows

Horizontal Circulation

4th February

Snapshots of spatial variability of subtidal, depth-averaged circulation and wave conditions are presented in Figures 6.15 and 16, respectively. On February 4, winds of the order of 10 ms^{-1} are directed towards the south. The subtidal circulation pattern (Figure 6.15a) reveals strong south/southwest directed flow on the east side of Cape Hatteras point, while on the leeward side (i.e., south side) the formation of a gyre is observed with weak southeastward flows. The wave field is relatively weak during

this period (Figure 6.15a) with significant wave height approximately 1.5 m on the east side propagating towards the south/southwest. These waves refract around the shoal leading to a loss in wave energy, which is augmented by bottom friction and depth-limited breaking. Waves on the south side are directed towards the west and the northwest.

6th February

On the example from February 6, winds are directed towards the northeast (Figure 6.15b). High wave conditions (H_{sig} ~ 3m) are observed on either sides of the shoal complex, with waves propagating almost perpendicular to the local coastline orientation (Figure 6.16b). Local wave refraction effects are evident near the Cape Hatteras point. The flow pattern observed during this period suggests southeastward flows on the south side and northeastward flow on the east side. It is further observed that the flow near the shoal region is also directed towards the northeast, which may be partially attributed to locally wave breaking driven flows (see section 7).

7th February

On February 7, the wave field and circulation pattern (Figures 6.15c and 16c, respectively) is similar to that discussed above for February 4, although the magnitudes of both wave height and flow are higher. These two examples confirm that when sea/swell waves are propagating from the north/northeast direction, the south side of Cape Hatteras is protected by the presence of shoal. Historical climatology analysis (see Fig. 6.2) suggests that this kind of wind pattern (i.e., from 150°N to 210°N) is common as it occurs for about 25% of the time in atypical year.

11th February

During southeastward winds (i.e., on February 11, Figure 6.15c), the wind direction is almost perpendicular to the local coastline on the east side, and parallel to that on the south side. Southeastward flows are present on the east and the south side, leading to a confluence at the shoal region where the flow continues towards the southeast. Weak eastward and southeastward directed waves are seen over the study region during this period (Figure 6.16d). According to wind climatology these conditions occur for almost 16% of the time in a typical year when the wind direction ranges from northeast to the southeast (i.e., from 60° N to 120°N).

27th February

Wind event on February 27 (Figures 6.15e and 16e) is similar to those observed on February 6 with strong east/northeast directed winds. In this case, the east side of Cape Hatteras point is the leeward side and as such protected from the waves approaching from the southwest direction and a tendency for gyre formation is present.

13th March

Finally, the model results show the shoal complex acts as a barrier to northward driven flows due to north/northwest winds (Figures 6.15f and 16f), separating the structure into alongshore flows on either side of the shoal complex. However, these local alongshore flows tend to create local circulation cell patterns (Figure 6.15f). Strong waves parallel to the shoal and almost perpendicular to the local coastlines are seen during these wind conditions, which constitute approximately 12

Vertical Circulation

Along- and cross-shoal variability of cross-, along-shoal and vertical flows are presented for the six events (February 4 to March 13) discussed in section 5.1 (Figs. 6.17 and 18, see Fig. 6.4c for location of Transect 3 and 4).

During southwestward directed winds (Figs. 6.15a and 15c), the cross-shoal flow follows the wind stress and is almost vertically uniform in both the along (Figs. 6.17a1 and 17c1) and the cross-shoal (Figs. 6.17a1 and 17c1) directions. Strongest flows occur along the shoal axis with a decrease in flow strength on either side of the shoal axis (Figs. 6.17a1 and 17c1). Along-shoal flow is weak and directed towards the southeast (Figs. 6.17a2 and 17c2), while the cross-shoal distribution of along-shoal flow (Figs. 6.18a2 and 18c2) suggests a change in sign from positive (northwestward) to negative (southeastward), pointing at local flow rotation about the shoal axis.

For winds directed towards the east and northeast (Figs. 6.15b and 15e), a reversed cross-shoal flow pattern is seen (Figs. 6.17b1, 17e1, 18b1, and 18e1). Along-shoal flow during these periods can be of similar magnitude as the cross-shoal flows (Figs. 6.17b2, 17e2, 18b2, and 18e2). Also, the flow rotation pattern about the shoal axis is reversed with southeastward flows on the south side and northwestward flows on the east side (see Figs. 6.18b2 and e2).

When the winds are directed to the southeast or the northwest (Figs. 6.12d and f), cross-shoal flows (Figs. 6.17d1, 17f1, 18d1, and 18f1) are relatively weaker than along-shoal flows (Figs. 6.17d2, 17f2, 18d2, and 18f2). During strong southeastward winds, the cross-shoal flow along the shoal axis is weak (Fig. 6.17d1), while northeastward and southwestward cross-shoal flows are observed perpendicular to the shoal axis (Fig. 6.18d1), suggesting a flow convergence towards the shoal complex. On the contrary for northwestward winds, a divergence of cross-shoal flows occurs (Fig. 6.18f1).

Vertical flows for all the events (Figs. 6.17a3-f3 and 18a3-f3) are at least an order of magnitude smaller than the horizontal flows. Nevertheless, rapid change of bathymetry along and perpendicular to the shoal axis leads to creation of circulation cells with vertical flows directed towards or away from the sea bed depending on the flow direction.

Stokes Drift

Stokes drift has a surface intensified vertical distribution (e.g., Eqn. [5] of Kumar et al., 2012). Snapshots of vertical profiles of along-shoal, cross-shoal and vertical Stokes drift for the six time periods (February 4-March 13) described above are presented in this section (Figs. 6.19 and 20). Horizontal Stokes drift velocities with magnitude 0.2-0.3 ms-1 are limited to the surface layer (Figs. 6.19 and 20) and are observed for all the events expect on February 4, when low waves were present. Vertical Stokes drift velocities (Figs. 6.19a3-f3 and 20a3-f3) are always two orders of magnitude smaller than the horizontal velocities; and at least an order of magnitude smaller than their Eulerian counterpart.

For all the events the cross-shoal Stokes drift velocities (Figs. 6.19a1-f1, Figs. 6.20a1-f1) are in the same direction as the Eulerian mean cross-shoal flows (Figs. 6.17a1-f1 and Figs. 6.18a1-f1). Also, for certain times at locations along the shoal axis farther away from the cape point, the cross-shoal Stokes drift at the surface (Figs. 6.19d1 and 20d1) is of similar magnitude or stronger than the Eulerian mean flow (Figs. 6.17d1 and 18d1).

The along-shoal Stokes drift augments the along-shoal Eulerian mean flow only on February 11, 27 and March 13 (Figs. 6.19d2-f2 and Figs. 6.20d2-f2), while on February 6 and 7, Stokes drift velocity (Figs. 6.19b2-c2) is directed opposite to the Eulerian mean counterpart on the south and the east side, respectively.

Overall, it is expected that the Stokes drift only slightly modifies the circulation pattern around the shoal complex by augmenting or diminishing the Eulerian mean flow. Nevertheless, the Stokes drift does not completely balance the Eulerian mean flow at locations adjacent to and farther offshore of the cape point, thus pointing that in general a balance between Coriolis acceleration and Hasselmann's wave stress (i.e., $fu(z) = fu^{St}(z)$) suggested by Lentz et al. (2008) does not occur within the shoal complex region.

6.5.2 Wind-Driven Alongshore Flows

The role of coastline variability around the Cape Hatteras region in modifying the wind driven circulation is investigated by considering alongshore flows at two cross-shore transects (Transect 1 and 2, Figure 6.3c) on either side of the Cape Hatteras point. The local co-ordinate system is oriented at an angle of 10° and 166° clockwise from the north for the east and the south side, respectively. A positive alongshore wind stress on the east side signifies northeastward driven winds, while on the south side, a positive alongshore wind stress is towards the southeast.

Time series of cross-shore distribution of local, subtidal, alongshore currents and wind stress is shown for transects 1 and 2 in Fig. 6.21. On the east side, the alongshore flows respond to local wind stress for the entire simulation period, making wind forcing a primary driver for the observed flow pattern. The correlation coefficient (r) between wind stress and current varies from 0.7 at locations closer to the shoreline, to 0.8 for locations farther offshore. Maximum correlation occurs at a lag time of 2-3 hours. The alongshore wind pattern is directed towards the south/southwest for most of the simulation period (Fig. 6.21b), while north/northeastward wind driven events are rare. This wind forcing does not allow for the east side to be the leeward side of the cape.

On the south side of Cape Hatteras (Fig. 6.21c), an interesting relation is observed between local alongshore wind stress and currents. At cross-shore locations near the shoreline, the flow direction is opposite to the wind stress ($r\sim$ -0.3), while at locations further offshore (>3-4 km) the flows can be in the same direction as the wind stress ($r\sim$ 0.6). These events of flow reversals usually occur during sustained periods of south/southwestward directed winds (Fig. 6.21d), when the south side becomes the leeward side with respect to the Cape Hatteras point. This pattern is further corroborated by flow measurements opposite to the local alongshore wind stress at sites N9 and O1 on February 4-5, and relatively weakened response to the

wind stress during rest of the experiment period (also see K13, their Fig. 8). The reversal or flow weakening usually occurs within 3-4 km from the shoreline (Fig. 6.21c), and is similar to findings based on field observations [Gan and Allen, 2002b; Gutierrez et al., 2006] and numerical modeling based studies [Gan and Allen, 2002a; Sanay et al., 2007].

6.6 Discussion

This section is focused on explaining (a) the dominant terms in alongshoal and cross-shoal momentum balance within the shoal complex region; and (b) on the east and south side of the shoal complex. The latter is presented as a time series of depth-averaged alongshelf momentum balance as a function of the cross-shelf distance, while the former is discussed through snapshots of depth-averaged cross-shoal and along-shoal momentum balance terms

6.6.1 Momentum Balances over the shoal

The circulation pattern around the shoal complex is complicated due to coastline variability and rapid bathymetric change. In this section the response of the shoal complex to different wind and wave conditions is discussed through dominant terms in momentum balance. The six periods presented earlier are chosen to represent varying wind and wave condition patterns. The momentum balance analysis presented is divided into an along and cross-shoal coordinate system (see Fig. 6.3c). In the cross-shoal momentum balance, positive value of a term suggests northeastward direction, and for the alongshoal momentum balance, a positive value corresponds to the northwest. Also, to provide greater details around the shoal complex we focus on a smaller part of the last child grid (see Fig. 6.3c).

4th February

On February 4, the winds and currents are directed towards the south/southwest, while weak waves (~1.5 m) approach the shoal from the northeast direction (Figs. 6.15a and 16a).

The major terms in the along-shoal momentum balance (Fig. 6.22) are pressure gradient (PG, Fig. 6.22a), nonlinear advective acceleration (NA, Fig. 6.22b) and bottom stress (BS, Fig. 6.22c). The PG term augments the wind stress term (Fig. 6.22f) in driving south/southwestward flows. Rapid bathymetric changes in the shoal complex also create local PG, which is balanced by the NA term (Fig. 6.22b). Overall, the dominant balance in alongshoal momentum balance occurs between the PG term and the sum of NA and the BS term. In the cross-shoal momentum balance (Fig. 6.22), the dominant contributors are PG (Fig. 6.22g), NA (Fig. 6.22h) and BS (Fig. 6.22i) terms. The PG term is negative (southwestward) and is responsible for development of cross-shoal flow pattern over the shoal complex. The contribution of breaking acceleration (BA), vortex force (VF) and surface stress (SS) is weak in both along and cross-shoal direction.

6th February

The winds are directed towards the east/northeast, while the waves approach the coastline on the south side from the southwest direction (Figs. 6.15b and 16b). These waves refract around the shoal complex, leading to northwestward directed waves on the east side.

Wave breaking around the shoal complex region leads to a strong contribution by the BA term in the alongshoal momentum balance (Fig. 6.23d). The other dominant terms are PG, NA and BS (Figs. 6.23a, b and c). Along the shoal axis, the BA term is positive (directed to the northwest), while the PG and NA terms are negative. The relative balance between PG and NA is analogous to that observed in cross-shore momentum balance in an alongshore uniform beach where gradient of radiation stress is

balanced by the pressure gradient. VF term (Fig. 6.23e) is not a dominant term, but around the cape point it is of similar magnitude as the BS term. In the cross-shoal momentum balance (Fig. 6.23), the effect of change in the wave direction due to refraction is reflected by a change in the sign of BA term on either sides of the shoal axis (Fig. 6.23j). Subsequently, the BA term is balanced by a combination of the PG (Fig. 6.23g), NA (Fig. 6.23h) and BS (Fig. 6.23i) terms on the south side of the shoal, while the sum of BA and BS balance the sum of PG and NA on the east side of the shoal.

7th February

The momentum balance on February 7 is similar to that observed on 4th February, with the only difference being the contribution of the BA term in this event. The major terms in the alongshoal momentum balance are BA (Fig. 6.24d), NA (Fig. 6.24b), BS (Fig. 6.24c) and the PG (Fig. 6.24a) term, with the latter three terms balancing the BA. The localized PG (Fig. 6.24g) and BA (Fig. 6.24j) terms in the cross-shoal momentum balance are negative (i.e., towards the southwest) and responsible for flow deflection from the south to the southwest (Fig. 6.12c). For most of the shoal region, the cross-shoal momentum balance constitutes of a balance between sum of PG and BA (Fig. 6.24j) and the sum of BS and NA (Fig. 6.24b) terms.

11th February

Figure 6.25 shows the along and cross-shoal momentum balance. In the alongshoal momentum balance, SS (Fig. 6.25f) and BA (Fig. 6.25d) are the dominant terms responsible for the observed flows. The balance occurs between the BS (Fig. 6.25c) and the sum of SS and BA. Locally, a balance between PG (Fig. 6.25a) and NA (Fig. 6.25b) is observed as well. Furthermore, the strong southward flows observed at locations further east of the shoal complex, occur due to relatively lower

sea surface elevation over the shoal (not shown here), creating a negative pressure gradient. In the cross-shoal balance, the pressure gradient contribution (Fig. 6.25g) is negative (southwestward) and is primarily balanced by the breaking acceleration term (Fig. 6.25j).

27th February

Similar balance as that observed for February 6 occurs during period (Figs. 6.23 and 26). However, the role of breaking acceleration is negligible (Fig. 6.26j) and the flows are directed towards the east (Fig. 6.15e) unlike northeastward flows (Fig. 6.15b).

13th March

Finally, when the winds and waves are directed towards the north/northwest direction, the alongshoal momentum balances at most of the locations (Fig. 6.27) suggest that the BA contribution (Fig. 6.27d) is balanced by the sum of PG (Fig. 6.27a), BS (Fig. 6.27c) and NA (Fig. 6.27b). It is further expected that the PG term in this case develops as a response to wind and wave induced setup in the alongshoal direction, with the Cape Hatteras point acting as the shoreline. The cross-shoal momentum balance in this case is similar to those observed for the 6th and 27th February events.

In an attempt to synthesize the cross and along-shoal momentum balance for the different wind and wave forcings described through the six cases presented above we can say that:

a) Local change in momentum balance dynamics near the shoal complex modifies the circulation pattern of flow advecting towards the Cape Hatteras point. This mechanism plays a dominant role in the turning of flow along the shoal axis to cross-shoal

flows.

b) During weak wave conditions, for southwestward directed winds, a pressure gradient is directed towards the shoal complex, which can augment the wind driven flows. This pressure gradient is partially balanced by the bottom stress.

c) The shallow regions of the shoal complex almost behave like an extended coastline. When waves approach from the southwest or northwest direction, the shoal responds by creating a cross-shoal pressure gradient directed towards the southeast, which is partially balanced by the breaking acceleration. A similar response is identified for waves approaching from the southeast and the northeast direction. Nevertheless, unlike a coastline, the shoal complex is not an impervious boundary and net imbalance between breaking acceleration and pressure gradient can create local cross-shoal flows.

d) For waves parallel to the shoal axis approaching the Cape Hatteras point, localized along-shoal breaking acceleration contribution is balanced by a combination of pressure gradient and nonlinear advective acceleration, which is also analogous to cross-shore momentum balance for an alongshore uniform coastline.

6.6.2 Momentum Balances on the East and South Sides

Cross-shore distribution of alongshore momentum balance (Fig. 6.28) is considered on the east side of the Cape Hatteras point (see Fig. 6.3c for transect location). In locations farther offshore, the major terms in momentum balance are bottom stress, Coriolis and local acceleration, wind stress and pressure gradient. Bottom stress (Fig. 6.28a1) is opposite to the wind stress (Fig. 6.28f1), but they do not completely balance each other at all times. During strong southwestward wind conditions, wind

stress is augmented by a pressure gradient (Fig. 6.28g1). However, when the wind stress forcing weakens or is directed towards the east/northeast (February 10 and 27) this pressure gradient contribution is opposing the wind stress, and is attributed to local variation in sea surface elevation due to change in shoreline orientation and the presence of the cape. Furthermore, the role of pressure gradient as identified here is similar to that suggested using field observations farther north [see Lentz et al., 1999]. Local acceleration term (Fig. 6.28e1) shows similar variability as the bottom stress (Fig. 6.28a1), but has a smaller magnitude.

In shallower waters, the nonlinear (Fig. 6.28b1) and wave breaking acceleration (Fig. 6.28h1) also become important. Vortex force (Fig. 6.28d1) is usually negligible in deeper waters, but becomes important during periods of intense wave breaking as on February 6-8. The role of pressure gradient contribution is slightly reduced in shallow waters (Fig. 6.28g1), except during wave breaking events. These findings are similar to those suggested by Kumar et al (2013) using the experimental data, with the exception of the role of pressure gradient acting in conjunction with the wind stress.

On the south side of Cape Hatteras (Transect 3, Fig. 6.12), the cross-shore distribution of local alongshore momentum balance is presented in Fig. 6.28 (right column). In deeper waters, major terms in the momentum balance are Coriolis acceleration (Fig. 6.28c2), wind stress (Fig. 6.28f2) and pressure gradient (Fig. 6.28g2). The pressure gradient is directed opposite to the wind stress direction. The momentum balance analysis reveals that the nearshore flow reversal on the south side of the cape occurs due to a pressure gradient acting against the wind stress. This finding also agrees with a simplified analysis presented through field observations in Kumar et al, (2013) and the results from Gutierrez et al. [2006].

Close to the shoreline, nonlinear acceleration (Fig. 6.28b2) and bottom stress (Fig. 6.28a2) also become important and together with the pressure gradient balance

the wind stress forcing. Nonlinear acceleration has the same spatial length scale as that identified for nearshore flow reversals (see Fig. 6.21c). Vortex force contribution (Fig. 6.28d2) is of smaller magnitude, while the breaking acceleration (Fig. 6.28h2) shows almost similar variability as the wind stress and become important only at certain periods.

Overall, the alongshelf momentum balance dynamics on the east side is similar to a traditional momentum balances valid for regions with simplified alongshelf bathymetry (e.g., off Central Oregon Coast, Kirincich and Barth, 2009; Martha's Vineyard, Fewings and Lentz, 2010; Mid-Atlantic Bight, Lentz et al., 1999). On the contrary, alongshelf momentum balance found on the south side has only been reported through modeling based studies (Gan and Allen, 2002a; Sanay et al., 2007) or thorough a linearized and approximate momentum balance through field observations (Gutierrez et al., 2006; Kumar et al., 2013).

6.6.3 Comparison between Tidal Residual and Mean Subtidal Flows

The relative importance of wind and wave driven versus tidally driven flows in maintenance of shallow seaward directed shoal attached to cuspate forelands has been speculative with relatively scarce information. McNinch and Luettich [2000] debated that the tidal residual flows can be a dominant source for long term maintenance of sand banks associated with Cape Lookout, NC. In this study we compare the relative importance of tidally rectified flows by running the circulation model for the same period (February 1 to March 20) with tides as the only forcing parameter. The bottom friction for this simulation was provided through a logarithmic bottom drag formulation. The tidal flows derived from the model were subjected to standard harmonic analysis to obtain the residual Eulerian flows.

Figure 6.29a shows the tidal residual flow over the study area. At locations adjacent to the Cape Hatteras point, the tidal residual circulation pattern is weak and

suggests formation of local gyres. Over the shoal complex and further offshore, the tidal residual flow is directed towards the southeast maintaining an angle with the along-shoal direction. The flow structure (Fig. 6.29a) is of the same order of magnitude but slightly different than the along-shoal symmetric structure presented by McNinch and Luettich [2000]. Nonetheless, the simulated flows in this study are directed seaward from the cuspate foreland, a behavior consistently seen in headland induced residual tidal flows [e.g., Signell and Geyer, 1991].

The time and depth-averaged subtidal Eulerian mean flow along with the averaged wind stress direction during the experiment period is presented in Figure 6.29b. These subtidal flows are directed towards the south on the east side of the Cape Hatteras point, changing to southwestward flows over the shoal complex. On the south side, flows are relatively weak over the simulation period. The overall subtidal flow pattern is consistent with respect to mean wind stress over the region. Mean Lagrangian flows (not shown here) for the same duration are similar to the Eulerian mean flows presented here.

It is interesting to note that at most of the locations, the wind-driven subtidal flows are almost always stronger than the tidal residual flows by a factor of 2 to 3. This finding suggests that the relative contribution of wind and wave driven flows for the Cape Hatteras region is substantially stronger than tidally rectified flows for the duration of the experiment. In addition it is also expected that any associated transport (sediment particles, pollutants etc.) of material over the shoal complex is primarily influenced by the wind and wave driven hydrodynamics. The role of tidal residual flow is limited in the present case, and it is expected that tidally driven transport is not the primary source for "short term" sediment transport in microtidal environments like Cape Hatteras, NC with narrow shelf and relatively strong wave activity.

6.7 Conclusions

We use the Coupled-Ocean-Atmosphere-Wave-Sediment Transport modeling system to study the nearshore circulation pattern and wave propagation in cuspate embayments. The modeling system is configured to study the Cape Hatteras region, a cuspate foreland system with dramatic shoreline variability and a subaqueous shoal complex system extending seaward. Model simulation is conducted for a period of 48 days from February 1 to March 20, 2010; a period of strong synoptic meteorological frontal passages and swells.

Comparison of modeled wave parameters (significant wave height, mean wave period and direction, frequency spectrum) to those at offshore NOAA-NDBC buoys and to measurements obtained through field study conducted at Cape Hatteras, NC suggests that the wave propagation model has a high skill in simulating the total energy within the wave spectrum and the bulk wave parameters, in mid-shelf, inner-shelf and within the surf zone. Three-dimensional and depth-averaged subtidal circulation pattern simulated by the model is compared against point measurements from acoustic current meters. The model has a fair skill in simulating vertical and depth-averaged temporal distribution of flow in the dominant (local alongshore) direction, and low skill in the cross-shore direction. The latter is partly attributed to lack of high resolution accurate bathymetric data within and around the shoal complex. Model performance in simulating the spatial variability of flow is ascertained by comparisons of surface Lagrangian currents to those obtained from VHF radar system. Overall the model correctly captures the flow dynamics due to various hydrodynamic forcing. The major findings from this study are:

The existing shoal complex extending seaward from the Cape Hatteras point regulates flow pattern in the Cape Hatteras region. For south/southwestward directed winds, flow pattern on the windward side of Cape Hatteras directly responds to the

wind stress, while a local gyre formation occurs on the leeward side. This flow structure has also been identified from other modeling based studies [e.g., Gan and Allen, 2002ab; Sanay et al., 2007], and field observations from Long Bay, SC [Gutierrez et al., 2006] and Cape Hatteras, NC [Kumar et al., 2013]. The east side of Cape Hatteras becomes the leeward side for east/southeastward directed winds, however, sustained southeastward winds were not observed during this study. Similar kind of flow pattern as a response to wind forcing is expected for other cuspate forelands in the South Atlantic Bight and on the west coast of the US.

The shoal complex protects the east and south side of the Cape Hatteras from waves approaching the region from the southwest and northeast direction, respectively. Enhanced dissipation due to wave refraction, bottom friction and depth-limited breaking occurs when waves propagate over the shoal complex. Similar sheltering of local coastlines to offshore waves has also been identified for other regions like Myrtle Beach, SC [Voulgaris et al., 2008].

Convergent flows at the shoal complex and enhanced along-shoal offshore transport occurs during east/southeastward directed winds. On the contrary, during northwestward winds, the flow pattern diverges from the shoal axis creating local gyres around the Cape Hatteras point. These flow mechanisms may play an important role in net movement of material from the littoral zone to the inner and the mid-shelf, thus providing a mechanism for shoal building.

Alongshore momentum balance analysis on the east side of the shoal complex suggests dominant role of wind stress and pressure gradient in deeper waters (>10m), with the latter term usually augmenting the former. This pressure gradient behavior occurs due to local variation in the coastline orientation relative to the wind stress. Bottom stress, local and Coriolis acceleration also play an important role in the momentum balance. In shallower waters, in presence of wave breaking, the vortex force, nonlinear acceleration and breaking acceleration also become important in the mo-

mentum balance. However, most of the previous momentum balance studies neglect the role of vortex force and the nonlinear acceleration in the transition zone between inner shelf and surf zone.

On the south side of Cape Hatteras, the dominant balance occurs between a local alongshore pressure gradient and wind stress. This balance restricts development of flow in response to the wind stress and also leads to flow opposite to the wind direction, especially near the shoreline. The latter finding is also supported through a simplified momentum balance analysis conducted by Kumar et al. [2013] and for Long Bay, SC by Gutierrez et al. [2006]. The length scale of these nearshore flow reversals vary can be up to 3-4 km. It is expected that a similar balance exists for leeward side of other capes and varying coastlines.

The behavior of the shoal complex is almost like a coastline for waves propagating both perpendicular and along the shoal axis. In the former case, for waves approaching from either side of the shoal axis, a pressure gradient is generated as a response to wave breaking acceleration. Nevertheless, in absence of a "real" boundary, this balance is not sustained and leads to flow perpendicular to the shoal axis. This mechanism is one of the reasons for advection of southward driven flows to the southwest or southeast.

Finally, tidal residual flows are compared to mean, depth-averaged, subtidal flows for the entire simulation period. The subtidal flows are of the same order as the tidal residual flows, and twice or three times stronger over the entire modeling domain. It is expected that for regions with same dynamic wind and wave forcing, the short term wind and wave induced flow and associated sediment transport pattern is a more dominant process for moving sediment through the shoal complex in comparison to tides.

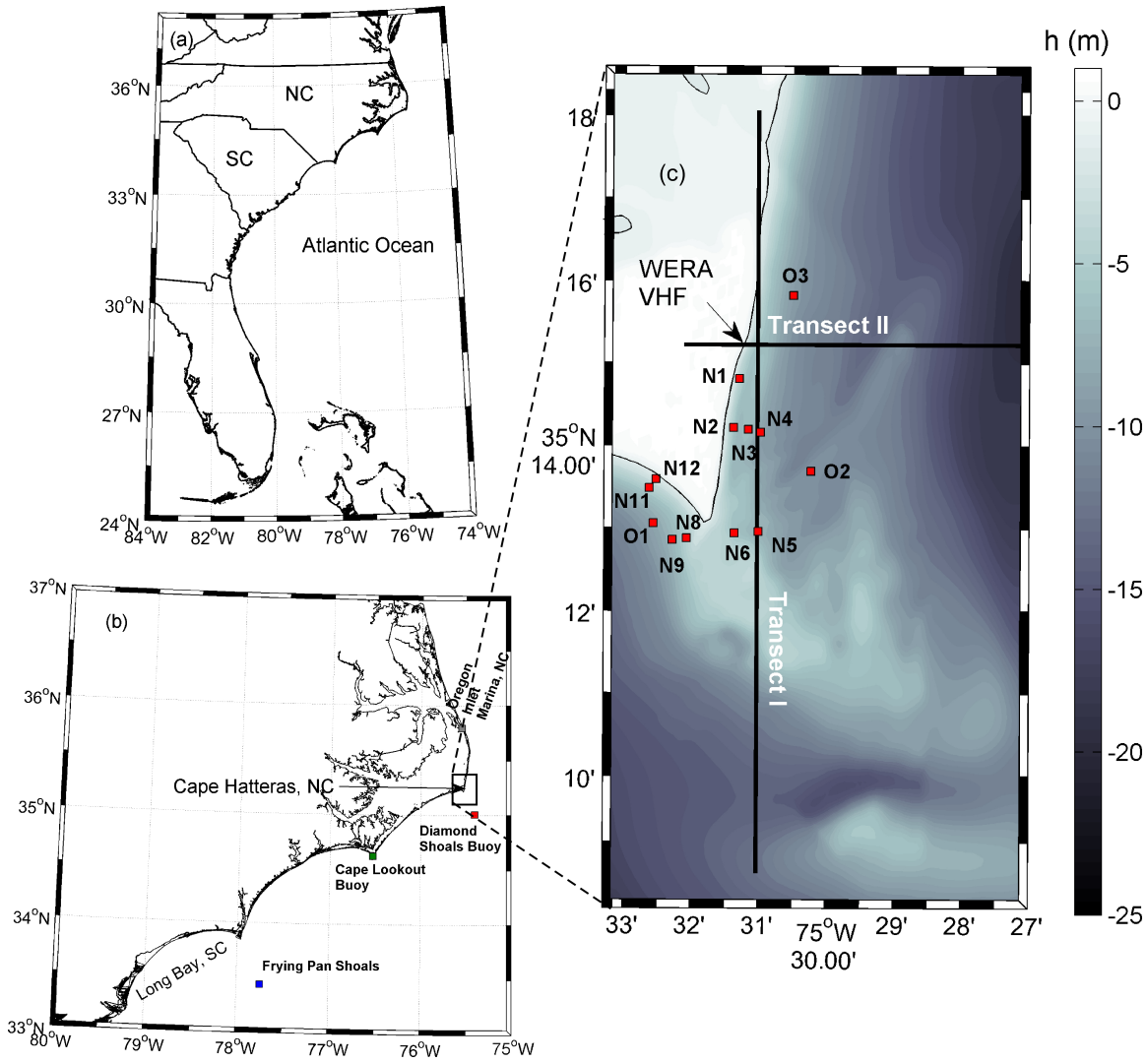

Figure 6.1: Map showing the study area (Cape Hatteras, NC, USA), the nearshore bathymetry and data collection sites (red squares). The prefixes "N" and "O" in the station names suggest nearshore (mean water depth less than 8 m) and offshore sites, respectively. Solid black lines in (c) show transects along which almost alongshelf (transect I) and cross-shelf (transect II) surface currents from the model and the VHF radar are compared (see Figure 6.12). The locations of NOAA Diamond Shoals buoy, Frying Pan Shoals, Cape Lookout Buoy and Oregon Inlet are shown in (b).

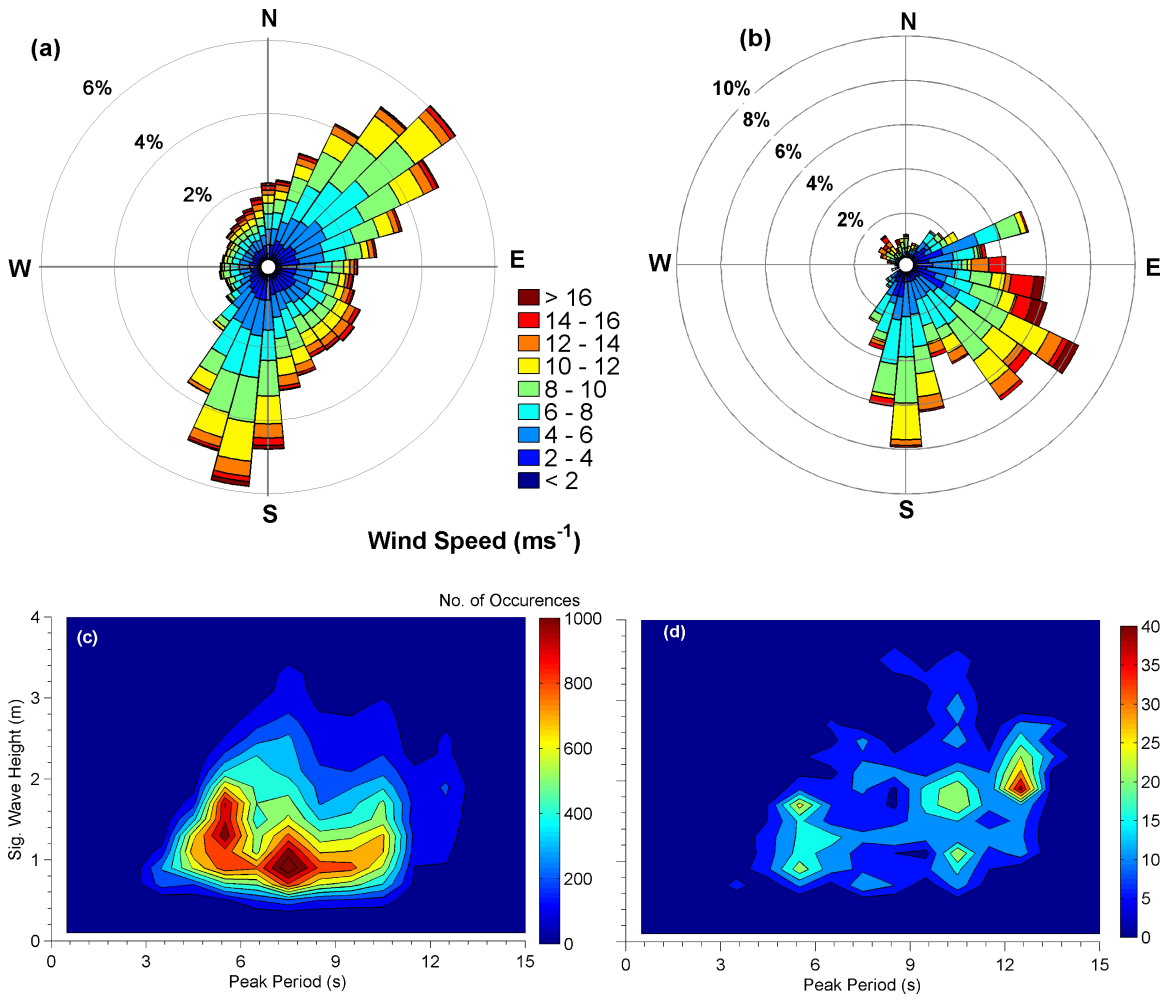

Figure 6.2: Wind rose diagram showing wind speed and direction (in oceanographic convention) using (a) 5 years (2006-2010) of meteorological data from Diamond Shoals NOAA-NDBC Buoy (Station ID-41025, Fig. 6.1b); (b) meteorological data from February 1 to March 20, 2010; (c) Joint probability distribution of peak period and significant wave height from 2005-2010. The color shading represents the number of observations; (d) same as in (c) but for Feb. 2010.

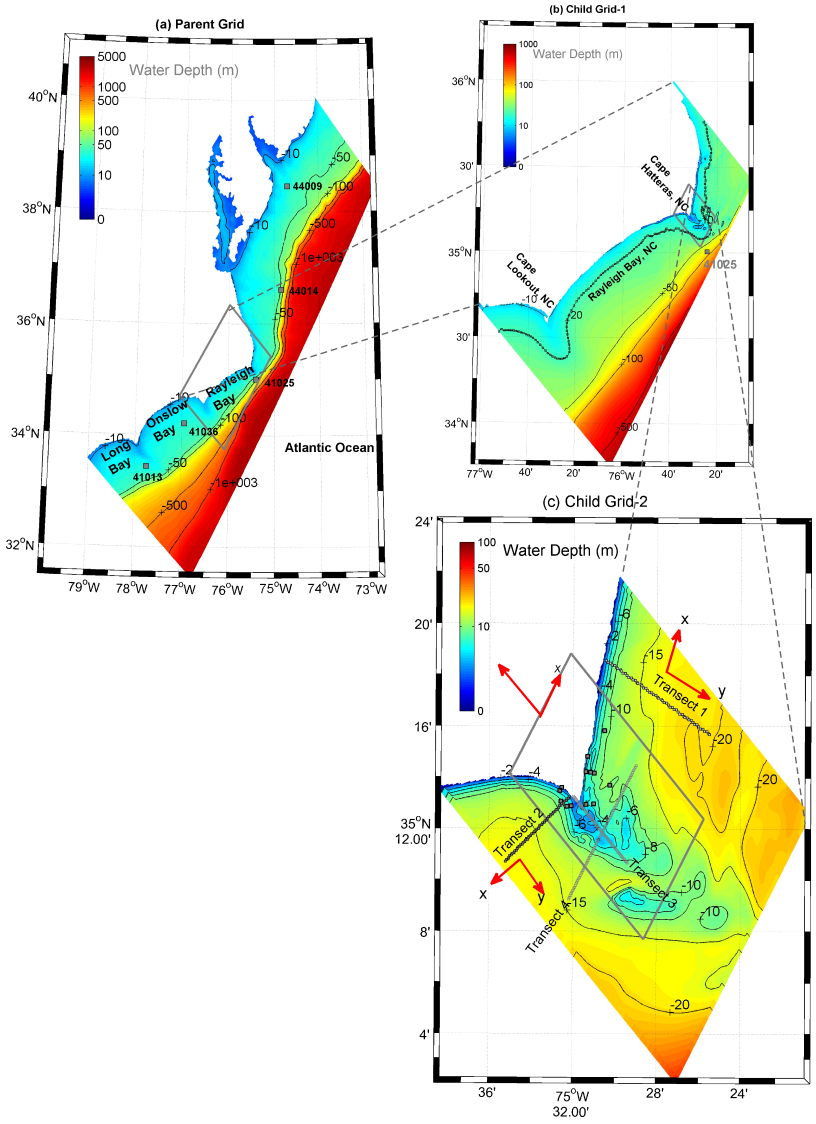

Figure 6.3: Numerical grid domains and bathymetry for the parent (a) and subsequent child grids (b and c) used for the circulation and the wave propagation models. Gray squares in (a) show the locations of NOAA-NDBC buoys. Solid black lines represent bathymetric contours in m. Transects along which flows and momentum balances are discussed in Figures 6.18 and 19 are shown as dotted black lines in (c). Along and cross-shoal transects for which vertical variability of flow is discussed in Figures 6.14-17 are shown as gray lines. Gray box in (c) shows the region for which along and cross-shoal momentum balances are discussed in Figures 6.20-26. Orthogonal coordinate systems for transects 1, 2 and 3 are shown using red arrows.

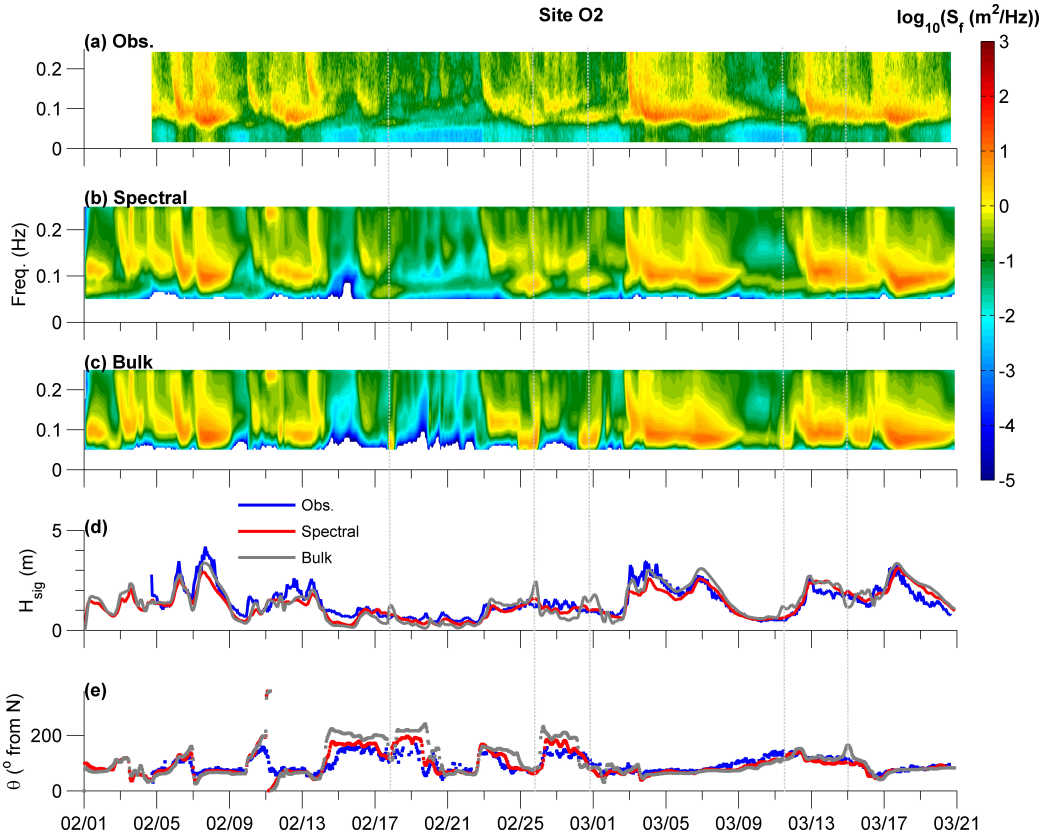

Figure 6.4: Color shading showing time stack of (a) observed frequency spectrum at Site O2; (b) simulated frequency spectrum using Spectral wave input at the open boundary; (c) simulated frequency spectrum using bulk wave input at the open boundary. Also the time series of (d) observed (solid blue) and simulated (red and gray) significant wave height (H_{sig}) and (e) observed (solid blue) and simulated (red and gray) mean wave direction are shown.

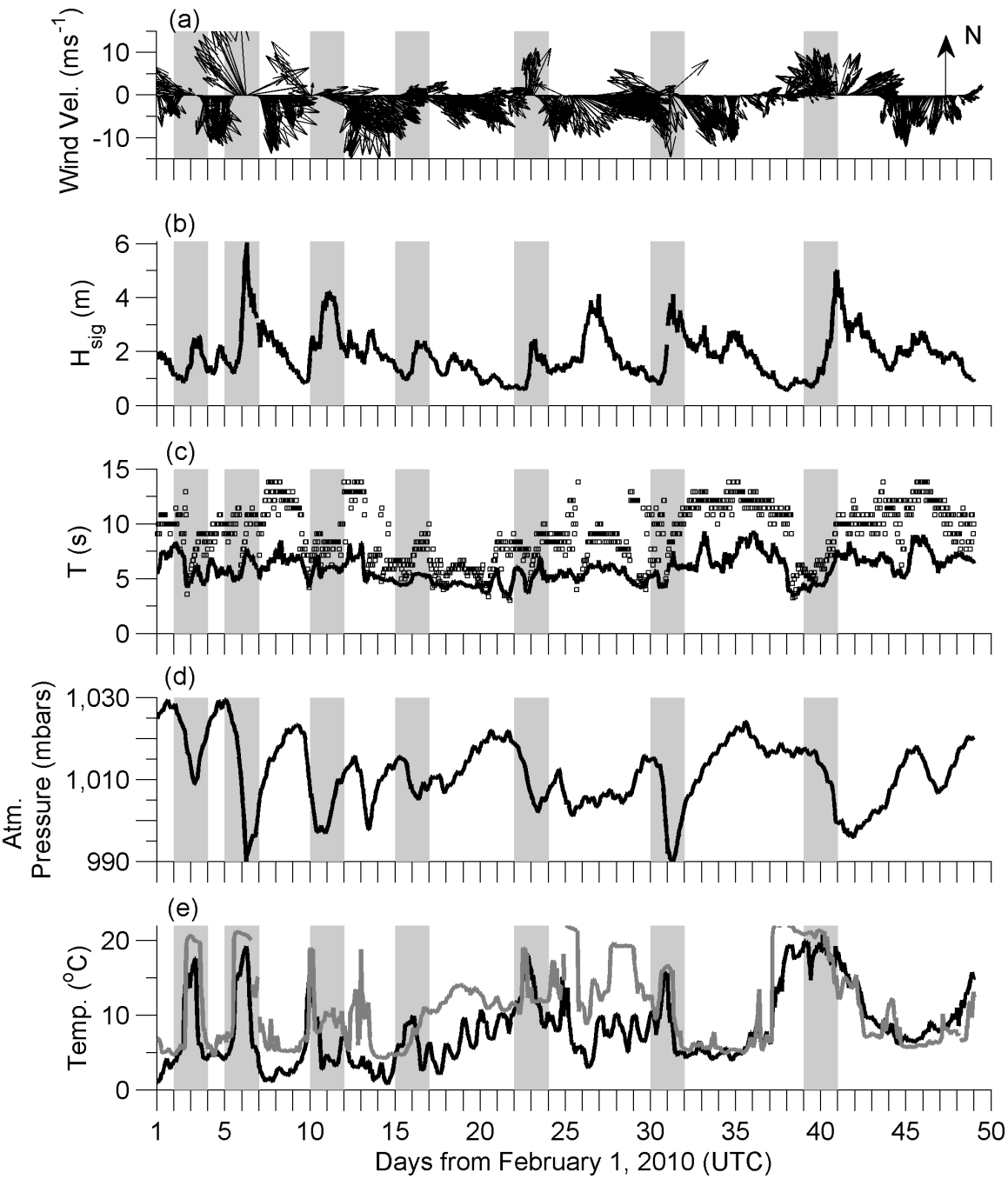

Figure 6.5: Meteorological and wave data from the Diamond Shoals buoy (NOAA/NDBC Station ID: 41025) for February and March, 2010. Time series of (a) wind velocity vector in oceanographic convention; (b) significant wave height; (c) peak (black squares) and mean (solid black line) wave period; (d) Atmospheric pressure (solid black line); and (e) air (black) and water (gray) temperature. Dark gray shaded areas correspond to passage of synoptic meteorological fronts.

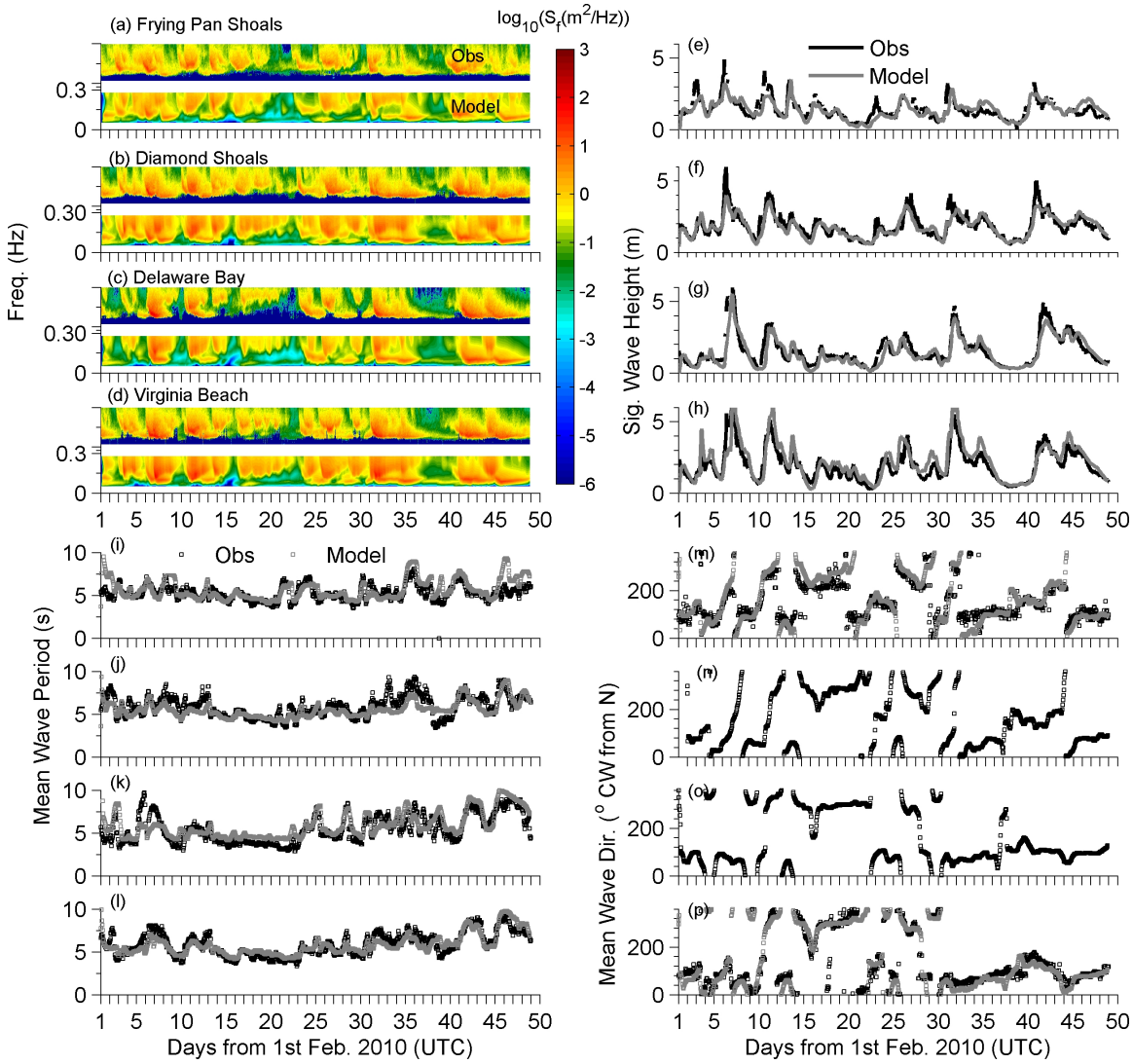

Figure 6.6: Comparison between simulated and measured frequency wave spectra (log10 (S_f), a, b, c and d), significant wave heights (H_{sig} in m, e, f, g and h), mean periods (T_m in s, i, j, k and l) and directions (θ_m in degrees from North, m, n, o and p) for the location (see Figure 6.3) of the NOAA-NDBC buoys at Frying Pan Shoals, Diamond Shoals, Delaware Bay and Virginia Beach. No wave direction is available for Diamond Shoals and Delaware Bay buoys during the model simulation period.

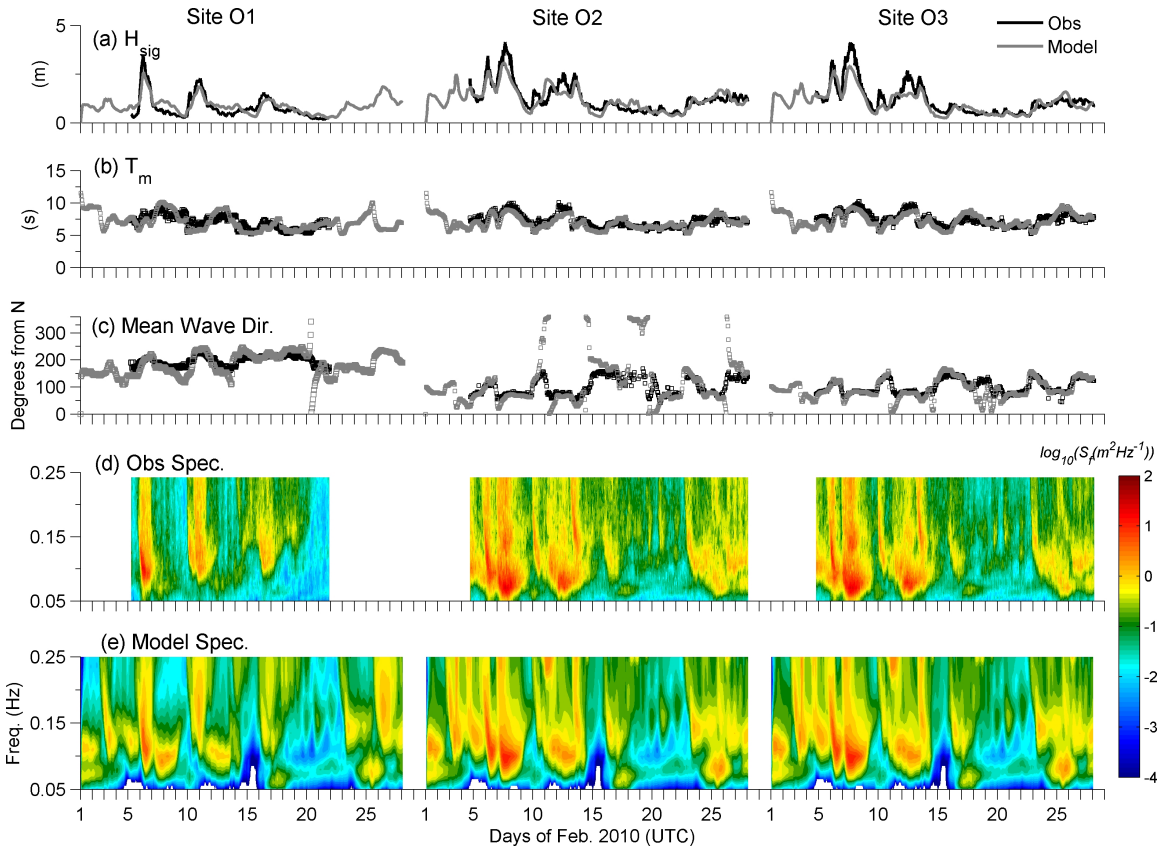

Figure 6.7: Time series of model simulated (solid gray) and measured (solid gray) (a) Significant wave height (H_{sig}, m); (b) Mean wave period (T_m, s); (c) Mean wave direction (θ_m, degrees from north) at sites O1, O2 and O3. Color shading representing time stack of observed and modeled frequency wave spectrum log10 (Sf) are shown in (d) and (e), respectively.

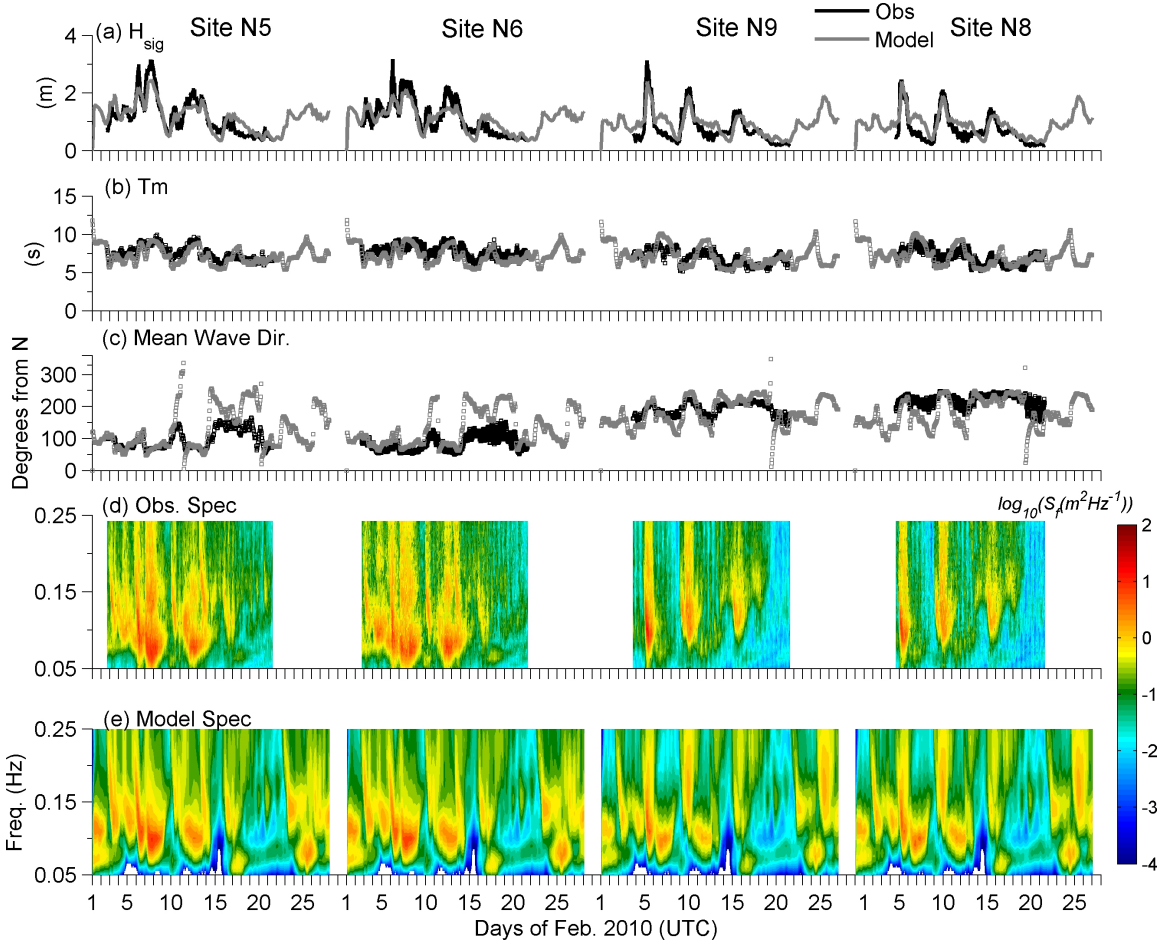

Figure 6.8: Time series of model simulated (solid gray) and measured (solid gray) (a) Significant wave height (H_{sig}, m); (b) Mean wave period (T_m, s); (c) Mean wave direction (θ_m, degrees from north) at sites N5, N6, N9 and N8. Color shading representing time stack of observed and modeled frequency wave spectrum log10 (Sf) are shown in (d) and (e), respectively.

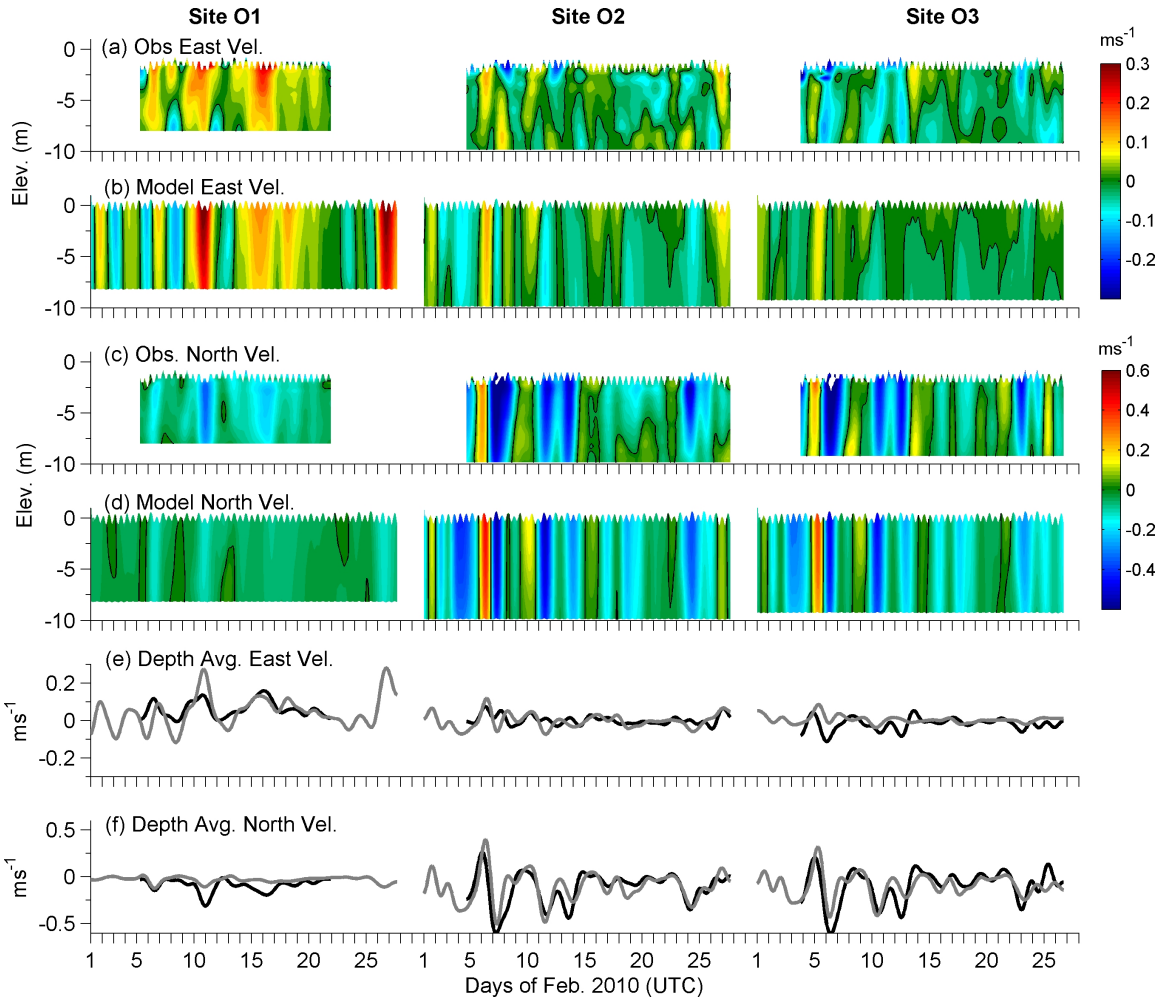

Figure 6.9: Time series of vertical variability and depth averaged subtidal flow components for sites O1, O2 and O3. Vertical variability of (a) observed and (b) simulated east flow component, (c) observed and (d) simulated north flow component. Time series of measured (solid black) and modeled (solid gray) depth-averaged, subtidal eastward and northward flows are shown in (e) and (f), respectively. All flows are in ms^{-1}.

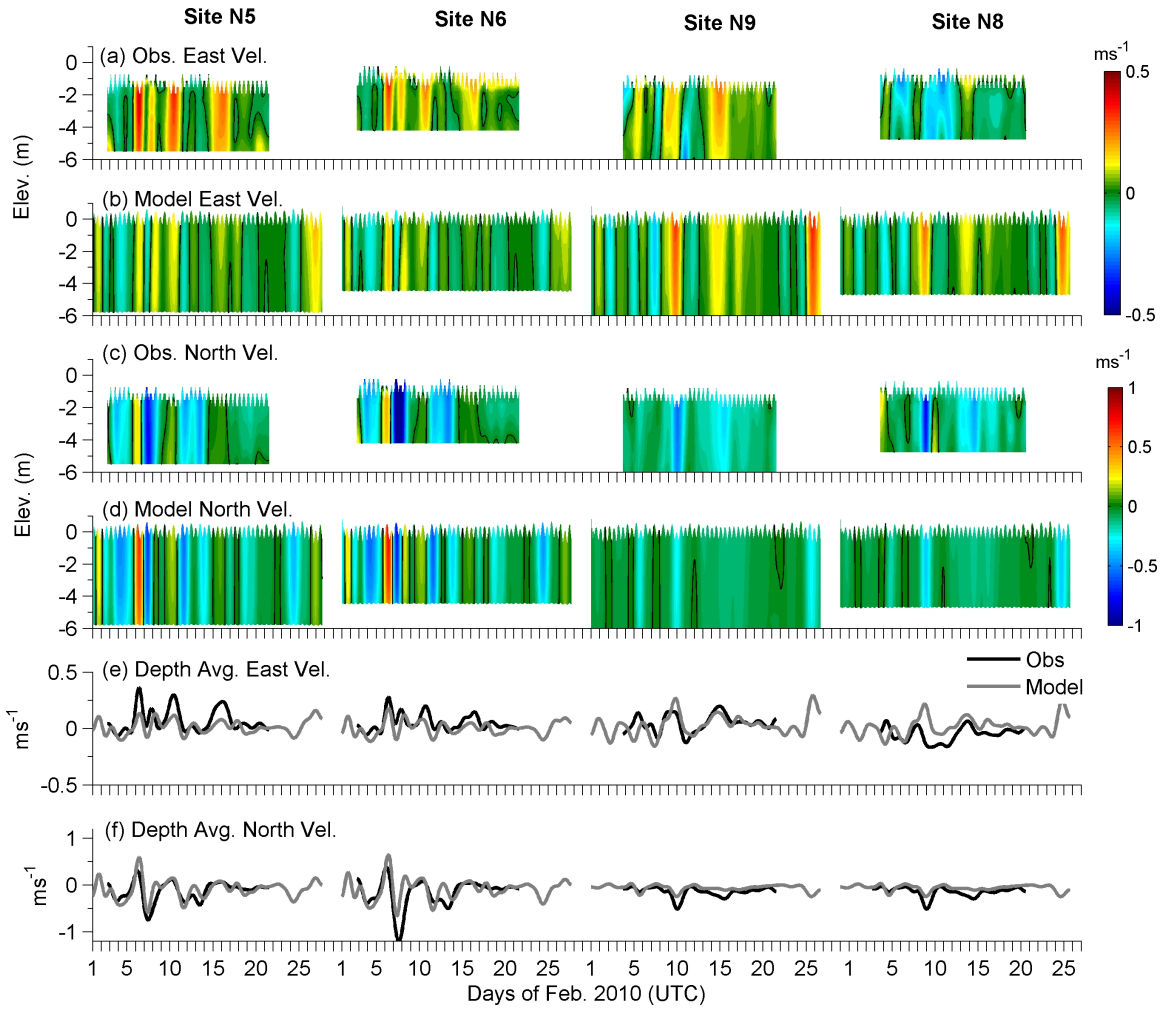

Figure 6.10: Time series of vertical variability and depth averaged subtidal flow components for sites N5, N6m N8 and N9. Vertical variability of (a) observed and (b) simulated east flow component, (c) observed and (d) simulated north flow component. Time series of measured (solid black) and modeled (solid gray) depth-averaged, subtidal eastward and northward flows are shown in (e) and (f), respectively. All flows are in ms^{-1}.

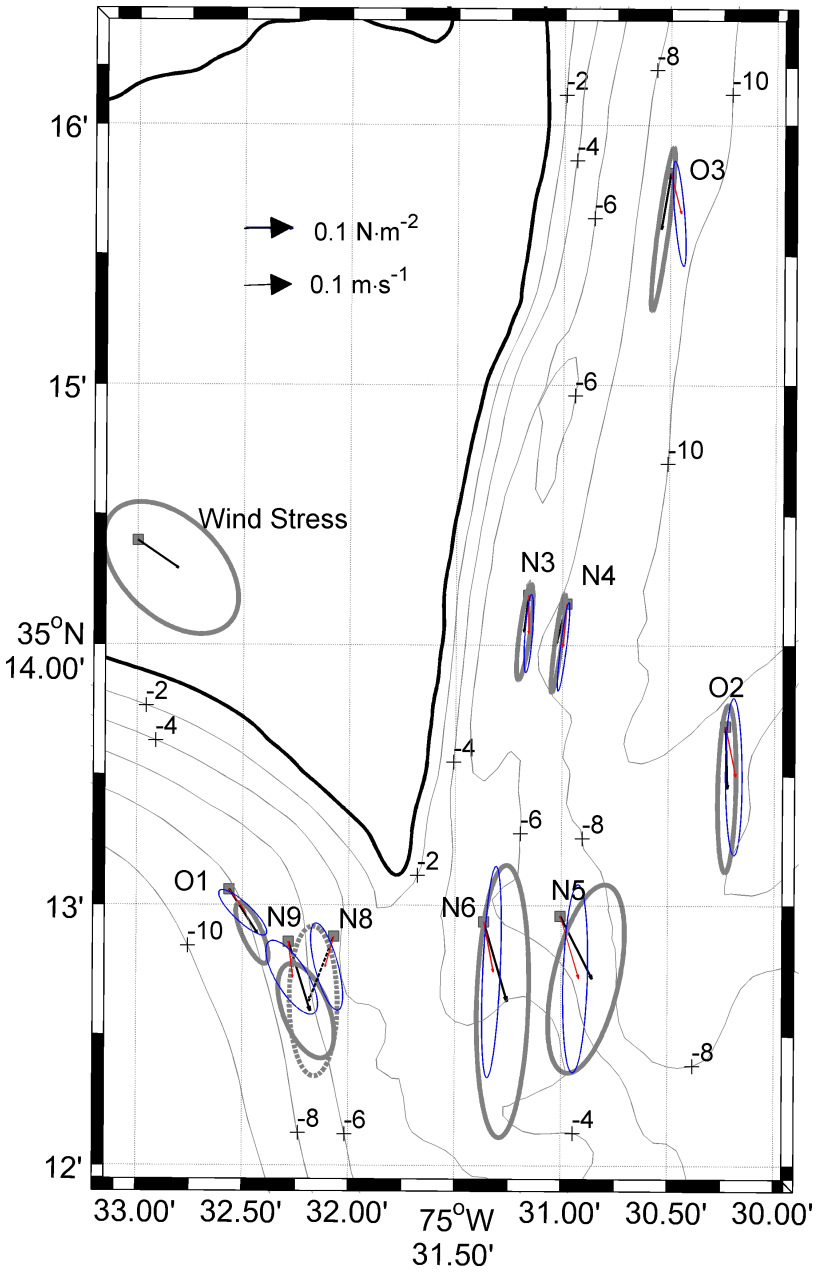

Figure 6.11: Comparison between measured and simulated depth-averaged subtidal flows described by their mean (black and red arrows, respectively) and vector variance ellipses (gray and blue, respectively) for the full period of data collection for each site.

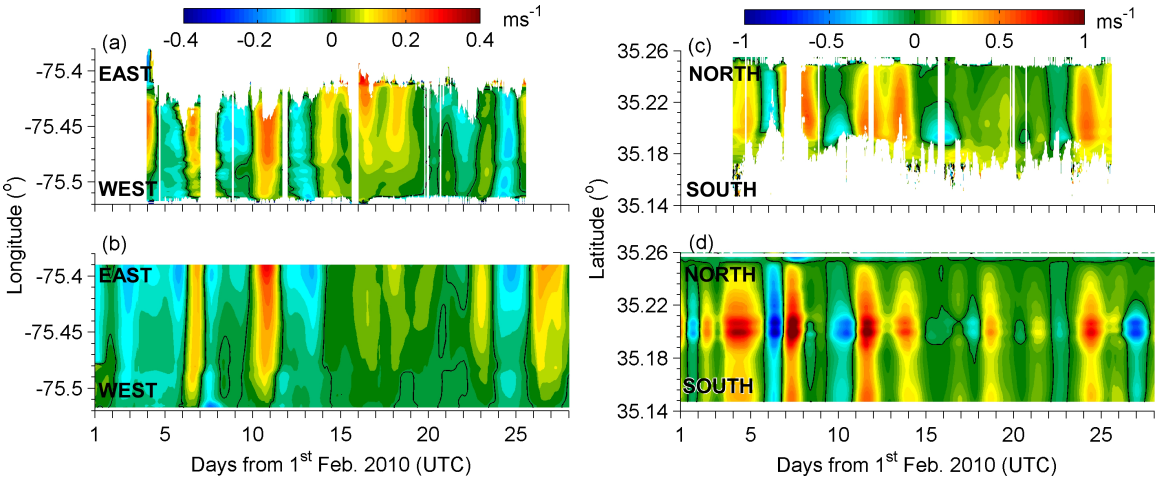

Figure 6.12: Color shading showing time stack of measured (a, c) and model simulated (b, d) subtidal, Lagrangian, radial surface currents at a cross-shore (a, b) and alongshore (c, d) transect. The location of these transects are shown in Figure 6.1c.

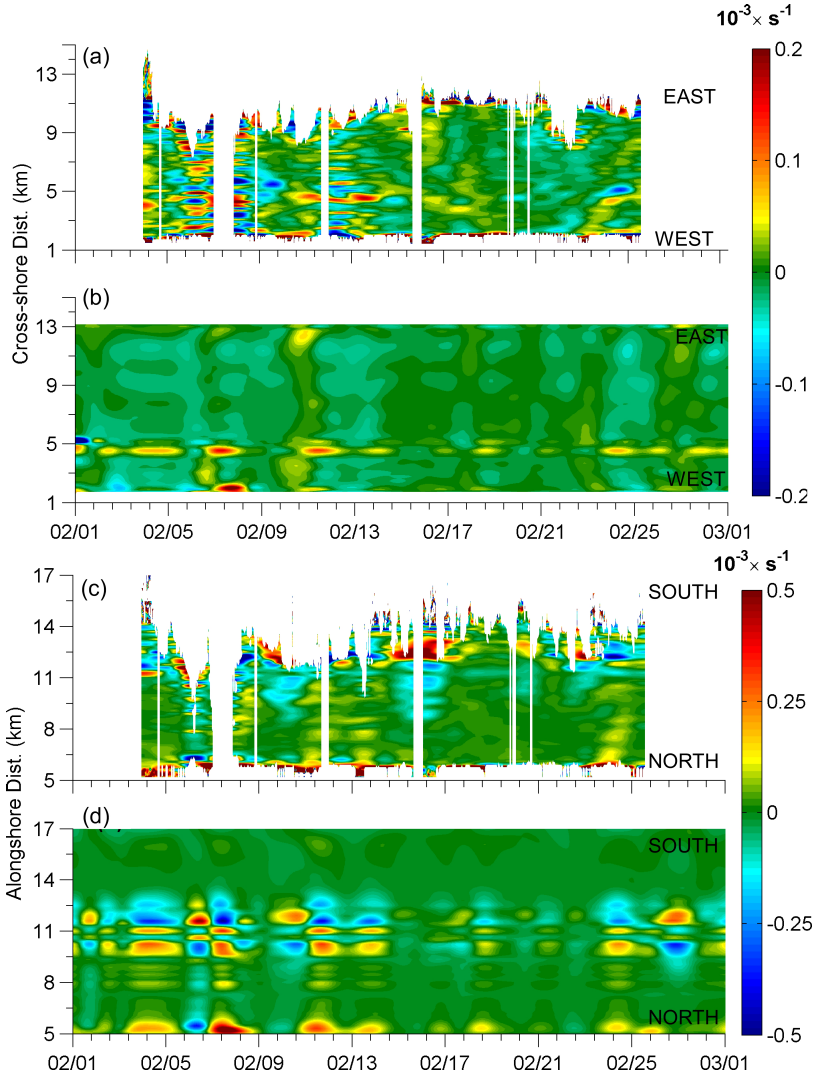

Figure 6.13: Color shading showing time stack of measured (a, c) and model simulated (b, d) gradient of cross-shore ($\partial u/\partial x$, a, b) and alongshore ($\partial v/\partial y$, c, d) subtidal, Lagrangian, radial surface current. The transect locations are same as in Figure 12.

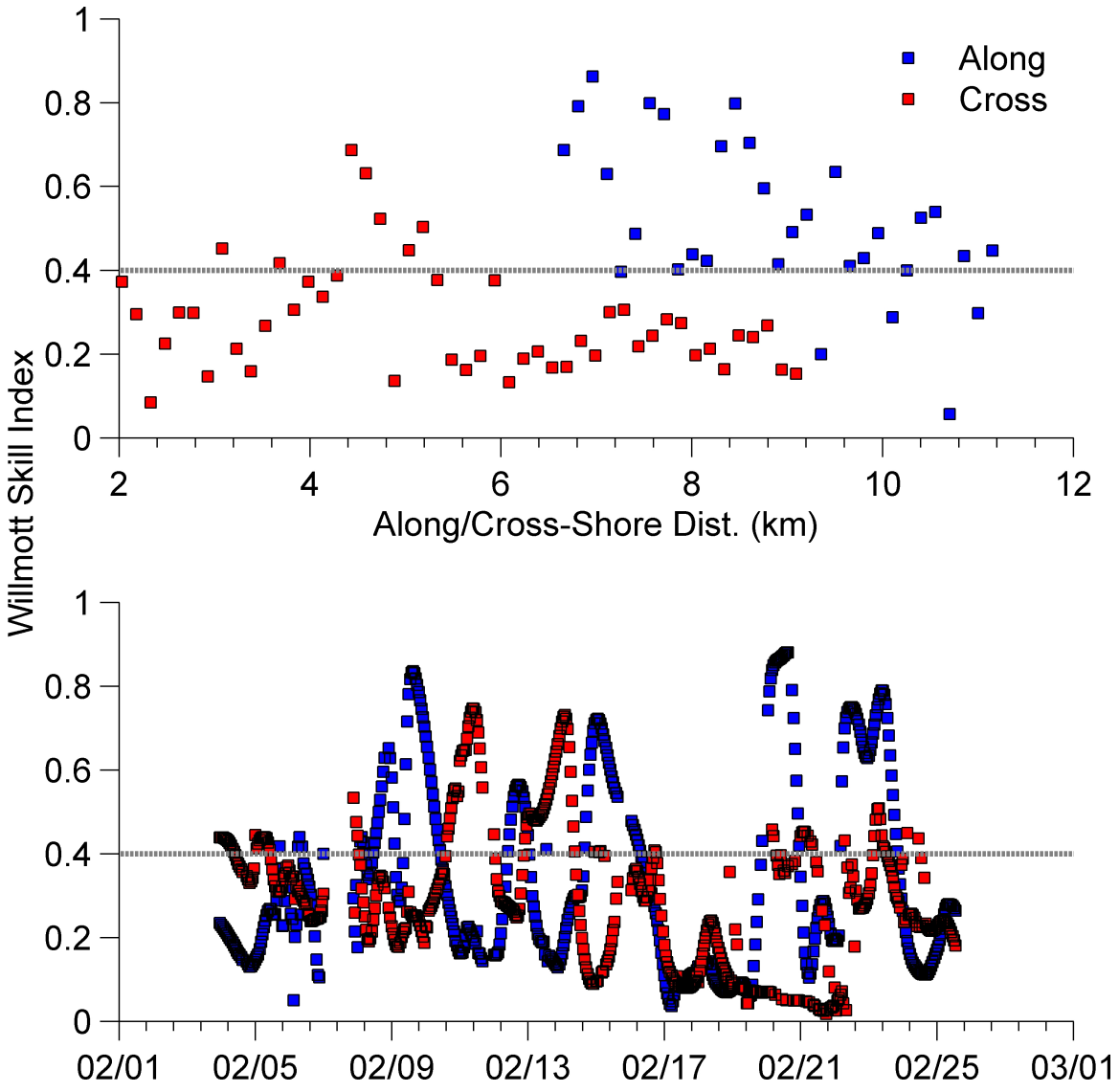

Figure 6.14: Model skill in simulating cross-shore gradient of cross-shore (red squares in a and b, $\partial u/\partial x$) and alongshore gradient of alongshore (blue squares in a and b, $\partial u/\partial x$) subtidal, radial velocities as a function of along/cross-shore distance (a) and time (b)

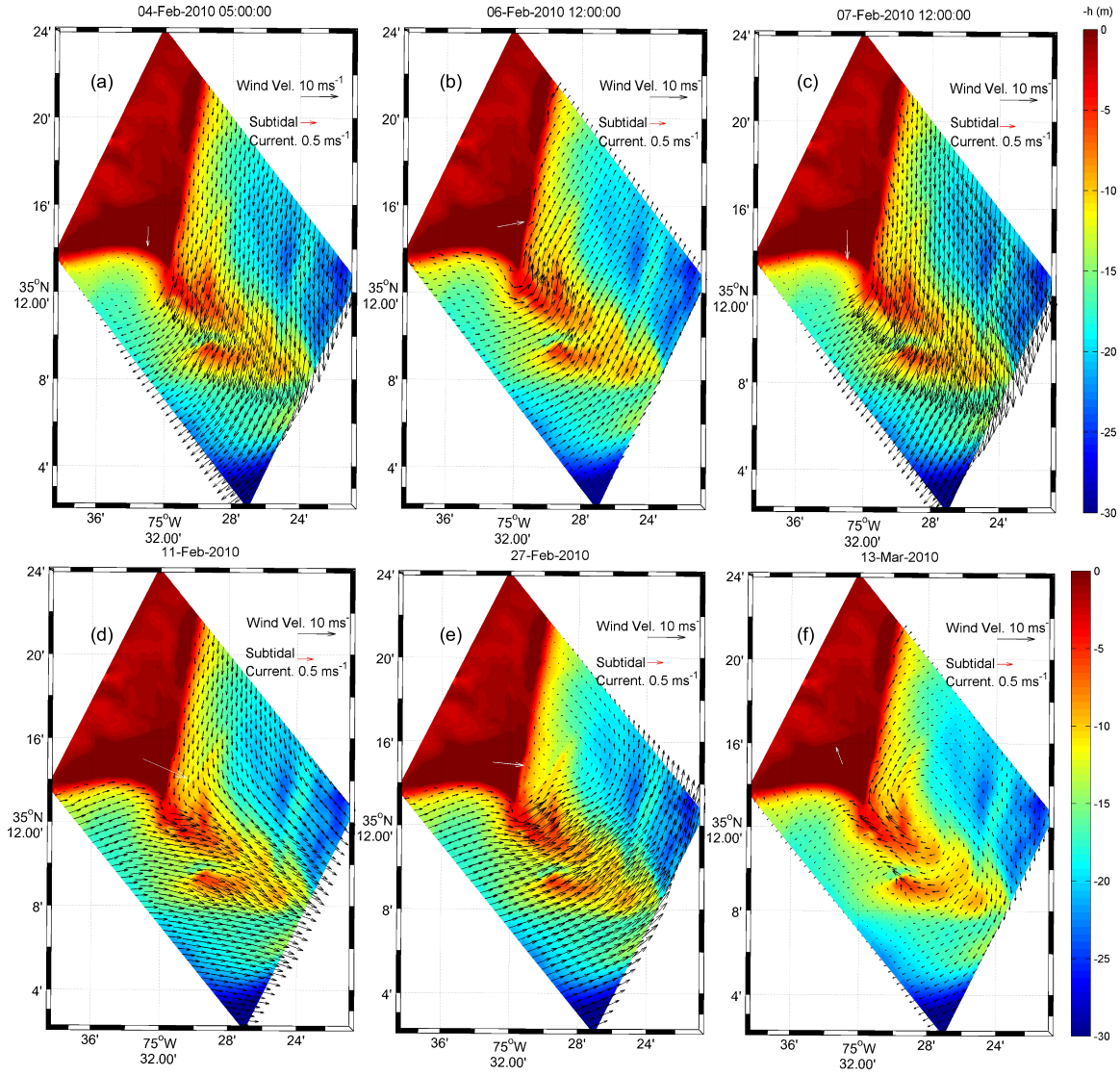

Figure 6.15: Spatial distribution of depth-averaged, subtidal flows (ms^{-1}, black arrows) over the smallest child grid (see Figure 4c) is shown on (a) Feb. 4; (b) Feb. 6; (c) Feb. 7; (d) Feb. 11; (e) Feb. 27 and (f) March 13, 2010. The color shading represents the bathymetry. Magnitude and direction of the flow vector are represented through the length and direction of the arrow, respectively. White arrows represent the magnitude and the direction of wind velocity vector.

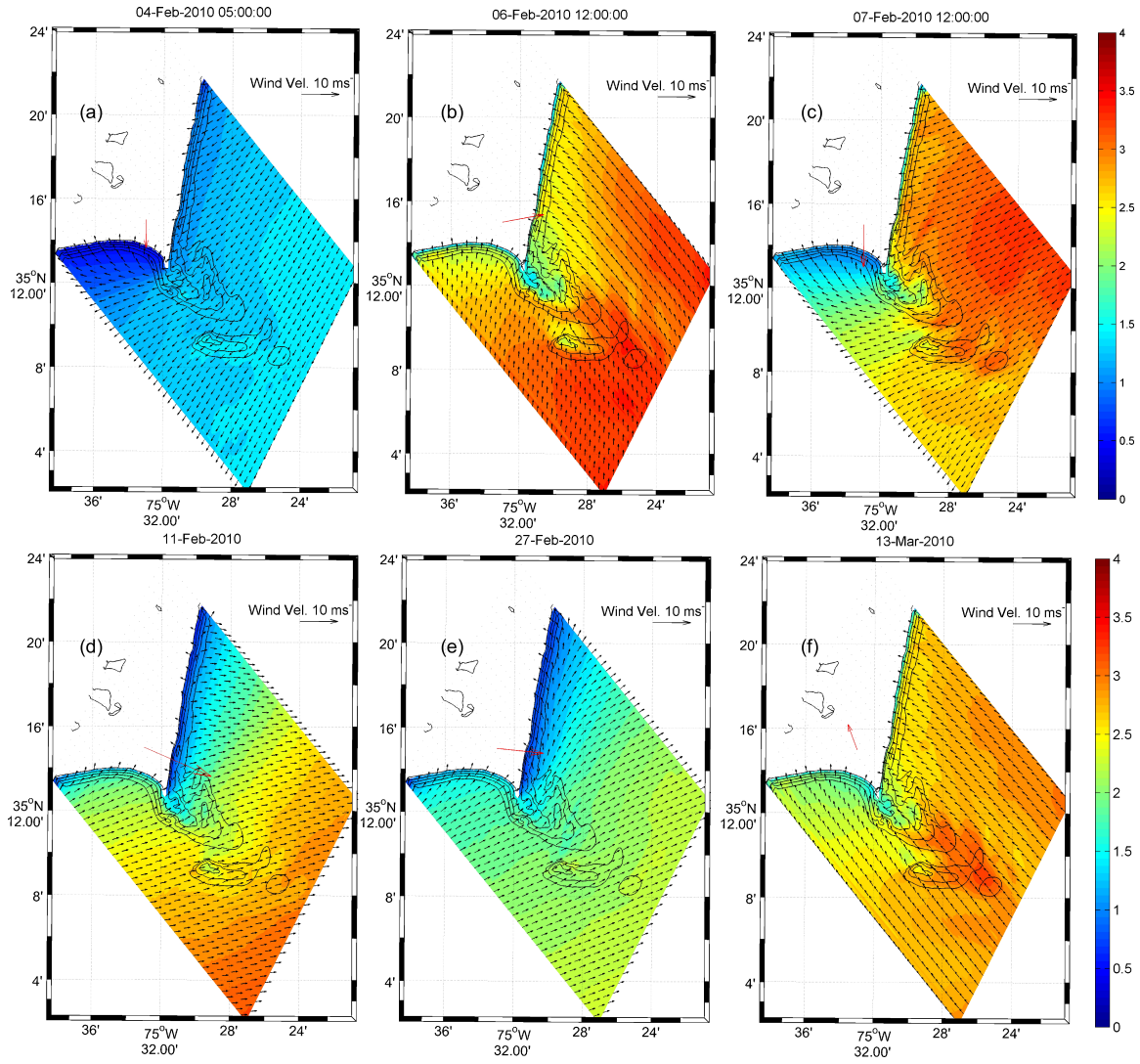

Figure 6.16: Color shading of significant wave height and mean wave direction (black arrows) over the smallest child grid (see Figure 6.3c) is shown on (a) Feb. 4; (b) Feb. 6; (c) Feb. 7; (d) Feb. 11; (e) Feb. 27 and (f) March 13, 2010. The arrows designate a direction, and their length do not have a physical meaning.

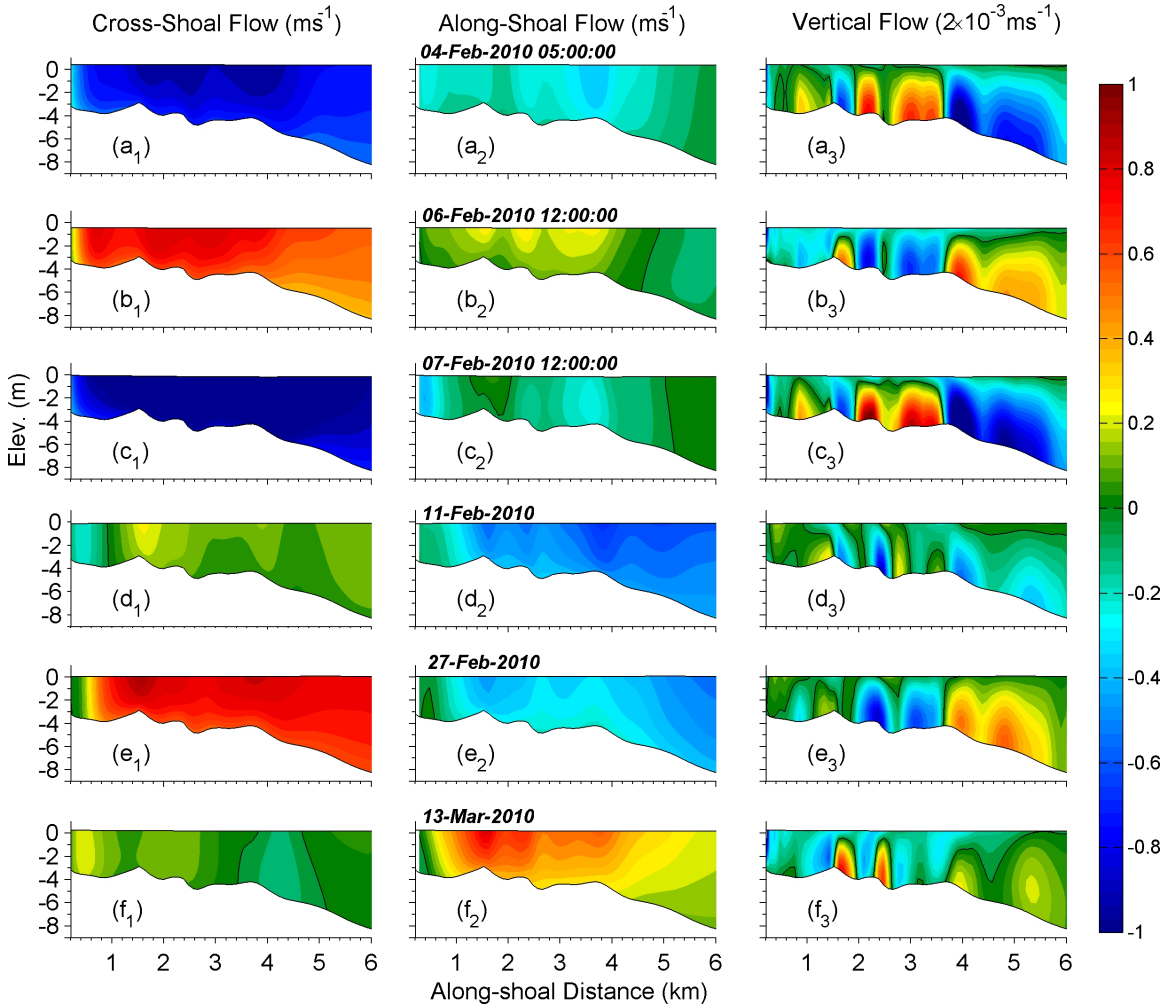

Figure 6.17: Color shading showing along-shoal variation of vertical profile of cross-shoal (ms^{-1}, a1-f1), along-shoal (a2-f2) and vertical (a3-f3) Eulerian mean flows on (a1-a3) Feb. 4; (b1-b3) Feb. 6; (c1-c2) Feb. 7; (d1-d3) Feb. 11; (e1-e3) Feb. 27 and (f1-f3) March 13, 2010. The location of the along-shoal transect is shown in Fig. 6.4c (see Transect 3). Positive cross-shoal flows are directed towards the northeast, while positive along-shoal flows are northwestward. Solid black line is the zero contour line.

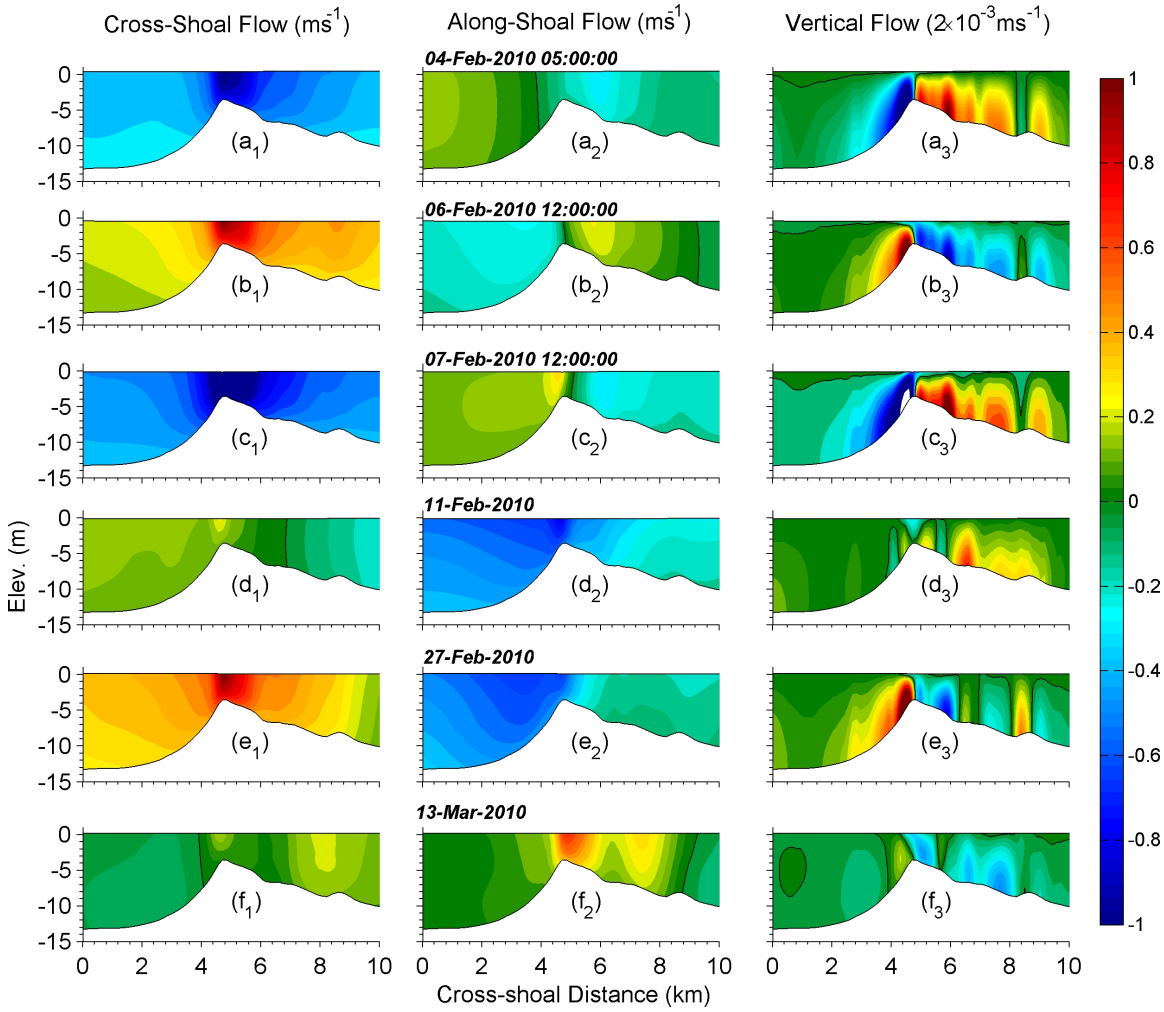

Figure 6.18: Color shading showing cross-shoal variation of vertical profile of cross-shoal (ms^{-1}, a1-f1), along-shoal (a2-f2) and vertical (a3-f3) Eulerian mean flows on (a1-a3) Feb. 4; (b1-b3) Feb. 6; (c1-c2) Feb. 7; (d1-d3) Feb. 11; (e1-e3) Feb. 27 and (f1-f3) March 13, 2010. The location of the cross-shoal transect is shown in Fig. 6.4c (see Transect 4). Positive cross-shoal flows are directed towards the northeast, while positive along-shoal flows are northwestward. Solid black line is the zero contour line.

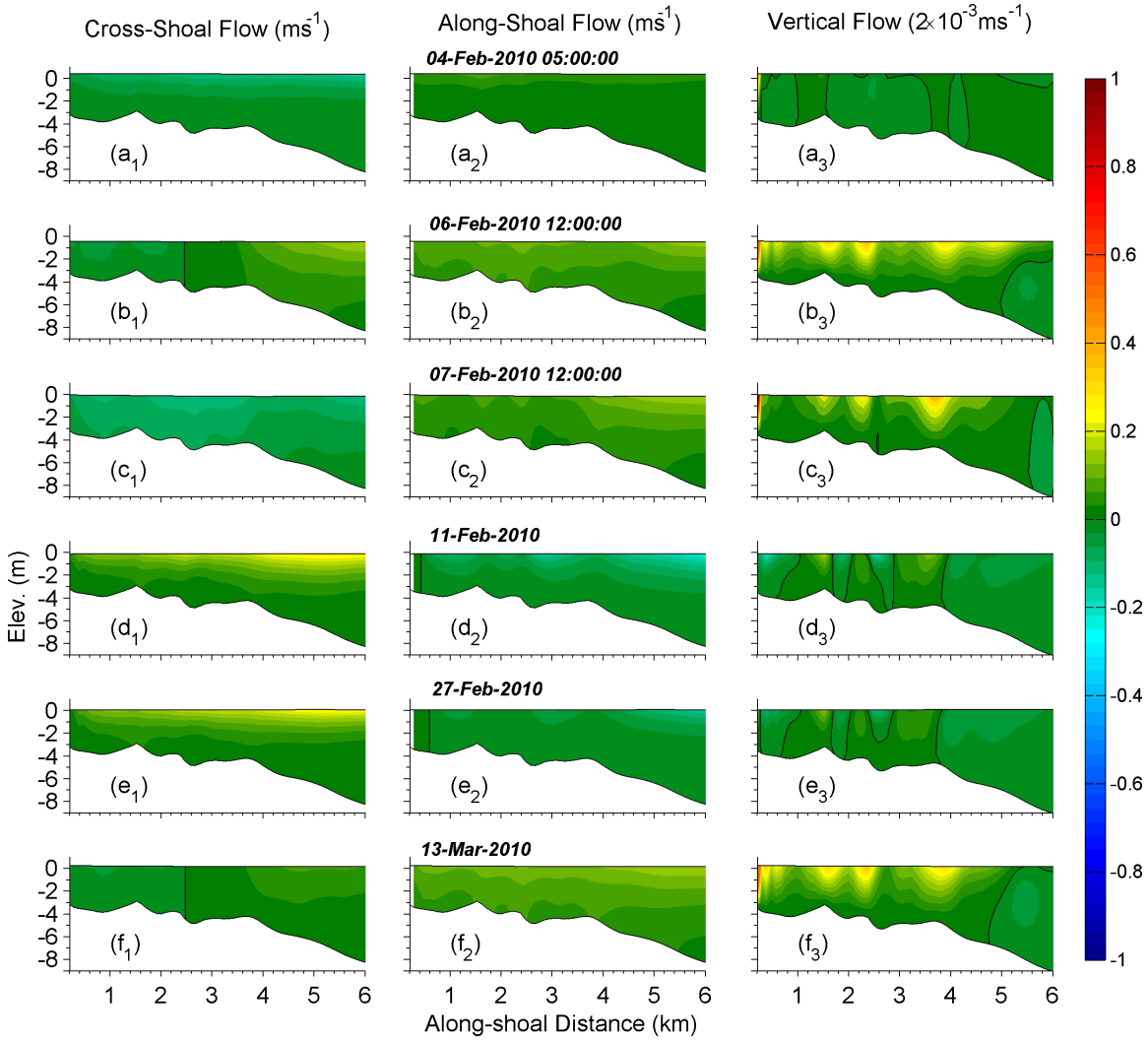

Figure 6.19: Color shading showing along-shoal variation of vertical profile of cross-shoal (ms^{-1}, a1-f1), along-shoal (a2-f2) and vertical (a3-f3) Stokes drift on (a1-a3) Feb. 4; (b1-b3) Feb. 6; (c1-c2) Feb. 7; (d1-d3) Feb. 11; (e1-e3) Feb. 27 and (f1-f3) March 13, 2010. The location of the along-shoal transect is shown in Fig. 6.4c (see Transect 3). Positive cross-shoal flows are directed towards the northeast, while positive along-shoal flows are northwestward. Solid black line is the zero contour line.

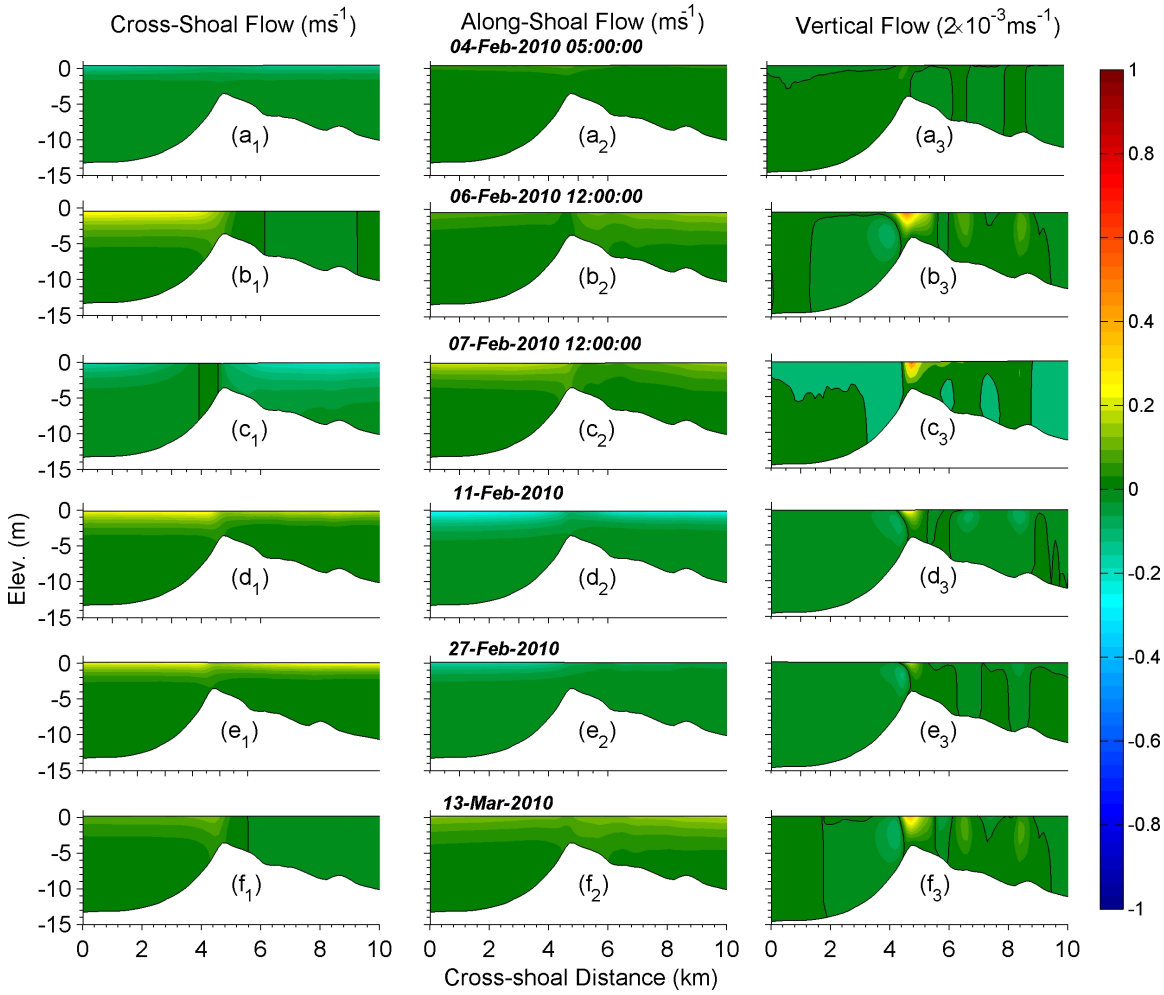

Figure 6.20: Color shading showing cross-shoal variation of vertical profile of cross-shoal (ms^{-1}, a1-f1), along-shoal (a2-f2) and vertical (a3-f3) Stokes drift on (a1-a3) Feb. 4; (b1-b3) Feb. 6; (c1-c2) Feb. 7; (d1-d3) Feb. 11; (e1-e3) Feb. 27 and (f1-f3) March 13, 2010. The location of the cross-shoal transect is shown in Fig. 6.4c (see Transect 4). Positive cross-shoal flows are directed towards the northeast, while positive along-shoal flows are northwestward. Solid black line is the zero contour line.

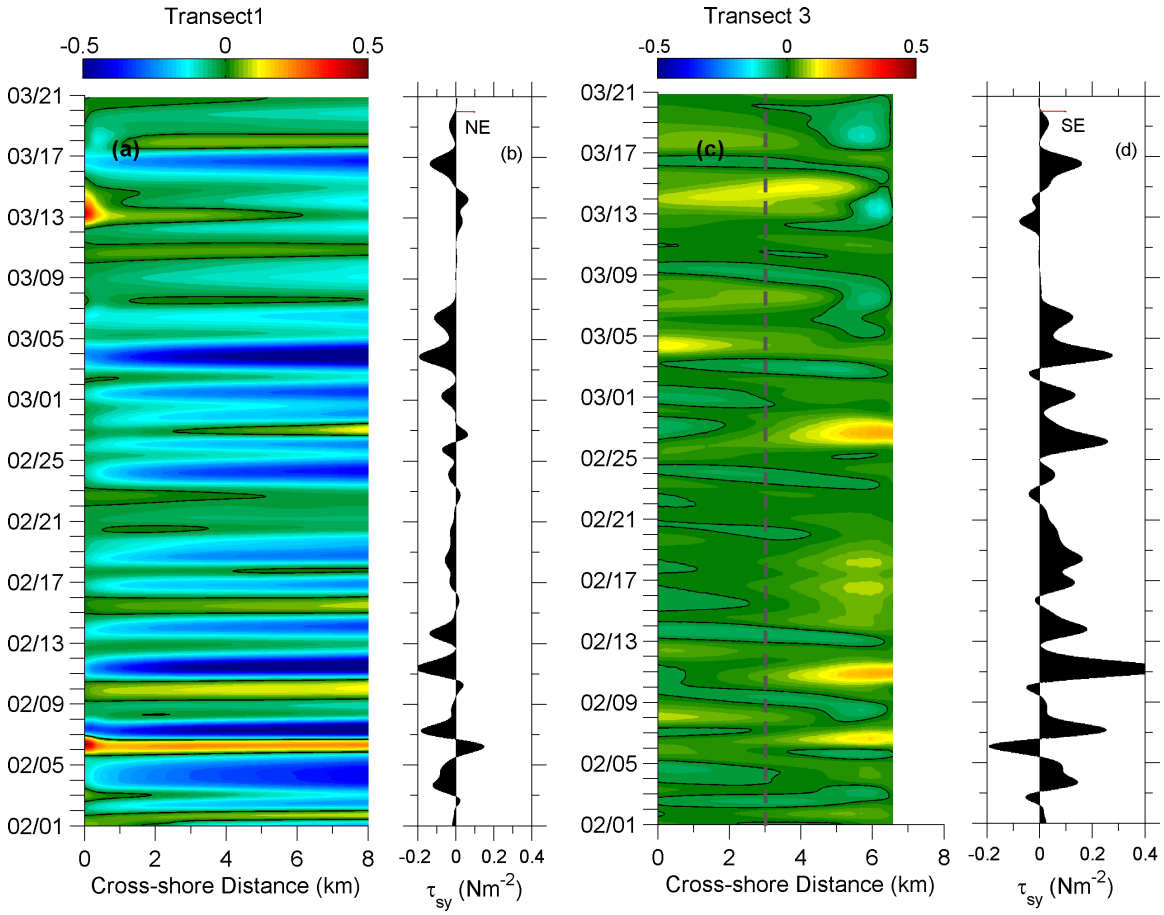

Figure 6.21: Color shading showing time stack of model simulated, subtidal, depth-averaged local alongshore velocities (in ms^{-1}, a, c) and wind stresses (in ms^{-2}, b, d) for two local cross-shore oriented transects on the east (Transect 1) and the south side (Transect 2) of Cape Hatteras point. The location and extent of these transects are shown in Figure 6.3c.

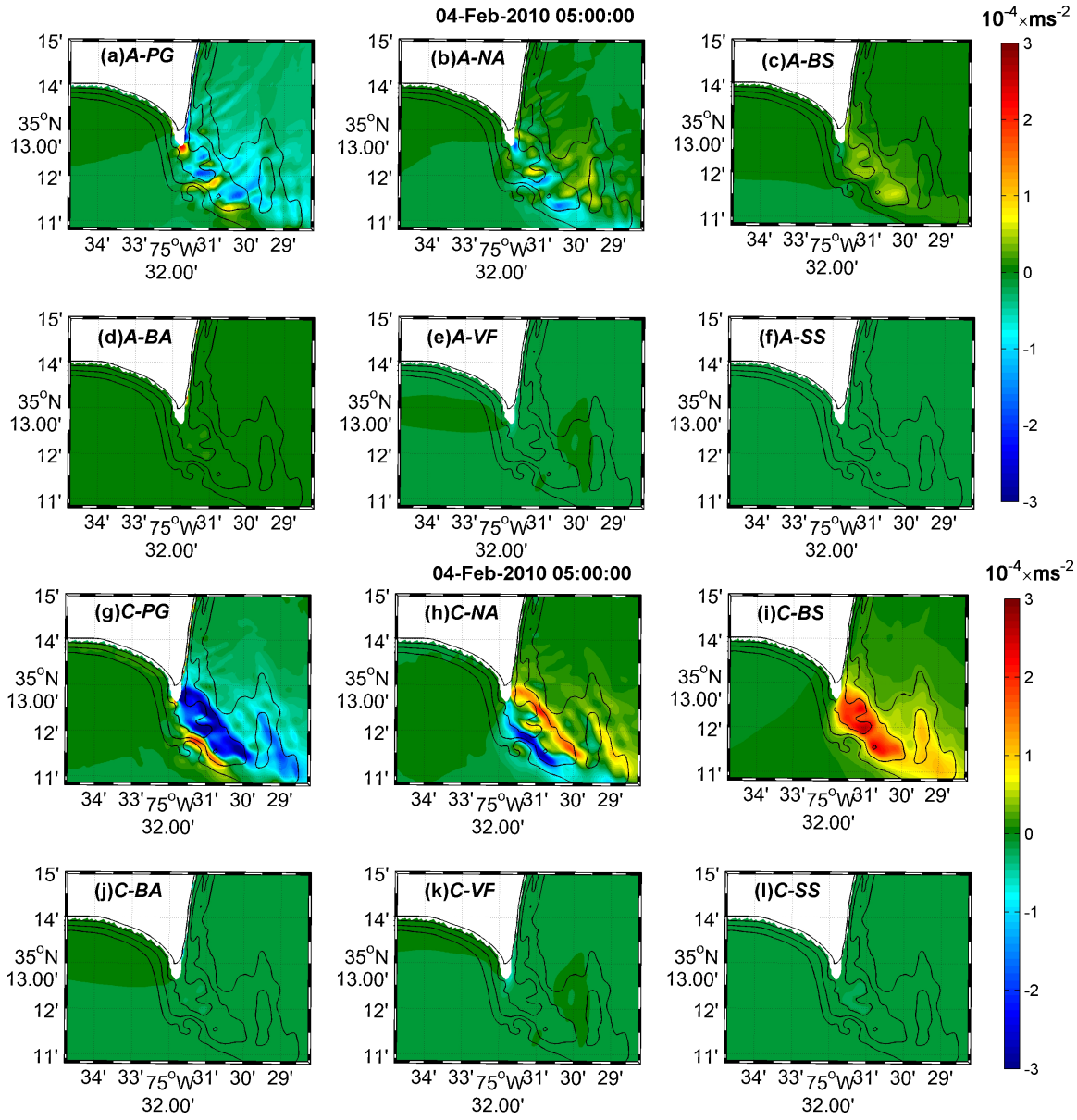

Figure 6.22: Color shading showing spatial distribution of along (a-f) and cross-shoal (g-l) momentum balance terms at locations within and adjacent to the shoal complex (see Figure 6.3c for the spatial extent of region shown area) for February 4, 2010. Key: PG (a, g)-Pressure gradient; NA (b, h)- Nonlinear advective acceleration; BS (c, i)- Bottom stress; BA (d, j)- Breaking acceleration; VF (e, k)- Vortex Force; and SS (f, l)- Surface stress. Prefix A and C represent along and cross. All units are in 10^{-4} ms^{-2}.

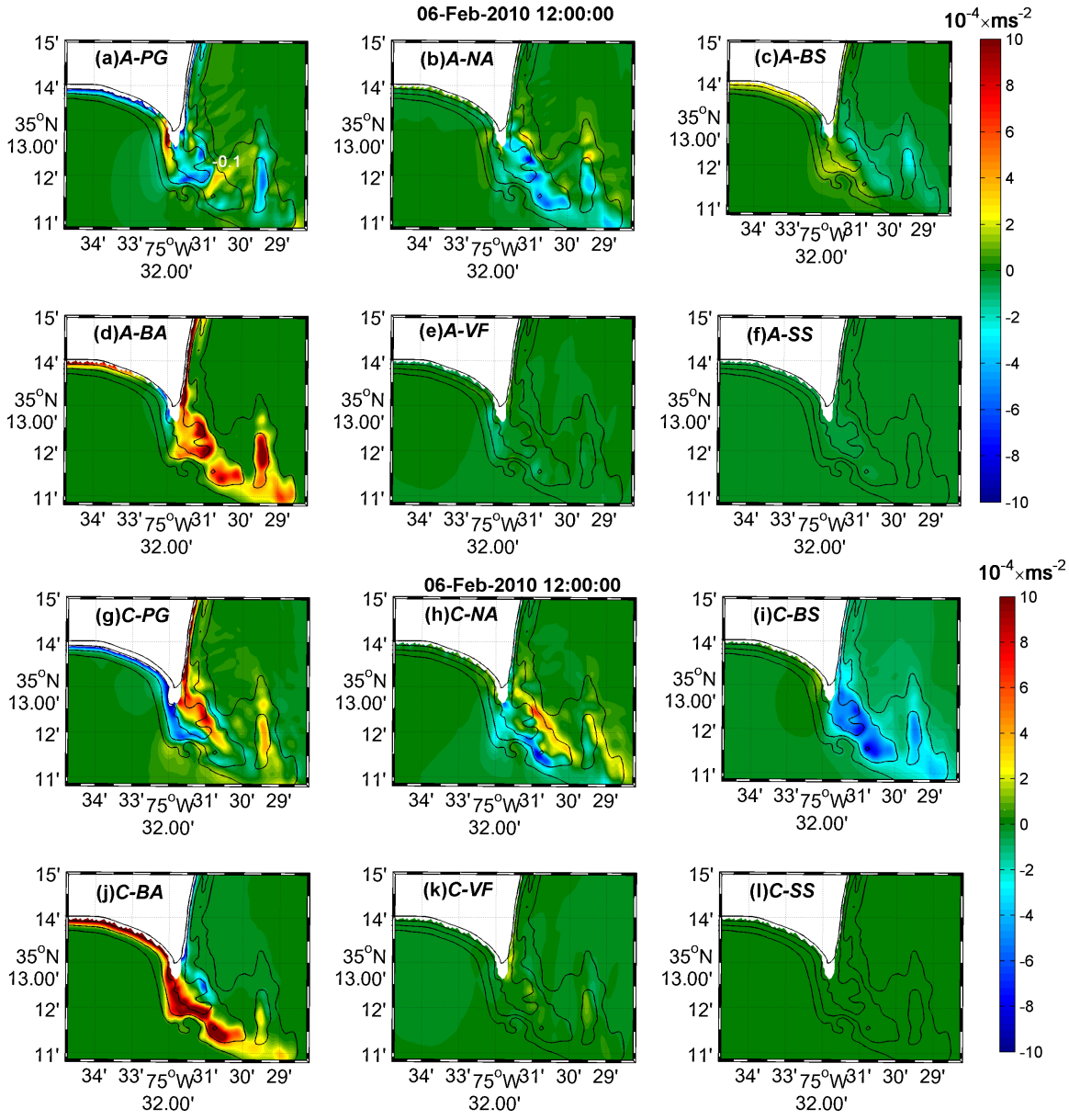

Figure 6.23: Same as in Figure 6.22 but for February 6, 2010.

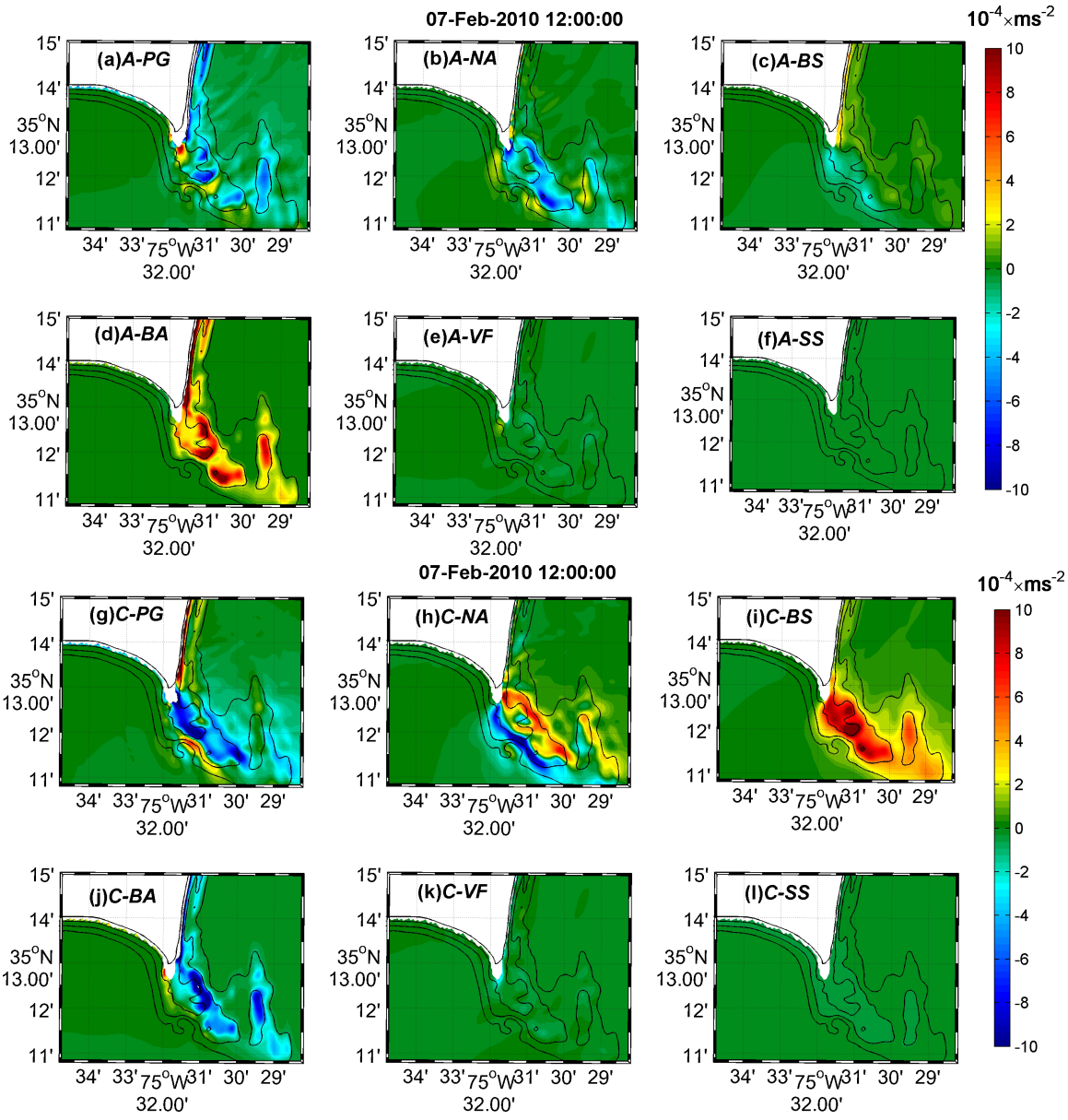

Figure 6.24: Same as in Figure 6.22 but for February 7, 2010.

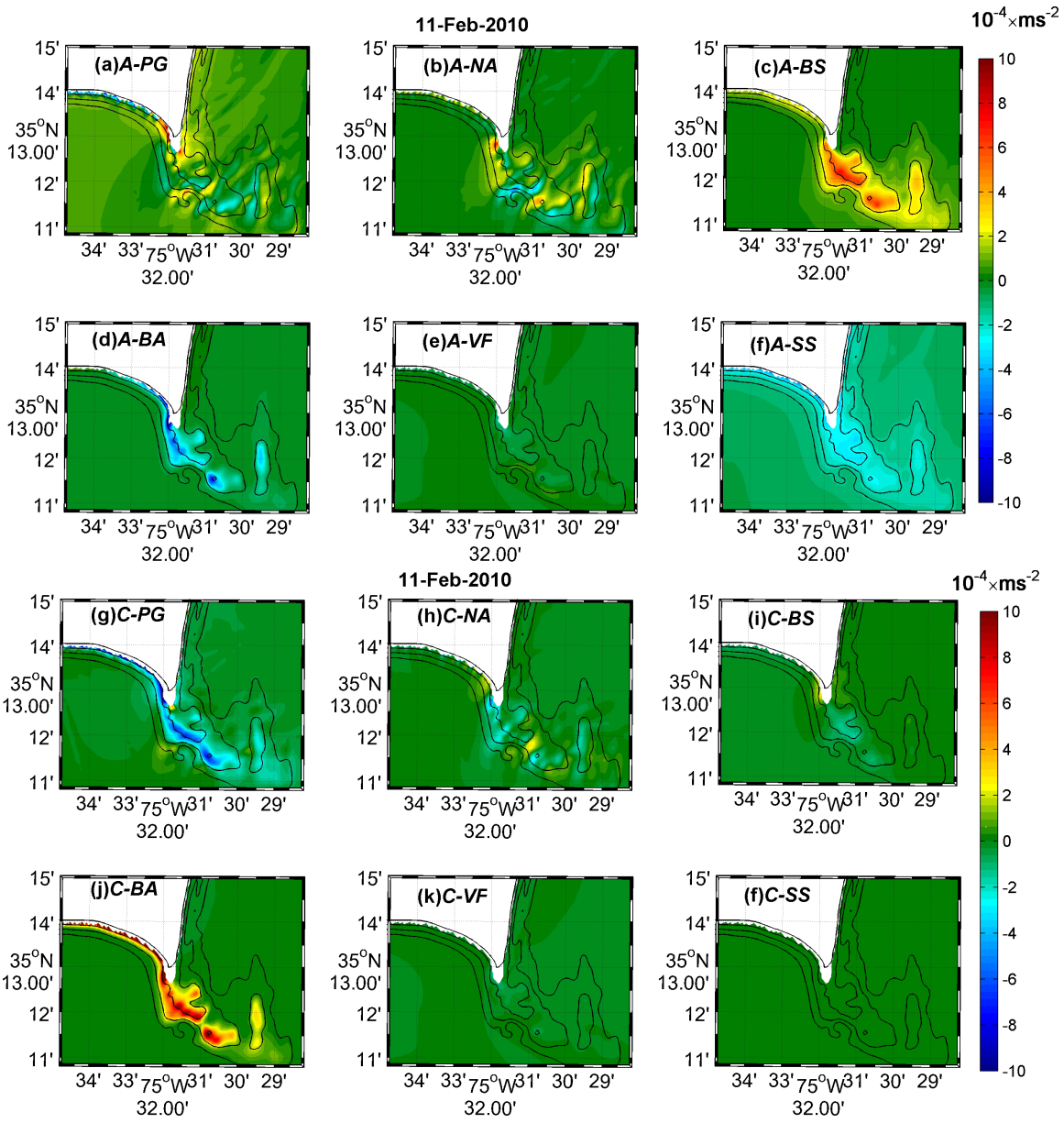

Figure 6.25: Same as in Figure 6.22 but for February 11, 2010.

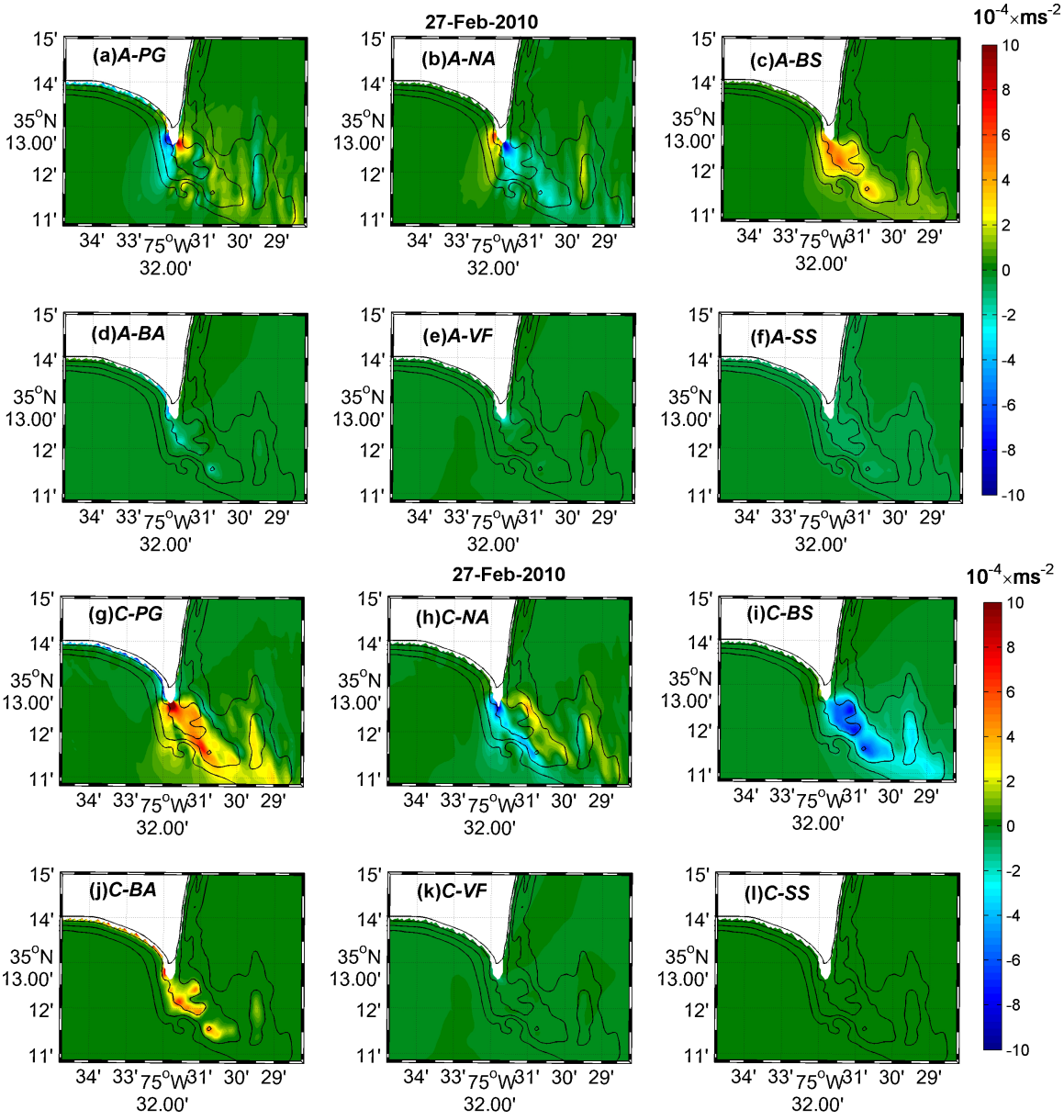

Figure 6.26: Same as in Figure 6.22 but for February 27, 2010.

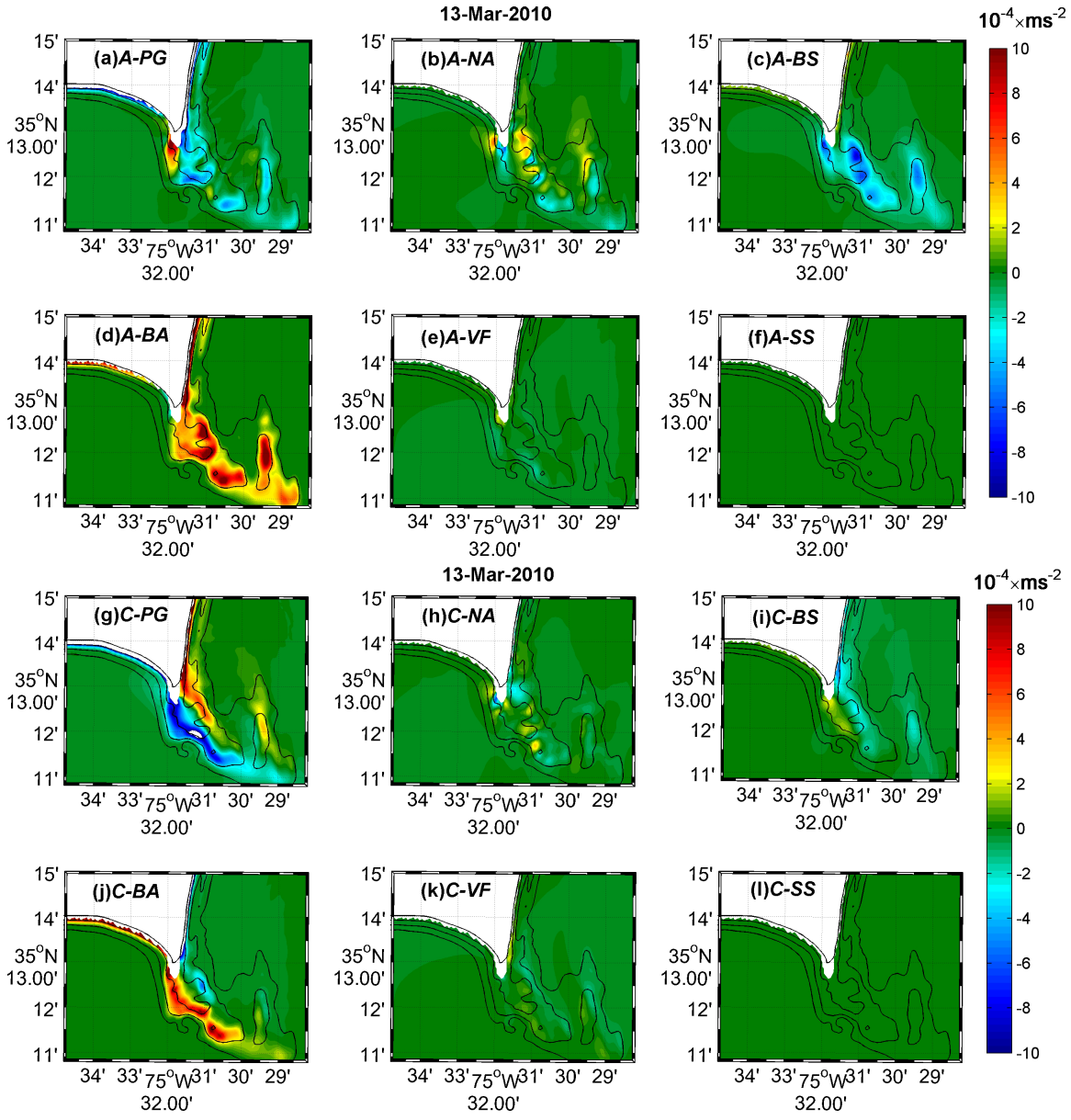

Figure 6.27: Same as in Figure 6.22 but for March 13, 2010.

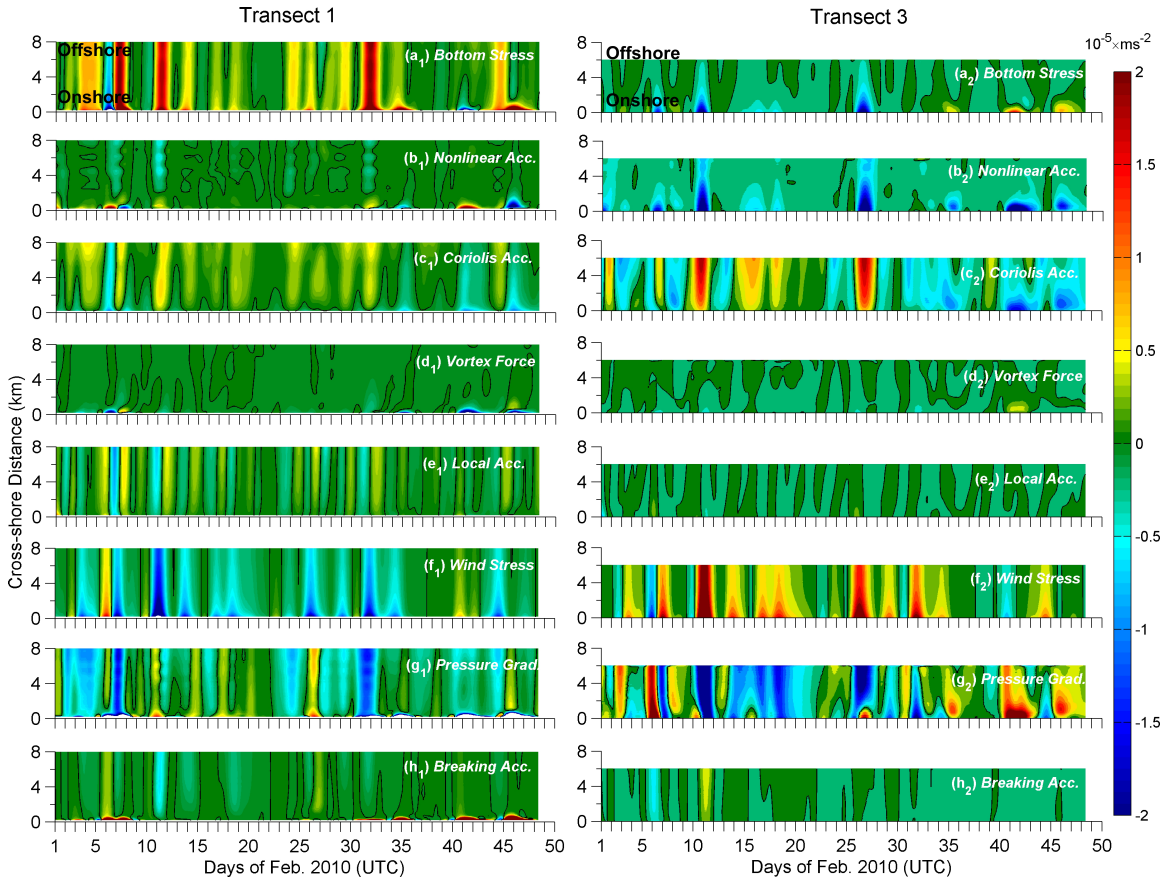

Figure 6.28: Cross-shore distribution of terms in local alongshore momentum balance for Transects 1 and 3, representing shorefaces with varying shoreline orientation (see Figure 6.3c for transect location). (a1, a2) Bottom stress; (b1, b2) Nonlinear advective acceleration; (c1, c2) Coriolis acceleration; (d1, d2) Vortex Force; (e1, e2) Local Acceleration; (f1, f2) Wind stress; (g1, g2) Pressure gradient and (h1, h2) wave breaking induced acceleration. All quantities have a unit of 10^{-5} ms^{-2}.

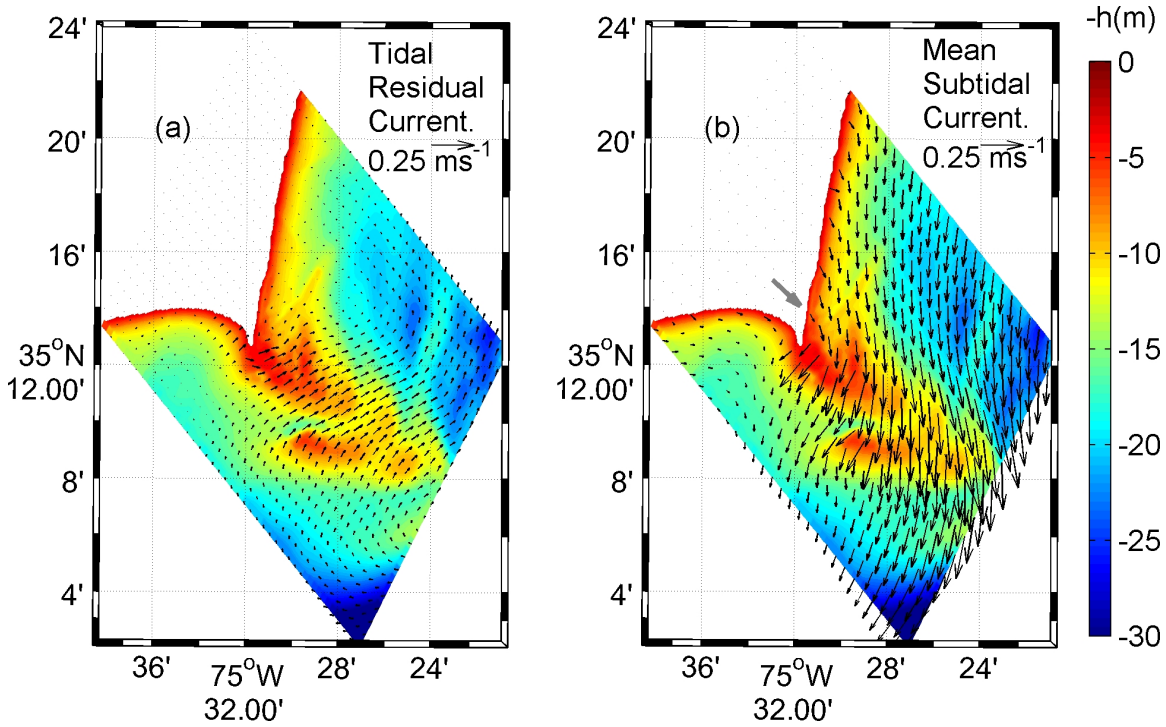

Figure 6.29: Spatial distribution showing magnitude and direction of (a) depth-averaged tidal residual current and (b) temporal mean of depth-averaged, subtidal currents for the entire simulation period. The arrow length and direction denote the flow magnitude and direction, respectively. Solid gray arrow is the mean wind velocity vector during the simulation period.

Table 6.1: Correlation coefficient (r) and model skill (S) for simulating wave parameters at offshore buoys

Site ID	H_{sig}		T_m		θ_m	
FPS	0.8	0.9	0.6	0.7	0.6	0.8
DS	0.9	0.9	0.7	0.8	-	-
DB	0.9	0.9	0.7	0.8	-	-
VB	0.9	0.9	0.8	0.9	0.6	0.8

Table 6.2: Correlation coefficient (r) and model skill (S) for simulating wave parameters around the shoal complex.

Site ID	H_{sig}		$\mathrm{T_m}$		θ_m	
	r	S	r	S	r	S
O1	0.9	0.9	0.8	0.7	0.8	0.7
O2	0.9	0.9	0.7	0.7	0.7	0.6
O3	0.9	0.9	0.7	0.7	0.7	0.8
N5	0.9	0.9	0.8	0.6	0.8	0.9
N6	0.9	0.9	0.8	0.6	0.8	0.5
N8	0.8	0.9	0.8	0.7	0.7	0.6
N9	0.9	0.9	0.7	0.7	0.8	0.7

Table 6.3: Correlation coefficient (r) and model skill (S) for simulating vertical profile (u_z, v_z) and depth-averaged (u_d, v_d) eastward and northward flows.

Site ID	u_d		v_d		u_z		v_z	
	r	S	r	S	r	S	r	S
O1	0.7	0.8	0.7	0.6	0.6	0.7	0.7	0.6
O2	0.5	0.7	0.7	0.9	0.3	0.6	0.7	0.8
O3	0.1	0.4	0.7	0.8	0.1	0.4	0.7	0.8
N5	0.7	0.7	0.7	0.9	0.7	0.7	0.7	0.8
N6	0.6	0.7	0.6	0.7	0.6	0.7	0.6	0.7
N8	0.2	0.5	0.8	0.7	0.3	0.5	0.8	0.7
N9	0.6	0.8	0.8	0.7	0.6	0.7	0.8	0.7

Table 6.4: Correlation coefficient (r) and model skill (S) for simulating along and cross-shore surface Lagrangian velocities against measurements from VHF Radar.

Transect	Surface Vel.	
	r	S
Along	0.6	0.8
Cross	0.5	0.7

Table 6.5: Description of wind direction, significant wave height, and wave direction for six events considered during the simulation period.

Case	**Time**	**Wind Dir.**	**Wave Forcing**	
			Magnitude	**Dir.**
(a)	Feb. 4	S/SW	$0 < H_{sig} < 2$ m	SW
(b)	Feb. 6	NE	$2 < H_{sig} < 4$ m	N/NW
(c)	Feb 7.	SW	$2 < H_{sig} < 3$ m	SW
(d)	Feb 11.	SE	$2 < H_{sig} < 3$ m	SE
(e)	Feb. 27	E/NE	$0 < H_{sig} < 2$ m	NE
(f)	Mar. 13	N	$2 < H_{sig} < 3$ m	NW

Chapter 7

Conclusions

The key questions addressed in this dissertation are:
[1] What are the limitations of using a three-dimensional radiation stress based approach and how does using a vortex force formalism based methodology removes these limitation?
[2] How does the role of vortex force vary in momentum balances within and outside the surf zone, and what is the balance between nonlinear advective acceleration and vortex force?
[3] Which dynamic momentum balances occur around a cuspate foreland system and within the shallow shoal complex as a response to different wind and wave forcing?

Radiation Stress vs. Vortex Force Formalism Approach in 3-D Modeling

In Chapter 2, a three-dimensional radiation stress approach (Mellor, 2011) was employed to study the wave driven circulation within the surf zone and the inner shelf. This approach correctly simulates the circulation pattern within the surf zone, however, at the interface of the wave shoaling and breaking zone, spurious offshore directed flows are observed. This discrepancy occurs due to the fact that the three-dimensional radiation stress formulation assumes same vertical distribution of both conservative and non-conservative processes. Nevertheless, in order to reduce the dis-

crepancy in the flow structure, an alternate vertical distribution is suggested through this work. This alternate methodology has recently been implemented by Moghimi et al. (2012) and a similar technique is also investigated by Mellor (2013). Overall, it is suggested that a vertical radiation stress based approach is reasonable of engineering oriented studies within the surf zone, but it is not recommended for applications that span larger regions extending from the inner shelf to the surf zone.

Given the shortcomings of the radiation stress method, the vortex force formalism method (McWilliams et al., 2004; Uchiyama et al., 2010) was implemented in the model as described in Chapter 3. This method allows for a clear delineation between conservative forcing with a known vertical distribution, like the Bernoulli head and the vortex force, and non-conservative forcing which can be further divided into depth-limited breaking acceleration, surface and bottom streaming and wave roller contribution. This approach was found to rectify the shortcomings of the Radiation Stress method and it allows for seamless simulation of flow structure from the open ocean to the surf zone, with no discrepancy at the interface of the wave shoaling and wave breaking zone.

It is important to point that the modifications made to the circulation models (Chapter 2 and 3) have been conducted on a public-domain modeling system. The modified radiation stress approach is presently distributed through the Rutgers ROMS version (https://www.myroms.org/), while the vortex force formalism has been implemented as a part of the Coupled-Ocean-Atmosphere-Wave and Sediment Transport modeling system
(http://woodshole.er.usgs.gov/project-pages/cccp/public/COAWST.htm).

In chapter 2, a three-dimensional radiation stress approach (Mellor, 2011) is employed to study the wave driven circulation within the surf zone and the inner shelf. This approach correctly simulates the circulation pattern within the surf zone, however, at the interface of the wave shoaling and breaking zone, spurious offshore di-

rected flows are observed. This discrepancy occurs due to the fact that the three-dimensional radiation stress formulation assumes same vertical distribution of both conservative and non-conservative processes. Nevertheless, in order to reduce the discrepancy in the flow structure, an alternate vertical distribution is suggested through this work. This alternate methodology has recently been implemented by Moghimi et al. (2012) and a similar technique is also investigated by Mellor (2013). Overall, it is suggested that a vertical radiation stress based approach is reasonable of engineering oriented studies within the surf zone, but cannot be used seamlessly from the inner shelf to the surf zone.

The second approach (Chapter 4) for including the three-dimensional effect of waves is based on vortex force formalism method (McWilliams et al., 2004; Uchiyama et al., 2010). The advantage of this method is a clear delineation between conservative forcing with a known vertical distribution, like the Bernoulli head and the vortex force, and non-conservative forcing which can be further divided into depth-limited breaking acceleration, surface and bottom streaming and wave roller contribution. This methodology allows for seamless simulation of flow structure from the open ocean to the surf zone, with no discrepancy at the interface of the wave shoaling and wave breaking zone.

It is important to point that the modifications made to the circulation models (Chapter 2 and 4) have been conducted on a public-domain modeling system. The modified radiation stress approach is presently distributed through the Rutgers ROMS version, while the vortex force formalism has been implemented as a part of the Coupled-Ocean-Atmosphere-Wave and Sediment Transport modeling system.

Role of Vortex Force in Momentum Balance

Vortex force physically represents the interaction between the Stokes drift and the

mean flow vorticity, and its contribution becomes important in the presence of strong horizontal shear in the alongshore velocity, and at locations within the surf zone where Stokes drift is intensified. Model simulation based momentum balance analysis suggests that the vortex force can be a dominant term inside the surf zone even for simple applications like obliquely incident waves on a planar, alongshore uniform beach. In addition, the contribution of this term becomes even more relevant in barred beaches and for complex rip current morphologies. In recent works by Olabarrietta et al. (2012, 2013) the role of vortex force is also found to be important for wave-current interaction around a tidal inlet.

One of the important findings in this study is the identification of the relative competition between nonlinear advective acceleration and the vortex force contribution. In a seminal work by Smith (2006) it was suggested that the alongshore advective flux due to vortex force in an alongshore uniform beach is completely balanced by the advective acceleration term, as long as the return cross-shore Eulerian mean flow is same in magnitude and opposite in direction to the Stokes drift. This balance is represented as:

$$\begin{aligned} \overline{u}\frac{\partial \overline{v}}{\partial x} + \overline{u^{st}}\frac{\partial \overline{v}}{\partial x} \\ \overline{u} + \overline{u^{st}} = 0 \end{aligned} \tag{7.1}$$

where, $\overline{u}$ and $\overline{v}$ are the depth-averaged cross-shore and alongshore velocities, respectively, while $\overline{u^{St}}$ is the depth-averaged, cross-shore Stokes drift.

However, the cross-shore and alongshore Eulerian mean flows, and the Stokes drift have distinct vertical distributions, and a vertical integration of advective acceleration and vortex force terms reveals that the balance depicted in Eqn. 7.1 does not really exist as:

$$\int_{-h}^{\eta} u(z)\frac{\partial v(z)}{\partial x}\partial z + \int_{-h}^{\eta} u^{St}(z)\frac{\partial v(z)}{\partial x}\partial z \neq 0 \tag{7.2}$$

This imbalance between vortex force and nonlinear advective acceleration leads to a net contribution in the momentum balance, which modifies the location of maximum alongshore velocity. This imbalance becomes even more important for barred beaches and complex morphologies with rip channels. In other words, the depth-averaged alongshore velocity obtained from a depth-averaged numerical model is different that obtained by vertically integrating the flows from a three-dimensional numerical model as the former cancels out the contribution of advective acceleration and vortex force (as in Eqn. 1), even though they have a net contribution (as in Eqn. 2).

These findings also have implications for cross-shelf exchange within and outside the surf zone. Differences in the vertical structure of cross-shore Eulerian mean flow and the Stokes drift (Figs. 1.1, 4.2, 4.9) can lead to a net Lagrangian mean flow. Thus the imbalance between nonlinear advective acceleration and vortex force is also exhibited through a net vertical Lagrangian transport, and may be one of the reasons for movement of material into or outside the surf zone over subtidal scales.

Momentum Balances around Cuspate Foreland Systems

The momentum balance analysis conducted around a cuspate foreland system using field observations (see Chapter 5) and a nested, coupled, three-dimensional ocean circulation and wave propagation model (see Chapter 4) has provided significant insights on the effect of coastline configuration on nearshore circulation.

During the data collection period, the dominant wind direction is towards the south/southwest making the east and northeast side of the Cape Hatteras point the windward side, while locations on the south/southwest are on the leeward side. On the windward side, dominant momentum balance occurs between wind and bottom stress in deeper waters (~10m), while in shallower waters the vortex force and nonlinear advective acceleration along with wave breaking contribution become important. It

is further suggested that in the transition zone between the inner shelf and the surf zone, the vortex force can have similar magnitude as the wind stress and the wave breaking contribution. However, most of the previous studies tend to ignore the contribution of vortex force in field based momentum balance analysis.

On the leeward side of the cape, the momentum balance is not closed; however, a linearized momentum balance analysis is used to show that pressure gradient as a response to wind stress is required for closing the momentum balance. Interestingly, pressure gradient estimates from adjacent tide gauges on both windward and leeward sides of the cape are of similar magnitude, and further analysis reveals that the pressure gradient generated is dependent on the relative angle of the coastline orientation with respect to the wind velocity vector. This finding is analogous to having a uniform coastline orientation with alongshore varying wind conditions. It is expected that the flow pattern revealed and the momentum balance analysis conducted for regions adjacent to Cape Hatteras, NC is similar to that occurring around other cuspate foreland systems in the South Atlantic Bight and those on the west coast of the US.

Momentum balance analysis from the same region using the model results (Chapter 6) endorses the findings from field observations, and allows further evaluation of momentum balance around the shoal complex attached to Cape Hatteras point. On the windward side, in addition to wind stress, pressure gradient contribution is found to be important which acts due to local change in coastline orientation relative to the wind forcing. During strong southwestward winds, the pressure gradient forcing augments the wind stress and their sum is primarily balanced by bottom stress, local and Coriolis acceleration. At this juncture it is important to point out that at locations in the inner shelf (water depth $>$ 10 m) the contribution of vortex force term is negligible in comparison to most of the other momentum balance terms, thus limiting its importance to within the surf zone and the wave shoaling region. On

the leeward side of the cape, the model suggests a balance between wind stress and pressure gradient, which is similar to the findings presented in Chapter 5. Previous momentum balance studies conducted around capes (Gan and Allen, 2002b; Gutierrez et al., 2006; Sanay et al., 2007) have revealed similar balances between pressure gradient and the wind stress term leading to flow reversals in the nearshore.

However, the role of shoal complex in modifying wind and wave propagation, and momentum balances within a shoal complex has not been investigated through previous studies. Model simulated circulation pattern and, along and cross-shoal momentum balances presented in Chapter 6 suggest that the shallow regions of the sub aqueous shoal complex act as extended coastline from the Cape Hatteras point, generating a pressure gradient force directed opposite to the wave breaking contribution. However, in absence of an impervious boundary this balance is not closed and leads to development of cross-shoal flows. Further, the shoal complex also allows for sheltering of either sides of the cape depending on the wind and wave propagation direction.

7.1 Future Directions

Spectral distribution of the Stokes drift

The present implementation of the vortex force formalism in the COAWST modeling system (Chapter 4) uses a bulk wave parameter based estimate of Stokes drift (Eq. 4.2), which is a simplification. For random wave fields in the ocean, the Stokes drift is a function of the frequency-directional ocean wave spectrum, and its vertical distribution is dependent on the wave number. This formulation is given as:

$$(u^{St}, v^{St}) = \int \sigma k(cos\theta, sin\theta) E(f,\theta) \frac{cosh(2kz + 2kh)}{sinh^2(kD)} df d\theta \tag{7.3}$$

where, σ is the angular frequency; k is the wave number; D is the total water depth; h is the resting depth; $E(f,\theta)$ is the frequency-directional ocean wave spectrum; f

is the frequency and θ is the direction. f varies from the given range of lowest to highest frequency, while θ varies from 0° to 360°.

In order to identify the differences between the two formulations, Stokes drift along the direction of wave propagation is estimated using the bulk parameter based formulation (Eqn. 4.2) and the spectral formulation (Eq. 7.3) for waves with a significant wave height of 2.3 m, peak period of 6 seconds and 13° angle of incidence. The bulk parameters were used to calculate a JONSWAP spectrum to be used with the spectral formulation. The Stokes drift estimate from the bulk parameter method is weaker at the surface in comparison to those obtained from Eq. 7.3; however in deeper waters this trend reverses (Fig. 7.1). These differences will lead to a change in calculation of momentum balance terms dependent on the Stokes drift, like the vortex force and the Stokes-Coriolis force.

Field estimates of vortex force

Most of the findings pointing at the importance of vortex force and nonlinear advective terms are based on model derived momentum balance analysis. The field observations presented in Chapter 5 does provide approximate estimates but a detailed estimation of cross-shore and alongshore distribution of vortex force and nonlinear advective acceleration could not be conducted. Future studies focused on resolving the momentum balances in the surf zone would require denser spatial resolution of instrumentation to appropriately categorize the magnitude and variability of these terms.

Pressure gradients as a response to wind forcing in cuspate embayments

Pressure gradient estimates from NOAA tide gauges (Chapter 5, Fig. 5.10) and model simulations (Figs. 6.19-6.25) suggest the development of pressure gradient as a response to the wind forcing. This pressure gradient may lead to flow reversals

(Gutierrez et al., 2006; Kumar et al., 2013), especially during periods when the wind forcing is relaxed. Accurate long term field observation of cross-shore and alongshore variation in alongshore pressure gradient within a cuspate embayment is required to correctly attribute the role wind forcing and large scale coastline shape.

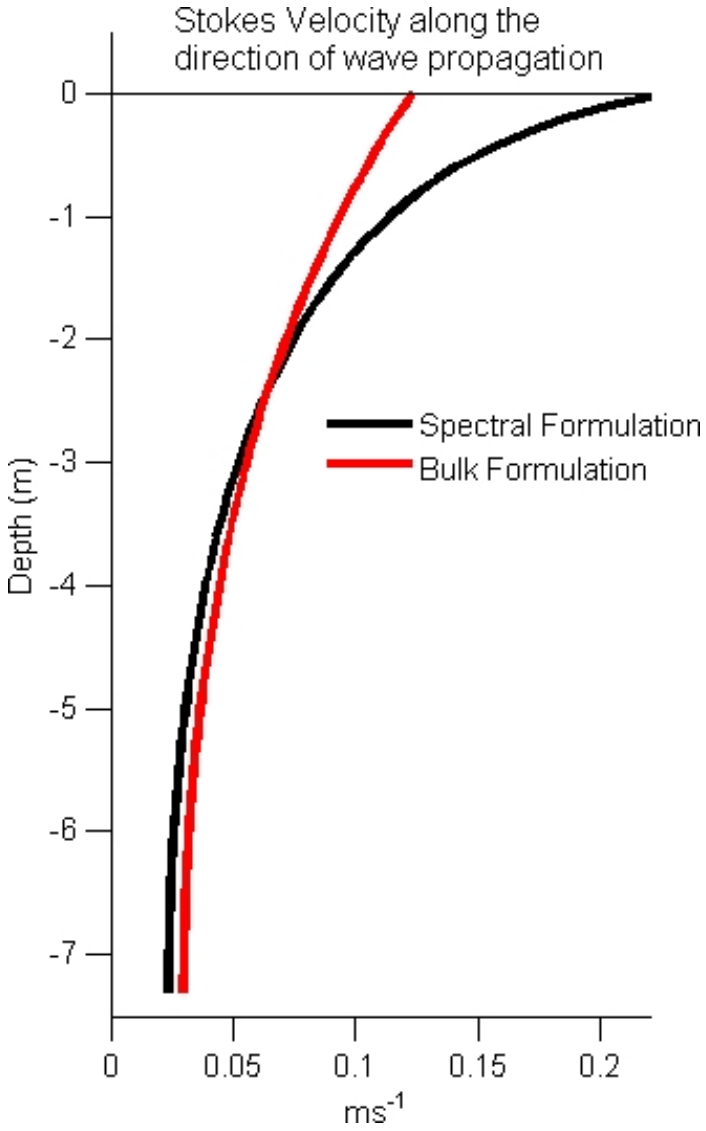

Figure 7.1: Vertical profile of Stokes drift along the direction of wave propagation (ms^{-1}) estimated using spectral formulation (solid black) in Eqn. 7.3 and bulk formulation (solid red) in Eqn. 3.2

Bibliography

Aagaard, T., Greenwood, B., Nielsen, J., 1997. Mean currents and sediment transport in a rip Channel. Marine Geology 140, 25-45.

Agrawal, Y.C., Terray, E.A., Donelan, M.A., Hwang, P.A., Williams, A.J., Drennan, M., Kahma, K.K., Kitaigorodskii, S.A., 1992. Nature, 359, 219-220.

Allard, R., J. Dykes, Y.L. Hsu a, J. Kaihatu and D. Conley, 2008. A real-time nearshore wave and current prediction system. Journal of Marine Systems 69: 37-58.

Ardhuin, F., Jenkins, A.D, Belibassakis, K.A., 2008a. Comments on "The three-dimensional current and surface wave equations". Journal of Physical Oceanography 38, 1340-1350.

Ardhuin, F., Rascle, N, Belibassakis, K.A., 2008. Explicit wave-averaged primitive equations using a generalized Lagrangian mean. Ocean Modeling, 20, 35-60.

Arthur, R. S. 1962. A Note on the Dynamics of Rip Currents. Journal of Geophysical Research 67(7), 2777-2779.

Andrews, D.G., McIntyre, M.E., 1978a. An exact theory of nonlinear waves on a Lagrangian-mean flow. Journal of Fluid Mechanics, 89, 609-646.

Andrews, D.G., McIntyre, M.E., 1978b. On wave-action and its relatives. Journal of Fluid Mechanics, 89, 647-664.

Apotsos, A., Raubenheimer, B., Elgar, S., Guza, R.T., Smith, J.A.., 2007. Effect of wave rollers and bottom stress on wave setup. Journal of Geophysical Research, 112, C02003, doi: 10.1029/2006JC003549

Aubrey, D.G., 1979. Seasonal Patterns of Onshore/Offshore Sediment Movement. Journal of Geophysical Research, 84(C10): 6,347-6,354.

Austin, J. and S. J. Lentz 1999. The Relationship Between Synoptic Weather Systems and Meteorological Forcing on the North Carolina inner shelf, Journal of Geophysical Research, 104 C8, 18,159-18,185.

Barth, J. A., S. D. Pierce, and R. M. Castelao (2005), Time-dependent, wind-driven flow over a shallow midshelf submarine bank, Journal of Geophysical Research, 110, C10S05, doi:10.1029/2004JC002761.

Battjes, J.A., Janssen, J.P.F.M., 1978. Energy loss and set-up due to breaking of random waves. Proc. 16th Int. Conf. Coastal Engineering, ASCE, pp. 569-587.

Beardsley, R. C., R., Limeburner, and L.K., Rosenfeld (1985), Introduction to the CODE-2 moored array and large-scale data report, edited by: Limeburner, R., Woods Hole Oceanographic Institution.

Bennis, A., Ardhuin, F., 2011. Comments on "The Depth-Dependent Current and Wave Interaction Equations: A Revision". Journal of Physical Oceanography, 41,

2008-2012. Bennis, A., Ardhuin, F., Dumas., F., 2011. On the coupling of wave and three-dimensional circulation models: Choice of theoretical framework, practical implementation and adiabatic tests. Ocean Modeling, 40, 260-277.

Bishop, C.T., and M.A. Donelan (1987), Measuring Waves with Pressure Transducers, Journal of Coastal Engineering, 11, 309-328.

Booij, N., Ris, R. C., Holthuijsen, L. H., 1999. A third-generation wave model for coastal regions 1. Model description and validation, Journal of Geophysical Research 104(C4), 7649-7666.

Bowen, A. J., 1969. Rip Currents 1. Theoretical Investigations. Journal of Geophysical Research 74(23), 5467- 5478.

Bowen, A. J., Inman D. L., 1969. Rip Currents 2. Laboratory and Field Observations. Journal of Geophysical Research 74(23), 5479-5490.

Brander, R.W., 1999. Field Observations on the Morphodynamic Evolution of Low Energy Rip-Current System. Marine Geology, 157: 199-217.

Brander, R.W., Short A.D., 2001. Flow kinematics of low-energy rip current systems. Journal of Coastal Research 17 (2), 468-481.

Brocchini, M., Kennedy, A. B., Soldini, L., Mancinelli, A., 2004. Topographically controlled, breaking-wave-induced macrovortices. Part 1. Widely separated breakwaters. Journal of Fluid Mechanics 507, 289-307.

Brodie, K. L., Slocum, R. K., and McNinch, J. E. (2012, October). New insights into the physical drivers of wave runup from a continuously operating terrestrial laser scanner. In Oceans, 2012 (pp. 1-8). IEEE.

Carniel S., Warner J.C., Chiggiato, J., Sclavo, M., 2009. Investigating the impact of surface wave breaking on modelling the trajectories of drifters in the Northern Adriatic Sea during a wind-storm event. Ocean Modeling, 30, pp. 225-239. DOI:10.1016/j.ocemod.2009.07.001.

Cambazoglu, M.K., Haas, K.A., 2011. Numerical modeling of breaking waves and cross-shore currents on a barred beach. Journal of Waterway, Port, Coastal and Ocean Engineering. doi:10.1061/(ASCE)WW.1943-5460.0000096

Castelao, R. M., and Barth, J. A. (2006). The relative importance of wind strength and along-shelf bathymetric variations on the separation of a coastal upwelling jet. Journal of physical oceanography, 36(3), 412-425.

Castelao, R. M., and Barth, J. A. (2007). The role of wind stress curl in jet separation at a cape. Journal of Physical Oceanography, 37(11), 2652-2671. Chapman, D. C., 1985: Numerical treatment of cross-shelf open boundaries in a barotropic coastal ocean model, J. Phys. Oceanography, 15, 1060-1075.

Chen, Y., R. T. Guza, and S. Elgar (1997), Modeling spectra of breaking surface waves in shallow water, Journal of Geophysical Research, 102, 25,035-25,046.

Chen, Q., Dalrymple, R. A., Kirby, J. T., Kennedy, A. B., Haller, M. C., 1999. Boussinesq modeling of a rip current system. Journal of Geophysical Research 104(C9),

20,617-20,637.

Church, J. C., Thornton, E.B., 1993. Effects of breaking wave induced turbulence within a longshore current model. Coastal Engineering 20, 1-28.

Churchill, J. H., and Gawarkiewicz, G. G. (2012). Pathways of shelf water export from the Hatteras shelf and slope. Journal of Geophysical Research: Oceans (1978-2012), 117(C8).

Collins, J.I., 1972: Prediction of shallow water spectra, Journal of Geophysical Research, 77, No. 15, 2693-2707.

Craik, A.D.D., Leibovich, S., 1976. A rational model for Langmuir circulations. Journal of Fluid Mechanics 73, 401-426.

Craig, P. D., Banner, M. L., 1994. Modeling wave-enhanced turbulence in the ocean surface layer. Journal of Physical Oceanography, 24, 2546-2559.

Crépon, M., C. Richez, and M. Chartier (1984), Effects of coastline geometry on upwellings, Journal of Physical Oceanography, 14, 1365-1382

Crépon, M., and C. Richez (1982), Transient upwelling generated by two dimensional atmospheric forcing and variability in the coastline, Journal of Physical Oceanography, 12, 1437-1457.

Crosby, D. S., Breaker, L. C., and W. H. Gemmill (1993). A proposed definition for vector correlation in geophysics: Theory and application. Journal of Atmospheric

and Oceanic Technology, 10(3), 355-367.

Dalrymple, R. A., 1975. A Mechanism for Rip Current Generation on an Open Coast. Journal of Geophysical Research 80(24), 3485-3487.

Dalrymple, R.A., 1978. Rip Currents and Their Causes. Proceedings of the 16th International Conference on Coastal Engineering, ASCE: 1,414-1,427.

Dingemans, M.W., Radder, A.C., Vriend, H.J.D, 1987. Computation of the driving forces of wave-induced currents. Coastal Engineering, 11, 539-563.

Devaliere, E., J. Hanson and R. Luettich, 2009. A High Resolution Near-Shore Wave Model for the Mid-Atlantic Coast, UCAR project S07-66810 Final Report, US Army Corps of Engineers, Field Research Facility.

Drønen, N., Karunarathna, H., Fredsoe, J., Sumer, M., Deigaard, R., 2002. An experimental study of rip channel flow. Coastal Engineering. 45, 223-238.

Dusek, G, H. Seim, J. Hanson and D. Elder, 2010. An Analysis of Rip Current Rescues at Kill Devil Hills, NC. This Volume

Durski, S.M., Glenn, S.M., Haidvogel, D., 2004. Vertical mixing schemes in the coastal ocean: Comparison of the level 2.5 Mellor-Yamada scheme with an enhanced version of the K profile parameterization. Journal of Geophysical Research, 109, C01015.

Ebersole, B. and R.A. Dalrymple (1980). Numerical Modeling of Nearshore Circula-

tion. Proc. 17th International Conference on Coastal Engineering, pp. 2710-2725.

Eldeberky, Y., Battjes, J. A., 1996. Spectral modeling of wave breaking: Application to Boussinesq equations. Journal of Geophysical Research 101, 1253-1264.

Elgar, S., Guza, R.T., Raubenheimer, B., Herbers, T.H.C., Gallagher, E.L., 1998. Spectral evolution of shoaling and breaking waves on a barred beach. Journal of Geophysical Research 103, 15797-15805.

Engle, J., MacMahan, J., Thieke, R.J. and Hanes, D.M., 2002. Formulation of a Rip Current Predictive Index Using Rescue Data. Proc. National Conf. On Beach Presearvation Technology, FSBA, January 23-5, Biloxi, MS.

Fairall, C. W., Bradley, E. F., Rogers, D. P., Edson, J. B., and Young, G. S. (1996). Bulk parameterization of air-sea fluxes for tropical ocean-global atmosphere coupled-ocean atmosphere response experiment. Journal of Geophysical Research, 101(C2), 3747-3764.

Flather, R. A., 1976: A tidal model of the northwest European continental shelf. Mern. Soc. Roy. Sci. Liege, Ser. 6, 10, 141-164.

Feddersen, F., Guza, R. T., Elgar, S., Herbers, T. H. C., 1998. Alongshore momentum balances in the nearshore. Journal of Geophysical Research 103, 15,667-15,676.

Feddersen, F., Trowbridge, J. H., 2005. The effect of wave breaking on surfzone turbulence and alongshore currents: a modeling study. Journal of Physical Oceanography, 35, 2187-2203.

Fewings, M. R. (2007), CrossâĂŘshelf circulation and momentum and heat balances over the inner continental shelf near MarthaâĂŹs Vineyard, Massachusetts, Ph.D. thesis, 267 pp., Massachusetts Institute of Technology (Available at http://hdl.handle.net/1721.1/42066.

Fewings, M. R., and S. J. Lentz (2010), Momentum balances on the inner continental shelf at MarthaâĂŹs Vineyard Coastal Observatory, Journal of Geophysical Research, 115, C12023, doi:10.1029/2009JC005578.

Gallagher, E.L., Boyd, W., Elgar, S., Guza, R.T., Woodward, B., 1996. Performance of a sonar altimeter in the nearshore. Mar. Geol. 133, 241-248.

Gallagher, E.L., Elgar, S., Guza, R.T., 1998. Observations of sand bar evolution on a natural beach. Journal of Geophysical Research 103, 3203-3215.

Gao, S., Collins, M. and Cross, J., 1998. Equilibrium Coastal Profiles: II. Evidence from EOF Analysis. Chinese Journal of Oceanology and Limnology, 16(3): 193-204.

Garcez Faria, A.F., Thornton, E.B., Stanton, T.P., Soares, C.V., Lippmann, T.C., 1998. Vertical profiles of longshore currents and related bed stress and bottom roughness. Journal of Geophysical Research 103, 15667-15676.

Garcez-Faria, A. F., Thornton, E. B., Lippmann, T. C., Stanton, T. P., 2000. Undertow over a barred beach. Journal of Geophysical Research 105, 16,999-17,010.

Garrett, C., 1976: Generation of Langmuir circulations by surface waves-A feedback mechanism. Journal of Marine Research, 34, 117-130.

Garrett, C.J.R., and Toulany, B. (1981), Variability of the flow through the Strait of Belle Isle, Journal of. Marine Research, 39, 163-189.

Gan, J., and J. S. Allen (2002a), A modeling study of the shelf circulation off northern California in the region of the Coastal Ocean Dynamics Experiment: 2. Simulations and comparisons with observations,
Journal of Geophysical Research, 107(C11), 3184, doi:10.1029/2001JC001190.

Gan, J., and J. S. Allen (2002b), A modeling study of the shelf circulation off northern California in the region of the Coastal Ocean Dynamics Experiment: Response to relaxation of upwelling winds, Journal of Geophysical Research, 107(C9), 3123, doi:10.1029/2000JC000768.

Grant, S. B., Kim, J. H., Jones, B. H., Jenkins, S. A., Wasyl, J., Cudaback, C., 2005. Surf zone entrainment, along-shore transport, and human health implications of pollution from tidal outlets. Journal of Geophysical Research, 110, C10025, doi:10.1029/2004JC002401.

Groeneweg, J., Klopman, G., 1998. Changes in the mean velocity profiles in the combined wave-current motion described in GLM formulation. Journal of Fluid Mechanics 370, 271-296.

Gutierrez, B. T., G. Voulgaris, and P. A. Work (2005), Cross-shore variation of wind-driven flows on the inner shelf in Long Bay, South Carolina, United States, Journal of Geophysical Research, 111, C03015, doi:10.1029/2005JC003121.

Haas, K. A., Svendsen, I. A., Zhao, Q., 2000. 3D modeling of rip currents. Proceedings 27th Coastal Engineering Conference, American Society Civil Engineers, Sydney, Australia, 2, pp. 1113-1126.

Haas, K. A., Svendsen, I. A., 2002. Laboratory measurements of the vertical structure of rip currents. Journal of Geophysical Research 107(C5), 3047, doi: 10.1029/2001JC000911.

Haas, K. A., Svendsen, I. A., Haller, M. C., Zhao, Q., 2003. Quasi-three-dimensional modeling of rip current systems, Journal of Geophysical Research, 108(C7), 3217, doi: 10.1029/2002JC001355.

Haas, K. A., Warner, J.C., 2009. Comparing a quasi-3D to a full 3D nearshore circulation model: SHORECIRC and ROMS. Ocean Modeling. 26, 91-103.

Haidvogel, D. B., Beckmann. A., 1999. Numerical Ocean Circulation Modeling: Series on Environmental Science and Management, Vol. 2, Imperial College Press, 319 pp.

Haidvogel, D. B., Arango, H. G., Hedstrom, K., Beckmann, A., Malanotte-Rizzoli, P., and Shchepetkin, A. F. (2000). Model evaluation experiments in the North Atlantic Basin: simulations in nonlinear terrain-following coordinates.Dynamics of Atmospheres and Oceans, 32(3), 239-281.

Haidvogel, D. B. , Arango, H.G., Budgell, W. P., Cornuelle, B. D., Curchitser, E., Di Lorenzo, E., Fennel, K., Geyer, W. R., Hermann, A. J., Lanerolle, L., Levin, J., McWilliams, J. C., Miller, A. J., Moore, A. M., Powell, T. M., Shchepetkin, A. F., Sherwood, C. R., Signell, R. P., Warner, J. C., Wilkin, J., 2008. Regional Ocean

Forecasting in Terrain-following Coordinates: Model Formulation and Skill Assessment, Journal of Computational Physics. 227, 3595-3624.

Haller, M. C., Dalrymple, R.A., Svendsen, I. A., 2002. Experimental study of nearshore dynamics on a barred beach with rip channels. Journal of Geophysical Research 107(C6), 3061, doi:10.1029/2001JC000955.

Haller, M. C., Dalrymple, R. A., 2001. Rip current instabilities. Journal of Fluid Mechanics. 433, 161-192.

Hasselmann, K. (1970), Wave-driven inertial oscillations, Geophys. Fluid Dyn., 1, 463-502.

Hasselmann, K., T.P. Barnett, E. Bouws, H. Carlson, D.E. Cartwright, K. Enke, J.A. Ewing, H. Gienapp, D.E. Hasselmann, P. Kruseman, A. Meerburg, P. M uller, D.J. Olbers, K. Richter, W. Sell and H. Walden, 1973: Measurements of windâĹŠwave growth and swell decay during the Joint North Sea Wave Project (JONSWAP), Dtsch. Hydrogr. Z. Suppl., 12, A8

Hayes, O.M., 1964. Lognormal distribution of inner continental shelf widths and slopes, Deep Sea Research and Oceanographic Abstracts, Vol. 11, 1, 53-78. doi: 10.1016/0011-7471(64)91082-4.

Herbers, T. H. C., S. Elgar, and R.T. Guza (1999), Directional spreading of waves in the nearshore, Journal of Geophysical Research, 104(C4), 7683-7693.

Herbers, T. H. C., E. J. Hendrickson, and W. C. O'Reilly (2000), Propagation of swell

across a wide continental shelf, Journal of Geophysical Research, 105(C8), 19729-19737, doi:10.1029/2000JC900085.

Hughes, S.A., 1993. Physical Models and Laboratory Techniques in Coastal Engineering. World Scientific, Singapore.

Huntley, D.A., Short, A.D., 1992. On the spacing between observed rip currents. Coastal Engineering. 17, 211-225.

Iwata, N., 1976. Rip current spacing. Journal of Oceanographic Society of Japan, 32, pp 1-10.

Jenkins, A.D., 1989. The use of a wave-prediction model for driving a near-surface current model. Ocean Dynamics, Vol. 42., pp 133-146. doi: 10.1007/BF02226291

Jones, N.L., Monismith, S.G, 2008. The influence of whitecapping waves on the vertical structure of turbulence in a shallow estuarine embayment. Journal of Physical Oceanography, 38, 7, 1563-1580.

Kanarska, Y., Shchepetkin, A., McWilliams, J.C., 2007. Algorithm for non-hydrostatic dynamics in the Regional Oceanic Modeling System, Ocean Modelling, Volume 18, Issues 3-4, 2007, Pages 143-174, ISSN 1463-5003, 10.1016/j.ocemod.2007.04.001.

Kennedy, A. B., Brocchini, M., Soldini, L., Gutierrez, E., 2006. Topographically controlled, breaking-wave-induced macrovortices. Part 2. Changing geometries. Journal of Fluid Mechanics 559, 57-80.

Kinsman, B., 1965. Wind Waves, Prentice-Hall, Inc., 676pp.

Kirby, J.T. and R. A. Dalrymple (1982). Numerical modeling of the nearshore region. Research Report: CE-82-24, Ocean Engineering Program, Department of Civil Engineering, University of Delaware.

Kirincich, A.R., and J. A. Barth (2009), Along-shelf variability of inner-shelf circulation along the central Oregon coast during summer, Journal of Physical Oceanography, 39, 1380-1398.

Komar, P.D. (1998a). Beach Processes and Sedimentation, Prentice-Hall, Upper Saddle River, N.J., 544pp.

Krystek, M., and M. Anton (2007), A weighted total least squares algorithm for fitting a straight line, Meas. Sci. Technol., 18, 3438-3442.

Kumar, N., Voulgaris, G., and J.C. Warner, 2010. Using Coupled Wave Current Models to Simulate and Predict Rip Currents. AGU 2010 Ocean Sciences Meeting, Abstract No. PO15E-12, Portland, OR, USA.

Kumar, N., Voulgaris, G., Warner, J.C., 2011a. Implementation and modification of a 3-D radiation stress formulation for surf zone and rip-current applications. Coastal Engineering, 58, 12, 1097-1117. doi: 10.1016/j.coastaleng.2011.06.009.

Kumar, N., Voulgaris, G., Warner, J.C., 2011b. Measurement and three-dimensional modeling of nearshore circulation on a South Carolina beach. Shore & Beach, Vol. 79, 2, pp. 9-18.

Kumar, N., G. Voulgaris, J.C. Warner, M. Olabarrieta (2012), Implementation of the vortex force formalism in the coupled ocean-atmosphere-wave-sediment transport (COAWST) modeling system for inner shelf and surf zone applications, Ocean Modelling, Vol. 47, 2012, Pages 65-95, ISSN 1463-5003, 10.1016/j.ocemod.2012.01.003.

Kumar, N., Voulgaris, G. List, J.H., and Warner, J.C., 2013. Alongshore momentum balance analysis on a cuspate foreland. Journal of Geophysical Research. Lai, Z., Chen, C., Cowles, G. W., Beardsley, R. C., 2010. A nonhydrostatic version of FVCOM: 1. Validation experiments, Journal of Geophysical Research, 115, C11010, doi: 10.1029/2009JC005525

Lane, E. M., Restrepo, J. M., McWilliams, J. C., 2007. Wave-current interaction: A comparison of radiation-stress and vortex-force representations, Journal of Physical Oceanography, 37, 1122-1141.

Large, W. G., and S. Pond (1981). Open ocean momentum flux measurements in moderate to strong winds, Journal of Physical Oceanography, 11, 324-336.

Lascody, L.L., 1998. East Central Florida Rip Current program. National Weather Digest. Vol. 22, Issue 2.

Lavrenov, I.V., 2003. Wind-Waves in Oceans, Springer, 376 pp.

LeBlond, P. H., Tang, C. L., 1974. On Energy Coupling Between Waves and Rip Currents. Journal of Geophysical Research 79(6), 811-816.

Lentz, S. J., and C. D. Winant (1986), Subinertial currents on the southern California shelf, Journal of Physical Oceanography, 16, 1737-1750.

Lentz, S. J (1994), Current dynamics on the northern California inner shelf, Journal of Physical Oceanography, 24, 2461-2478.

Lentz, S., R. T. Guza, S. Elgar, F. Feddersen, and T. H. C. Herbers (1999), Momentum balances on the North Carolina inner shelf, Journal of Geophysical Research, 104, 18,205-18,226.

Lentz, S. J (2001), The Influence of Stratification on the Wind-Driven Cross-Shelf Circulation over the North Carolina Shelf. Journal of Physical Oceanography, 31, 2749-2760.

Lentz, S. J (2008), Observations and a model of the mean circulation over the Middle Atlantic Bight continental shelf, Journal of Physical Oceanography, 38, 1203-1221.

Lentz, S. J., Fewings, M., Howd, P., Fredericks, J., Hathaway, K., 2008. Observations and a model of undertow over the inner continental shelf. Journal of Physical Oceanography, 38, 2341-2357.

Lentz, S.J., and M. R. Fewings (2012), The wind-and wave-driven inner-shelf circulation. Annual Review of Marine Science, 4, 317-343, doi: 10.1146/annuvrev-marine-120709-142745.

Lesser, G.R., Roelvink, J.A., van Kester, J.A.T.M., Stelling, G.S., 2004. Development and validation of a three-dimensional morphological model. Coastal Engineering. 51,

883-915.

List, J.H., J.C. Warner, E.R. Thieler, K. Haas, G. Voulgaris, J.E. McNinch, and K.L. Brodie (2011), A nearshore processes field experiment at Cape Hatteras, North Carolina, USA. Proceedings of the Coastal Sediments, World Scientific, pp. 2, 144-2,157, 2011.

Liu, Y., MacCready, P., Hickey, B. M., Dever, E. P., Kosro, P. M., and Banas, N. S. (2009). Evaluation of a coastal ocean circulation model for the Columbia River plume in summer 2004. Journal of Geophysical Research: Oceans (1978-2012), 114(C2).

Long, C.E., 1996. Index and bulk parameters for frequency-direction spectra measured at CERC Field Research Facility, June 1994 to August 1995. US Army Corps of Engineers Waterway Experiment Station, Vicksburg, MI, USA.

Long, J. W., Özkan-Haller, H. T., 2009. Low-frequency characteristics of wave group-forced vortices. Journal of Geophysical Research 114, C08004, doi:10.1029/2008JC004894.

Longuet-Higgins, M.S. (1953), Mass Transport in Water Waves, Philosophical Transactions of the Royal Society of London, Series A 245: 535-581.doi: 10.1098/rsta.1953.0006.

Longuet-Higgins, M. S., Stewart, R.W., 1964. Radiation stresses in water waves: a physical discussion, with applications. Deep-Sea Res. 11, 529-562.

Longuet-Higgins, M. S., 1970. Longshore Currents Generated by Obliquely Incident Sea Waves. a, b, Journal of Geophysical Research 75(33), 6778-6801.

Luettich, R. A.Jr., J. J. Westerink, and N. W. Scheffner (1992), ADCIRC: An advanced three-dimensional circulation model for shelves coasts and estuaries, report 1: Theory and methodology of ADCIRC-2DDI and ADCIRC-3DL, Dredging Research Prog. Tech. Rep.DRP-92-6, 137 pp., Waterw. Exp. Sta., U.S. Army Corps of Eng. Res. and Dev. Cent., Vicksburg, Miss.

Lushine, J.B., 1991. A study of rip current drownings and related weather factors. National Weather Digest, Vol. 16.

MacMahan, J.H., Thornton, E. B., Stanton, T.P., Reniers, A.J.H.M, 2005. RIPEX: Observations of a rip current system. Marine Geology. 218 (1-4), 113-134, doi:10.1016/j.margeo.2005.03.019.

Madsen, O.S., Poon, Y.K., Graber, H.C., 1988. Spectral wave attenuation by bottom friction: Theory. Proc. 21th Int. Conf. Coastal Engineering, ASCE, pp. 492-504

Madsen, O.S., 1994. Spectral waveâĂŞcurrent bottom boundary layer flows. In: Coastal Engineering 1994. Proceedings of the 24th International Conference on Coastal Engineering Research Council, Kobe, Japan, pp. 384-398.

McNinch, J. E., and Wells, J. T. (1999). Sedimentary processes and depositional history of a cape-associated shoal, Cape Lookout, North Carolina. Marine Geology, 158(1), 233-252.

McNinch, J.E. and R.A. Luettich, Jr (2000), Physical processes around a cuspate foreland headland: implications to the evolution and long-term maintenance of a cape-associated shoal, Continental Shelf Research, 20 (17), 2367-2389.

McNinch, J.E., 2006, Bar And Swash Imaging Radar (BASIR): a mobile X-band radar designed for mapping sand bars and swash-defined shorelines over large distances, Journal of Coastal Research, 23 (1).

McWilliams, J.C., Restrepo, J.M., Lane, E.M., 2004. An asymptotic theory for the interaction of waves and currents in coastal waters. Journal of Fluid Mechanics. 511, 135-178.

Mei C.C. and P.L.-F. Liu, 1977. Effects of Topography on the Circulation in and near the Surf Zone; Linearized Theory. Journal of Estuarine and Coastal Marine Science, 5: 25-37.

Mellor, G. L., 2003. The three-dimensional current and surface wave equations. Journal of Physical Oceanography 33, 1978-1989.

Mellor, G. L., 2005. Some consequences of the three-dimensional currents and surface wave equations. Journal of Physical Oceanography 35, 2291-2298.

Mellor, G. L., 2008. The depth-dependent current and wave interaction equations: A revision. Journal of Physical Oceanography 38, 2587-2596.

Mellor, G. L., 2011a. Wave Radiation Stress. Ocean Dynamics. 61, 5, 563-568. doi: 10.1007/s10236-010-0359-2.

Mellor, G. L., 2011b. CORRIGENDA: The three-dimensional current and wave equations. Journal of Physical Oceanography In Press.

Mellor, G.L., 2011c. Reply to comments by Bennis and Ardhuin, 2011

Murray A.B., M. LeBars and C. Guillon, 2003. Tests of a New Hypothesis for Non-Bathymetrically Driven Rip Currents. Journal of Coastal Research, 19(2): 269-277.

Nairn, R.B., Roelvink, J.A., and H.N. Southgate, Transition zone width and implications for modeling surf zone hydrodynamics. In: Proceedings of the 22nd International Conference on Coastal Engineering Delft, American Society of Civil Engineers, New York (1990), pp. 68-81.

Newberger, P. A., Allen, J. S., 2007. Forcing a three-dimensional, hydrostatic, primitive-equation model for application in the surf zone: 1. Formulation, Journal of Geophysical Research 112, C08018, doi: 10.1029/2006JC003472.

Newberger, P. A., Allen, J. S., 2007. Forcing a three-dimensional, hydrostatic, primitive-equation model for application in the surf zone: 2. Application to DUCK94, Journal of Geophysical Research 112, C08019, doi: 10.1029/2006JC003474.

NOAA, 2004, National Weather Service Instruction 10-310, July 16, 2004, Operations and Services, Marine and Coastal Weather Service Program, NWSPD10-3 (http://www.nws.noaa.gov/directives)

Noda, E. K., 1974. Wave-Induced Nearshore Circulation. Journal of Geophysical Research 79(27), 4097-4106.

Olabarrieta, M., Warner, J. C., Kumar, N., 2011. Wave-current interaction in Willapa

Bay. Journal of Geophysical Research, 116, doi:10.1029/2011JC007387.

Olabarrieta, M., Warner, J. C., Armstrong, B., Zambon, J. B., and He, R. (2012). OceanâĂŞatmosphere dynamics during Hurricane Ida and Nor'Ida: An application of the coupled ocean-atmosphere-wave-sediment transport (COAWST) modeling system. Ocean Modelling, 43, 112-137.

Park, J. Y., and Wells, J. T. (2005). Longshore transport at Cape Lookout, North Carolina: Shoal evolution and the regional sediment budget. Journal of coastal research, 1-17.

Patankar, S.V., 1980. Numerical heat transfer and fluid flow, Hemisphere Publishing Corporation, Washington, DC.

Phillips, O. M., The Dynamics of the Upper Ocean, 2nd ed., Cambridge Univ. Press, New York, 1977.

Rapp, R. J., Melville, W. K., 1990. Laboratory measurements of deep-water breaking waves. Phil.Trans. R. Soc. Lond. A 331, 735-800.

Raymond, W. H., and Kuo, H. L. (1984). A radiation boundary condition for multidimensional flows. Quarterly Journal of the Royal Meteorological Society,110(464), 535-551.

Reniers, A. J. H. M., Battjes, J. A., 1997. A laboratory study of longshore currents over barred and non-barred beaches, Coastal Eng., 30, 1-22.

Reniers, A. J. H. M., Van Dongeren, A. R., Battjes, J. A., Thornton, E. B., 2002b. Linear modeling of infragravity waves during Delilah, Journal of Geophysical Research, 107(C10), 3137, doi: 10.1029/2001JC001083.

Reniers, A. J. H. M., Roelvink, J. A., Thornton, E. B., 2004a. Morphodynamic modeling of an embayed beach under wave group forcing. Journal of Geophysical Research 109, C01030, doi:10.1029/2002JC001586.

Reniers, A. J. H. M., Thornton, E. B., Stanton, T. P., Roelvink, J. A., 2004b. Vertical flow structure during Sandy Duck: Observations and modeling. Coastal Eng., 51, 237-260.

Reniers, A.J.H.M., MacMagan, J.H., Thornton, E.B., Stanton, T.P., Henriquez, M., Brown, J.W., Brown, J.A., Gallagher, E., 2009. Surfzone Surface Retention on a rip channeled beach, Journal of Geophysical Research, 114, C10010, 2009.

Ribas, F., de Swart, H.E., Calvete, D., Falqués, A., 2011. Modeling waves, currents and sandbars on natural beaches: The effect of surface rollers. Journal of Marine Systems, Vol. 88, 1, pp 90-101.

Ris, R.C., 1999. Model convergence of SWAN in the Westerschelde estuary. WL|Delft Hydraulics, Report H3496.

Ris, R.C., Booij, N., and Holthuijsen, L.H., 1999. A third-generation wave model for coastal regions. Part II: Verification. Journal of Geophysical Research, C4(104), 7997-7681.

Ruessink, B. G., Miles, J. R., Feddersen, F., Guza, R. T., Elgar, S., 2001. Modeling the alongshore current on barred beaches. Journal of Geophysical Research 106(C10), 22,451-22,463.

Roelvink, J.A., Reniers, A.J.H.M., 1994. LIP 11D Delta flume experiments; A dataset for profile validation. Delft Hydraulics report No. H2130.

Rogers, W.E., Hwang, P.A., Wang, D.W., 2003. Investigation of wave growth and decay in the SWAN model: three regional-scale applications, Journal of Physical Oceanography, 33, 366-389.

Roughan, M., A. J. Mace, J. L. Largier, S. G. Morgan, J. L. Fisher, and M. L. Carter (2005), Subsurface recirculation and larval retention in the lee of a small headland: A variation on the upwelling shadow theme, Journal of Geophysical Research, 110, C10027, doi:10.1029/2005JC002898.

Sanay R., G. Voulgaris, and J.C. Warner (2007), Influence of Tidal Asymmetry and Residual Circulation on Sediment Transport in Linear Sandbanks: A Processes-Oriented Numerical Study. Journal of Geophysical Research, Oceans, Vol. 112, C12015, doi: 10.1029/2007JC004101.

Sanay, R., Yankovsky, A., and Voulgaris, G. (2008). Inner shelf circulation patterns and nearshore flow reversal under downwelling and stratified conditions off a curved coastline. Journal of Geophysical Research, 113(C8), C08050.

Savidge, D. K., and Bane, J. M. (2001). Wind and Gulf Stream influences on alongshelf transport and offshelf export at Cape Hatteras, North Carolina. Journal of

Geophysical Research: Oceans (1978-2012), 106(C6), 11505-11527.

Sclavo, M., Benetazzo, A., Carniel, S., Bergamasco, A., Falcieri, F. M., and Bonaldo, D. (2013). Wave-current interaction effect on sediment dispersal in a shallow semi-enclosed basin.

Shchepetkin, A. F., McWilliams, J.C., 2005. The Regional Oceanic Modeling System: A split-explicit, free-surface, topography-following coordinate oceanic model. Ocean Modeling 9, 347-404 doi:10.1016/j.ocemod.2004.08.002.

Shchepetkin, A. F., McWilliams, J. C., 2009. Correction and commentary for âĂIJOcean forecasting in terrain-following coordinates: Formulation and skill assessment of the regional ocean modeling systemâĂİ by Haidvogel et al., J. Comp. Phys. 227, pp. 3595-3624.âĂİ. Journal of Computational Physics. 228, 8985-9000.

Sheng, P., Liu, T., 2011.Three-dimensional simulation of wave-induced circulation: Comparison of three radiation stress formulations. Journal of Geophysical Research, Vol. 116, C05021, doi: 10.1029/2010JC006765.

Shepard F.P. and D.L. Inman, 1950. Nearshore Water Circulation Related to Bottom Topography and Wave Refraction. Trans. AGU Vol 31. 196-213.

Shi, F., Svendsen, I.A., Kirby, J.T. and J.McKee-Smith, 2003. A curvilinear version of a quasi-3D nearshore circulation model. Coastal Engineering, 49: 99-24.

Short, A.D., 1985. Rip current type, spacing and persistence, Narrabeen Beach, Australia, Marine Geology, 65: 47-71

Signell, R. P., and Geyer, W. R. (1991). Transient eddy formation around headlands. Journal of Geophysical Research: Oceans (1978-2012), 96(C2), 2561-2575.

Smith, J.A., 2006. Wave-current interactions in finite-depth, Journal of Physical Oceanography. 36, 1403-1419.

Sonu, C. J., 1972. Field Observation of Nearshore Circulation and Meandering Currents. Journal of Geophysical Research 77 (18), 3232-3247.

Soulsby, R.L., 1995. Bed shear-stresses due to combined waves and currents. In: M.J.F. Stive, Editor, Advances in Coastal Morphodynamics: An Overview of the G8-Coastal Morphodynamics Project, Co-Sponsored by the Commission of The European Communities Directorate General XII (1995), 4.20-4.23.

Stacey, M. W., 1999. Simulations of the wind-forced near-surface circulation in Knight Inlet: A parameterization of the roughness length. Journal of Physical Oceanography, 29, 1363-1367.

Stive, M. J. F., De Vriend, H.J., 1994. Shear stresses and mean flow in shoaling and breaking waves. Proc. of the 24th Coastal Engineering International Conference 1994, Kobe, Japan. American Society of Civil Engineers, New York, pp. 594-608.

Styles, R., and S. M. Glenn (2000), Modeling stratified wave and current bottom boundary layers on the continental shelf, Journal of Geophysical Research, 105(C10), 24,119-24,139, doi:10.1029/2000JC900115.

Svendsen, I., A., 1984a. Wave heights and set-up in a surf zone, Coastal Eng., 8, 303-329.

Svendsen, I. A., Haas, K. A., Zhao, Q., 2000. Analysis of rip current systems. In Proceedings 27th Coastal Engineering Conference, ASCE, Sydney, pp. 1127-1140.

Svendsen, I.A., Haas, K.A., Zhao, Q., 2002. Quasi-3D nearshore circulation model SHORECIRC, UserâĂŹs Manual, Draft Report, Center for Applied Coastal Research, Department of Civil Engineering, University of Delaware, Newark.

Tajima, Y., Madsen, O.S., 2006. Modeling near-shore waves, surface rollers and undertow velocity profiles. Journal of Waterways, Port, Coastal and Ocean Engineering ASCE, 132(6), 429-438

Tam, C. K. W., 1973. Dynamics of Rip Currents. Journal of Geophysical Research 78(12), 1937-1943.

Terrile, E., Brocchini, M., 2007. A dissipative point-vortex model for nearshore circulation. Journal of Fluid Mechanics, 589, pp. 455-478.

Thornton, E.B., 1970. Variations of Longshore Currents Across the Surf Zone, Proceedings of 12th International Conference on Coastal Engineering, ASCE, 291-308.

Thornton, E. B., Guza, R. T., 1983. Transformation of wave height distribution, Journal of Geophysical Research, 88, 5925-5938.

Ting, F.C.K., Kirby, J.T., 1994. Observations of undertow and turbulence in a labo-

ratory surf zone. Coastal Engineering. 24, 177-204.

Uchiyama, Y., McWilliams, J.C., Restrepo, J.M., 2009. Wave-current interaction in nearshore shear instability analyzed with a vortex-force formalism, Journal of Geophysical Research, 114, C06021, doi:10.1029/2008JC005135.

Uchiyama, Y., McWilliams, J.C., Shchepetkin, A.F., 2010, Wave-current interaction in an Oceanic Circulation Model with a Vortex-Force Formalism: Application to the Surf Zone. Ocean Modeling, doi: 10.1016/j.ocemod.2010.04.002.

Umlauf, L., Burchard, H., 2003. A generic length-scale equation for geophysical turbulence models. Journal of Marine Research, 61, 235-265.

van Dongeren, A.R., Sancho, F.E., Svendsen, I.A., Putrevu, U., 1995. Application of the Q3d SHORECIRC model to surfbeat. Proc. Coastal Dynamics, Gdynia, Poland, ASCE, New York, pp. 233-244.

van der Westhuysen, A.J., Zijlema, M., Battjes, J.A., 2007. Nonlinear saturation-based whitecapping dissipation in SWAN for deep and shallow water. Coastal Engineering, Vol. 54, 2, pp. 151-170.

Voulgaris, G., T. Mason and M.B. Collins, 1996. The Energetics Approach for Suspended Sand Transport in Macrotidal Ridge and Runnel Beaches. Proc. 25th Int. Conference on Coastal Engineering, Coastal Engineering Research Cancel/ASCE Orlando, Florida: 3948-3961.

Voulgaris, G., and M.B. Collins, 2000. Sediment Resuspension on Beaches: Re-

sponse to Breaking Waves. Marine Geology, 167: 167-187.

Voulgaris, G., D. Michel, D. Simmonds, H. Howa, M.B. Collins, and D.A. Huntley, 1998. Measuring and Modelling Sediment Transport on a Macrotidal Ridge and Runnel Beach: An Intercomparison. Journal of Coastal Research, 14(1): 315-330.

Voulgaris, G., J. C. Warner, P. A. Work, D. M. Hanes and K. A. Haas, 2004. The South Carolina Coastal Erosion Study: Integrated Circulation and Sediment Transport Studies. A Project Overview. Eos Trans. AGU, 85(47), Fall Meet. Suppl., Abstract No. OS21B-1224.

Voulgaris, G., Haus, B. K., Work, P., Shay, L. K., Seim, H. E., Weisberg, R. H., and Nelson, J. R. (2008). Waves initiative within SEACOOS. Marine Technology Society Journal, 42(3), 68-80.

Voulgaris G., Kumar, N., Warner, J.C., 2011. A Methodology for the Prediction of Rip Currents using a 3-D Numerical, Coupled, Wave-Current Model. In: Rip Currents: Beach Safety, Physical Oceanography, and Wave Modeling. S. Leatherman and J. Fletemeyer (Eds). CRC Press. ISBN: 9781439838969.

Voulgaris, G., Kumar, N., Gurgel, K. W., Warner, J. C., and List, J. H. (2011, March). 2-D inner-shelf current observations from a single VHF WEllen RAdar (WERA) station. In Current, Waves and Turbulence Measurements (CWTM), 2011 IEEE/OES 10th (pp. 57-65). IEEE.

Walstra, D. J. R., Roelvink, J.A., Groeneweg, J., 2000. Calculation of wave-driven currents in a 3D mean flow model. Proc. of the 27th Coastal Engineering Interna-

tional Conference 2000, Sydney, Australia. American Society of Civil Engineers, New York, pp. 1050-1063.

Wang, J., Shen., Y., 2010. Modeling oil spills transportation in seas based on unstructured grid, finite volume, wave-ocean model. Ocean Modeling (in press)

Warner, J.C., C. Sullivan, G. Voulgaris, P. A. Work, K. A. Haas, and D. M. Hanes, 2004.The South Carolina Coastal Erosion Study: Numerical modeling of circulation and sediment transport in Long Bay. Eos Trans. AGU, 85(47), Fall Meet. Suppl., Abstract No. OS21B-1226.

Warner, J. C., Geyer, W. R., and Lerczak, J. A. (2005). Numerical modeling of an estuary: A comprehensive skill assessment. Journal of Geophysical Research: Oceans (1978-2012), 110(C5).

Warner, J.C., Sherwood, C.R., Arango, H.G., Signell, R.P., Butman, B., 2005. Performance of four turbulence closure models implemented using a generic length scale method. Ocean Modeling. 8, 81-113.

Warner, J.C., Sherwood, C.R., Signell, R.P., Harris, C., and Arango, H.G., 2008. Development of a three-dimensional, regional, coupled wave, current, and sediment-transport model. Computers and Geosciences. 34, 1284-1306.

Warner, J.C., Perlin, N., Skyllingstad, E.D., 2008b. Using the Model Coupling Toolkit to couple earth system models. Environmental Modeling and Software, Vol. 23, 10-11, pp 1240-1249.

Warner, J.C., Armstrong, B., He, R., Zambon, J.B., 2010, Development of a Coupled Ocean-Atmosphere-Wave-Sediment Transport (COAWST) modeling system: Ocean Modeling, v. 35, no. 3, p. 230-244.

Warner, J. C., Armstrong, B., Sylvester, C. S., Voulgaris, G., Nelson, T., Schwab, W. C., and J. F. Denny (2012), Storm-induced inner-continental shelf circulation and sediment transport: Long Bay, South Carolina. Continental Shelf Research Vol. 42, pp. 51-63.

Weber, J. E., G. Broström, and ϕ Saetra, 2006: Eulerian versus Lagrangian approaches to the wave-induced transport in the upper ocean. Journal of Physical Oceanography, 36, 2106-2118.

Welch, P.D. (1967), The Use of Fast Fourier Transform for the Estimation of Power Spectra: A Method Based on Time Averaging Over Short, Modified Periodograms, IEEE Transactions on Audio Electroacoustics, AU-15, 70-73.

Willis, M.C, E.Devaliere, J.Hanson, R. Hawkins, J. Lewitsky, D. King, T. Nicolini, S. Tjaden, C. Morgan, Scott Schumann, M. Colby, and J. Elardo, 2010. Implementing the SWAN Wave Model at Three East Coast National Weather Service Offices. 14th Symposium on Integrated Observing and Assimilation Systems for the Atmosphere, Oceans, and Land Surface (IOAS-AOLS)/AMS Annual Meeting, Atlanta, GA. Extended Abstract 5B.7

Willmott, Cort J., Steven G. Ackleson, Robert E. Davis, Johannes J. Feddema, Katherine M. Klink, David R. Legates, James O'Donnell, and Clinton M. Rowe. "Statistics for the evaluation and comparison of models." Journal of Geophysical Re-

search: Oceans (1978-2012) 90, no. C5 (1985): 8995-9005.

Wright, L.D. and Short, A.D., 1984. Morphodynamic variability of surf-zone and beaches. Marine Geology, 56: 93-18.âĂČ

Xu, Z., Bowen, A.J., 1994. Wave- and wind-driven flow in water of finite depth, Journal of Physical Oceanography, 24, 1850-1866.

Yu, J., Slinn, D. N., 2003. Effects of wave-current interaction on rip currents. Journal of Geophysical Research 108(C3), 3088, doi:10.1029/2001JC001105.

Zijlema, M., Stelling, G., Smit, P., 2011. SWASH: An operational public domain code for simulating wave fields and rapidly varied flows in coastal waters, Coastal Engineering, Vol. 58, Issue 10, October 2011, pp. 992-1012, doi: 10.1016/j.coastaleng.2011.05.015.

Appendix A- Copyright Permissions

Copyright Clearance Center RightsLink®

Home | Account Info | Help

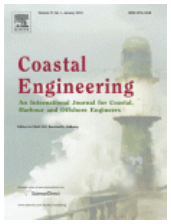

Title: Implementation and modification of a three-dimensional radiation stress formulation for surf zone and rip-current applications

Author: N. Kumar,G. Voulgaris,J.C. Warner

Publication: Coastal Engineering

Publisher: Elsevier

Date: December 2011

Copyright © 2011, Elsevier

Logged in as:
Nirnimesh Kumar
LOGOUT

Order Completed

Thank you very much for your order.

This is a License Agreement between Nirnimesh Kumar ("You") and Elsevier ("Elsevier"). The license consists of your order details, the terms and conditions provided by Elsevier, and the payment terms and conditions.

Get the printable license.

License Number	3154811267557
License date	May 23, 2013
Licensed content publisher	Elsevier
Licensed content publication	Coastal Engineering
Licensed content title	Implementation and modification of a three-dimensional radiation stress formulation for surf zone and rip-current applications
Licensed content author	N. Kumar,G. Voulgaris,J.C. Warner
Licensed content date	December 2011
Licensed content volume number	58
Licensed content issue number	12
Number of pages	21
Type of Use	reuse in a thesis/dissertation
Portion	full article
Format	both print and electronic
Are you the author of this Elsevier article?	Yes
Will you be translating?	No
Order reference number	
Title of your thesis/dissertation	Measurement and three-dimensional modeling of hydrodynamic processes in the inner shelf and the surf zone
Expected completion date	Aug 2013
Elsevier VAT number	GB 494 6272 12
Permissions price	0.00 USD
VAT/Local Sales Tax	0.00 USD
Total	0.00 USD

ORDER MORE... CLOSE WINDOW

Copyright © 2013 Copyright Clearance Center, Inc. All Rights Reserved. Privacy statement.
Comments? We would like to hear from you. E-mail us at customercare@copyright.com

Copyright Clearance Center RightsLink®

Account Info Help

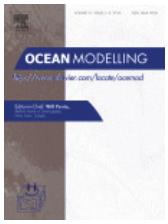

Title: Implementation of the vortex force formalism in the coupled ocean-atmosphere-wave-sediment transport (COAWST) modeling system for inner shelf and surf zone applications

Author: Nirnimesh Kumar,George Voulgaris,John C. Warner,Maitane Olabarrieta

Publication: Ocean Modelling

Publisher: Elsevier

Date: Jan 1, 2012

Copyright © 2012, Elsevier

Logged in as:
Nirnimesh Kumar
Account #:
3000659928

LOGOUT

Order Completed

Thank you very much for your order.

This is a License Agreement between Nirnimesh Kumar ("You") and Elsevier ("Elsevier") The license consists of your order details, the terms and conditions provided by Elsevier, and the payment terms and conditions.

License number	Reference confirmation email for license number
License date	May 23, 2013
Licensed content publisher	Elsevier
Licensed content publication	Ocean Modelling
Licensed content title	Implementation of the vortex force formalism in the coupled ocean-atmosphere-wave-sediment transport (COAWST) modeling system for inner shelf and surf zone applications
Licensed content author	Nirnimesh Kumar,George Voulgaris,John C. Warner,Maitane Olabarrieta
Licensed content date	2012
Licensed content volume number	47
Number of pages	31
Type of Use	reuse in a thesis/dissertation
Portion	full article
Format	both print and electronic
Are you the author of this Elsevier article?	Yes
Will you be translating?	No
Order reference number	
Title of your thesis/dissertation	Measurement and three-dimensional modeling of hydrodynamic processes in the inner shelf and the surf zone
Expected completion date	Aug 2013
Elsevier VAT number	GB 494 6272 12
Billing Type	Invoice
Billing address	701 Sumter Street, EWS 617

Dept. of Earth and Ocean Sciences
COLUMBIA, SC 29201
United States

Permissions price	0.00 USD
VAT/Local Sales Tax	0.00 USD
Total	0.00 USD

CLOSE WINDOW

Copyright © 2013 Copyright Clearance Center, Inc. All Rights Reserved. Privacy statement.
Comments? We would like to hear from you. E-mail us at customercare@copyright.com

Account Info Help

Title: Rip Currents: Beach Safety, Physical Oceanography, and Wave Modeling

Publisher: Taylor and Francis Group LLC Books

Copyright © Taylor and Francis Group LLC Books, 1969

Logged in as:
Nirnimesh Kumar
Account #:
3000659928

LOGOUT

Order Completed

Thank you very much for your order.

This is a License Agreement between Nirnimesh Kumar ("You") and Taylor and Francis Group LLC Books ("Taylor and Francis Group LLC Books") The license consists of your order details, the terms and conditions provided by Taylor and Francis Group LLC Books, and the payment terms and conditions.

License number	Reference confirmation email for license number
License date	May 23, 2013
Licensed content publisher	Taylor and Francis Group LLC Books
Licensed content title	Rip Currents: Beach Safety, Physical Oceanography, and Wave Modeling
Licensed content author	Stephen Leatherman and John Fletemeyer
Licensed content date	05/09/2011
Type of use	Thesis/Dissertation
Requestor type	Academic institution
Format	Print, Electronic
Portion	chapter/article
Number of pages in chapter/article	20
Title or numeric reference of the portion(s)	Methodology for Prediction of Rip Currents Using a Three-Dimensional Numerical, Coupled, Wave-Current Model, Chapter 5, Pg No. 87-106 in the book "Rip Currents: Beach Safety, Physical Oceanography, and Wave Modeling"
Title of the article or chapter the portion is from	"Methodology for Prediction of Rip Currents Using a Three-Dimensional Numerical, Coupled, Wave-Current Model"
Editor of portion(s)	Stephen Leatherman and John Fletemeyer
Author of portion(s)	Nirnimesh Kumar, George Voulgaris and John C. Warner
Volume of serial or monograph	N/A
Page range of portion	87-106
Publication date of portion	05/09/2011
Rights for	Main product
Duration of use	Life of current and all future editions
Creation of copies for the disabled	no
With minor editing privileges	no
For distribution to	Worldwide
In the following language(s)	Original language of publication
With incidental	no

promotional use	
Lifetime unit quantity of new product	0 to 499
Made available in the following markets	No
Specified additional information	I am an author of one of the chapters in the aforementioned book, and I would like to use this chapter as a part of my doctoral dissertation. The dissertation is published by ProQuest.
The requesting person/organization	Nirnimesh Kumar
Order reference number	
Author/Editor	Nirnimesh Kumar
The standard identifier	NKUMARDISSERTATION1
The proposed price	None
Title	Measurement and three-dimensional modeling of hydrodynamic processes in the inner shelf and the surf zone
Publisher	ProQuest
Expected publication date	Aug 2013
Estimated size (pages)	300
Billing Type	Invoice
Billing address	701 Sumter Street, EWS 617 Dept. of Earth and Ocean Sciences COLUMBIA, SC 29201 United States
Total (may include CCC user fee)	0.00 USD

CLOSE WINDOW

Copyright © 2013 Copyright Clearance Center, Inc. All Rights Reserved. Privacy statement.
Comments? We would like to hear from you. E-mail us at customercare@copyright.com